



**HAL**  
open science

# Integration of functions for endoscopy by designing multistable mechanisms produced by additive manufacturing

Benjamin Calme

► **To cite this version:**

Benjamin Calme. Integration of functions for endoscopy by designing multistable mechanisms produced by additive manufacturing. Micro and nanotechnologies/Microelectronics. Université de Montpellier, 2023. English. NNT : 2023UMONS016 . tel-04231779

**HAL Id: tel-04231779**

**<https://theses.hal.science/tel-04231779>**

Submitted on 6 Oct 2023

**HAL** is a multi-disciplinary open access archive for the deposit and dissemination of scientific research documents, whether they are published or not. The documents may come from teaching and research institutions in France or abroad, or from public or private research centers.

L'archive ouverte pluridisciplinaire **HAL**, est destinée au dépôt et à la diffusion de documents scientifiques de niveau recherche, publiés ou non, émanant des établissements d'enseignement et de recherche français ou étrangers, des laboratoires publics ou privés.

# THÈSE POUR OBTENIR LE GRADE DE DOCTEUR DE L'UNIVERSITÉ DE MONTPELLIER

En Systèmes Automatiques et Micro-Électroniques

École doctorale : Information, Structures, Systèmes

Unité de recherche : LIRMM

## Intégration de fonctions pour l'endoscopie par conception de mécanismes multistables produits par fabrication additive

Integration of functions for endoscopy by designing multistable  
mechanisms produced by additive manufacturing

Présentée par Benjamin Calmé  
Le 17 mars 2023

Sous la direction de Yassine HADDAB et Lennart RUBBERT

Devant le jury composé de

Jacques GANGLOFF	Professeur des Universités	ICube - Université de Strasbourg	Président du jury
Michaël GAUTHIER	Directeur de recherche	Institut Femto-st – CNRS	Rapporteur
Jérôme SZEWCZYK	Professeur des Universités	ISIR – Sorbonne Université	Rapporteur
Simon HENEIN	Professeur des Universités	Instant Lab - EPFL, Neuchâtel	Examineur
Yassine HADDAB	Professeur des Universités	LIRMM - Université de Montpellier	Directeur de thèse
Lennart RUBBERT	Maître de Conférence	ICube – INSA Strasbourg	Co-encadrant de thèse



UNIVERSITÉ  
DE MONTPELLIER



# Abstract

By definition, surgery is an invasive procedure because it requires the surgeon to make an incision in the patient's body to gain access to the surgical site. Minimally invasive surgery (MIS) strives to reduce trauma and recovery time by minimising the size and number of incisions. The use and the availability of appropriate tools play a major role in the success of this objective. The devices currently in use are either straight and rigid, allowing a linear trajectory, or flexible, allowing complex curved or multi-curved trajectories. The flexible instruments used, such as flexible endoscopes, extend the scope of surgery and are particularly useful in less accessible areas. They also allow the incision to be made as close to the area of interest as possible.

In the same way that a snake continually adapts the shape of its body as it moves forward, the shape of the instrument must evolve within the human body and therefore be fully controllable. A serial robotic design based on the use of compliant mechanisms with monolithic structures and shape-memory alloy actuators has proven to be an interesting way to build such architecture. The use of compliant mechanisms has allowed the design of elementary modules to meet the constraints of dimensioning and downscaling, where memory alloys are suited for their small size and high energy density. The designed modules have three stable states and are repeatable and mechanically robust. Their superposition allows high precision discrete displacements without the need for sensors (open loop control).

In order to optimise the elementary modules a design of a new version of the flexible mechanisms was carried out and an approach using electroactive polymers to replace shape memory alloys was considered to minimise the assembly phase.

The complex geometry of the mechanisms and their monolithic nature make additive manufacturing, and in particular 3D printing, a suitable manufacturing process. This parsimonious manufacturing process is part of an approach to manufacturing affordable and patient-specific robots. A prototype has been designed to validate the proposed approach.



## Résumé

Par définition, la chirurgie est une procédure invasive car elle nécessite que le chirurgien fasse une incision dans le corps du patient pour accéder au site opératoire. La chirurgie mini-invasive (MIS) s'efforce de réduire le traumatisme subi et le temps de convalescence en minimisant la taille et le nombre d'incisions. La disponibilité et l'utilisation d'outils adaptés jouent un rôle prépondérant dans la réussite de cet objectif. Les outils actuellement utilisés sont soit des éléments rigides, permettant une trajectoire linéaire, soit des structures flexibles, permettant le suivi de trajectoires complexes. Les instruments flexibles utilisés, tel que les endoscopes flexibles, étendent la portée de la chirurgie et sont particulièrement utiles dans les zones moins accessibles. Ils permettent également de réaliser l'incision au plus près de la zone d'intérêt.

La forme des instruments doit évoluer dans le corps et être contrôlable à la manière d'un serpent qui adapte continuellement la forme de son corps en avançant. Une conception robotique sérielle fondée sur l'emploi de mécanismes compliants à structures monolithiques et d'actionneurs en alliage à mémoire de forme s'est avérée être un moyen intéressant d'y parvenir. L'utilisation de mécanismes compliants a permis de concevoir des modules élémentaires pour répondre aux contraintes de dimensionnement et de réduction d'échelle. Les alliages à mémoire de forme se distinguent par leur petite taille et leur haute densité énergétique permettant l'actionnement des modules. Les modules conçus présentent trois états stables et sont extrêmement répétables et mécaniquement robustes. Leur superposition permet de générer un déplacement discret de haute précision sans avoir besoin de capteurs (contrôle en boucle ouverte).

Afin d'optimiser les modules élémentaires, une nouvelle version du module a été réalisée et une approche utilisant des polymères électroactifs a été envisagée pour remplacer les alliages à mémoire de forme afin de minimiser la phase d'assemblage.

La géométrie complexe des mécanismes et leur nature monolithique font de la fabrication additive, et plus particulièrement de l'impression 3D, un procédé de fabrication adapté à la réalisation de notre robot. Cette approche de fabrication parcimonieuse s'inscrit dans une démarche de fabrication de robots à faible coût et spécifiques à l'anatomie de chaque patients. Un prototype a été conçu et analysé pour valider l'approche proposée.



# Contents

<b>Abstract</b>	<b>i</b>
<b>List of Figures</b>	<b>ix</b>
<b>List of Tables</b>	<b>xvii</b>
<b>Introduction</b>	<b>1</b>
<b>1 Challenges of a new companionship: the medical robotics</b>	<b>5</b>
1.1 Decline of open surgery and keyhole surgery . . . . .	5
1.1.1 Minimally invasive surgery or the promise of scarless surgery . . . . .	7
1.1.2 Autopsy of an endoscope and its limitations . . . . .	8
1.2 Robotics craze and how it redefines surgery . . . . .	10
1.2.1 Definition and classification of continuum robots . . . . .	10
1.2.2 Actuation of continuum manipulators . . . . .	12
Extrinsic actuation . . . . .	12
Intrinsic actuation . . . . .	15
1.3 Current limitations of continuum robots . . . . .	18
1.3.1 Modeling of continuum robots . . . . .	18
Most common modelling approaches . . . . .	19
1.3.2 Continuum robots control strategies . . . . .	24
Approaches based on kinematic models . . . . .	25
Wrench-based control strategies . . . . .	25
Adaptive control and reinforcement learning approaches . . . . .	26
1.3.3 Manufacturing process . . . . .	27
1.3.4 Discussion on the use of continuum robots . . . . .	28
1.4 Towards a snake-like robot based on multistable modules . . . . .	30
1.4.1 Hyper-Redundancy and snake-like robot in Medicine . . . . .	30
1.4.2 Digital Robotics . . . . .	31
1.4.3 Contributions . . . . .	33
<b>2 Specification for the design of a new kind of robot based on multistable modules</b>	<b>35</b>
2.1 Constraints and design considerations . . . . .	36
2.1.1 Anatomical constraints and required performances . . . . .	36

## Contents

---

2.1.2	Choice of a serial modular architecture . . . . .	37
2.2	Module design: compliant mechanism and actuation principle . . . . .	38
2.2.1	Compliant Mechanism and (multi-)stability principle . . . . .	38
	Compliant mechanisms . . . . .	38
	Multistable mechanisms . . . . .	39
2.2.2	Choice of actuators and implementation in the modules . . . . .	41
	Smart materials for robotics actuation . . . . .	42
	SMA operating principle and mechanical model . . . . .	43
2.3	Manufacturing . . . . .	45
	Additive manufacturing process . . . . .	45
	Material characterisation . . . . .	46
2.4	Conclusions . . . . .	47
<b>3</b>	<b>Design of the elementary multistable module</b>	<b>49</b>
3.1	Design and sizing of a tristable mechanism . . . . .	50
3.1.1	Analytical modelling of a preformed-beams bistable mechanism . . . . .	51
	Stress analysis . . . . .	51
	Stress and strain energy analysis . . . . .	53
3.1.2	Modelling of the vertical beam of the tristable mechanism . . . . .	54
3.2	Positioning compliant mechanism . . . . .	56
3.2.1	Flexible joint . . . . .	56
3.2.2	Operation and sizing of the mechanism . . . . .	58
3.2.3	Kinematic model of the mechanism . . . . .	59
3.3	Design of the linear guiding mechanism . . . . .	60
3.3.1	Parallel spring stage . . . . .	60
3.3.2	Compound parallel spring stage . . . . .	61
3.4	Actuation . . . . .	61
3.4.1	Joule effect thermal activation . . . . .	62
3.4.2	SMA wires actuators sizing . . . . .	63
3.5	Convergence of analytical and numerical models to obtain a set of parameters, and experimental validation . . . . .	65
3.5.1	Finite element analysis, simulation and validation . . . . .	65
3.5.2	Experimental validations . . . . .	67
	Design and manufacture of a tristable module . . . . .	67
3.5.3	Tristable mechanism characterisation . . . . .	68
3.5.4	Experimental validation of a macroscopic module . . . . .	69
3.5.5	Conclusion . . . . .	70
<b>4</b>	<b>Distributed actuation snake-like robot</b>	<b>73</b>
4.1	Direct kinematic model and working space of the robot . . . . .	74
4.1.1	Direct kinematic model . . . . .	74
4.1.2	Robot workspace . . . . .	75
4.1.3	Addressing robot configurations . . . . .	76

---

4.2	Prototype assembly and experimental validation . . . . .	76
4.2.1	Experimental validation . . . . .	78
4.3	Inverse kinematic model and Path planning . . . . .	80
4.3.1	Geometrical Method for Computing the Inverse Kinematics . . . . .	80
	Search for the closest position to a desired position . . . . .	80
	Geometric resolution of the inverse kinematic model . . . . .	82
4.3.2	Path planning . . . . .	84
	Dynamic programming and Hidden Markov Model to find an optimal configuration . . . . .	85
	Dynamic programming and Hidden Markov Model to find an optimal configuration . . . . .	86
	Consideration of anatomical constraints . . . . .	88
4.4	Conclusion . . . . .	89
<b>5</b>	<b>Enhancement of the mechanisms and contribution of 3D printing of composites</b>	<b>91</b>
5.1	Enhanced bistable mechanism for improved lifetime and manufacturability by hyperstaticism analysis . . . . .	92
5.1.1	Degrees-of-freedom and constraint of a mechanism . . . . .	93
5.1.2	Screw algebra . . . . .	95
5.1.3	Theoretical optimal version of the double preshaped beam bistable mech- anism . . . . .	97
5.1.4	Mechanism characterisation . . . . .	100
	Classical bistable mechanism . . . . .	100
	Enhanced bistable mechanism . . . . .	101
5.1.5	Experimental set-up and protocol validation . . . . .	102
5.1.6	Experimental results . . . . .	103
	Inflection points and fatigue . . . . .	103
	Mechanism lifetime comparison . . . . .	104
	Parasitic error quantification . . . . .	106
	Benefit on manufacturing using the enhanced mechanism . . . . .	108
5.1.7	Integration of the new bistable mechanism within the module . . . . .	109
5.2	Fully 3D printed module with integrated actuation system . . . . .	110
5.2.1	Design and modelling of the electrothermal actuator . . . . .	111
	V-shape actuator analytical model . . . . .	112
5.2.2	Design and analysis of a proof of concept: the $XYZ\theta$ positioning system .	114
	Compliant mechanism for X and Y linear motions . . . . .	114
	Compliant mechanism for rotational guiding . . . . .	116
	Implementation of a motion along Z . . . . .	119
5.2.3	Voltage distribution in the monolithic in the XY compliant mechanism .	120
5.2.4	Finite element analysis and experimental characterisation . . . . .	121
	Multiphysics Finite Element Analysis . . . . .	121
	Experimental characterisation of the material . . . . .	122

## Contents

---

Experimental characterisation of the V-shaped electrothermal actuator .	123
Experimental characterisation of the positioning system . . . . .	124
5.2.5 Control strategy of the actuator . . . . .	127
5.3 Conclusions . . . . .	129
<b>6 Perspectives</b>	<b>131</b>
6.1 Explore areas for improvement in 3D printing . . . . .	131
6.1.1 Stereolithography (SLA): a miniaturisation approach . . . . .	131
6.2 Implementation of communication protocols for robot control . . . . .	132
6.2.1 Communication protocol and evaluation . . . . .	133
6.2.2 Implementation of PCBs . . . . .	134
6.3 Considerations for improving the robot architecture . . . . .	135
6.3.1 Extension to a second bending plane . . . . .	135
6.3.2 The last but not least module . . . . .	135
<b>Conclusion</b>	<b>137</b>
<b>7 List of publications</b>	<b>139</b>
<b>A Stiffness and compliance matrix analysis</b>	<b>141</b>
<b>Bibliography</b>	<b>145</b>

# List of Figures

1.1	Medical robotics Benjamin Calmé . . . . .	5
1.2	Endoscopic surgery today. The surgeon in the front manipulates the handle of the endoscope with one hand and controls the insertion of the tool with the other hand. The assistant surgeon holds only the tool actuator in his hand. . . .	6
1.3	The three main approaches to minimally invasive surgery. Extraluminal on the left, endoluminal in the centre and transluminal on the right. . . . .	7
1.4	(1.) Illustration of the functioning principle of an endoscope: (1.A) The generation of an angle at the control section causes a deformation of the flexible section, the detail of which is shown in (1.B)[116]. (2.) Degrees of freedom of flexible endoscope for therapeutics [175]. . . . .	8
1.5	Categorisation of medical robots according to their kinematics. a. Redundant [66], b. Hyper-redundant and discrete (OC Robotics), c. Hyper-redundant (continuum) [167] and d. Soft [38] . . . . .	11
1.6	Extrinsic actuation method: 1. cable actuated robot [144], 2. Concentric tube robot (adapted from [62, 63]) . . . . .	13
1.7	Flexibility problem of an endoscope in MIS. In practice: the configuration taken by the endoscope results from contact with the tissue. These contacts can be those linked to the insertion of the endoscope and those generated by the operation of the tools. Desired situation: the endoscope moves within the hollow organ without generating friction and is able to stabilise itself for the procedure.	14
1.8	Intrinsic actuation method: 1. Pneumatic artificial muscles [211], 2. and 3. Fluidic elastomer actuators in gelatin [188] or silicon. . . . .	15
1.9	Demonstrators exploiting the different actuation principles mentioned: 1. Cable actuated Robot (STRASS) [144] 2. Concentric tube robot [140] 3. Fluidic elastomer actuator (STIFF-FLOP) [38] 4. Multi-backbone [140] . . . . .	16
1.10	Schematic representation of the classical modelling approaches of continuum robots : (a) Variable curvature, a transformation derivative integrated along the robot length, (b) Constant curvature, arc segment to segment transformations, and (c) Pseudo-rigid body, rigid link to link transformations. $f(s)$ and $\tau(s)$ represent the forces and torques along the robot respectively. (Adapted from [167, 40]) . . . . .	19

## List of Figures

---

1.11	Concept of dual-arm concentric tube continuum robots and its control block-diagram. Gray box represents the primary task, pink is the secondary task, green is the robot's kinematic model, blue stands for exteroceptive sensing. A: robot A, AB: dual-arm robot, d: desired, r: resultant, s: sensors, c: current, e: end-effector, $\lambda$ : control gain and X: pose. [34]. . . . .	25
1.12	Compliant motion controller. The compensation term $\lambda$ enters a Moving Average Filter (MAF) prior to entering the feedback loop. The feedback signal is filtered through a dead-band to minimize chattering [71]. . . . .	26
1.13	Flowchart of the Kalman-filter-based control scheme used to estimate the Jacobian of the continuum robot [124]. . . . .	27
1.14	Overview of a machine learning-based closed-loop kinematic controller for a continuum manipulator [202]. . . . .	28
1.15	Compliant cable actuated device [83] and pneumatic actuator [221] made by 3D printing. . . . .	29
1.16	Follow the leader deployment strategy (FTL). Illustration of the video game Nibbler (1980) in which a snake moves through a maze using the FTL method (left) a shape-shifting mechanisms able to performe FTL motion (right) [84]. . .	30
1.17	Digital robot architecture designed with components from traditional mechanics: 1. the VGT [170], and flexible mechanics: 2. the BRAID [125],. The architecture of the VGT is given for 3 modules and is accompanied by details of the hydraulic actuation, the active linkage and joint, respectively from top to bottom. 3. A binary hyper- redundant electromagnetically actuated manipulator [200].	32
2.1	Representation of the anatomical curvature to be crossed to reach the throat. .	36
2.2	Principle of the 3-states module based snake-like robot developed to perform complex trajectories in a confined environment. Each state of the module is identified as a balanced ternary signed-digit, i.e. $\bar{1}, 0, 1$ . . . . .	38
2.3	Representation of the stable and unstable states of a pendulum and a bistable actuator. . . . .	39
2.4	Strain energy, reaction force and tangential stiffness of a bistable mechanism (on the right) where $s_1, s_2$ are stable positions, $u$ is unstable position and $\zeta_1, \zeta_2$ correspond to zero stiffness positions. [224] . . . . .	40
2.5	Example rendering of a hyper-redundant robot based on multistable modules.	41
2.6	Usual actuation force vs. response time for actuators based on "smart" materials. Abbreviations: EAC, electroactive (normally piezoelectric) ceramics; EAP, electroactive polymers; SMP, shape-memory polymers; SMA, shape-memory alloys; MEMS, microelectromechanical systems; magMEMS, Magnetic microelectromechanical systems; NEMS, nanoelectromechanical systems [45] . . . .	42
2.7	Stress-strain-temperature curvature of a NiTi SMA wire . . . . .	43
2.8	Characterisation of the most common materials used in 3D printing (adapted from formlabs) . . . . .	44

2.9	Characterisation of the most common materials used in 3D printing based on experiments conducted during this work and supplier data. . . . .	48
3.1	Illustrations of the 3 mechanisms composing the module as well as the module as it was manufactured by 3D printing. Illustrations of the 3 mechanisms composing the module as well as the module as it was manufactured by 3D printing. . . . .	49
3.2	Photography of all states of an hexastable mechanism. . . . .	50
3.3	Geometric parameter identification of a double double beam bistable mechanism. . . . .	51
3.4	Representation of the first three buckling modes. . . . .	53
3.5	Representation of a tristable double-beam based mechanism illustrated in its three stable equilibrium positions. The fabricated configuration corresponds to the first stable state. . . . .	54
3.6	Representation of a pre-curved bistable mechanism and the evolution of the force $f$ as a function of the position $d$ (subfigure a). The subfigures b and c illustrate respectively a buckling beam in the case of theoretical guided-fixed end condition and in the real end condition with a slider. . . . .	55
3.7	Photograph of flexible mechanisms produced monolithically in a glass needle [225, 61]. . . . .	57
3.8	Schematic representation of an elliptical notch flexure hinge. . . . .	58
3.9	Geometric model of half of the compliant structure in initial configuration on the left and deflected on the right. Mechanical correspondence in the initial configuration in red in the CAD model. . . . .	59
3.10	Parallel spring stage to the equilibrium and deformed by a force. . . . .	60
3.11	Diagram of the tristable mechanism showing the three states assumed by the vertical beam on the left, and the effect of the deformation of the vertical beam on the parallel spring stage on the right. . . . .	61
3.12	Principle scheme for the actuation of the tristable mechanism integrating the SMA wires . . . . .	62
3.13	Electrical circuit for actuating the SMAs. . . . .	64
3.14	Displacement and force exerted by the SMA wires as a function of time. Representation of the states of the corresponding module. . . . .	64
3.15	Algorithm to assist in module design and actuator sizing. . . . .	65
3.16	FEA rendering of the bistable mechanism (a.) and the tristable mechanism (b.) deformations (displacement in mm) . . . . .	66
3.17	Force-displacement curves comparison between analytic modelling and finite element analysis . . . . .	67
3.18	Comparison between the maximal stress evolution during deflection between the analytic model and the FEA results . . . . .	68

## List of Figures

---

3.19	Curves of the evolution of the deformation energy during the displacement. (a.) comparison of the analytical and numerical results of the energy study for the bistable mechanism, and (b.) result of the numerical analysis in the case of the tristable mechanism. . . . .	68
3.20	Tristable module CAD model: Exploded view of the three mechanical components. The numbers indicate the pieces and the colours and the letters indicate the mechanisms. Actuators are shown schematically for ease of understanding (Left). 3D printed tristable module assembled (Right). . . . .	69
3.21	Experimental setup to characterise the mechanism. The frame containing the tested mechanism measures 32×21mm. . . . .	70
3.22	Force-Displacement curves of the bistable mechanism: analytical model presented in continuous line, Finite Element Analysis (FEA) in dashed line and experimental results conducted on 10 mechanisms in orange. . . . .	71
3.23	Experimental setup used to validate the operation of the module A with a load. In this case the load is 5 times the weight of the module (63g). . . . .	71
3.24	Planar tristable mechanism: as fabricated on the right and, in the two other stable equilibrium positions on the left. The experimental setup is detailed in Fig. 5.8. . . . .	72
4.1	Representation of a tristable double-beam based mechanism illustrated in its three stable equilibrium positions and their integration into the module based snake-like robot. The fabricated configuration corresponds to the first stable state. . . . .	74
4.2	End-effector workspace generated for a 4-module architecture with fixed proximal end and some configuration examples. . . . .	75
4.3	Prototype with 4 modules in reference position without power supply. . . . .	77
4.4	Schematic representing routing and operating principle. . . . .	77
4.5	Photos of three configurations taken by the robot with the associated ternary words. . . . .	78
4.6	Representation of the robot's workspace envelope, with the estimated positions in blue ring and the measured positions in black star. A zoom is made along the X-axis with respect to Fig. 4.1 for the sake of readability. . . . .	79
4.7	Realistic rendering of the insertion of the robot into the body at three given moments. The modules used in this illustration have smaller dimensions than those of the prototype. In this case, the dimensions are those of the miniaturised modules presented in the outlook. . . . .	80
4.8	Illustration of the search for the closest positions to a desired position for a 4-module robot. The desired position is in red and the closest positions that the robot can reach are in green. The tolerance has been increased in the case of the figure on the right. The position along the X and Y axes is given in mm. . . . .	81

4.9	Inverse kinematics model parameters identification: (top) locating the mid-point for the inverse kinematic computation and (bottom) alternative poses of a 8-modules robot for different values of the base angle $\phi$ . . . . .	83
4.10	End-effector workspace generated for a 4-module architecture with fixed proximal end and some configuration examples. . . . .	84
4.11	Determination of an optimal trajectory with the Viterbi algorithm. The path in blue is the surviving path. . . . .	87
4.12	Illustration of the steps to deploy the structure to a desired position according to an optimal configuration defined by the algorithm. $L_m$ is the module length. . . . .	87
4.13	Illustration of the steps involved in anatomically constrained modelling. . . . .	89
5.1	DOF calculated for the planar mechanism according to the Kutzbach-Grübler criterion. . . . .	93
5.2	Application of the generalised formula [147, 6] for the determination of the degrees of freedom of a flexible beam in the plane. . . . .	94
5.3	Constraint and freedom space of compliant mechanisms : (a) a 3-DOF leaf spring, (b) a 1-DOF parallel spring stage, and (c) a 1-DOF double parallel spring stage use as basis for bistable mechanisms. The illustrations show the mechanism before axial loading, but this does not affect the analysis of the bistable. . . . .	96
5.4	A rod-based version (a) of the mechanism and a hybrid rod-blade version (b) justifying the realisation of a design with minimal constraints. . . . .	97
5.5	Comparison of the permissible stroke between a beam and a rod, obtained after successively calculating the diameter $d$ for different $t - w$ ratios . . . . .	99
5.6	Representation of a theoretical bistable mechanism, before axial loading and buckling of the rods, justifying minimal constraints based on the FACT method. . . . .	100
5.7	Constraint and freedom space of enhance bistable mechanism . . . . .	100
5.8	Set-up used for the experimental characterisation of bistable mechanisms. . . . .	102
5.9	Comparative graph of analytical, numerical and experimental results of the evolution of the snapping force in function of displacement for the <i>classic</i> and <i>enhanced</i> mechanism. . . . .	104
5.10	Illustrations of half-mechanisms showing the beams of <i>classic</i> bistable mechanisms in various buckling mode. . . . .	105
5.11	Illustration of the alteration of the initial shape of the beams due to the relaxation of the material three weeks after printing for one of the mechanism used. . . . .	105
5.12	Photograph of an <i>enhanced</i> mechanism made with 3D printing in its two stable configurations: a. Fabricated and b. Deformed . . . . .	105
5.13	Experimental triggering force $f_{top}$ distribution for each of the mechanisms studied over time. . . . .	106
5.14	Experimental triggering force $f_{bot}$ distribution for each of the mechanisms studied over time. . . . .	107
5.15	Comparison of the experimentally measured maximum number of actuations before breaking for each of the two variations (10 of each). . . . .	107

## List of Figures

---

5.16	Evolution of the parasitic displacement of the shuttle $\xi$ during the state change.	108
5.17	Extraction of information from the G-code commands of a 3D printer. . . . .	109
5.18	Illustration of the operation of the module including the 3-beam bistable mechanism. . . . .	110
5.19	Electrical representation based on a resistor set equivalent to the monolithic positioning system. . . . .	110
5.20	Schematic representation of the analytical modelling of the actuator . . . . .	111
5.21	CAD model illustration of the V-shaped electrothermal actuator and parameter identification. . . . .	112
5.22	Temperature distribution within the actuator based on the analytical model. .	113
5.23	Structure of the 3D-printed monolithic $XYZ\theta$ positioning system. . . . .	115
5.24	Structure of the 3D-printed monolithic $XYZ\theta$ positioning system (unit: mm). The movements allowed per component are indicated by the arrows. . . . .	116
5.25	3D-printed monolithic compliant mechanism for XY linear guiding (unit: mm).	116
5.26	Operational principle of the linear compliant mechanism for two axes translational motions. . . . .	117
5.27	3D-printed monolithic compliant mechanism for $\theta$ rotational guiding (unit: mm).	117
5.28	Schematic of a two-blade RCC pivot and its integration into a half-pin (symmetrical on both sides of the axis) . . . . .	118
5.29	Schematic of a two-blade RCC pivot and its integration into a half-pin (symmetrical on both sides of the axis) . . . . .	119
5.30	3D-printed monolithic Z linear guiding (unit: mm). . . . .	119
5.31	Electrical representation based on a resistor set equivalent to the monolithic positioning system. . . . .	120
5.32	Finite element simulation result for a 2D positioning system. (5.32a) represents the CAD of the positioning system manufactured in bi-material. (5.32b) and (5.32c) illustrate the simulation results obtained by FEA following the actuation of the left actuator and the left and bottom actuators. (5.32d) represents the CAD of the monolithic positioning system. (5.32e) and (5.32f) illustrate the thermo-mechanical and electrothermal FEA results of the same simulation, following the actuation of the left actuator with the monolithic positioning system. The sub-figures (5.32d)(5.32e)(5.32f) are illustrated in perspective in order to visualise the pattern used to increase the resistance of the sections between actuators. .	121
5.33	Finite element simulation result of the rotational guiding system (displacement in mm). . . . .	123
5.34	Finite element simulation result of the monolithic $XYZ\theta$ system (displacement in mm). . . . .	124
5.35	Experimental set-up for the characterisation of the electro-thermal actuator . .	124
5.36	Displacement obtained for the electrothermal actuator as a function of the input voltage. . . . .	125
5.37	Experimental setup of the XY positioning system. . . . .	125

5.38	Experimental characterisation of the XY positioning system. The numbers on the dials of the Keyence sensor show the displacement in centimetres. The top image (a.) represents the initial state and the middle (b.) and bottom (c.) images show the amount of displacement in the direction of the arrows in response to an actuation. . . . .	126
5.39	3D printed monolithic XYZ $\theta$ positioning system . . . . .	127
5.40	On the left, the step response of the system representing the displacement of the actuator as a function of time following power-up. On the right, the intermediate response of the system where the temperature evolution after power up is represented. The delay is present during the temperature rise of the system. . . . .	128
5.41	Structure of Smith predictor based on PI control strategy. . . . .	129
5.42	Schematic of the experimental set-up used to validate the actuator control strategy and step response in open-loop, with the PI controller and with the Smith Predictor. . . . .	129
6.1	Photograph of miniaturised modules obtained by stereolithography (in grey) and representation of the achievable workspace, and some configurations (solid, dashed and dotted lines), with a prototype of equivalent length but composed of the miniaturised module. . . . .	132
6.2	Scale illustration with realistic rendering for the mechanism printed in SLA. . .	133
6.3	Illustration of the movement performed by the robot following the sending of information from a master board to slave boards controlling the motors. . . . .	134
6.4	Realistic rendering of the holding system of the electronic board inside the module and the 3D printed version. . . . .	135
6.5	Simulated workspace of the ternary robot with 8 modules alternating successively by an angle of $\pi/2$ . The positions in the X, Y and Z axes are given in millimetres. . . . .	136



# List of Tables

1.1	Comparison of the characteristics and performance of three selected endoscopes used in the operating theatre (unit in mm). . . . .	9
1.2	Comparison of properties and characteristics of continuum robots based in the literature review (*actuators number). DOFs include only those of the endoscope without the addition of tools. . . . .	17
1.3	Comparison of properties and characteristics of hyper-redundant robots in the literature. . . . .	32
3.1	Tristable mechanism design parameters . . . . .	65
5.1	Design parameters in mm . . . . .	99
5.2	Design parameters . . . . .	122
5.3	Performance comparisons between the proposed XY positioning system and previous reported parallel stages (*FEA results). . . . .	127
5.4	Performance comparisons between the proposed XYZ $\theta$ positioning system and previous reported parallel stages (*estimated). . . . .	128



# Introduction

At the end of the 1980s, the fiction described by Karel Capek and Issac Assimov in the 1920s and 1940s started to emerge into the real world. The use of robots is no longer limited to industrial applications such as production lines and are now part of environments where they are in contact with humans, such as operating theatres.

The first surgical robots attempted to address the problems faced by the surgeon in performing repetitive and precise tasks and in achieving telepresence. The first of these to be used on human patients had to be pre-programmed to fixed, patient-specific, anatomical landmarks and could not be used on dynamic surgical targets [119, 2]. Teleoperation and master-slave systems appeared shortly afterwards and gave a new impetus through the Space Exploration Initiative (SEI). The objective was to carry out medical operations in space from Earth. However, the marketing of automated systems did not begin until 1993 with the approval of the first endoscopic manipulator by the U.S. Food and Drug Administration (FDA). Despite this, the first generations of surgical robots were criticized due to their excessive cost and questioned added value [146].

The robotic platforms that were subsequently developed were designed in collaboration with surgeons. They have become more specific and better adapted to the constraints of the operating theatre. At the same time, the surgical practice has also evolved to become minimally invasive, even described as scarless. The most representative example of this is laparoscopy, for which there has been a rapid development of an adapted robotic platform. This surgical procedure limits the size of the scars to the insertion of trocars allowing the passage of instruments through the abdominal wall and the observation and intervention on the organs of the abdominal or pelvic cavity. These constraints complicate the surgeon's manipulation by reducing accessibility to the operating site. Hence, the robot provides greater comfort and dexterity.

A more recent alternative to laparoscopy is to perform surgery using natural orifices, i.e. Natural Orifice Transluminal Endoscopic Surgery (NOTES). With this approach, the incision is made as close to the surgical site as possible, from inside the body, e.g. from the stomach.

In this case, the comfort for the patient implies considerable constraints in terms of engineering. Indeed, access through the natural route involves moving through confined and tortuous environments. Robotic architectures capable of performing such tasks are therefore inspired by the robots initially developed for the maintenance of nuclear power plants or

## Introduction

---

oil platforms. However, one constraint remains very challenging, namely downscaling. The miniaturisation and assembly of structures embedding motors and sensors is complex and tedious. Continuum robots, and in particular cable-driven robots, have therefore been widely favoured because of their remote operation and very small footprint. However, the control of these robots remains complex and energy consuming.

Our contribution consists in proposing an alternative architecture allowing to reduce the assembly phase and whose mechanical robustness avoids complex control laws. The proposed structure follows the concept of digital robotics and binary manipulators described in the literature. More precisely, the proposed robot extends the principle of using bistable modules to that of multistable modules and makes it possible to propose an innovative and original serial architecture.

The module is based on flexible mechanisms that can be manufactured monolithically and are characterised by good mechanical performance and the ability to be miniaturised as required. The use of these mechanically robust modules allows for precise positioning of the end effector through open loop control, as the structure does not require sensors. Furthermore, this structure only needs to be operated to change its configuration and not to maintain it, which is more energy efficient than the approaches described in literature.

A discrete tree-like workspace with high redundancy is derived from the modelling of this digital robot. As a result, the robot can perform "follow the leader" motion which is useful for minimally invasive surgical procedures.

This manuscript is divided into 6 chapters. In Chapter 1, the context of the medical application is presented, specifically minimally invasive surgery, and the main robotic approaches that have been studied to assist the surgeon are presented. In particular, the case of continuum robotics is discussed, with the strengths and limitations of each of the research axes highlighted. The positioning of this work and its contributions are then given.

Anatomical constraints specific to minimally invasive surgery of the upper gastrointestinal tract are introduced in Chapter 2. Afterwards, the design choices that led to the proposed robotic architecture are addressed.

Chapter 3 gathers the different phases of design of the elementary module allowing to design the robot. The dimensioning was carried out according to the complex trajectory and manufacturing constraints of the mechanism introduced in the previous chapter. A validation of the behaviour of this module was carried out by a finite element analysis as well as an experimental characterisation allowing to validate the coherence of the approach.

In Chapter 4, the core contribution of this research is addressed, namely the design and validation of the new robotic architecture. The kinematics of this digital serial architecture is detailed as well as an experimental characterization. The first steps of path planning are also introduced.

Chapter 5 presents the approaches investigated in order to improve the operation of the

module and therefore the robot. Firstly, an approach is described that increases the life span of bistable mechanisms by reducing the problem of hyperstatism. Then, in a second part, the feasibility of designing a module limiting the assembly phase by printing the actuators directly in the structure is explored.

Chapter 6 proposes different perspectives to the work carried out, such as the embedding of PCBs (Printed Circuit Boards) within the modules and the communication between the modules.

Finally, a conclusion is given on these 3 years of PhD and on the proposed approach to the design of a serial digital robot for applications in the context of minimally invasive surgery.



# 1 Challenges of a new companionship: the medical robotics



Medical robotics  
Benjamin Calmé

## 1.1 Decline of open surgery and keyhole surgery

In 1901, on the fringes of the first Nobel Prize ceremony, medicine witnessed the beginning of what is now known as minimally invasive surgery (MIS) or keyhole surgery. A new kind of operating procedure, that unlike open surgery, aims at reducing the size of incisions. The basic operating concept of MIS is to insert the surgical instrument, e.g. endoscopic camera, percutaneous needle, grasper, etc., into the patient's body through an entry port, either natural or created by a small incision. In that respect, the surgical procedure can be performed inside



Figure 1.2 – Endoscopic surgery today. The surgeon in the front manipulates the handle of the endoscope with one hand and controls the insertion of the tool with the other hand. The assistant surgeon holds only the tool actuator in his hand.

the patient's body at the tip of the instrument. The first principles of these laparoscopic surgeries and thoracoscopy were laid by Kelling and Jacobaeus [127]. The latter was also the first to define the constraints and limitations of such procedures, particularly related to the risk of injuring organs when inserting the trocar. He will express the first need for the development of specific tools and equipments to best perform this new type of surgery [104].

With the advent of MIS and the development of specific tools, the ideal of the barber-surgeon<sup>1</sup>, whose greatness was proportional to the size of his scars, is disappearing. This change in philosophy is accompanied by net post-operative benefits for the patient and by an increase in the complexity of the operations for the surgeon [117, 206]. The technical gestures become procedure-specific (multi-port or single-port surgery) and are accompanied by a loss of traditional references and feedbacks. The tactile information taken during the palpation of a tissue disappears and is done through the tool, handled from the outside. Despite an extremely precise monitoring of the patient through numerous probes and imaging devices, the surgery requires greater efforts of interpretation, as illustrated in Fig. 1.2.

In the following sections of this chapter, the challenges of MIS are discussed, as well as the

---

<sup>1</sup>A barber-surgeon was a medical practitioner in the Middle Ages who combined the roles of barber and surgeon. They were responsible for performing a wide range of medical procedures, including bloodletting and wound treatment, as well as cutting hair and shaving beards. The term "barber-surgeon" is no longer in use, as the two professions have since become separate and specialized. Its use is now restricted to caricature the performance of particularly invasive procedures. Ambroise Paré, recognised as the father of modern surgery, was a master barber-surgeon.

## 1.1. Decline of open surgery and keyhole surgery

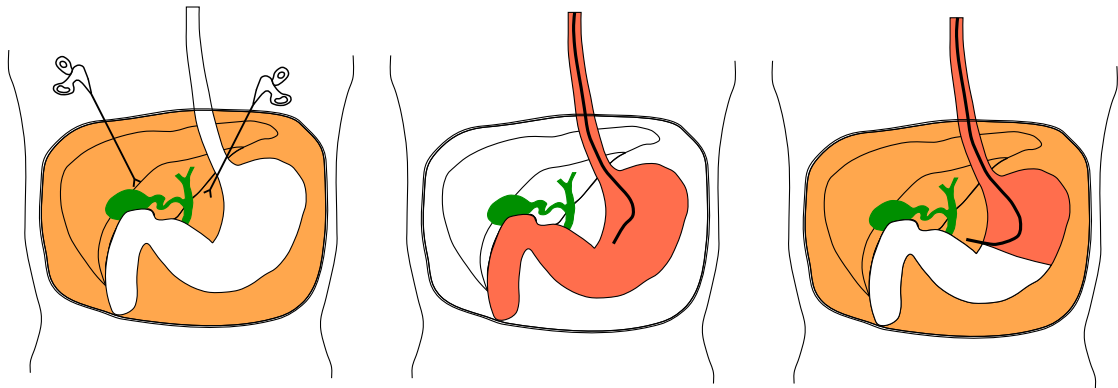


Figure 1.3 – The three main approaches to minimally invasive surgery. Extraluminal on the left, endoluminal in the centre and transluminal on the right.

robotic solutions provided and their limitations, to finally position our contributions.

### 1.1.1 Minimally invasive surgery or the promise of scarless surgery

In medicine, any procedure that requires an infraction of the covering epithelia is considered as invasive. In other words, this refers to any procedure that may affect the body by breaching the skin or mucous membranes covering the lumen of hollow organs.

Minimally invasive surgery limits incisions to the strict material requirements (number and size of tools). This approach makes it possible to reduce the risk for the patient, the trauma to the body, the post-operative pain, and consequently the recovery time [201]. The literature reports 3 approaches to MIS [210], also represented in Fig. 1.3:

- The extraluminal approach: the surgeon makes 3 to 4 incisions whose dimensions correspond to the diameter of the trocars used in order to stabilise the entry points of the instruments. The first incision is used to insert the endoscope and realise a pneumoperitoneum (air insufflation in the peritoneal cavity) and the others are for the insertion of the tools into the body cavity. This approach is mainly used for therapeutic and exploratory purposes. More recently, a variant of this approach has been developed, the *single port surgery*. This technique reduces the invasiveness by using a single incision, typically made at the umbilicus, through which all the instruments are inserted. This technique has a similar rate of success, patient safety, and recovery-time to laparoscopy.
- The endoluminal approach: this technique uses natural orifices to access hollow anatomical structures such as the oesophagus or intestines. This approach is particularly used by gastroenterologists in the context of digestive endoscopy. It allows visual exploration of the different parts of the digestive tract, but also the performance of diagnostic (polypectomies and biopsies) or therapeutic procedures (radio-frequency ablation in the treatment of Barrett's oesophagus)

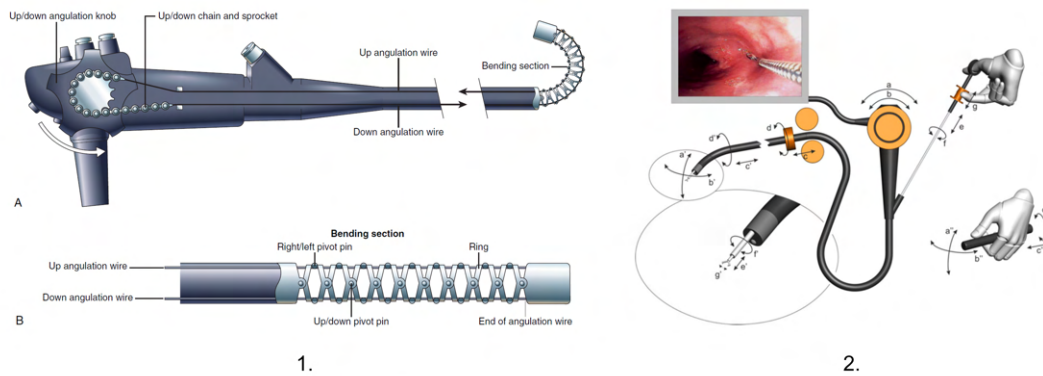


Figure 1.4 – (1.) Illustration of the functioning principle of an endoscope: (1.A) The generation of an angle at the control section causes a deformation of the flexible section, the detail of which is shown in (1.B)[116]. (2.) Degrees of freedom of flexible endoscope for therapeutics [175].

- The transluminal approach: this approach involves accessing the peritoneal cavity, through an incision in the lumen. This technique, also known as Natural Orifice Transluminal Endoscopic Surgery (NOTES), involves inserting instruments into the body from the natural orifices and then making an incision in the intestinal barrier or stomach. The feasibility was demonstrated in 2004 [109] and leaves the patient with no externally visible scar, hence the name "no scar surgery".

The use of rigid endoscopes and rigid tools limits applications to operating areas close to the insertion points and makes manipulation in a restricted area more complex. This constraint has therefore led to an increased use of endoluminal and transluminal approaches despite the challenge to reach the operating site. Indeed, access to the organ through natural openings requires the deployment of a flexible tool that must be able to follow complex trajectories in a narrow environment and whose integrity must be respected.

### 1.1.2 Autopsy of an endoscope and its limitations

The most commonly used device in MIS is a manual flexible endoscope, as illustrated in Fig. 1.2, which allows the visualisation of the lumen of hollow organs and the exploration of most segments of the gastrointestinal tract. The vast majority of them are based on similar mechanical architectures, as shown in Fig. 1.4 and whose characteristics are given in Tab. 1.1. This table highlights the strong similarity of the endoscopic devices regardless of the supplier. However, there is a difference between gastroscopes and interventional endoscopes. The latter have larger diameters to allow the passage of multiple and larger instruments. Their channels tend to stiffen the structure and decrease its performance.

This architecture consists of three parts: a control section, a flexible tube, and a bending section.

## 1.1. Decline of open surgery and keyhole surgery

Ref	diameter	length	architecture	DOF	Actuator	Deflection	Control
Standard gastroscopes							
STORZ Silver scope	9.3	1100	vertebrae	2	cables (manual)	up/down 210°/100°, left/right 120°/120°	-
PENTAX Medical EG29 -i10	9.8	1050	vertebrae	2	cables (manual)	up/down 210°/100°, left/right 120°/120°	-
Interventional endoscopes							
OLYMPUS TJF TYPE Q180V	13.7	1240	vertebrae	2	cables (manual)	up/down 120°/90°, left/right 90°/110°	-

Table 1.1 – Comparison of the characteristics and performance of three selected endoscopes used in the operating theatre (unit in mm).

- The flexible tube is the passive part of the endoscope. It is made up of different braided metal layers that ensure robustness and are "used" by surgeons through certain postures to transmit torque and forces to the tip of the endoscope. For safer interactions with soft tissues, different layers of polymer cover this tube.
- The appearance of the control section may vary between suppliers, but most often it is a handle from which the bending of the flexible part can be controlled by a set of wheels. The majority of endoscopes have two control wheels that allow the flexible section to be bent in two orthogonal planes.
- The flexible section consists of a succession of vertebrae, the morphology of which will also depend on the supplier and model of endoscope. The cables that allow its actuation are attached at the distal end of this section. By rotating one of the wheels of the control section, tension is created in the cables. This causes the vertebrae to rotate and the bending of the section on the side of the cable.

Most of the difficulties identified by gastroenterologists and endoscopic surgeons stem from manipulating the endoscope. Operating the knob that controls the robot is not intuitive and control is complicated by the fact that the configuration of the endoscope inside the patient's body is not known. Indeed, during insertion, the endoscope is in contact with tissues and the shape vary between patients as they depend on anatomical constraints [191].

During procedures, the use of these endoscopes remains a challenge. The lack of triangulation<sup>2</sup> due to the parallel positioning of the instruments, the lack of manoeuvrability of the flexible section, and the difficulty in obtaining a stable view, make this instrument complex to handle [156]. As a result, this procedure is only performed routinely by a small number of skilled endoscopists [148]. In addition, endoscopes used for MIS, equipped with at least two standard

<sup>2</sup>Triangulation is a technique used in minimally invasive surgery, such as laparoscopic surgery or flexible endoscopic surgery, to create a stable working area and improve visualization of the surgical field. It is achieved by positioning the surgical instruments at different angles, creating a "triangle" of instruments. This allows the surgeon to work from different angles and improves access to the target.

instruments, have up to 8 Degrees-of-Freedom<sup>3</sup> (DOF). Several surgeons therefore have to coordinate in order to perform precision procedures in a limited space around the control handle. Due to these constraints, the development of numerous robotic structures has been proposed to assist practitioners during MIS [53].

### 1.2 Robotics craze and how it redefines surgery

In developing robotic platforms, two objectives were pursued, namely assisting the deployment of the device and assisting the practitioner during the procedure. The first objective covers the planning aspects as well as the effective deployment at the target site. Trajectories through the natural tract are defined in advance using preoperative imaging, avoiding sensitive tissue [126]. The second objective is automating the management of the large number of degrees of freedom, simplifying tool positioning and orientation for the surgeon, and making control more intuitive.

Teleoperated robotic platforms offer advanced mobility and control of instruments through small incisions. However, these platforms still rely on the use of industrial robots, adapted to meet the disinfection constraints of the operating theatre but not the footprint requirements [206]. Moreover, these platforms use rigid instruments, the limitations of which we have already indicated. It therefore seems interesting to focus on the development of a miniaturisable, compliant robotic structure that can evolve in confined and tortuous environments. The robots must also provide a wide range of motion options and simplified control for the practitioner. The design evolve from discrete architectures built with a series of rigid links to mechanisms whose number of joints tends to infinity, from the hyper-redundancy to continuum robotics, capable of continuous bending along their length, as shown in Fig. 1.5.

Among the different robotic architectures used in MIS, three main families can be distinguished on Fig. 1.5. Robotic manipulators, such as antropomorphic arms, are mostly used as tool holders rather than as dedicated structures for the procedure. For this reason, they will not be studied more specifically. However, the predominance of continuum robots can be noted, which explains their detailed analysis in the next section. The hyper-redundant approach will therefore be discussed in a second step for comparison.

#### 1.2.1 Definition and classification of continuum robots

Continuum Robots (CR) can be characterised as actuated structures whose deformation takes place along curves with continuous tangent vectors [22]. It can therefore be considered that these robots have an infinite number of joints and degrees-of-freedom (DOF), giving them the ability to change their shape at every point of their structure [60]. This property makes them ideal for deployment in confined and variable environments where compliance and

---

<sup>3</sup>Degree-of-Freedom (DOF) refers to the number of independent variables that determine the motion of a system.

## 1.2. Robotics craze and how it redefines surgery

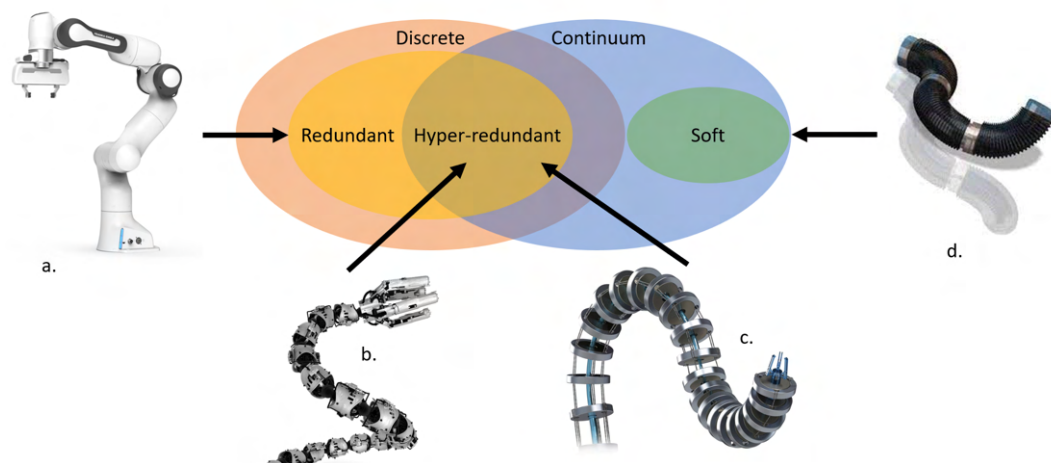


Figure 1.5 – Categorisation of medical robots according to their kinematics. a. Redundant [66], b. Hyper-redundant and discrete (OC Robotics), c. Hyper-redundant (continuum) [167] and d. Soft [38]

adaptability to external constraints are required [22]. However, the actuation of these types of structures is a real challenge, since there is usually a law of proportionality between the dexterity and the number of actuators required to achieve it. Actuator sizing is therefore a key design issue, especially when size aspects are involved. As the volume of the structure increases, the range of motion decreases [22].

At the same time, the emergence of soft robotics has made it possible to address the problem of manipulating delicate structures. These robots, made of elastomeric materials, can be considered as CRs due to their continuous deformation. However, the debate remains open concerning the number of degrees of freedom. In fact, the soft robots are usually actuated by pressurising a cavity, the deformation of which is described by some as a degree of freedom [43] and by others as an infinite number of degrees of freedom [136]. In both case, compared to rigid CRs, soft robots have desirable traits for MIS applications such as exhibiting safer interactions with tissues. This characteristic comes from their ability to deform according to external constraints without deforming the tissue during their actuation [177]. They are therefore extremely compliant with their environment and able to follow complex, constantly evolving trajectories. Soft robots have already shown potential for targeted drug delivery and MIS procedures [48, 65], but they face various limitations, in terms of force transmission and dimensions [176].

### 1.2.2 Actuation of continuum manipulators

#### Extrinsic actuation

Extrinsic actuation characterise the use of solid elements to transmit forces and torques distantly. Due to dexterity and sizing constraints in medical applications, mechanical control systems for continuous robots have differed from conventional designs. Among the approaches adopted, a myriad of robot designs have been studied, of which two main approaches have emerged: concentric tubes [22] and cable-actuated robots [153, 167], as shown in Fig. 1.6.

#### Concentric tube designs

As their name suggest concentric tube actuators correspond to a nesting of pre-curved tubes inside one another, most often made from nitinol (NiTi). With relative rotation and translation, varied sets of curvature are achievable with a further increase in workspace possible through coupled motions [214]. Each tube is driven by a set of 2 motors, one for each degree-of-freedom.

In its initial configuration, the forces and torques induced by the elastic interaction between the tubes are distributed along a neutral fibre. This equilibrium state will be modified by successive rotations and translations by means of linear and rotary actuators. Each tube is connected to a pair of actuators. By coupling these movements, it is possible to obtain different sets of curvatures modifying the position and orientation of the distal tip. The kinematic performance of this type of robot depends on the number of tubes used, the precurvature of the tubes, and their mechanical properties [52].

Although first used for needle-steering [214], they have since been considered for many medical applications [69]. The reason lies in their ability to perform tortuous trajectories in very confined environments, with "follow-the-leader"<sup>4</sup> deployment, and the possibility of miniaturisation due to the absence of a complex assembly part [70].

It should be noted that the curvature variations of this type of robot are linked to changes in length. In addition, their ability to follow a specific planned trajectory is dependent on the accurate precurvature of the tubes and an important optimization phase of the design parameters [5, 126]. However one of the main limitations for medical applications lies in what is commonly referred to as the snapping effect. This phenomenon is related to the accumulation of elastic energy during motions, which can cause uncontrolled jumps between two stable states when a storage limit value is exceeded [52]. The energy stored is proportional to the length of the interaction and the precurvature of the tubes. A choice must be made between the desired working space and the length to be deployed. This phenomenon of elastic instability also leads to increased complexity in the control of the robot [52].

The second major limitation regarding MIS concerns the payload that can be carried by the deployed concentric tube [40].

---

<sup>4</sup>Control strategy defined in Section 1.4.1

## 1.2. Robotics craze and how it redefines surgery

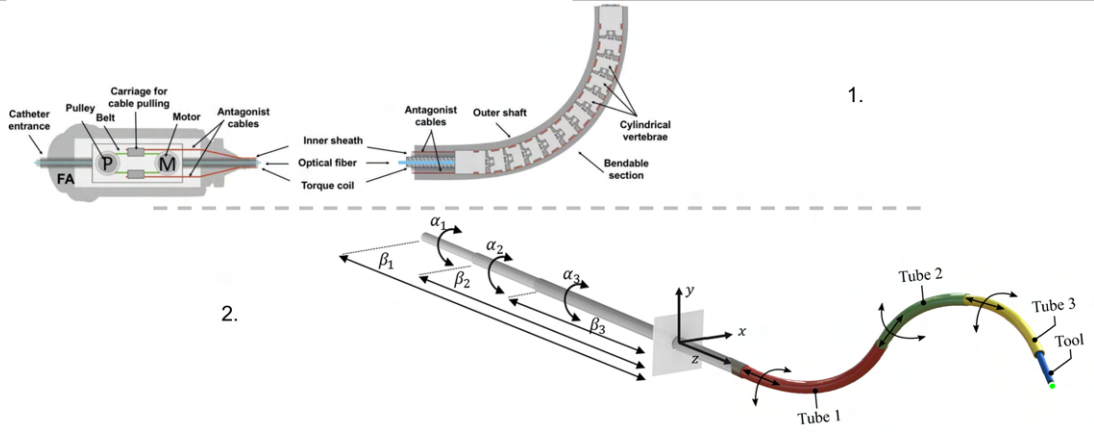


Figure 1.6 – Extrinsic actuation method: 1. cable actuated robot [144], 2. Concentric tube robot (adapted from [62, 63])

### Cable actuation and backbone-based designs:

A widely adopted approach to design continuous robots is to use cable actuation, similar to what is done with the endoscope described in Sec. 1.1.2. The design of the continuous cable actuated robots is based on a central backbone to support the vertebrae and the transmission elements. This column is made of polymers or NiTi rods and allows for continuous deformation due to its elastic properties.

One to two pairs of antagonistic cables are used to obtain one or two bending planes and are actuated using motors [148] or Shape Memory Alloy actuators (SMA) [182]. To obtain a larger number of DOFs, it is possible to superimpose a number of independently operated bending sections. Alternative designs for achieving extension/contraction use magnetic spacing discs [150]. This approach is particularly interesting for follow-the-leader motions [5, 149].

As with the manual endoscope, the cables are routed along the backbone to a specific distal anchor point. During tensioning, the cables transmit forces to the distal anchor point, generating bending-inducing torques.

For this actuation principle, a set of 3 equations is used to model the tension  $T(\phi)$  and the elongation  $\delta(\phi)$  as a function of the bending angle  $\phi$  [212].

$$\phi = \int_0^{\phi L} |\dot{\phi}| = \sum_{i=1}^n |\phi_i| \quad (1.1)$$

$$T_\phi = - \int_0^\phi \mu \zeta T(\varphi) \dot{\varphi} + T_{in} \quad (1.2)$$

$$\delta(\varphi) = \rho T_{in} \int_0^\varphi r e^{-\mu \zeta \varphi} \dot{\varphi} \quad (1.3)$$

where  $\varphi$  the curve angle,  $L$  is the total length of the tendon,  $\mu$  is the friction coefficient,  $\zeta$  is the

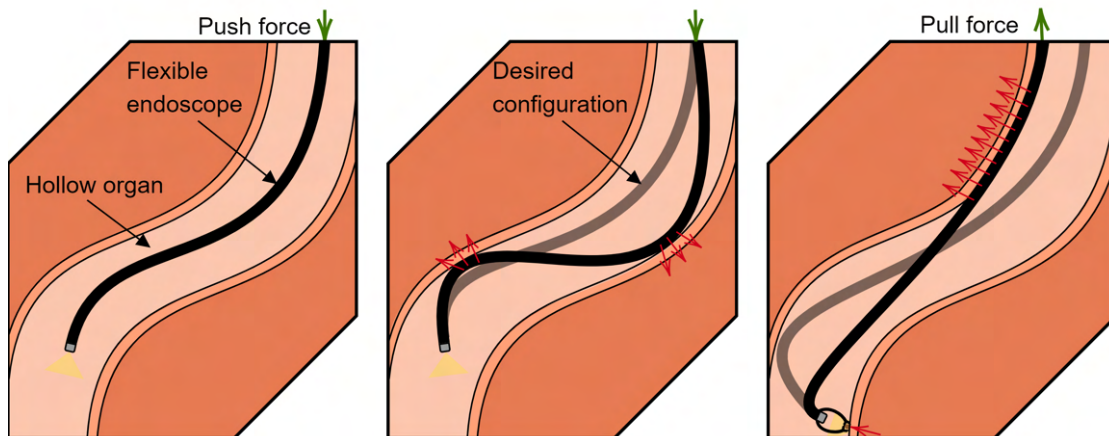


Figure 1.7 – Flexibility problem of an endoscope in MIS. In practice: the configuration taken by the endoscope results from contact with the tissue. These contacts can be those linked to the insertion of the endoscope and those generated by the operation of the tools. Desired situation: the endoscope moves within the hollow organ without generating friction and is able to stabilise itself for the procedure.

direction index,  $T_{in}$  the input tension,  $\rho = 1/EA$  with  $E$  the Young modulus and  $A$  the cross section area, and  $r$  the radius.

The coefficient of friction  $\mu$ , which is involved in the tension and elongation Eq. (1.2) and Eq. (1.3), is particularly high in this application due to the presence of sheaths and the shape of the robot during insertion. The internal friction associated with the loss of tension in the cables during actuation results in a high level of hysteresis. In this model, the cable is considered rigid; therefore, non-linearities due to the tension are ignored. However, in order to be able to bend, over-tensioning of the cables must be avoided and the antagonistic nature of the actuation automatically introduces mechanical play [47]. The tensioning of the cables induces a deformation in the shape of the robot [130, 178], as shown in Fig. 1.7, which greatly complicates its identification in real time. The mechanical play in the cables and the unknown configuration of the flexible tube are responsible for considerable backlash during bending [142]. The lack of knowledge of the robot configuration is an important limitation in the establishment of the geometrical model due to the numerous flexible sections. For the practitioner, these phenomena appear as a delay that complicates the fine and small amplitude motions [159].

Moreover, the use of this type of elastic backbone column results in a restoring force that counteracts deformation. When the actuating forces are removed, the spine will return to its neutral configuration. During an operation, a configuration can be maintained for several hours, thus requiring a high energy cost of actuation.

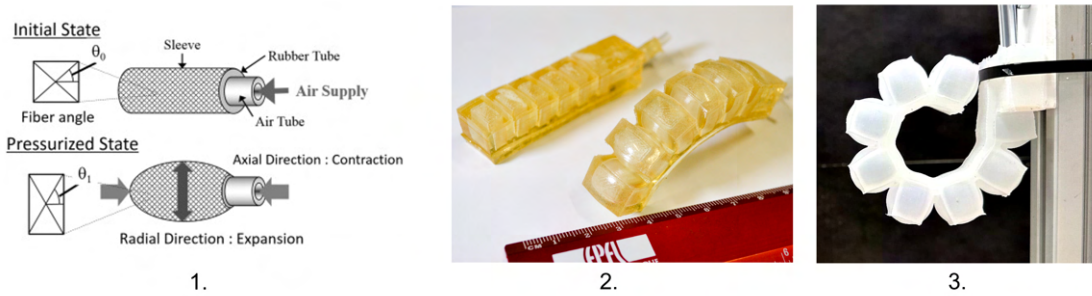


Figure 1.8 – Intrinsic actuation method: 1. Pneumatic artificial muscles [211], 2. and 3. Fluidic elastomer actuators in gelatin [188] or silicon.

### Intrinsic actuation

Intrinsic actuators are nowadays mainly fluidic actuators while assembly and sterilisation of micromotors are major obstacles to their use in hyper-redundant structures [120]. Fluidic actuators are a hot research topic due to the soft-robotics increasing interest and their use in these structures. Their operating principle is based on the extraction and injection of a fluid in order to produce inflation or pressurisation of fluidic channels, as shown in the right picture of Fig. 1.8. For the medical field, the fluids used are restricted to air and water. These constraints are related to both their availability in the operating theatre and, above all, to the safety of the patient. The hydraulic or pneumatic nature of the actuation greatly influences the performance of the actuator. The control of the actuator is easier with water than air as it is considered incompressible. Conversely, air is more suitable for miniaturisation due to its lower viscosity and weight. This last point is particularly important because of the "scepticism" that exists within a part of the research community, notably with regard to the size of the devices [183]. Even if certain devices have proved to be miniaturisable, notably thanks to the tip extending robots, their use still poses a number of problems, such as their folding after deployment [13]. Depending on the design, fluidic actuators allow bending, twisting and expansion/contraction. Two specific designs used are artificial muscles and elastomer actuators.

- **Artificial muscles:** Pneumatic Artificial Muscles (PAM) consist of an air chamber surrounded by a flexible double-helix braided sleeve. When the chamber is pressurised and expands, the mesh geometry allows the radial expansion to be converted into linear motion. Although linear motions of the order of  $\sim 40\%$  are obtained with some materials, average performance is generally in the order of 25%. These actuators have the advantage of being lightweight, easy to manufacture, and self-limiting with a maximum contraction amplitude [50]. However, these actuators have some disadvantages such as failure due to friction between the mesh and the inner tube or fatigue of the inner tube due to the required deformation. In addition, there are problems of controllability at

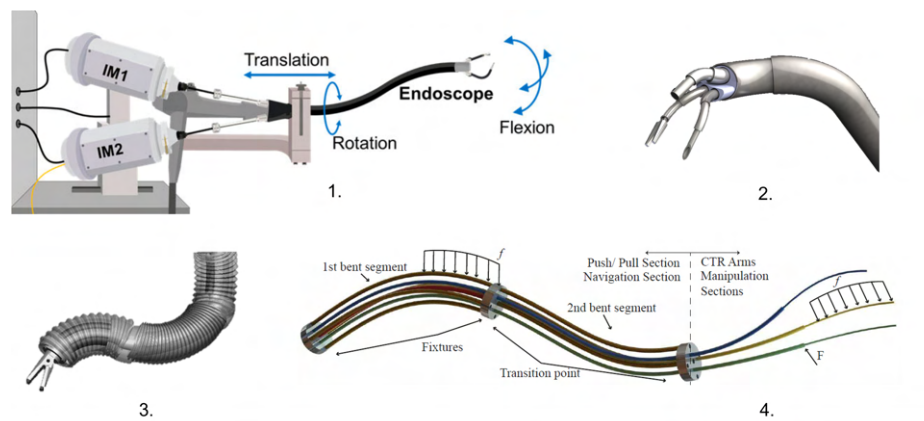


Figure 1.9 – Demonstrators exploiting the different actuation principles mentioned: 1. Cable actuated Robot (STRASS) [144] 2. Concentric tube robot [140] 3. Fluidic elastomer actuator (STIFF-FLOP) [38] 4. Multi-backbone [140]

low pressure [219].

- Fluidic Elastomer Actuators:** FEA are elastomeric structures with embedded channels which, when pressurised, cause bending or expansion [177, 136]. The nature of the strain may be related to the material's topology or to a layering comprising an arrangement of extensible and non-extensible layers [40, 183]. These actuators have the advantage that they can be designed to meet various strain requirements, such as cylindrical tubes, eccentric tubes [155], pneumatic networks [145]. These deformations are however highly non-linear and therefore difficult to model and control. Because of their completely soft body, they require lower actuation pressures than artificial muscles [135]. The maximum force they can exert is however lower.

In the context of MIS applications, robots must be able to deform in multiple directions to reach the operation site [68, 176]. In the case of continuum soft robots, this requires a modular structure [39]. However, this type of architecture requires a large number of supply lines, especially if each line is specific to a single actuator. This aspect leads to two main problems when miniaturising [103]. The first is the minimal space requirement related to the number of lines and actuators. The second is that the smaller the diameter of a line, and the longer the line, the greater the pressure to be supplied.

In addition, the manufacturing technologies are still in an experimental state and need to be improved (subsection 1.15) [176]. The final risk addressed is that of material rupture and safety [15]. If we disregard the risk related to pressurisation, there is still the risk of damaging the structure during the operation due to the use of a surgical blade and a cutting/cauterise electrical tool.

## 1.2. Robotics craze and how it redefines surgery

Ref	Application	Architecture	Actuation	DOF	Diameter	Length	Bending radius	Max force	Control
CR - Extrinsic actuation									
[139]	MIS (single port)	CTR	Manual	2	9.5	90	-	-	CL
[140]	MIS (single port)	Hybrid (CTR - push/pull)	Continuous RS motors	2	9	83	-	-	CL
[190]	MIS (throat)	Backbone	push-pull actuation	20	4.2	35	35mm (min)	-	CL
[44]	MIS (Cardiac)	Backbone	50 tendons	105	12	300	±15° per DOF	-	CL
[158]	MIS	vertebrae	Cable-driven	2	16	150	-	5.2	CL
[42]	MIS	vertebrae	Cable-driven	3	18	57	rotation: ±145 translation: 10mm	225 133	CL
[26]	MIS	vertebrae	Cable-driven	3	20	-	-	-	CL
[1]	MIS	vertebrae	Cable-driven	2	16	90	-	3	CL
[184]	MIS	vertebrae	SMA wire	3	13	-	-	-	CL
[182]	Gastroscopy	vertebrae	SMA wire	2	-	80	50mm / 9 per DOF	-	CL
			SMA spring	-	-	-	11.5 per DOF	-	
[5]	-	backbone	tendon - neodymium magnets	3	7	165	-	-	OL
CR - Intrinsic actuation									
[3]	Fetal surgery	PAM	Pneumatic	2	4	-	90	-	CL
[57]	MIS	FEA	pneumatic	1	25	165	248	-	CL
[166]	MIS	FEA	pneumatic	-	32	135	132	7.9	CL
[134]	Colonoscopy	FEA	hydraulic	5	18	-	130	2	CL
[43]	Brachytherapy	FEA	pneumatic	2	6	90	180°	20-80 mN	CL
[38]	MIS	FEA + ganular jamming	pneumatic	6	35	100	120° (×1*) 80° (×2*)	24.6 N (×1*), 41.4 N (×2*) 47.1 N (×3*)	CL
[25]	Gastroscopy	FEA	hydraulic	3	12	60	94°	0.1N	CL

Table 1.2 – Comparison of properties and characteristics of continuum robots based in the literature review (\*actuators number). DOFs include only those of the endoscope without the addition of tools.

### 1.3 Current limitations of continuum robots

Mechanical and fluidic actuation approaches have enabled the development of a variety of continuum robot designs as shown in Fig. 1.9. Despite the relevance of some approaches to medical applications, they still have major limitations to overcome. They pay the price of compromises in terms of stiffness, footprint and steerable DOF as it is presented in Tab. 1.2 from literature review.

The more dexterity a robot needs, the more DOFs it requires, the larger its diameter becomes. Indeed, in order to control a large number of degrees of freedom, this type of architecture requires the design of a larger number of fluidic channels or cable routes.

Because of their deployment in contact with soft tissue, this type of robot must strike a balance between stiffness and compliance. In the case of mechanical architectures, stiffness dominates compliance. Regarding risk analysis, this leads to safety problems when operating and interacting with tissues. Therefore, complex control strategies have to be used.

Conversely, soft architectures are, by their flexible nature, compliant. Their lack of rigidity leads to a risk of failure and a reduction in the forces that can be transmitted. The problem of failure during pressurisation is one that still needs to be addressed in order to be effective and safe. On the other hand, the transmittable forces are directly related to the pressure exerted. However, these operating pressures are often still far too high to be considered.

Although the above-mentioned points are obstacles to the use of this type of architecture, it is mainly the challenges of modelling, manufacturing and controlling that are currently the limiting factors.

#### 1.3.1 Modeling of continuum robots

The mechanical properties of rigid link manipulators have been known for a long time and their modelling is widely described in the literature [111, 189]. Conversely, the modelling and control aspects of continuum robots are not the subject of consensus and are the topic of many debates [174, 167].

This lack of standardised approaches is due to the great diversity of architectures that have been presented previously. The existence of a large number of different actuators also makes the development of possible unifying and more generalised approaches to modelling and control more complex. This lack of a general approach makes the understanding and implementation of these robots less straightforward. Moreover, the mechanical behaviour of these robots is far from trivial as it often appears to be closer to material science.

Low stiffness is one of the main functional advantages of continuum robots over traditional robotic architectures. The counterpart of this low stiffness is the complexity of modelling.

Kinematics and differential kinematics modelling is difficult to apply with continuum robots

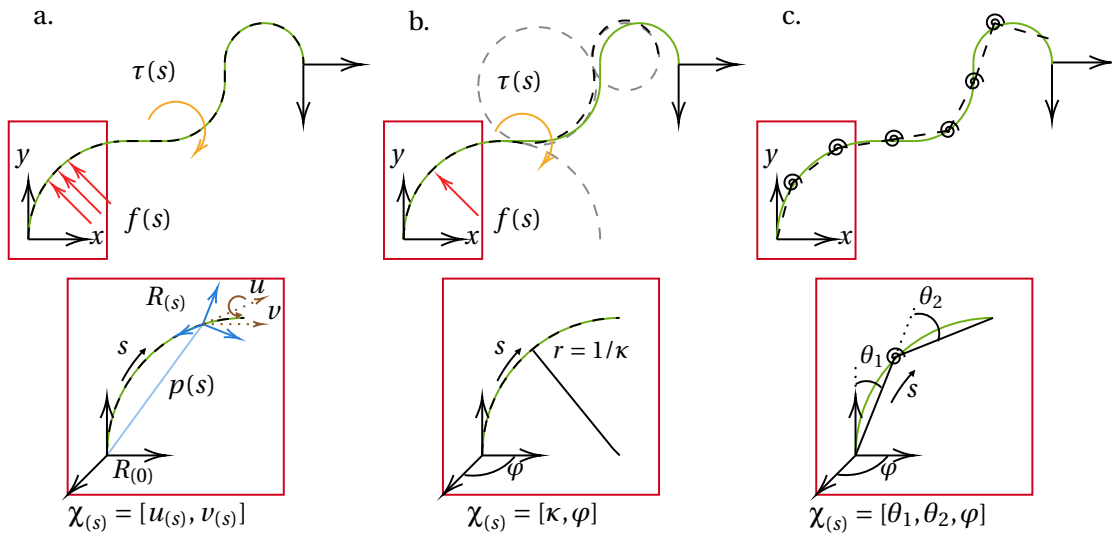


Figure 1.10 – Schematic representation of the classical modelling approaches of continuum robots : (a) Variable curvature, a transformation derivative integrated along the robot length, (b) Constant curvature, arc segment to segment transformations, and (c) Pseudo-rigid body, rigid link to link transformations.  $f(s)$  and  $\tau(s)$  represent the forces and torques along the robot respectively. (Adapted from [167, 40])

due to the lack of rigid coupling links between the elements. The lack of stiffness also makes the dynamic modelling more complex.

The case of concentric tube robots is somewhat different, since it is possible to describe the dynamic behaviour of this type of robot as the outcome of the balance of an external wrench  $(f\tau)^T$ , which represent the force and torque vectors as a function of the robot length, and the internal forces (friction, damping and elasticity), as illustrated in Fig. 1.10.

As a result of this force balance, the continuum manipulator would shape itself to a minimal energy configuration. The robot can be positioned in this equilibrium point. It is then possible to design controllers based on static [173] and dynamic models [59]. For the other cases of architecture it will be necessary to choose between classical modelling methods [167](such as Cosserat rod theory [20], constant curvature [213], rigid link models [169]).

### Most common modelling approaches

The choice of the modelling method for a continuum robot depends on the assumptions the designer makes.

- The Cosserat rod theory, presented in Fig. 1.10.a, aims to completely solve the static equilibrium of the manipulator with a minimum of (simplifying) assumptions [173]. Indeed, the only limitation of this model lies on the description of the non-linear behaviour of structure made of hyperelastic material. In fact the deformation of such structure,

especially at the cross-section, does not respect the assumptions considered by Cosserat model. The latter presumes that the cross-section remains plane, which is not the case of hyperelastic structures. In other words, the set of directing vectors associated to and describing the deformation of each cross-section becomes insufficient.

- Constant curvature modelling is based on the assumption that the shape of the robot follows the arc of one or more circles [213], as illustrated in Fig. 1.10.b.
- The rigid link assumption is the simplest modelling approach, as it consists in subdividing the robot into a succession of (infinitesimal) rigid links and can therefore be compared to traditional approaches [169], as shown in Fig. 1.10.c.

These approaches have been ranked in order of increasing assumption. This order will now be maintained in order to describe the different approaches in more details and to highlight their advantages and disadvantages.

### **The Cosserat rod theory**

The Cosserat rod theory is certainly the most accurate approach to establish the static model of a continuous robot because it limits these assumptions to internal variations due to the material's own deformations [20].

In this approach, each point on the neutral fibre of the robot is parametrised along its arc length  $s \in [0, l]$  by locally defined frames, as illustrated in Fig. 1.10. The position is described by the vector  $p(s) \in \mathbb{R}^3$  indicating the origin of the local frame with respect to the base. In the same way, the orientation is represented by a rotation matrix  $R(s) \in \text{SO}(3)$ . Thus, a homogeneous transformation matrix,  $T(s) \in \text{SE}(3)$ , can be used to describe the pose of the local frame:

$$T(s) = \begin{bmatrix} R(s) & p(s) \\ 0 & 1 \end{bmatrix} \quad (1.4)$$

The linear velocity of the rigid body and the rotation of the attached frame  $R(s)$  are represented by the strain variables  $v(s) \in \mathbb{R}^3$  and  $u(s) \in \mathbb{R}^3$  respectively. These variables compose the twist vector  $\mathcal{T}$  which represents the variation rate of  $T(s)$  with respect to  $s$ . If  $\mathcal{T}$  and  $T(0)$  are known, the deformed shape of the robot is then defined differentially by

$$\dot{T}(s) = T(s)\tilde{\mathcal{T}}(s) \quad (1.5)$$

Or equivalently used to represent the robot parameters:

$$\dot{R}(s) = R(s)\tilde{u}(s) \quad (1.6)$$

$$\dot{p}(s) = R(s)v(s) \quad (1.7)$$

### 1.3. Current limitations of continuum robots

The tilde operator depicts the mapping from  $\mathbb{R}^3$  to  $SO(3)$ <sup>5</sup>. In most cases, these equations are solved by employing numerical integration as the twist vector is not constant with respect to  $s$ .

The robot is modelled using constitutive laws such that it undergoes linear elastic deformation and the stresses are linearly proportional to the strain. This model is based on the assumption that the robot is inextensible. By setting  $v^*(s)$  and  $u^*(s)$  as the strains in the reference position, it is then possible to describe the force and internal moment vectors [173], respectively  $n$  and  $m$  as:

$$n(s) = (v(s) - v^*(s))K_{SE} \quad (1.8)$$

$$m(s) = (u(s) - u^*(s))K_{BT} \quad (1.9)$$

where  $K_{SE}$  is the stiffness matrix for shear and extension and  $K_{BT}$  is the stiffness matrix for bending and torsion.

$$K_{SE} = \begin{bmatrix} GA(s) & 0 & 0 \\ 0 & GA(s) & 0 \\ 0 & 0 & GJ \end{bmatrix} \quad (1.10)$$

$$K_{BT} = \begin{bmatrix} EI_{xx}(s) & 0 & 0 \\ 0 & EI_{yy}(s) & 0 \\ 0 & 0 & GJ \end{bmatrix} \quad (1.11)$$

where  $G$  is the shear modulus,  $A$  is the cross section area,  $J$  is the polar second moment of cross section area,  $E$  is the Young modulus and  $I_{xx}$  and  $I_{yy}$  are the second area moments.

In the case of static equilibrium, the forces and internal moment can be expressed by taking into account the distributed forces  $f(s)$  and the applied moment  $\tau$  [174]

$$\begin{aligned} \dot{n}(s) + f(s) &= 0 \\ \dot{m}(s) + \dot{p}(s)n(s) + \tau(s) &= 0 \end{aligned} \quad (1.12)$$

However, despite the accuracy of the solution obtained for a static model, its extension to dynamics is not trivial [174]. Indeed, due to the need to solve a complex system of partial differential equations, the solution can only be calculated numerically. The time and computational cost make it difficult to be viable with real-time control approaches. This is exacerbated by the lack of a sensor to close the control loop.

---

<sup>5</sup>For  $\mathcal{F} = \begin{bmatrix} u_x \\ u_y \\ u_z \\ v_x \\ v_y \\ v_z \end{bmatrix} \in \mathbb{R}^3$  the skew symmetric matrix is  $\tilde{\mathcal{F}} = \begin{bmatrix} \tilde{u} & v \\ 0 & 0 \end{bmatrix} = \begin{bmatrix} 0 & -u_z & u_y & v_x \\ u_z & 0 & -u_x & v_y \\ -u_y & u_x & 0 & v_z \\ 0 & 0 & 0 & 0 \end{bmatrix}$

**(Piece-wise) Constant curvature model**

The assumption made with constant curvature models is that the deflection of continuum robots can be represent by a set of circular arcs. This constitutes a significant simplification as the path of the robot can de described according to the radius of curvature  $\kappa$  and  $\phi$  the angle its bending plane makes with a reference axis. The coordinates in the task space can be obtained from the arc parameters by various formulations such as arc geometry, Frenet-Serret frames, Denavit–Hartenberg (D-H) parameters or exponential coordinates [213]. These representations are equivalent as they yield the same mapping between configuration and task space. The method, which use the geometry of the arc to obtain the resulting homogeneous transformation matrix, is detailed below. The position of any point on the arc, relative to the arc base at a distance  $s$  is given by

$$X(s) = \begin{bmatrix} \frac{\cos \phi}{\kappa} (1 - \cos(\kappa s)) \\ \frac{\sin \phi}{\kappa} (1 - \cos(\kappa s)) \\ \frac{1}{\kappa} \sin(\kappa s) \end{bmatrix} \quad (1.13)$$

In an other way, according to [190], using the curvature components along  $x$  and  $y$  axis of the local frame, the curvature and bending angle can be represented as

$$\kappa = \sqrt{\kappa_x^2 + \kappa_y^2} \quad (1.14)$$

$$\phi = \text{atan2}(\kappa_y, \kappa_x) \quad (1.15)$$

The coordinate frame of any point on the arc, expressed with respect to the frame attached to the base of the section can be obtained by two consecutive rotations about the  $z$  and  $y$  axis.

$$T(s) = \begin{bmatrix} R_z(\phi)R_y(\kappa s)R_z(-\phi) & p(s) \\ 0 & 1 \end{bmatrix} \quad (1.16)$$

with

$$R_z(\phi) = \begin{bmatrix} \cos(\phi) & -\sin \phi & 0 \\ \sin \phi & \cos \phi & 0 \\ 0 & 0 & 1 \end{bmatrix}, \quad R_y(\kappa s) = \begin{bmatrix} \cos(\kappa s) & 0 & \sin \kappa s \\ 0 & 1 & 0 \\ -\sin \kappa s & 0 & \cos \kappa s \end{bmatrix} \quad (1.17)$$

This simplification drastically reduces the needed variable number and leads to possible analytical solutions for kinematics, statics and dynamics models.

For robot modelling using constant curvature, it is assumed that effects of shear and twist are negligible and Euler Bernoulli beam theory can be used. The bending moment is assumed to be proportional to the beam curvature and expressed as a one dimensional equation using Hooke's law:

$$m = \kappa EI \quad (1.18)$$

### 1.3. Current limitations of continuum robots

This equation can be extended in order to take into account the twist  $\varepsilon$  about  $z$  axis while  $\kappa_i$  is the curvature of the  $i^{th}$  subsegment [180].

$$m_i = R_x(\phi)R_y(\theta_j) \begin{bmatrix} EI_{xx} & 0 & 0 \\ 0 & EI_{yy} & 0 \\ 0 & 0 & Gj/\lambda \end{bmatrix} \begin{bmatrix} 0 \\ \kappa_i \\ \varepsilon_i \end{bmatrix} \quad (1.19)$$

The force and moment acting on the distal segment of the robot is written as follows [223]

$$F_{dist} = \sum_{k=1}^m F_{k,dist} + f_{ext} \quad (1.20)$$

$$M_{dist} = \sum_{k=1}^m M_{k,dist} + \overrightarrow{O_{dist-1}O_{dist}} F_{dist} \quad (1.21)$$

where  $k$  represents one actuator, e.g. an actuation cable following the continuous path and  $F_k$  the force it will apply.  $O$  is the center of the cross section. The force and moment acting on the following subsegments are obtained by the recursive equation [223]

$$F_j = \sum_{k=1}^m F_{k,j} + F_{j+1} \quad (1.22)$$

$$M_j = \sum_{k=1}^m M_{k,j} + \overrightarrow{O_{j-1}O_j} F_j + M_{j+1} \quad (1.23)$$

However, as the robot is modelled as a series of arcs, one of the drawbacks results from the assumption of constant curvature which is not respected, which lead to a deviation from the real robot's behaviour. Even if some extension to polynomial curvature have been proposed, further analysis are still needed. Moreover, this assumption is not valid when the robot is subject to non-negligible external loads.

#### Rigid-link model

This approach is based on the assumption that a continuum robot can be divided into a series of small segments which have the same behaviour as rigid links. This is the most significant modelling assumption.

The length of each link  $i = 0, 1, 2, 3$  is defined with respect to the length of the sub-segment using a factor  $\gamma_i$ . Each sub-segment, is assumed to bend in a plane rotated by an angle  $\phi$ . Assuming for this example that the local frame is constructed such that the local  $z$ -axis is tangent to the backbone, the transformation matrix from the end of a link  $i$  to its base in the

bending plane is given by

$$T_{j,i} = \begin{bmatrix} \cos(\theta_{j,i}) & 0 & \sin(\theta_{j,i}) & \gamma_i l_j \sin(\theta_{j,i}) \\ 0 & 1 & 0 & 0 \\ -\sin(\theta_{j,i}) & 0 & \cos(\theta_{j,i}) & \gamma_i l_j \cos(\theta_{j,i}) \\ 0 & 0 & 0 & 1 \end{bmatrix} \quad (1.24)$$

Then, the transformation matrix from the base of the next subsegment to the current one is given by

$$T_j^{j+1} = T_z(\phi_j) T_{j,0} T_{j,1} T_{j,2} T_{j,3} T_z(-\phi_j) \quad (1.25)$$

As introduced, the robot is approximated by rigid links connected by torsion springs [196]. In each spring,  $s = 1, \dots, n$ , the bending component of the moment is proportional to the angle  $\theta$  such as:

$$M_{j,s} \gamma_j = k_s \theta_{j,s} \quad (1.26)$$

$$k_s = K_{\theta_s} \frac{EI}{l} \quad (1.27)$$

where  $\gamma$  and  $K_{\theta_s}$  are optimized characteristic parameters [31].

From these equations it is possible to find a static model close to the one defined with the constant curvature [167], but this time the gap between this model and reality is also proportional to the refinement of the discretisation. The use of few segments will lead to a model far from the real behaviour. Conversely the more the segments and the variables used, the closer the model will be to the real behaviour. This approach also has many problems when modelling a 3D manipulator [95]. However, it is useful in a prototyping phase, when one wishes to obtain preliminary results. It has the advantage of using the well-established control methods of rigid body manipulators. It is possible to partially compensate for the assumptions made by using sensors and quantifying the deformation of the robot. A balance can then be found between the complexity of the model, i.e. the number of segments needed, and the number of sensors to find an optimal approach.

In addition to these analytical approaches, numerical approaches have been studied (SOFA). Finite Element analysis can provide accurate deformable models for soft-robots. However, these models are very difficult to use in a real-time control system [14, 115, 51].

### 1.3.2 Continuum robots control strategies

Once the design and modelling have been addressed, a fundamental issue is the control of this new robotic architecture. However, according to the literature, this aspect is certainly the least addressed in the field of continuum robotics. It can be assumed that this is a consequence of the complexity of the implementation of the models or a tendency towards a more mechanical design. In addition, the absence of sensors or their difficulty in being assembled into the structure limits the possibilities of obtaining feedback and thus the implementation of closed-

### 1.3. Current limitations of continuum robots

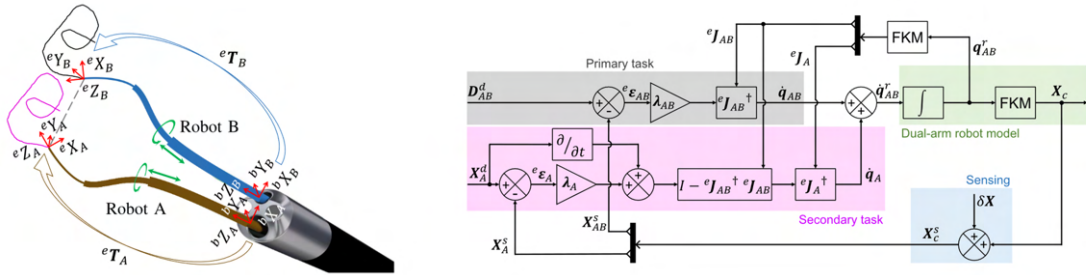


Figure 1.11 – Concept of dual-arm concentric tube continuum robots and its control block-diagram. Gray box represents the primary task, pink is the secondary task, green is the robot’s kinematic model, blue stands for exteroceptive sensing. A: robot A, AB: dual-arm robot, d: desired, r: resultant, s: sensors, c: current, e: end-effector,  $\lambda$ : control gain and X: pose. [34].

loop control. Although there are some approaches based on a combined feedforward/feedback control, most of the time, the control is done in open loop. However, this type of control is based on model inversion and therefore refers to the problem discussed in the previous section.

In order to illustrate this, the three main control strategies will be described in more details, namely: kinematic and differential kinematic control, the use of wrench-based controllers, and adaptive and reinforcement learning control.

#### Approaches based on kinematic models

The establishment of a kinematic control scheme is based on the use of inverse kinematics or inverse differential kinematics, assuming that the direct kinematic model is known. In general, the use of inverse kinematics to control a robot manipulator is the most common approach. However, continuum robotics is an extreme case of hyper-redundancy and therefore the use of inverse kinematics is less efficient [19]. Indeed, the kinematics of a redundant manipulator robot is not bijective and there are an infinite number of solutions to the inverse kinematics model.

On the other hand, differential kinematics lends itself rather well to the redundant robot because it allows multi-task control [133, 34], as presented in Fig. 1.11. However, given the approximations made in the modelling, the presumption that the differential kinematics are known remains a strong assumption and accuracy may be particularly affected.

#### Wrench-based control strategies

In contrast to previous methods that use kinematic models, these approaches are based on static [71] and dynamic models [58]. Assuming that for a continuum robot, actuation can be related to the interaction between the compliant nature of the structure and the actuating

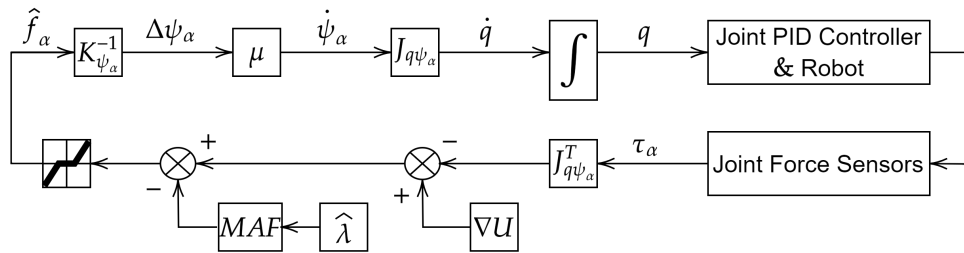


Figure 1.12 – Compliant motion controller. The compensation term  $\lambda$  enters a Moving Average Filter (MAF) prior to entering the feedback loop. The feedback signal is filtered through a dead-band to minimize chattering [71].

wrenches, it is possible to address the control aspect through this wrench.

To this end, various studies have been conducted on the stiffness/compliance ratio [71] and force control [9] of continuous robots. This aspect is essential in medical applications [216]. However, the measurement of the force that this type of robot can exert is not obvious in the absence of sensors. Furthermore, due to material non-linearities, self-sensing aspects are still at a preliminary stage. The same applies to force estimation methods based on deterministic approaches [216].

The two previous approaches are model-based. However, due to the mechanical complexity of the continuum robot and the difficulty to obtain an accurate characterisation, control errors arise. This explains the use of adaptive or reinforcement methods which are discussed in the next subsection.

### Adaptive control and reinforcement learning approaches

In order to compensate for the unknowns in the kinematic models, it is possible to use approximation methods based on data gathering. Two types of methods are most often used:

- Mechanical adaptive methods whose aim is to compensate for the approximations of the mathematical model by real-time adaptation.
- Data-driven modelling approaches or learning-based methods.

**Mechanical adaptation approach** This approach is used in the case where modelling uncertainties can be balanced by a feedback loop. The estimation of the mechanical parameters is performed online, the robot pose is treated as a Fourier series expansion and updating of the parameters is performed using a recursive least squares method [112]. A variant of this approach is based on the use of locally weighted projection regression, the approximation of the robot model by means of a set of linear models, and an adaptation done by means of stochastic gradient descent [56].

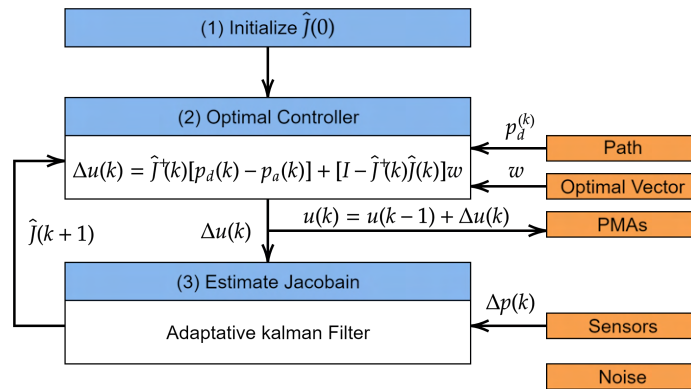


Figure 1.13 – Flowchart of the Kalman-filter-based control scheme used to estimate the Jacobian of the continuum robot [124].

More recently, an approach exploiting the adaptive observer of a Kalman filter has been used to estimate the Jacobian matrix of the robot [124] as shown in Fig. 1.13. The results are however preliminary, as the simplicity of the state evolution model used does not take into account the mathematical properties of the Jacobian matrix.

**Data-driven modelling approaches** Machine learning-based control approaches have attracted increasing interest in recent years. The strength of these methods lies in the possibility of getting rid of complex and approximate analytical models. The first mentions of this type of approach were made by Thuruthel et al. [202] and Xu et al. [218] as shown in Fig. 1.14. The former describes a formulation for learning the inverse kinematics of a continuum robot by integrating end-effector feedback. The latter uses a combination of three regression methods (K-nearest neighbour regression, extreme machine learning and Gaussian mixture regression) to learn a non-linear mapping from the 3D positional states of the robot to the control inputs.

One of the inherent limitations of these methods is that they do not take into account the real mechanical interactions. This lack of physical meaning and understanding can lead to potentially undetected inaccuracies. This factor is unacceptable in the industrial field and even more so in the medical field.

### 1.3.3 Manufacturing process

The manufacturing of traditional mechanical robots has reached the stage of industrial production and their process are well mastered, whether they are subtractive manufacturing techniques (milling, electrical discharge machining, etc.) or additive manufacturing. However, the fabrication of fluidic actuators is newer and a less explored area of research.

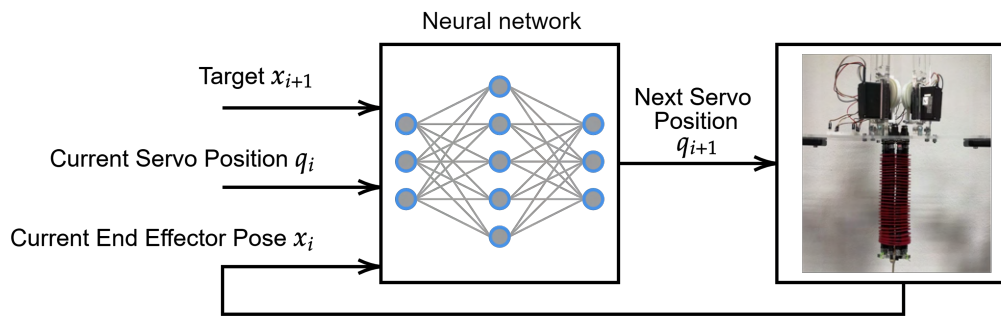


Figure 1.14 – Overview of a machine learning-based closed-loop kinematic controller for a continuum manipulator [202].

Soft lithography (lamination casting) is a frequently used process that involves accurately reproducing the features of a model by pouring a liquid polymer into a mould [135]. Once cured, the polymer can be removed from the mould. Closed chambers can be produced by assembly using an uncured elastomer as a binder [135]. The short life of the materials used limits this method to prototyping purposes. The quality of the mould and the minimum size of the components determine the resolution.

As is often the case, there are approaches that can be used to produce a higher resolution model, such as photolithography, but the production costs and time are high. Conversely, low-cost mould making can, for example, be achieved using additive manufacturing techniques. This method allows low costs to be kept to a reasonable time frame. The major limitation is the consequent decrease in resolution compared to other methods. A balance must also be struck between creativity and limited achievable complexity.

Recently, 3D printers have been developed for direct printing of silicone elastomers [221, 192], as shown in Fig. 1.15. The first results are promising, but the prototypes require higher actuation pressures than their moulded counterparts for identical dimensions. In addition, this approach imposes significant design constraints and face fabrication variability and repeatability limitations.

### 1.3.4 Discussion on the use of continuum robots

Through the different previous paragraphs, the strengths of continuum robots in the context of MIS have been identified. Continuum robots in minimally invasive surgery have several advantages, such as their small diameter, high flexibility, and ability to reach deep and confined spaces within the body. These characteristics make them well suited for procedures such as MIS, where access is limited.

However, continuum robots also have certain limitations, particularly in terms of modelling and control, as well as manufacturing. In the case of soft-robotics, the use of elastomers

### 1.3. Current limitations of continuum robots

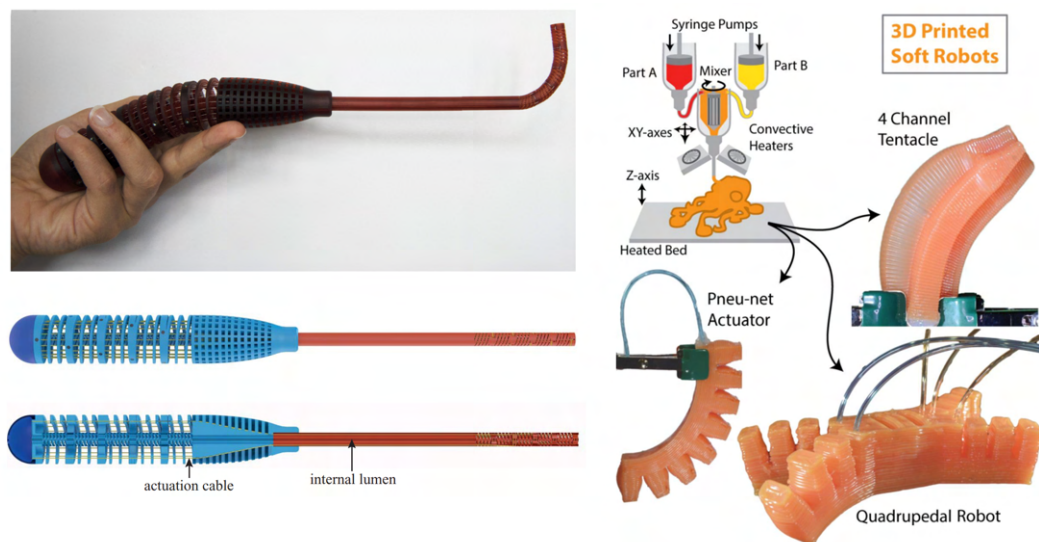


Figure 1.15 – Compliant cable actuated device [83] and pneumatic actuator [221] made by 3D printing.

characterised by highly non-linear behaviour makes the development of accurate models complex. Furthermore, due to their fluidic actuation and flexible behaviour, their operation in dynamic environments and when interacting with tissues makes it difficult to predict their deformation and therefore their control. More generally, the principle of actuating continuum robots is a source of non-linearity, as was illustrated with friction in cable drives. These continuum robot control issues therefore require complex laws to be driven, which limits the precise and delicate tissue manipulation required in surgery.

Furthermore, they are complex and expensive to manufacture, which can make them less accessible to some medical facilities. In the case of soft robots, the manufacturing process is still in a developing stage and needs more testing and validation.

In practice, patients often recall the pain associated with the friction between the device and the tissue when the device is removed. This is due to the fact that the device is removed by the surgeon without regard to the configuration of the device in the body. However, continuum robots, known to be tissue-compliant, especially soft robots, are always in contact with the tissue and the problem of friction persists during insertion and removal. In order to address this need, hyper-redundant robotic architectures and control strategies such as follow-the-leader seem particularly suitable. Because of this hyper-redundancy, they are mechanically robust and ensuring that the procedure is carried out despite a dysfunction.

Furthermore, although one of the major limitations of hyperredundant robots is related to the complexity of solving the inverse model due to the large number of joints, it has recently been shown that they can be simplified by means of what are described as binary manipulators, or more generally digital robots. The simplification of control strategies also relies on the fact that these robots can be used without sensors.

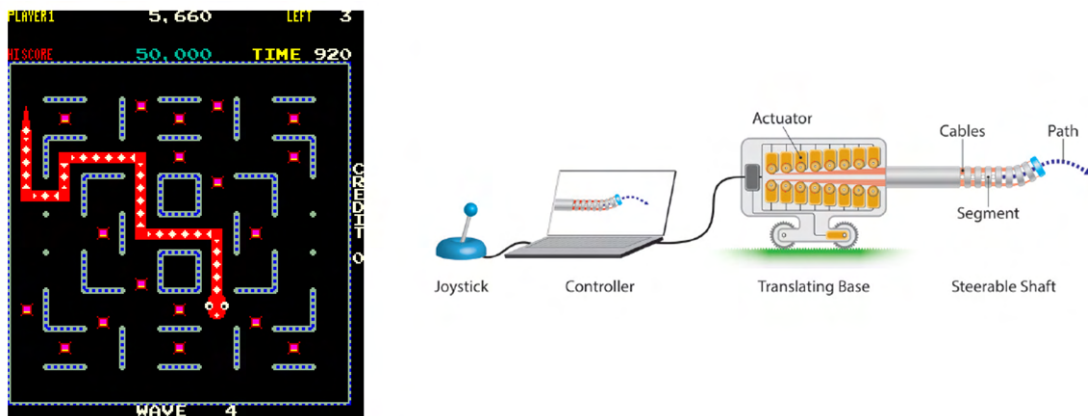


Figure 1.16 – Follow the leader deployment strategy (FTL). Illustration of the video game Nibbler (1980) in which a snake moves through a maze using the FTL method (left) a shape-shifting mechanisms able to perform FTL motion (right) [84].

## 1.4 Towards a snake-like robot based on multistable modules

### 1.4.1 Hyper-Redundancy and snake-like robot in Medicine

Hyper-redundant robots have a mechanical structure that can exhibit kinematic redundancy, with a very high number of passive joints in relation to the actuated degrees of freedom, or actuation redundancy in case the number of available actuators is higher than the number of actuators required to carry out the task without any risk of failure [35].

Hyper-redundant robots have been considered in minimally invasive procedures because of their wide range of mobility and their ability to deploy in tortuous pathways while maintaining the ability to position and orient tools. In addition, their passive mobilities allow them to deform on contact with their environment and thus adapt to the geometry of the organ rather than damage it.

The design of hyper-redundant structure consists in considering rigid members connected to each other by mechanical links of the same kinematic nature. Contrary to the previously introduced continuum robot, the number of degrees of freedom of these structures is finite and depends on the number of elements used. The latter can be relatively high [114, 44].

The architecture of these robots is similar to that of the widely described serial manipulators. The difference is that by using links of equivalent kinematic nature, they drive the same degrees of freedom of the structure in terms of positioning the end effector.

Snake like robots are known for their use in constrained environments such as nuclear plants [85], but in medical applications, when inserting the robot into the body the control strategy must be adapted to conform to anatomical constraints [120].

## 1.4. Towards a snake-like robot based on multistable modules

---

For this purpose, a particularly interesting approach is the so-called "Follow-the-Leader"<sup>6</sup> deployments where the shape of the robot corresponds to the trajectory taken by the distal module during deployment, as illustrated in Fig. 1.16. It is thus possible to deploy it in the channels while limiting the risks of friction with the walls and thus respecting their integrity. This is all the more true when the device is removed. However, due to the miniaturisation constraints inherent to their use, the snake-like robots are not able to be deployed in the channels. Nonetheless, snake-like robots are often bulky on a macroscopic scale. The transition to the mesoscopic scale is generally made by scaling down the traditional components used in anthropomorphic or in cable robots. The miniaturisation of motors and their complex assembly are challenging. Cable driven robots, although having the particular advantages of allowing remote actuation and having a small footprint, has limitations related to the friction of the cables within the sheath, yielding control issues due to hysteresis, backlash, and overvoltage. This may result in inaccurate positioning and motions of the end-effector [161, 8]. Moreover, snake-like robot designs based on individualised sections with independent actuation have limitations in increasing the number of actuation cables and consequently the friction [33]. The energy cost to sustain a configuration with this type of robot is a real issue.

In addition, the models used to describe these behaviours are more complex and costly in terms of computing time, and their accuracy is difficult to control. Besides, the closed-loop control of snake-like robots with these two types of actuation requires small and expensive sensors. The incorporation of these sensors into a mesoscopic robotic structure is also not trivial.

These trade-offs have motivated the development of a new snake-like robotic architecture, belonging to digital robotics, offering an answer to the problems of miniaturisation, actuation, and control.

### 1.4.2 Digital Robotics

In the literature several robotic architectures based on the use of bistable actuators are described as shown in Fig. 1.17 and in Tab. 1.3. At the macroscopic scale, one finds in particular the Variable Geometry Truss (VGT) manipulator [141, 96]. This is a multi-modular planar robot, whose modules are driven by 3 binary actuators. Each module has  $2^3$  stable states. The concept of binary paradigm in robotics was introduced by G.S. Chirikjian [36]. He is also the author of many works aiming at improving the VGT, in particular concerning the calculations related to the establishment of direct and inverse models [122, 123, 37, 54]. The 3D equivalent of the VGT is called Binary Robotic Articulated Intelligent Device (BRAID) [75, 199]. This manipulator consists of 5 cascaded modules providing  $2^{15}$  stable states in a 3D workspace. However, as these architectures require more complex kinematic models as the number of

---

<sup>6</sup>Follow-the-Leader was originally a children's game in which one child is followed by a line of other children, who have to copy everything the first child does [157]. This game was democratised by the Disney cartoon, Peter Pan. Its first mechatronic significance is in the modelling of traffic flows where a column of cars follow each other, transmitting information from one to the other, starting from the leading car [67].

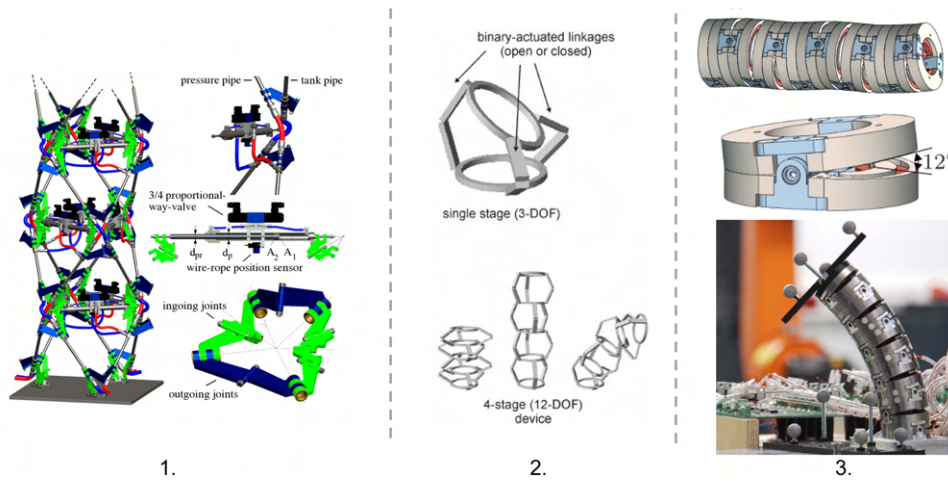


Figure 1.17 – Digital robot architecture designed with components from traditional mechanics: 1. the VGT [170], and flexible mechanics: 2. the BRAID [125]. The architecture of the VGT is given for 3 modules and is accompanied by details of the hydraulic actuation, the active linkage and joint, respectively from top to bottom. 3. A binary hyper- redundant electromagnetically actuated manipulator [200].

Ref	Application	Architecture	Actuation	DOF	Diameter	Length	Bending radius	Max force	Control
Motorised									
[185]	MIS	multiarticulated	micro motor	7	12.7	50	±90° vertically ±225° horizontally	-	CL
Binary actuator									
[200]	Colonoscopy	multiarticulated	electromagnetic	10	45mm	-	6°	-	CL
[229]	-	multiarticulated	cables + SMA	7	40mm	-	15°	5N	OL

Table 1.3 – Comparison of properties and characteristics of hyper-redundant robots in the literature.

logic states increases, the computational time to achieve trajectory tracking is expensive [122, 123]. Moreover, as for the continuous robots presented above, the inverse kinematic model is complicated to obtain and contains a very large number of solutions [37, 54]. Taking into account the mechanical backlash at each joint is also a challenge in itself.

Digital robotics was described as an approach to robot design based on elementary bistable mechanical modules [74]. This bottom-up design approach was initially described in the context of micro robotics, taking advantage of MEMS technologies and open-loop digital control. It is inspired by digital electronics and electronic flip-flop, where the flip-flop allows the storage of one bit of data. The success of this approach is based on its reproducibility, the robustness of the device and its modularity. The latter is represented by the combination of flip-flops that allowed the construction of the registers and later the microprocessor. These different aspects are found in digital robotics through the use of flexible bistable mechanisms

[72, 226]. This is what differentiates a digital robot from the approaches introduced earlier.

Digital robotics will necessarily be modular. Indeed, if we start from the principle that we wish to carry out a somewhat complex manipulation task, it is necessary to combine modules in order to increase the number of states and to be able to carry out the task [32]. Each module has 2 states, corresponding to the presence or absence of actuation. The position of the final device can be easily recalculated by accumulating the discrete movements of each module. This position can also be represented by a binary word that can be used as a command.

The workspace of these robots is defined by the performance of the modules used, their number  $n$  ( $2^n$  logical states) and their arrangement. It can also be the result of the arrangement of several chains of bistable modules, for example in parallel [32].

The performances of digital robotics, namely accuracy and repeatability, are directly related to the robustness of the manufactured modules. This argument again supports the use of compliant bistable mechanisms, which will be discussed in more details thereafter.

### 1.4.3 Contributions

This work is in line with the work done in the field of digital robotics. Different areas of improvement will be addressed here, such as the transition to a mesoscopic scale application or the transition to the use of multistable elementary modules. This is made possible by the generalisation of access to manufacturing processes such as 3D printing and the realisation of complex geometric mechanisms in a monolithic manner.

The objective of this thesis is to develop a new robotic architecture suitable for endoscopic use. The contributions are therefore divided into three parts: dimensioning, design, and control. Each of them will be described through the different chapters of this manuscript.

In order to develop our structure, it was necessary to define the constraints and specificities related to the application context (size, mobility, stiffness, workspace,...). Following the sizing, a reflection phase was necessary concerning the technological choices (mechanism, manufacturing processes, etc.) and the nature of the actuation.

*Contribution: A multistable module, with three stable states, is designed to be reproducible and to be assembled in series. Due to the size, the actuation is done with a smart active material.*

The assembly of the modules was then used to design a prototype to validate the proposed approach and the feasibility of a follow-the-leader motion.

*Contribution: a new snake-like robot architecture with discrete workspace and simplified open loop control.*

In order to propose the most optimal architecture possible, a mechanical optimisation and actuation replacement phase was then carried out. The objective was to reduce the assembly phase to a strict minimum.

## **Chapter 1. Challenges of a new companionship: the medical robotics**

---

*Contributions: Based on a theoretical study, an enhanced version of the module is proposed to increase its stability and longevity while reducing manufacturing costs. In a second step, by exploiting the principle of printing active polymers, it is proposed to develop an approach allowing the printing of actuators incorporated in the mechanism itself.*

## 2 Specification for the design of a new kind of robot based on multistable modules

Chapter 1 introduced the emergence of new robotic architectures to meet the growing need in order to improve the quality of medical procedures. In particular, continuum robots have taken a major place in minimally invasive surgery due to their ability to operate in confined and tortuous environments. However, these architectures face increasingly complex control requirements as well as time-consuming and expensive assembly [40].

In addition to continuous robots, the use of soft robotics was also discussed in Section 1.3.2, but the complexity of the models and the lack of precision of model-free controls are major obstacles to their use for operational procedures [124, 202]. It was also pointed out that there was a risk of damage to the structure due to the use of certain tools [15]. In endoscopy, during the procedure, the practitioner may use a number of tools to perform the operation, e.g. a biopsy needle or a scalpel. The use of these tools, which can cause damage to soft structures, remains an obstacle to their use in this type of intervention.

These approaches are considered as an alternative to rigid body mechanisms due to the significant constraints induced by downscaling. One of the main constraints discussed in Section 1.4.1, concerns the complexity of the assembly [159]. It is observed that these robotic architectures present some limitations such as mechanical play and friction. These phenomena generate non-linear behaviours and inaccuracies which are not negligible and which are difficult to compensate by the control laws [161, 8].

It therefore appeared that it is not necessarily appropriate to draw on existing continuum architectures and rigid body robots to develop a robotic structure suitable at the mesoscopic scale. The use of digital robots has opened up new perspectives by proposing a modular approach, some of which are based on the use of flexible mechanisms. This approach thus combines the advantage of hyper-redundant robotics with the scalability of compliant mechanisms. Indeed, as presented earlier, digital robots have already demonstrated the value of their hyper-redundancy, e.g. providing a kinematically hyper-redundant workspace, at both macroscopic and microscopic scales.

The objective of this second chapter is to define the specifications for the design of the robot.

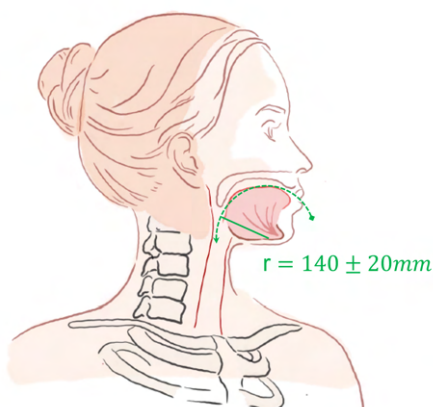


Figure 2.1 – Representation of the anatomical curvature to be crossed to reach the throat.

The choices that were made to lead to a robot able to perform the required complex movements are introduced.

## **2.1 Constraints and design considerations**

Digestive endoscopy is a medical procedure in which a thin and flexible tube equipped with a light and a camera is inserted in the body through the mouth to visually examine the digestive tract. Esophagogastroduodenoscopy (EGD) is used to examine the esophagus, stomach, and the upper part of the small intestine (duodenum). The procedure is used to diagnose and treat a wide range of conditions, such as gastrointestinal bleeding, ulcers, polyps, and cancer. It allows gastroenterologists to see the interior of the digestive tract without the need of invasive surgery and can be used to take biopsies or remove foreign objects. Digestive endoscopy is considered a safe and effective diagnostic tool that can help detect and prevent serious health problems.

This procedure, whether for diagnostic or surgical purposes, sets as objectives the design of a robot to be inserted gradually into the body and moved in confined environments in order to reach a desired target position.

### **2.1.1 Anatomical constraints and required performances**

The first step in designing the robot is to take into account the constraints inherent to the application: it must be able to pass through the body's natural ducts. In the case of endoscopy, this means that its external diameter must not exceed 25mm (15mm for a child). During its insertion, it will be confronted with the passage through the oral cavity, the pharynx, the oesophagus and the stomach. It must therefore be able to follow a curvature that is a circular

arc with a radius of  $140\pm 20\text{mm}$  (120mm for a child) [29] as shown in Fig. 2.1.

The length of the robot is mainly determined by the length of the oesophagus, 250 to 300mm (120mm for a child) and the location of the operation. This criterion is therefore the one with the most variability.

### 2.1.2 Choice of a serial modular architecture

Given the anatomical constraints described above, a macroscopically serial architecture is adapted. The advantage of the serial structure is to ensure the largest possible working space and a high degree of repeatability of the achievable positions. The workspace redundancy allows the end-effector to be optimally positioned during the procedure.

These characteristics lead to consider a snake-like robot design. Moreover, in order to meet the criterion of operative variability, for example an adult or child patient, the modular nature of the robot makes sense. Indeed, the architecture is based on the duplication of an elementary module, the length of the robot is then adapted. Depending on a preoperative imaging result, the robot can become patient-specific.

The nature of this robot means that it is based on a mechanical module that can be stacked and provide the ability to move. In the initial case, i.e. the insertion of the robot to the stomach, the robotic motion is assumed to be planar. Assuming that the first version of the robot is planar, it can already be used and it is then necessary to define the number of configurations that each module of the robot should exhibit to achieve the task.

From the operational space point of view, it is known that a digital robot made up of binary actuator gives  $2^n$  positions, where  $n$  is the number of modules. The question of using binary actuators to follow a line is not optimal. It is necessary to operate two successive actuators in opposition to each other to follow a straight line.

In this case, the expected number of states for a module is 3. Indeed, from a functional point of view, this provides a neutral stable state and two stable states for the orientation of the end-effector as shown in Fig. 2.2. The use of a module with 3 states makes it possible to obtain  $3^n$  positions<sup>1</sup>.

Fig. 2.2 also illustrates the principle of digital robotics where each of the three states corresponds to a digit, in this specific case a ternary digit, also called a trit. Sending a control signal to this robot is therefore done by a sequence of trits, also referred to as a word.

In addition to anatomical constraints, there are functional constraints. In practice, it is necessary to design a module that can be easily duplicated and assembled. Given the scale, the question of actuation will also be an important design factor. For the design of the mechanical part as well as the actuation part, the weight of the other modules and the environment should

---

<sup>1</sup>For an 8-module architecture, the number of achievable positions in the working space is 6561.

## Chapter 2. Specification for the design of a new kind of robot based on multistable modules

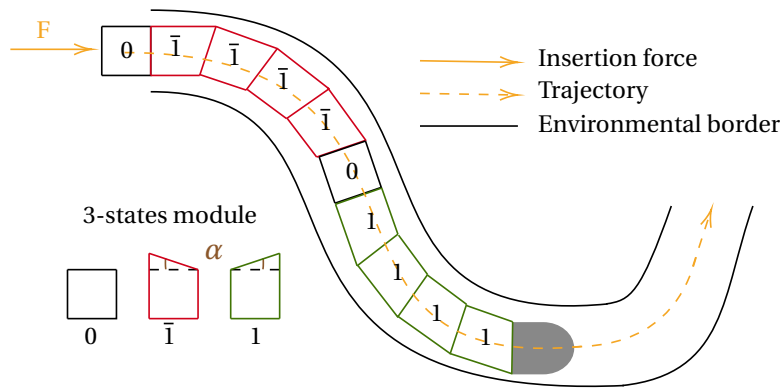


Figure 2.2 – Principle of the 3-states module based snake-like robot developed to perform complex trajectories in a confined environment. Each state of the module is identified as a balanced ternary signed-digit, i.e.  $\bar{1}, 0, 1$ .

be considered. The proximal module should support the weight of all the modules that make up the robot in each state, and it should be able to be actuated despite this load.

## 2.2 Module design: compliant mechanism and actuation principle

One approach for digital robot design is based on the use of compliant (=flexible) mechanisms. This approach exploits the discrete states of the bistable mechanism to accurately position the end effector, where the flexible joints ensure the kinematics of the structure [28]. This approach offers many advantages such as accuracy, mesoscale manufacturing, and monolithic design.

### 2.2.1 Compliant Mechanism and (multi-)stability principle

#### Compliant mechanisms

Compliant mechanisms attracted a lot of interest in the early 2000s in response to the need to design high precision robots [82, 92]. Initially, these robots were derived from industrial robots whose mechanical structure and control laws were adapted to meet the needs of precision manipulation. However, friction and mechanical backlash due to manufacturing tolerances imposed limits in terms of precision. The guiding principle of the mechanisms, based on the absence of assembly and on the principles of material elasticity, made it possible to overcome these problems. Furthermore, compliant mechanisms often have better energy efficiency and durability than their rigid counterparts. Indeed, compliant mechanisms derives some or all of its motion from the deflection of the elastic deformation of its slender parts. In this thesis, the deformation of flexible joints has been carried out under some fundamental assumptions regarding the material constitution, stress-strain proportionality and consequently the small

## 2.2. Module design: compliant mechanism and actuation principle

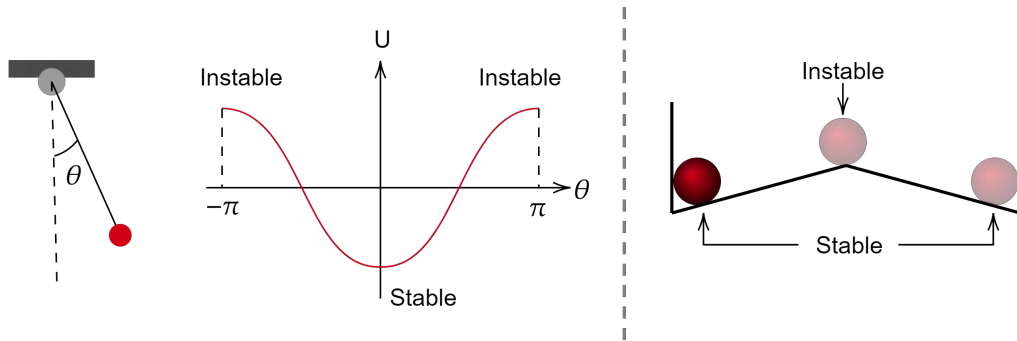


Figure 2.3 – Representation of the stable and unstable states of a pendulum and a bistable actuator.

strain assumption.

### Multistable mechanisms

Bistable actuators are mechanisms that have two stable equilibrium positions in their range of motion, as shown Fig. 2.3. Their advantage lies in their ability to remain in one of these stable positions despite small external disturbances. The switching is achieved by applying a sufficient force. In the case of flexible mechanisms, the bistable mechanism exploits a controlled deformation of the structure following a change in the boundary conditions. The most common case in the literature is the well-known double precurved beam bistable mechanism.

*The principle of stability of a system can be illustrated through the use of a pendulum. This system consists of a mass connected to a pivot joint via a rod with negligible mass, so that the mass is subject only to gravity. This system has one stable state in  $\theta = 0$ , two unstable state in  $\theta = \pm\pi$ , as shown in Fig. 2.3.*

In terms of applicability, a simple example would be a hair clip that can be bent and locked into two different shapes. More advanced examples of multistable mechanisms include space-based deployable structures [110]. These structures can be folded up for storage and transportation, and then deployed in space to create large structures, such as solar panels. The multistable property of these structures enables them to be lightweight and compact during transportation, while being large and stable during deployment.

The stability of a flexible mechanism is characterised by its stiffness  $K_i$ . This parameter corresponds to the ratio between the force  $F$  or moment  $M$  applied on the mechanism input and the induced displacement  $\delta$  or  $\alpha$  according to a translation or a rotation [82].

$$K_\delta = \frac{dF}{d\delta}, \quad K_\alpha = \frac{dM}{d\alpha} \quad (2.1)$$

In these equations, stiffness is defined as the derivative of the reaction force of the mechanism with respect to its displacement. The study of the sign of this stiffness can therefore be used

## Chapter 2. Specification for the design of a new kind of robot based on multistable modules

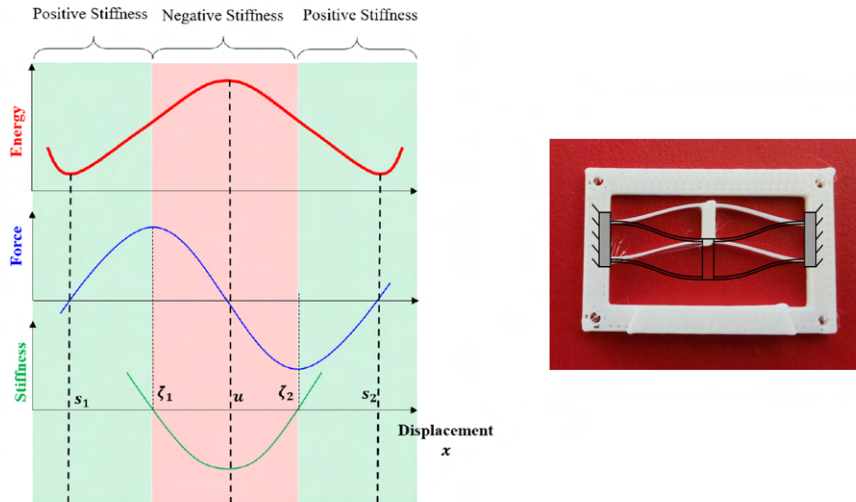


Figure 2.4 – Strain energy, reaction force and tangential stiffness of a bistable mechanism (on the right) where  $s_1$ ,  $s_2$  are stable positions,  $u$  is unstable position and  $\zeta_1$ ,  $\zeta_2$  correspond to zero stiffness positions. [224]

to study the stability behaviour of the compliant mechanism [132]. The mechanism is stable when the value of the stiffness is positive, and it is unstable when the stiffness is negative. This qualitative criterion is particularly interesting for the characterisation of multistable mechanisms with highly non-linear stiffness.

In the case of the double precurved beam bistable mechanism as illustrated in Fig. 2.4, the stability states come from a controlled mechanical phenomenon called buckling. This phenomenon is observed for thin beams, where the thickness is very small compared to the length ( $t \ll L$ ). When an axial load is applied to the beam and it exceeds a critical value, namely the Euler critical load, the beam buckles and becomes bistable.

The relationship between the reaction force of the mechanism, the strain energy and the stability of the mechanism is represented in Fig. 2.4. In this case,  $s_1$  and  $s_2$  represent the stable positions at the energy minima and  $u$  represents the position of the unstable state of the mechanism, where the energy is maximum [224].

The stability of this flexible mechanism has been studied in particular when the load exceeds the critical load [208, 181], and in energy harvesting scenarios [160]. The problem with this mechanism is that it requires two actuating forces, an axial force for buckling and a lateral force for switching states [27, 24]. The design of pre-curved mechanisms allows reduction to a single source of actuation. A first version was made from preformed curved beams manufactured in their first stable state without residual stress [164]. This approach, although easier to manufacture and integrate into a monolithic structure, leads to the loss of symmetry and therefore has a shorter stroke. Some designs have been presented to improve the symmetry

## 2.2. Module design: compliant mechanism and actuation principle

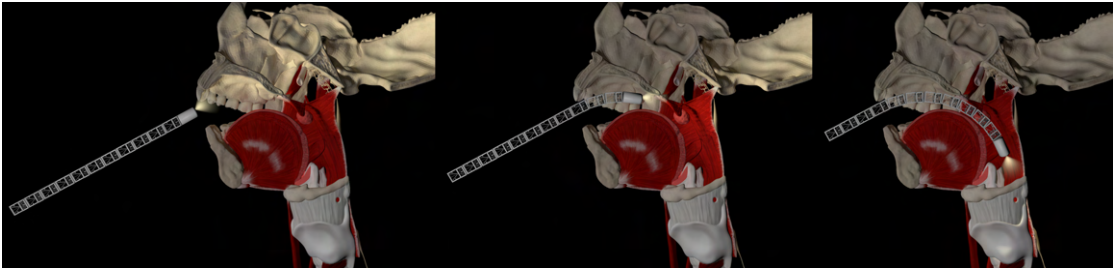


Figure 2.5 – Example rendering of a hyper-redundant robot based on multistable modules.

[105, 165]. Design [99], modeling [100], stress analysis and snap-through behaviour was extensively studied for many initial shapes of bistable mechanisms [102]. This has allowed the development of precision digital micro-robots that integrate them into their design [28, 98].

To obtain a higher degree of multistability, mechanisms can be designed to have highly nonlinear stiffness so that multiple stable states can exist [224]. This is often achieved by combining bistable mechanisms. The basis of this work is an orthogonal combination of bistable mechanisms [30, 224] resulting in tristability and quadrastability.

In all of the above examples, the mechanisms are used independently, as part of a structure. The foundations laid by Chalvet et al.[28] through the Dimibot have demonstrated the feasibility of building a discrete robot based on a combination of bistable modules [17]. This has motivated us to design a hyper-redundant serial robot based on multistable modules.

It is important to remember that this type of mechanism produces small amplitude motions, but as they are compact, this design approach is viable as shown in Fig. 2.5.

### 2.2.2 Choice of actuators and implementation in the modules

An ideal snake-like robot only requires energy input when changing configuration. However, in practice, whether it is a motor drive or a cable drive, energy is consumed to maintain a configuration. However for multistable mechanisms, discrete actuation is achieved by an on-off energy input required for triggering. In fact, bistable mechanisms have the advantage that once a stable configuration is reached, it is maintained as long as no energy input generates a deformation towards another stable state. The proposed tristable module must be capable of supporting a load equivalent to the weight of the other modules and should have low actuating forces.

However, the actuation remains a significant challenge. Constraints include the output force/size ratio and the capacity to be implemented after manufacturing.

## Chapter 2. Specification for the design of a new kind of robot based on multistable modules

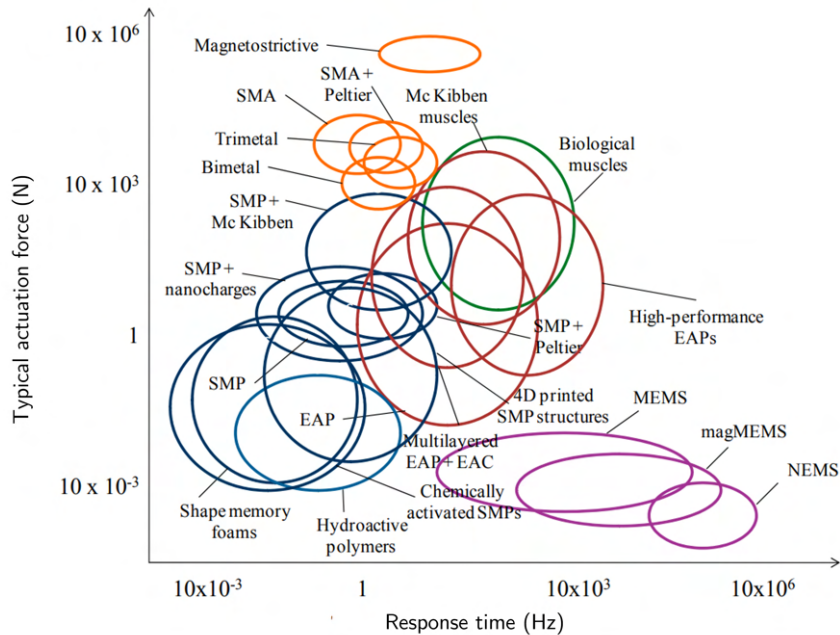


Figure 2.6 – Usual actuation force vs. response time for actuators based on “smart” materials. Abbreviations: EAC, electroactive (normally piezoelectric) ceramics; EAP, electroactive polymers; SMP, shape-memory polymers; SMA, shape-memory alloys; MEMS, microelectromechanical systems; magMEMS, Magnetic microelectromechanical systems; NEMS, nanoelectromechanical systems [45]

### Smart materials for robotics actuation

In the literature, there are several definitions to describe smart materials. These definitions are sometimes ambiguous, even contradictory, but they all agree in describing a smart material as one that is capable of reversibly changing its physical and/or chemical properties in response to an appropriate external stimulus [193, 143, 209]. This definition is not sufficient, train rails expand reversibly when heated and yet steel is not considered a smart material. It therefore seems appropriate to point out that in our case, these materials have unconventional properties.

Of the many materials classified as intelligent, only those that can cause a mechanical response, by changing shape, to a stimulus will be examined as they can be used as actuators. The most prominent of these are listed below:

- Piezoelectric smart materials: Piezoelectric ceramics, Piezoelectric single-crystals, Piezoelectric polymers,...
- Thermostrictive materials: Shape memory alloys, Shape memory polymers, Shape memory foams,...
- Thermoactive materials

## 2.2. Module design: compliant mechanism and actuation principle

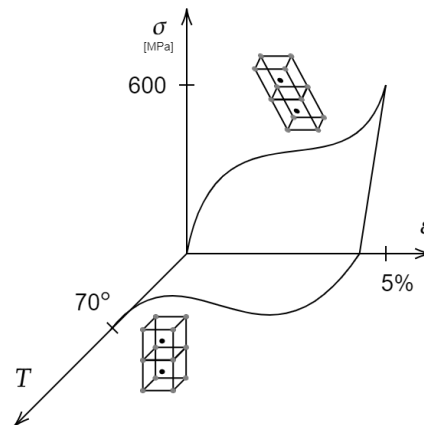


Figure 2.7 – Stress-strain-temperature curvature of a NiTi SMA wire

- Electroactive polymers: Conductive polymers, Dielectric elastomers, Polyelectrolyte gels,...
- Electrostrictive smart materials
- Magnetostrictive/magnetoelastic smart materials
- Electrorheological materials

Each of these materials has its own characteristics which are the basis for a classification according to the criteria of interest. In the context of a robotic application, an actuation force/actuation frequency classification such as the one shown in Fig. 2.6 allows an initial selection to be made. Specifically, in this case, the task to be done is to pull the vertical beam of the tristable mechanism in such a way as to cause the buckling of the beam and tilting of the bistable mechanism. It is therefore imperative that the actuators have a high energy density to produce sufficient stroke and force. Energy density is defined as the energy available for work as a function of material stress and strain such that:

$$E = \sigma \varepsilon \quad (2.2)$$

Of all the actuators considered for repeatable actuation, shape memory alloys (SMA) have the highest energy density due to their high volume expansion combined with a high load bearing capability.

### SMA operating principle and mechanical model

Shape memory alloys (SMAs) are materials with thermomechanical properties that are quite distinguishable from metals and other alloys. Among these properties, two give them an important application potential: superelasticity and shape memory effect.

## Chapter 2. Specification for the design of a new kind of robot based on multistable modules

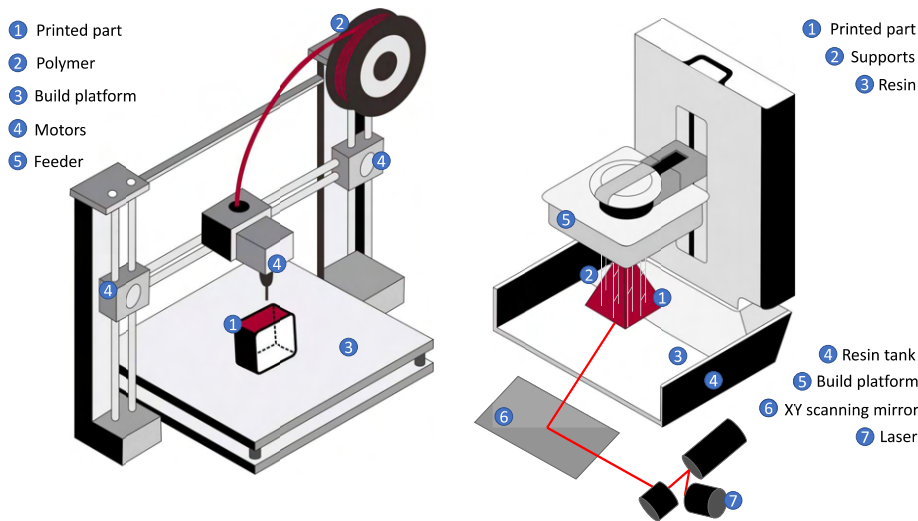


Figure 2.8 – Characterisation of the most common materials used in 3D printing (adapted from form-labs)

The deformation of an SMA wire is due to a change in the structure of the crystalline phase of the material resulting in a length shortening. This shortening is the consequence of an increase in temperature of the material. The Joule effect is usually chosen as the method of actuation by applying a defined current. An increase of temperature converts the martensitic phase (body-centered tetragonal) into an austenitic phase (face-centered cubic), as shown in Fig. 2.7. The recovery of the initial length is achieved by the application of mechanical stresses, after cooling.

Once heated, the wire will be converted to the austenitic phase. To bring it back to a martensitic phase, one approach used in robotics is to use two opposing SMA wires.

As SMAs are thermal actuators, the question of actuation frequency and cooling arises. In the standard case, the actuation frequency is considered to be around 0.1 Hz, but it can reach few Hertz in proper conditions [121], which is sufficient to ensure the deployment of the robot. Furthermore, during the procedure, once the robot has reached the target position, its overall configuration is less likely to change. In order to improve the performance, the cooling aspect will be taken into account and for this purpose different strategies can be used such as the use of calloduc or watercooling.

### 2.3 Manufacturing

In terms of manufacturing, the fabrication of flexible mechanisms imposes certain constraints. The geometry chosen affects not only the mechanical behaviour of the mechanism, but also the ease of fabrication. Some flexible components of the mechanism may be difficult to produce with certain manufacturing processes. This is particularly true when this constraint is combined with the desire to produce a monolithic mechanism. The downscaling is accompanied by a desire to reduce the assembly phase and to favour monolithic designs.

It is also necessary to characterise the material according to the used manufacturing process. The same material will not have the same properties depending on the process, especially in the case of additive manufacturing.

The mechanical behaviour of the mechanism depends on both the geometry and the material properties. The characteristics of a material affect the strength and compliance. It must therefore be assessed whether the designed mechanism can reasonably achieve the strength and fatigue characteristics necessary for a good mechanical performance with the materials available for each manufacturing technology.

In this case, additive manufacturing has many advantages and is particularly suited for the fabrication of bistable mechanisms in a mesoscopic scale [11]. In addition, it allows the production of monolithic mechanisms with complex geometry, or at least with a reduced number of parts [21], which is an advantage over other manufacturing processes because it reduces the tedious assembly phase.

All of this is part of a parsimonious design approach where the design uses the least amount of elements, material and resources required to achieve its purpose, while remaining effective. This principle is used to create a simple, effective, and elegant design.

From a prospective point of view, it is also conceivable that hospitals will have access to additive manufacturing processes, such as 3D printers, allowing the design of patient-specific robots based on pre-operative examinations (imaging). The availability of biocompatible materials supports this hypothesis.

Finally, the ease of access to this type of manufacturing process facilitates the prototyping and experimentation phases.

#### **Additive manufacturing process**

Additive manufacturing encompasses a large number of manufacturing processes whose method is based on the deposition of thin layers of material through a physical transformation of a material. Each of these processes is governed by a number of material and manufacturing specifications. In this work, the manufacturing process chosen in the first instance is fused deposition modelling (FDM) then stereolithographic 3D printing (SLA). This choice was based

## **Chapter 2. Specification for the design of a new kind of robot based on multistable modules**

---

on various criteria such as the availability of the material and the possibility of multi-material manufacturing.

The principle of FDM 3D printing is to extrude a previously melted thermoplastic material and deposit it in the form of superposed layers. The material is liquefied by the temperature rise of an extrusion nozzle and pressurisation is achieved by the feeder pushing the filament. However, this technology has some disadvantages such as the size and precision limit, and above all the anisotropic behaviour of the final material, whose internal stress relaxation may affect the behaviour of the mechanism over time. This is because FDM printed parts are microporous structures [11]. As a result, the actual cross-section of the part varies in each direction from the apparent cross-section. In addition, the cohesion between layers does not occur in a reproducible way. The Young's modulus is therefore variable in all three axes. This anisotropy can be minimised by varying the printing direction between each layer to obtain orthotropic behaviour along the X and Y axes.

Stereolithographic printing is a manufacturing technology known as vat photopolymerisation. The device relies on the use of a light source to polymerise a liquid resin and thus cause it to solidify. Resins are thermosetting materials that react to exposure to light. Under the effect of certain wavelengths of light, short molecular chains fuse together. This chemical principle is described as the polymerisation of monomers and oligomers and causes the solidification of the material. Most of resins are acrylate-based. Of all the additive manufacturing processes, stereolithography allows parts to be manufactured with the highest precision and resolution. This approach is limited by its low printing volume and its use constraints (toxicity, waste management, etc.).

### **Material characterisation**

Choosing the right polymer is also important to achieve the right properties of a structure, especially if its functional use depends on the flexibility of the joints obtained. The properties of the polymer can be modified by the addition of additives, but in the first stage only "simple" materials are used.

The data presented in Fig. 2.9 is produced from supplier data (RS Components, Ultimaker, Stratasys) and weighted by in-use observations. This information, while consistent with some of the work in the literature [154], has not been standardised and should be taken as an indication of use. The performance criterion is based on the assumption of an average polymer with a general chemical formula, although this factor may vary between suppliers. On the basis of Tab. 2.9, it is clear that in the case of bi-material printing, the rigid elements should be made of PLA and the links of TPU.

Depending on the needs, this graphic chart allowed us to choose the most suitable material. Thanks to its consistent performance, PLA will always be the material of first choice according to the different criteria used. ABS and especially PC were then used because of the conservation

of their mechanical properties in response to thermal stress. This thermal stress is due to the use of SMA actuators.

In the third stage, with stereolithographic printing, the resins must be chosen even more carefully. Although there are resins whose mechanical properties tend to be similar to those of PLA and ABS, many remain more fragile.

## 2.4 Conclusions

In this chapter, a review of the literature highlighted the constraints in terms of dimensions to meet the geometry of the digestive tract. In view of the complex trajectories to be realised, an innovative architecture has been proposed based on the use of intelligent modules and actuators.

The module will be designed using compliant mechanisms, as these are well suited to the need for downscaling, especially as multi-stable mechanisms have already proved their worth in the design of digital robots.

The actuation will be achieved using a small active material, namely shape memory alloys (SMAs), which will be sized to achieve the required triggering force.

In order not to be constrained in terms of geometry and to produce monolithic mechanisms, the choice of 3D printing was made. The module will be described in Chapter 3 and the assembly and modelling of the robot in Chapter 4.

# Chapter 2. Specification for the design of a new kind of robot based on multistable modules

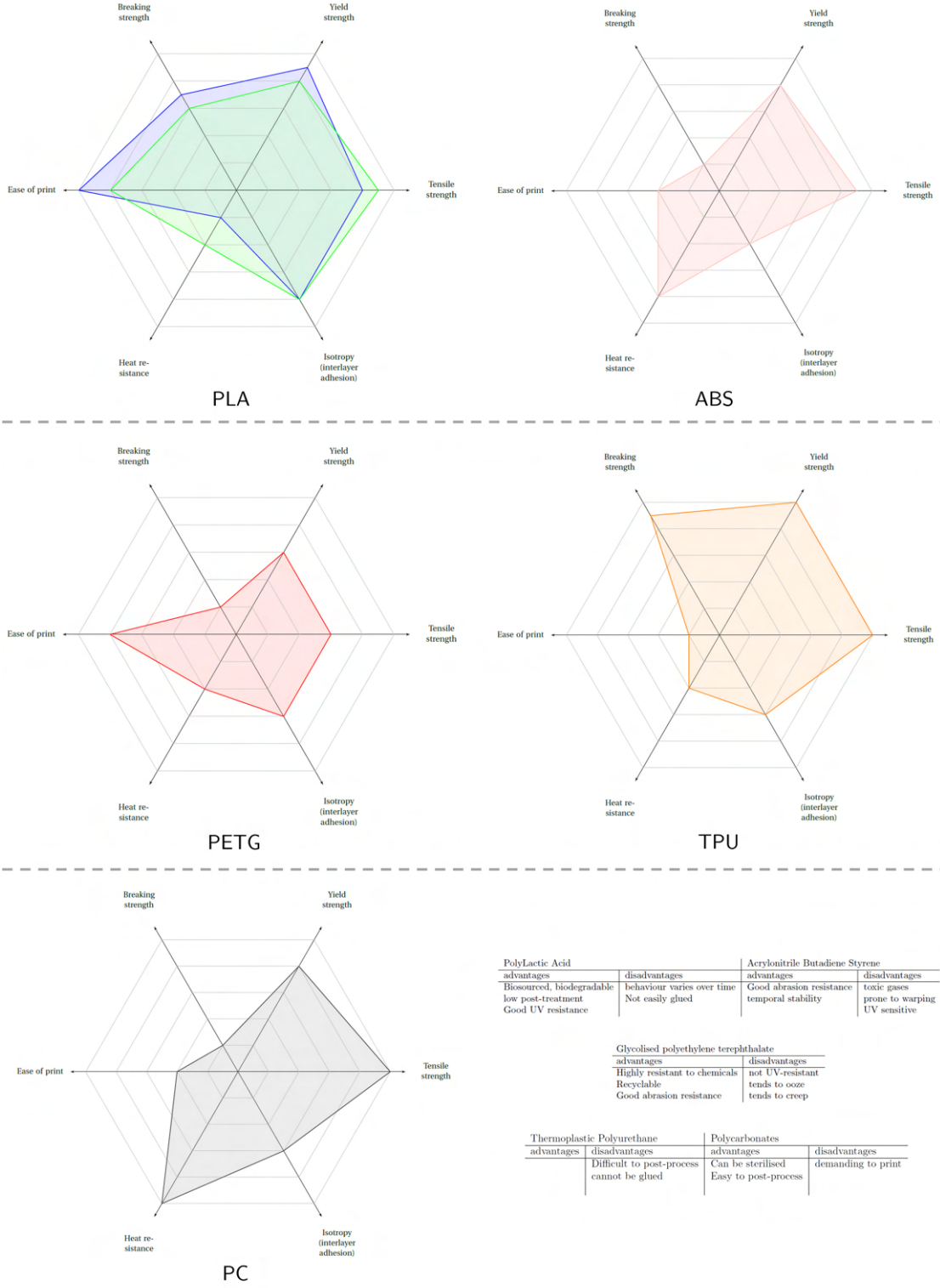


Figure 2.9 – Characterisation of the most common materials used in 3D printing based on experiments conducted during this work and supplier data.

### 3 Design of the elementary multistable module

In the previous chapter, the interest of designing a snake-like robot from a superposition of modules was presented. Due to the mesoscopic scale of the architecture, the choice was made to design the module with flexible mechanisms.

The use of bistable and multistable modules, characterised by their stability and mechanical robustness, enables precise, repeatable motions to be achieved. However, the latter require significant dimensioning.

This chapter describes the design and dimensioning phases of the elementary module of our architecture following the presentation of the specifications to be met. This tristable module results from the combination of 3 mechanisms, as illustrated in figure 3.1. These mechanisms independently ensure a function (orientation, maintaining configuration, guiding) which, when combined, allows the mechanism to operate correctly and whose dimensioning will be detailed in the following sections.

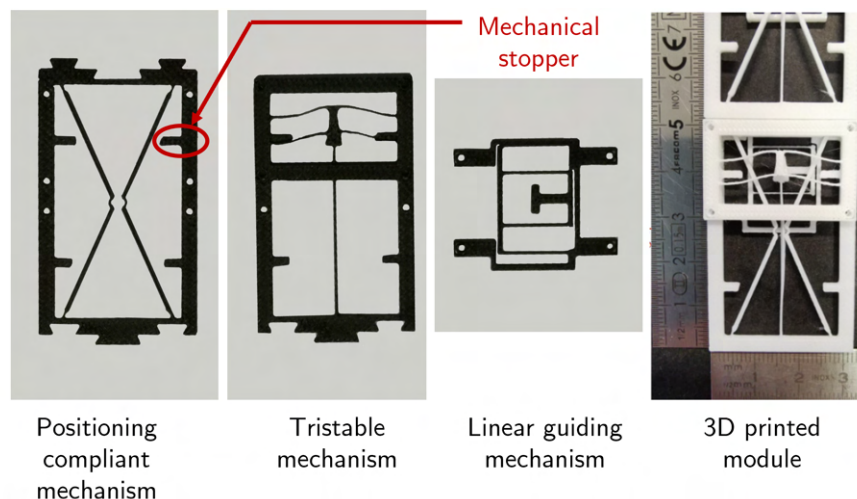


Figure 3.1 – Illustrations of the 3 mechanisms composing the module as well as the module as it was manufactured by 3D printing. Illustrations of the 3 mechanisms composing the module as well as the module as it was manufactured by 3D printing.

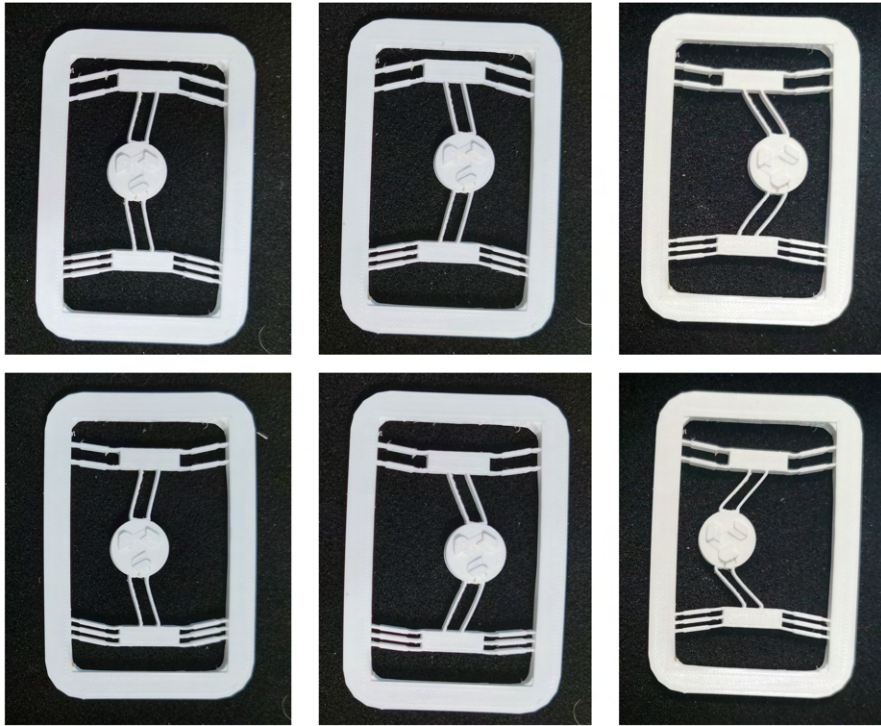


Figure 3.2 – Photography of all states of an hexastable mechanism.

### 3.1 Design and sizing of a tristable mechanism

Two important notions have been introduced beforehand. The first is the advantage of using tristable modules rather than bistable modules, in order to significantly increase the number of achievable positions. The second concerns the manufacturability of the module and the impact of the material on mechanical behaviour. The first step is therefore to characterise the multistable mechanism of this module.

A multistable compliant mechanism can be designed by combining several bistable compliant mechanisms in series [151]. A series combination of three orthogonal bistable mechanisms produces up to four stable equilibria is shown in Fig. 3.2. The case of two bistable compliant mechanisms producing three stable equilibria, such as T-shaped mechanisms, have been extensively studied in previous works [30, 224].

The tristable mechanism is based on a combination of straight and preformed beams rigidly joined together, as shown in Fig. 3.1. An actuation resulting in a deflection of the straight beam allows the preformed bistable beams to buckle due to the occurrence of a shuttle loading. Maintaining this deformed configuration is possible because of the difference between the force needed to deform the vertical beam and the force needed to actuate the bistable beams. The analytical model detailed in this section is inspired by the work of Hussein et al. [99] and the theory of buckling.

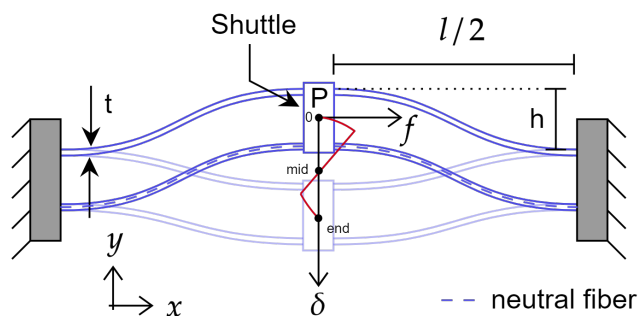


Figure 3.3 – Geometric parameter identification of a double double beam bistable mechanism.

#### 3.1.1 Analytical modelling of a preformed-beams bistable mechanism

There are three main ways to produce a bistable mechanism. It can be precompressed, i.e. the beams are manufactured rectilinearly and then compressed to buckling by means of an axial load. It is also possible to obtain this type of mechanism by means of stress, which may be related to the residual stress after manufacture or by applying thermal stress. In the last approach, the beams are manufactured directly pre-shaped in the first buckling mode without residual stress and without strain energy. The latter method is particularly suited in the context of additive manufacturing to produce complex mechanics with a minimum of assembly. Furthermore, an analytical model has already been proposed in previous research work [73].

##### Stress analysis

Pre-shaped beams, as shown in Fig. 3.3, are characterised by a number of geometrical parameters, namely length  $l$ , thickness  $t$  and width  $w$ . These beams are also governed by a number of manufacturing parameters in the pre-shaped state, namely the initial height  $h$  and the shape of the beam governed by the equation  $\eta(x)$ . In this model, it is assumed that the force causing the deformation is applied pointwise at the centre of the beam.

Assuming small deformation, Timoshenko described the buckling of the pre-shaped beam by the following equation [204]:

$$\frac{d^2}{dx^2} \left( EI \frac{d^2 \eta}{dx^2} \right) + P \frac{d^2 \eta}{dx^2} = 0, \quad I = \iint z^2 dy dz \quad (3.1)$$

Where  $E$  is the Young's modulus and  $I$  is the quadratic moment. Considering the embedding stresses of the beam, the nature of the solutions is modal and it corresponds to the sum of the

### Chapter 3. Design of the elementary multistable module

different buckling modes:

$$\eta(x) = \sum_{j=1}^{\infty} a_j \eta_j(x) \quad (3.2)$$

$a_j$  and  $\eta_j$  correspond respectively to the  $j$ th mode which reflects the contribution of each buckling mode to the solution and the  $j$ th buckling shape mode. According to [99], it can be written:

$$\left. \begin{aligned} \eta_j &= 1 - \cos N_j \frac{x}{l} \\ N_j &= (j+1)\pi \end{aligned} \right\} j = 1, 3, 5, \dots$$

$$\left. \begin{aligned} \eta_j &= 1 - 2 \frac{x}{l} - \cos N_j \frac{x}{l} + \frac{2 \sin N_j \frac{x}{l}}{N_j} \\ N_j &= 2.86\pi, 4.92\pi, 6.94\pi, 8.95\pi, \dots \end{aligned} \right\} j = 2, 4, 6, \dots \quad (3.3)$$

with  $N_j$  the  $j$ th mode of the normalized force  $N$ . The calculation of the snapping forces has been detailed by Qiu [165] and Hussein [99] and leads to three types of solutions. The first solution correspond to the domain where the beam is in a compressed state, the second is where the beam is not subjected to any mechanical stress and the third occurs when mode 2 is constrained, the buckling modes are shown in Fig. 3.4. As the stability margin of a simple beam is relatively small, mode 2 is constrained by connecting two curved blades at their centre. As it is extensively detailed in the previous Hussein's work, not all the calculation steps will be repeated to obtain the characteristic equations of mode 1 and mode 3 which are the ones we are interested in:

$$f = \frac{N^3}{(N/4) - \tan(N/4)} \left( \frac{N^2}{N^2 - 4\pi^2} - \Delta \right) \quad (3.4)$$

$$\frac{3}{16N^4} \left( 1 + \frac{\tan^2(N/4)}{3} - \frac{\tan(N/4)}{(N/4)} \right) f_1^2 - \frac{4\pi^2}{(N^2 - 4\pi^2)^2} f_1 + \frac{N^2}{12Q^2} - \frac{N^2 \pi^2 (N^2 - 8\pi^2)}{4(N^2 - 4\pi^2)^2} = 0 \quad (3.5)$$

These equations give the relationship between the applied force  $f$ , the axial stress  $N$  and the deflection  $\Delta$  for the first type of solution. The solution is done numerically by dichotomy. The third type of solution is simpler to establish. Assuming that the force  $N_3$  is constant, Eq. 3.4 can be simplified as:

$$F_3 = 64\pi^2 \left( \frac{4}{3} - \Delta \right) \quad (3.6)$$

This equation characterises a linear force-displacement interaction in this 3rd type of solution. It is possible to calculate the exact positions where the third mode appears:

$$d_{top}, d_{bot} = h \left( \frac{28}{27} \pm \frac{2\pi}{3} \sqrt{\frac{1}{6} + \frac{16}{81\pi^2} - \frac{1}{Q^2}} \right) \quad (3.7)$$

and whose corresponding force value can be calculated by entering the results of Eq. 3.7 in Eq. 3.6

$$f_{top}, f_{bot} = \frac{Ewt^3 h}{l^3} \frac{32\pi^2}{9} \left( \frac{4}{9} \mp \pi \sqrt{\frac{1}{6} + \frac{16}{81\pi^2} - \frac{1}{Q^2}} \right) \quad (3.8)$$

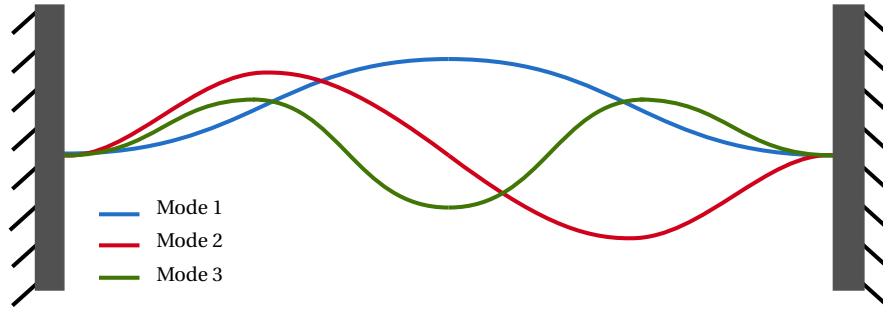


Figure 3.4 – Representation of the first three buckling modes.

The force-displacement curve of the applied force  $f$ , along  $\vec{y}$  at P, as a function of the displacement of the shuttle center  $d$  exhibits two extrema values, identified in Fig. 3.6a. These values obtained from the previous equations make it possible to identify the maximum force values, i.e  $f_{top}$  and  $f_{bot}$ , to be provided in order to operate the mechanism and the stroke value for which the following are obtained, i.e  $d_{top}$  and  $d_{bot}$ .

Due to the manufactured initial precurved shape, the value of the snapping force is not symmetric for leaving the stable states. The force  $f_{top}$ , which is greater than  $f_{bot}$  is the maximal reaction force of the bistable mechanism, as shown in Fig. 3.6a and later in the results Fig. 3.22.

Furthermore, in the case of a bistable mechanism where the shape of the beams is governed by the following equation:

$$\omega(x) = \frac{h}{2} \left( 1 - \cos\left(2\pi \frac{x}{l}\right) \right) \quad (3.9)$$

And where the shuttle shown in Fig. 3.5 is inserted in the middle of the pre-shaped beam section to prevent this section to rotate and constrain mode 2. In order to ensure bistability, the following condition on the ratio  $Q$  of the apex  $h$  to the thickness of the beam  $t$  is required :

$$Q = h/t > 2.31 \quad (3.10)$$

#### Stress and strain energy analysis

In order to ensure the proper operation of the mechanism, a study of the evolution of the maximum stresses inside the beams during deflection must be carried out for the chosen geometrical parameters and physical properties of the material. Then, knowing the restoring force of the mechanism according to the direction of its displacement, it is possible to calculate the deformation energy. From the study of this stored energy in the mechanism due to its elastic deformation, it is possible to derive the equilibrium states of the mechanism.

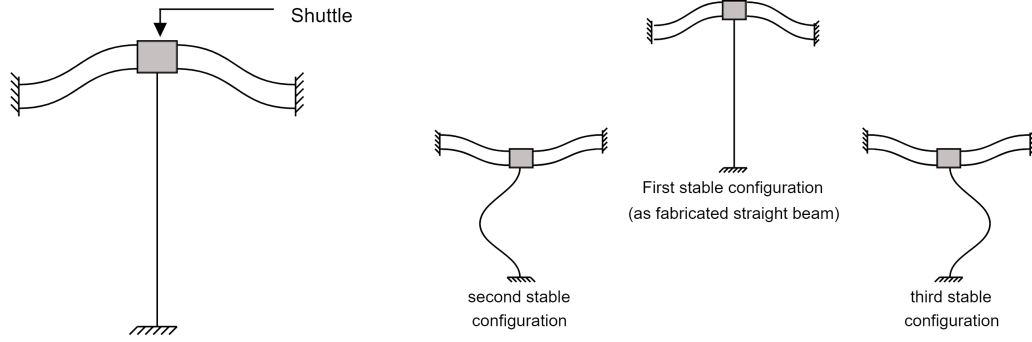


Figure 3.5 – Representation of a tristable double-beam based mechanism illustrated in its three stable equilibrium positions. The fabricated configuration corresponds to the first stable state.

The total stresses in the beam are calculated as the sum of the axial stresses  $\sigma_a$  and bending stresses  $\sigma_b$ .

$$\sigma_a = \frac{Et^2}{12l^2} N^2 \quad (3.11)$$

$$\sigma_b = \pi^2 \frac{Ezh}{l^2} \left[ 2 \cos 2\pi \frac{x}{l} - \sum \frac{4 \frac{fl^3}{EIh}}{N_j^2(N^2 - N_j^2)} (j+1)^2 \cos(j+1)\pi \frac{x}{l} \right] \quad (3.12)$$

where  $z$  is the distance between arc lines throughout the thickness and the neutral line. According to [97], the maximal stress for the first and third kind of solution can be expressed as:

$$\sigma_{max|1}^{N,\Delta} = E \left( \frac{t}{l} \right)^2 \left[ \frac{\pi^2 N^2 Q}{N^2 - 4\pi^2} + \frac{N^2}{12} + N^2 Q \left( \frac{N^2}{N^2 - 4\pi^2} - \Delta \right) \frac{\tan \frac{N}{4}}{4 \left( \frac{N}{4} - \tan \frac{N}{4} \right)} \right] \quad (3.13)$$

$$\sigma_{max|1}^{N,\Delta} = E \left( \frac{t}{l} \right)^2 \frac{4\pi^2}{3} \left[ 1 + Q + Q \sqrt{\frac{-27}{\pi^2} \Delta^2 + \frac{56}{\pi^2} \Delta + 2 - \frac{80}{3\pi^2} - 12/Q^2} \right] \quad (3.14)$$

The strain energy is then calculated as the integral of the reaction force with respect to its displacement.

$$U = \int_0^\delta \frac{f^2}{2Ewt} dx \quad (3.15)$$

### 3.1.2 Modelling of the vertical beam of the tristable mechanism

The second part of the mechanism, represented in Fig. 3.6b, concerns the initially vertical beam whose buckling will result in large deflections and a sudden change of configuration

### 3.1. Design and sizing of a tristable mechanism

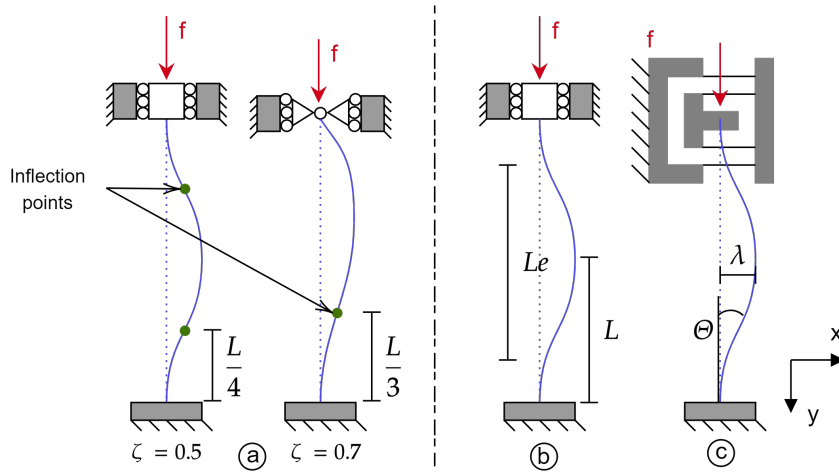


Figure 3.6 – Representation of a pre-curved bistable mechanism and the evolution of the force  $f$  as a function of the position  $d$  (subfigure a). The subfigures b and c illustrate respectively a buckling beam in the case of theoretical guided-fixed end condition and in the real end condition with a slider.

of the bistable mechanism. The choice of using an initially straight beam is justified here in response to footprint constraints and by obtaining a symmetrical snap-through behaviour between the two buckling sides. This beam therefore has an initial stable configuration and two buckled stable configurations.

The beam attached orthogonally to the shuttle of the bistable mechanism is straight. When the shuttle changes state, it generates a compressive force greater than a critical value so that the beam buckles. Buckling describes the sudden change of state induced by the excess compression energy translated into buckling energy.

In our model, the vertical beam is fixed in the frame on one side and in the shuttle on the other side as shown in Fig. 3.5. In order for the beam to buckle, the following condition must be met [204]

$$f \geq \frac{\pi^2 EI}{(\zeta L)^2}. \quad (3.16)$$

This equation describes the minimum force that can trigger the buckling of a beam whose material and geometrical parameters are known. These parameters are the Young modulus of the material  $E$ , the second moment of area  $I$ , the actual length  $L$  and the effective length factor  $\zeta$ , i.e. a ratio to obtain the effective length  $L_e$  as a function of the length of the beam, as illustrated in Fig. 3.6.  $L_e$  corresponds to the section of the beam between two inflection points (zero bending moment points) on the buckled shape for a specific type of connection.

To achieve multistability in the design,  $f_{bot}$  must be higher than the force required to hold the vertical beam in a buckling state. If this condition is satisfied, there is a point of intersection between the force-displacement curves of the bistable mechanism and the vertical beam. A

## Chapter 3. Design of the elementary multistable module

---

stable equilibrium state exists at this position. As the beam is initially vertical, its buckling modes are symmetrical. It therefore has a stable state on either side of its manufactured position. The vertical beam has three stable states in this mechanism, the as-fabricated state and the two buckling states.

Considering the slenderness ratio,  $t \ll l$ , and the vertical beam boundary conditions, the maximal stress,  $\sigma_{max}$ , is estimated using Euler's formula [204]

$$\sigma_{max} = \frac{\pi^2 E}{\left(\zeta \frac{L}{r}\right)^2}, \text{ with } \sigma_{max} \leq \sigma_{adm} \quad (3.17)$$

where  $r$  is the radius of gyration of the cross section. The  $\sigma_{max}$  value was calculated and compared to an admissible stress value  $\sigma_{adm}$ , defined according to the yield strength of the material, in order to ensure the proper functioning of the mechanism.

The boundary conditions are controlled by means of a flexible slider inspired by that used by Rubbert et al. [171], represented in Fig. 3.6c and detailed in Section 3.11. It should be noted that for the analytical model, the vertical beam was initially described as doubly embedded, with an effective length factor of  $\zeta = 0.5$ , however during experiments and in spite of the compensation mechanism, it turned out that the buckling mode of the beam corresponded more to the case of a pinned-fixed beam and thus  $\zeta = 0.7$ .

The selection of the configuration is done by means of actuators whose properties will be described in Chapter III.

The two elements described above form the first mechanism that provides the three stable configurations of the module. It will be associated with the mechanism described in the following section which will provide angle orientation.

## 3.2 Positioning compliant mechanism

### 3.2.1 Flexible joint

Compliant mechanisms are characterised by their particular flexible joint that consist of deformable structures. These monolithic mechanisms obtain their relative mobility between rigid body from material elastic deformation of slender elements. The motions allowed by elastic deformation is not comparable in range with traditional mechanism but are particularly well adapted to miniaturisation as shown in Fig. 3.7.

Various flexible connections can be used. They differ in size and kinematic performance. The most representative connection allowing rotation is the circular hinge. It is widely used because its behaviour is similar to that of a traditional pivot joint. However, it requires a significant design phase or the addition of mechanical stops to counteract the effects of stress concentration in the centre of the joint. Sometimes a more oval profile is preferred in order

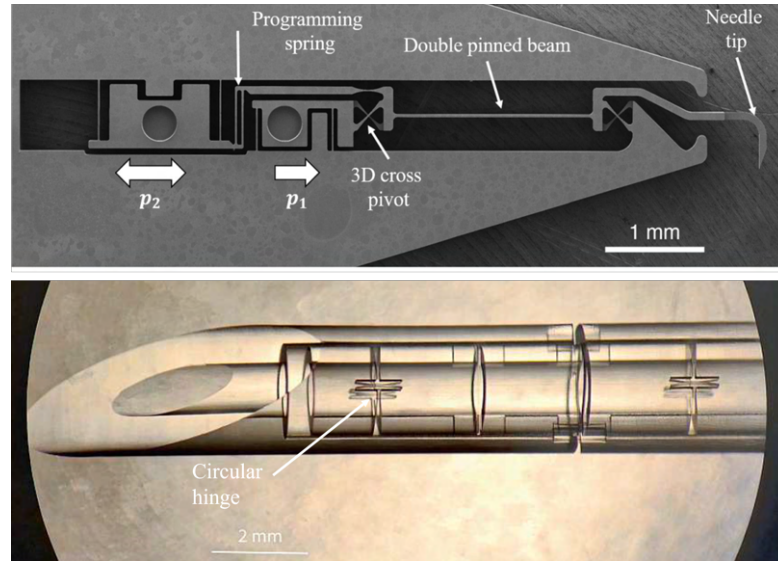


Figure 3.7 – Photograph of flexible mechanisms produced monolithically in a glass needle [225, 61].

to distribute the internal stresses a little better as illustrated in Fig. 3.8. Cross spring hinges are normally preferred due to their advantageous kinematic performance and better stress tolerance. However, cross spring hinges are bulkier and more demanding to produce in 3D printing.

The flexible linkages used for this prototype, as shown in Fig. 3.9, are modelled as thin section beams. These hinges were preferred due to their smaller footprint and manufacturing constraints [82, 172].

$$\beta_c = \frac{3\pi\sigma_{adm}\sqrt{r}}{4E\sqrt{t}} \quad (3.18)$$

$$\sigma_c^{max_h} = k_T \frac{F}{t \cdot w} + k_b \frac{6M}{t^2 w} \quad (3.19)$$

where  $r$  is the radius of the hinge and  $t$  the thickness,  $F$  and  $M$  are the forces and moments acting on the joint,  $w$  describes the width of the joint and  $k_t$  and  $k_b$  are the correction factors for tensile and compressive loads. As the resolution of the printer limits the printing of notched hinges, this type of hinge was therefore designed and modelled as a beam, whose loading could be similar to that of a cantilever beam loaded at the ends. This model was carried out in accordance with beam theory [203] such as

$$\beta_b = (Fl_{hinge}^2)/(2EI) \quad (3.20)$$

$$\sigma_b^{max_h} = My/I \quad (3.21)$$

where  $\beta$  is the slope,  $F$  is the force exerted by the tristable mechanism,  $l_{hinge}$  is the length

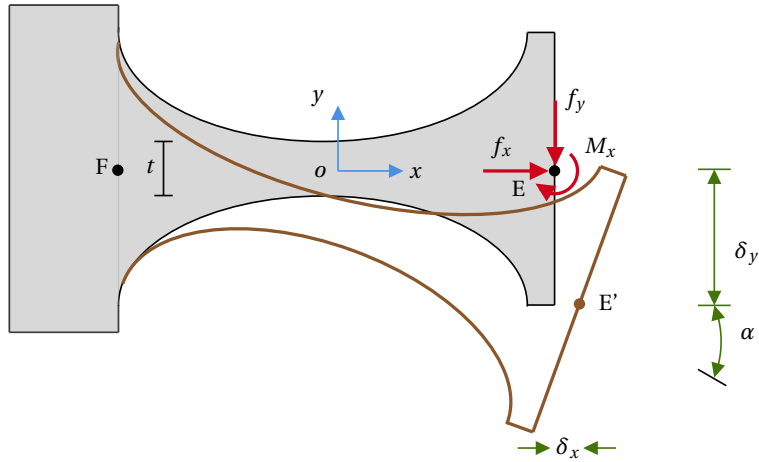


Figure 3.8 – Schematic representation of an elliptical notch flexure hinge.

of the joint, and  $M$  and  $y$  are the moment and distance to the neutral axis. The maximal constraint  $\sigma_{max_h}$  was compared to the same admissible stress criteria as previously defined  $\sigma_{adm}$ . The mechanical stoppers have been sized so as not to exceed the allowable stroke,  $\beta = 14^\circ$ , and constraint,  $\sigma_{max_h} = 53.33MPa$ , values of these hinges.

### 3.2.2 Operation and sizing of the mechanism

The positioning mechanism can be modelled as a 6-bar mechanism as shown in Fig. 3.9. The symmetry of this mechanism makes it possible to simplify the geometrical model and to analyse only half of it.

This mechanism must deform under the effect of the tristable mechanism and produce an angle  $\alpha$ . This angle is both the one of the mechanism and the one of the module. The second objective of this mechanism is to sustain the configurations against external loads acting on the module. The tristable module is locked in the as fabricated state by this mechanical obstacles and not by elastic equilibrium.

Although this mechanism is subsequently linked to the tristable mechanism previously described, these two mechanisms are partially decoupled to isolate the multistable mechanism from external solicitations when it is not actuated.

As the structure of this mechanism is composed of flexible joints, over-constraints due to external interactions must be taken into account during the design. These constraints are included by means of a safety coefficient and mechanical stoppers. Those stoppers have a double purpose, they prevent deformations beyond the elastic limit and allow the transmission of the forces acting on the mechanism.

For practical reasons, it was chosen to size a prototype to 8 modules. This implies that, in

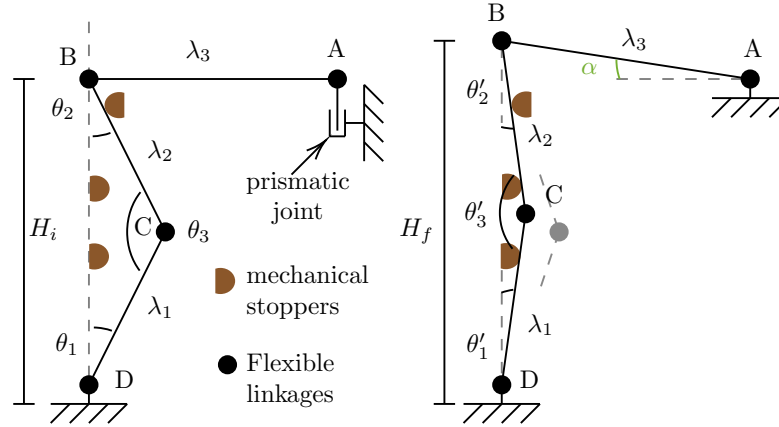


Figure 3.9 – Geometric model of half of the compliant structure in initial configuration on the left and deflected on the right. Mechanical correspondence in the initial configuration in red in the CAD model.

the worst case, the most proximal module must support and be able to be actuated against the weight of the other seven modules. It was therefore necessary to take into account the weight of each module, which is 2.5g, and the weight of future printed circuit boards (PCB), also estimated at 2.5g. Knowing the length,  $L_m$ , and the weight of each  $i$  module,  $W_i$ , and the number of modules,  $n$ , the moment that this module have to sustain can be calculated  $\sum_{i=1}^{n-1} i L_m W_i$ . The demonstration is developed in the experimental part by operating the module against an equivalent load of 7N for the first module, for the following modules the bending moment is lower.

### 3.2.3 Kinematic model of the mechanism

If we refer to the kinematic model of the structure shown in Fig. 3.9, the objective is to maximise the mechanism orientation given by the signed angle  $\alpha$ . For our prototype this angle is set at  $7^\circ$ . This angle value may seem low, but within the flexible mechanisms, it already belongs to the long stroke mechanisms. This value may be subject to further optimisation in order to be increased. Once actuated, due to the constraints on the stoppers, it is possible to neglect the vertical displacement at A and assume that it is fixed.

After that the length  $\lambda_k$  of the segments, represented in Fig. 3.9, is determined using the following equations, knowing that the  $\theta_k$  represent the angles between the segments, that  $H_i$  represents the initial height of our mechanism and  $H_f$  the height once the structure is deformed by the tristable mechanism.

$$\alpha = \arcsin(H_f - H_i) \quad (3.22)$$

$$H_i = \lambda_1 \cos \theta_1 + \lambda_2 \cos \theta_2 \quad (3.23)$$

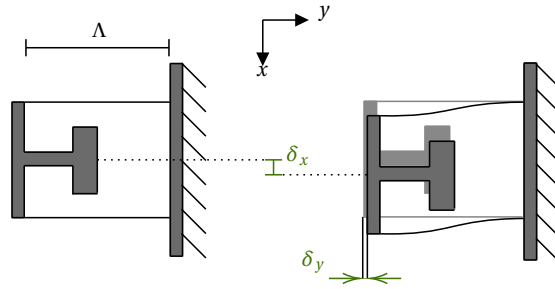


Figure 3.10 – Parallel spring stage to the equilibrium and deformed by a force.

$$H_f = \lambda_1 \cos\theta'_1 + \lambda_2 \cos\theta'_2 \quad (3.24)$$

### 3.3 Design of the linear guiding mechanism

The correct operation of the bistable mechanism is conditioned by its boundary conditions. However, these conditions change when the mechanism reaches an intermediate position, between the two stable positions (e.g. halfway). In this position, if the mechanism is symmetrical, then the 4 beams buckle and the stiffnesses of the mechanism along  $y$  (transverse translation) and  $rz$  (rotation in the plane of the mechanism) directions drop drastically, which transforms the supposed 1 DOF guidance into a 3 DOF guidance. This phenomenon, which is simple to verify experimentally (or by simulation), is often poorly described in the literature [80]. This phenomenon has a significant impact on our mechanism and justifies the need for a guiding mechanism shown in figure 3.11. Moreover, when the bistable mechanism is triggered, the beam orthogonal to it buckles and exerts a torque. Therefore, the mechanism was also designed to ensure good coupling of the bistable mechanism to the orthogonal beam. One of the approaches recommended is that of parallel spring stage [82]. Knowing that the beam will buckle on one side or the other, the choice will be made to assemble two parallel spring stages reversed by an angle  $\pi$  with respect to each other.

#### 3.3.1 Parallel spring stage

A parallel spring stage consists of a mobile block attached to a fixed base by means of two parallel flexible beams. When a force is exerted on the mobile block, the two beams deform and the trajectory followed is not a pure translation but a parabola. The displacement therefore has a component along the X-axis and along the Y-axis, as shown in figure 3.10, such that :

$$A' = \begin{bmatrix} x \\ y \end{bmatrix} = \begin{bmatrix} x \\ \frac{-3x^2}{5\Lambda} \end{bmatrix} \quad (3.25)$$

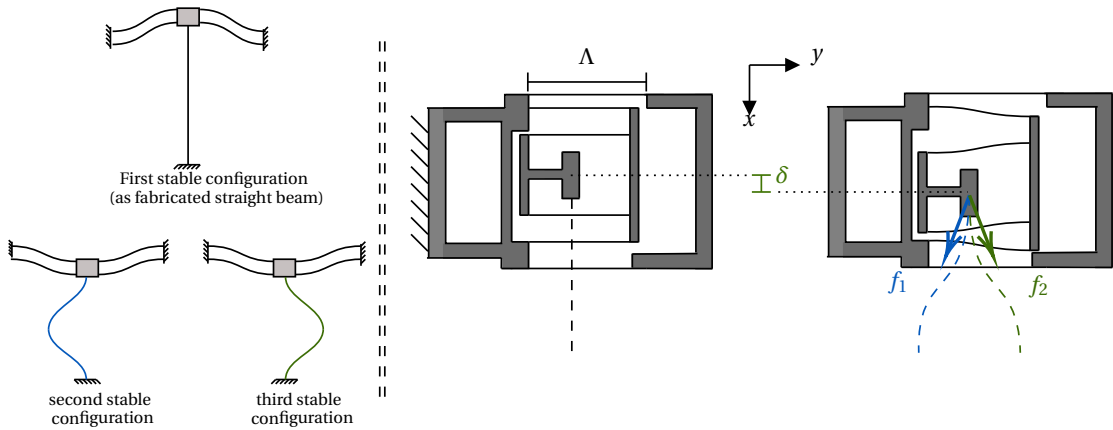


Figure 3.11 – Diagram of the tristable mechanism showing the three states assumed by the vertical beam on the left, and the effect of the deformation of the vertical beam on the parallel spring stage on the right.

Where  $\Lambda$  is the length of the beam. Taking into account that the force can be oriented in such a way as to induce a tensile or compressive force, and according to [171] the stiffness is very well approximated by

$$K_x = \frac{24EI}{\Lambda^3} + \frac{6f_y}{5\Lambda} \quad (3.26)$$

### 3.3.2 Compound parallel spring stage

One way to achieve a perfectly linear motion and to compensate for parasitic movements is to assemble two tables  $\pi$  oriented. The beams of each table are governed by the same geometric parameters. The stiffness of the two tables is therefore identical and governed by Eq. 3.26 and the displacement can then be written as

$$A' = \begin{bmatrix} x \\ y \end{bmatrix} = \begin{bmatrix} 2\frac{f_x}{k_x} \\ \frac{3x^2}{5\Lambda} + \frac{-3x^2}{5\Lambda} \end{bmatrix} = \begin{bmatrix} 2\frac{f_x}{k_x} \\ 0 \end{bmatrix}, \quad \forall x_{s1} = x_{s2}, k_{x_{s1}} = k_{x_{s2}} \quad (3.27)$$

where  $_{s1}$  and  $_{s2}$  refer to slider 1 and slider 2.

## 3.4 Actuation

In the case of the module, an active bidirectional mechanism is desired. To achieve this, two SMA wires must be mounted in opposition to each other. By heating the left wire, its martensitic deformation is cancelled (return to the austenitic state). This deformation is added by compensation to that of the right-hand wire (which is thus further transformed into oriented martensite). When the left wire cools, the restoring force is exerted by the right wire,

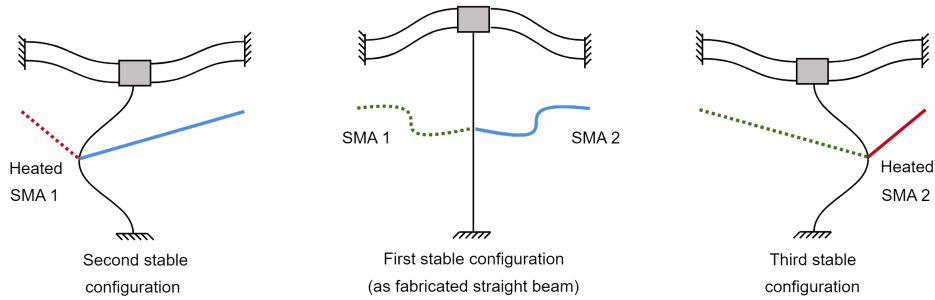


Figure 3.12 – Principle scheme for the actuation of the tristable mechanism integrating the SMA wires

which moves the midpoint in the other direction by partial transformation of the left wire. By alternately heating and cooling the two wires, the midpoint is moved alternately.

Inside the module, the alloys are attached to the structure and the middle of the straight beam. By varying the length of one of the wires by heating, the shortening will apply a force and initiate a displacement sufficient to change the state of the tristable mechanism, as shown in Fig. 3.12.

Each module is able to change its configuration following an actuation or, if not actuated, to maintain its configuration. Each configuration is the result of a precise sequence of SMA wire actuation.

### 3.4.1 Joule effect thermal activation

Due to the application, the choice was made to use current as a means of activation, i.e. thermal activation by Joule effect. According to Ohm's law, the SMA wire absorbs an electrical power.

$$P = UI = RI^2 \quad (3.28)$$

Where the resistance  $R$  depends on the cross-sectional area  $\omega$ , the length  $L$  and the resistivity  $\mu$  of the SMA wire.

$$R = \frac{\mu L}{\omega} \quad (3.29)$$

The power absorbed per unit volume can then be determined

$$P_a = \frac{RI^2}{\omega L} = \frac{\mu I^2}{\omega^2} \quad (3.30)$$

It is also necessary to calculate the power dissipated per unit area due to the convection effect.

$$P_c = k_c(T_w - T_{amb}) \quad (3.31)$$

where  $k_c$  is the convection coefficient,  $T_{amb}$  the ambient temperature and  $T_w$  the wire temperature. The temperature of the wire stabilises when the Joule effect power compensates for that dissipated by convection. This can be expressed as follows for a portion  $dx$ :

$$P_a(\pi r^2 dx) = P_c(2\pi r dx) \quad (3.32)$$

This defines a key relationship for control, namely the relationship between wire temperature and transmitted current.

$$T_w = T_{amb} + \frac{\mu I^2}{k_s 2\pi^2 r^3} \quad (3.33)$$

Without a dedicated cooling system the actuation frequency of this type of actuator is 0.1 Hz. The cooling is achieved by thermal convection or conduction. But usually, snake-like robots operating in confined environments are faced with low convection capacity and therefore the dynamic response of the actuator depends on the cooling efficiency.

In this case, the advantage of using small actuators is that it requires only minimal heat generation, thus requiring little dissipation. In addition, short current pulse actuation is limited to configuration changes.

#### 3.4.2 SMA wires actuators sizing

The SMA wires used in the design of the module are from Dynalloy Inc. (CA, United States). The selection of these wires was based on their transition temperature and the dimensioning of the mechanisms carried out beforehand. Regarding the transition temperature of the SMA wires, the choice was made to use 70°C in order to do not risk of damaging the prototype, which for this test was made of polycarbonate and whose supplier describes a conservation of mechanical properties up to 80°C. In addition, considering higher temperature limits the cooling time and gives a higher heating/actuation time ratio.

In order to introduce the actuators and their sizing, we refer here to some of the results demonstrated in the next section. To actuate the structure, it was experimentally considered necessary to provide a bending displacement of at least 1.3mm orthogonal to the beam attached to the bistable and an estimated force greater than 1.04N. The manufacturer describes a maximum shortening of approximately 5%, so the wire must be at least 26mm long to achieve the required shortening. Within a small margin of error, the wire length was set at 30mm. The diameter of the wire was then chosen according to the required force. After some testing, it was found that 150 $\mu$ m wires supporting up to 600 MPa of continuous stress could provide an average force of 1.06N. This value being higher than the required one, the latter was retained. In view of the required stroke, an SMA wire is currently sufficient to actuate the tristable structure.

The electronic circuit necessary for the actuation was made using an Arduino Mega allowing the individual control of each SMA wire and a power stage as shown in the Fig. 3.13. Each SMA

### Chapter 3. Design of the elementary multistable module

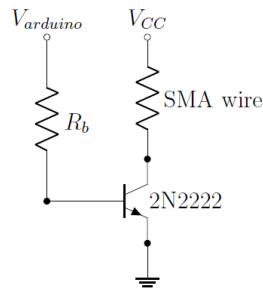


Figure 3.13 – Electrical circuit for actuating the SMAs.

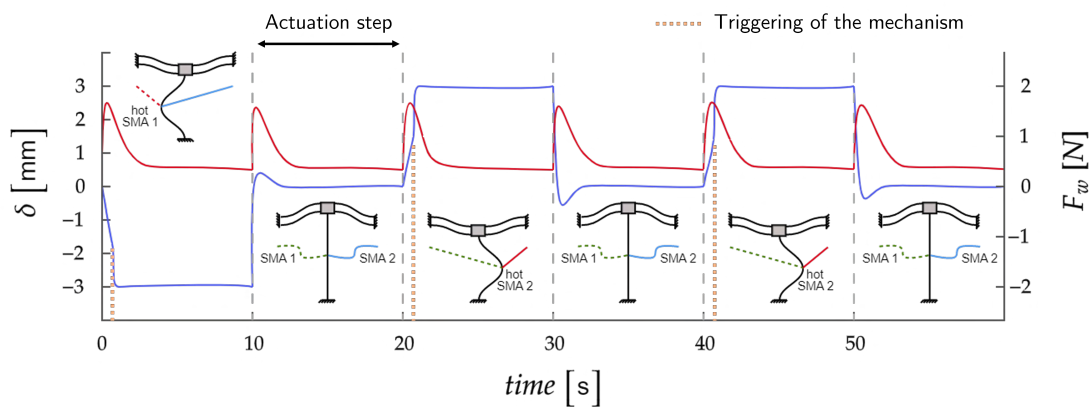


Figure 3.14 – Displacement and force exerted by the SMA wires as a function of time. Representation of the states of the corresponding module.

wire are supply by a current of 0.1mA under a voltage of 3V.

The sizing was validated experimentally. The displacement sensor was placed to measure the displacement of the connection point between the two wires (in this case, the centre of the vertical blade). The SMA wires were attached to the frame at one end by screws and to the load cell at the other.

Fig. 3.14 shows the evolution of the force in the wires and the displacement of the centre point as a function of time. In this test, the first wire was heated to start the mechanism and the second to return to the initial state. The second wire was heated to bring the mechanism into its third stable state, and then the first was heated to return to the initial configuration. This step was repeated twice to validate the ability to react consecutively in the same direction. For this test the actuations were made every 10 seconds.

This sizing method has been generalised through a Matlab script whose operating principle is presented in Fig. 3.15. This algorithm first sizes a module from the previously established models and then sizes the actuator according to the required forces. The sizing of the module is done either according to parameters set by the user or according to a performance criterion.

### 3.5. Convergence of analytical and numerical models to obtain a set of parameters, and experimental validation

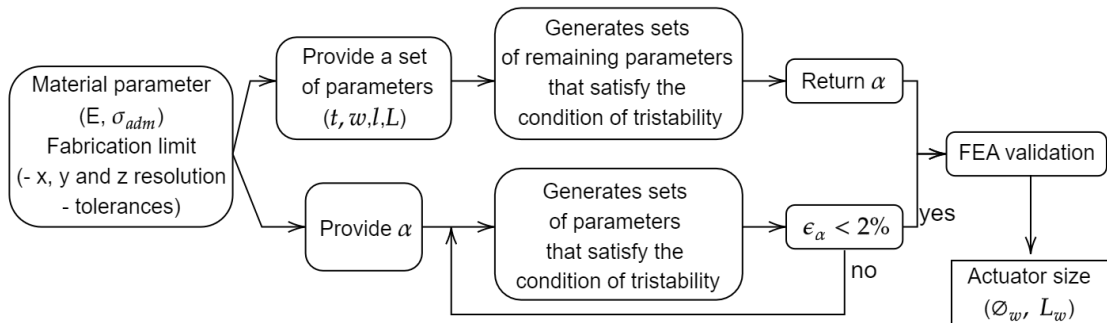


Figure 3.15 – Algorithm to assist in module design and actuator sizing.

Table 3.1 – Tristable mechanism design parameters

	Parameters	Mechanism
Bistable mechanism	$E$	1944MPa
	$t$	0.25mm
	$h$	2mm
	$l$	23mm
	$w$	1.5mm
Vertical beam	$\zeta$	0.7
	$L$	34mm
	$t$	0.4mm
	$w$	1.5mm
	$\sigma_{adm}$	55MPa

In the case of future optimisation and the need for a longer stroke, the SMA wire can be replaced by an SMA spring.

### 3.5 Convergence of analytical and numerical models to obtain a set of parameters, and experimental validation

#### 3.5.1 Finite element analysis, simulation and validation

In this section, the results obtained from the analytical models described above are compared with the results of finite element simulations performed using Creo Simulate. The simulations were performed taking into account non-linearities and load history and using the buckling module. Mesh refinement was performed locally at the anchoring point of the mechanisms.

The simulations were carried out on a bistable mechanism with two preformed blades as well as on a tristable mechanism, as shown on Fig. 3.16 whose geometrical parameters are given in Table 3.1.

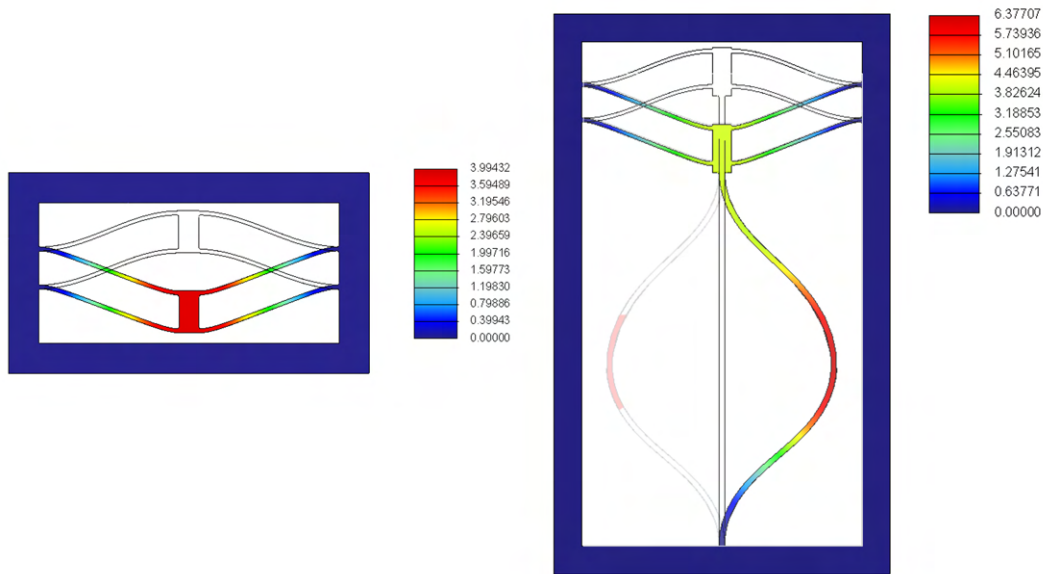


Figure 3.16 – FEA rendering of the bistable mechanism (a.) and the tristable mechanism (b.) deformations (displacement in mm)

The curves shown in Fig. 3.17 give the force-displacement curve of a bistable mechanism. The error between the model and the simulation for  $d_{top}$ ,  $f_{top}$ ,  $d_{bot}$  and  $f_{bot}$  is 26.6%, 10%, 1.8% and 0.06% respectively, which illustrates the agreement between the theory and the finite element analysis.

This agreement is important because these characteristic points represent the stroke and the force that the actuators have to provide. Thus, the accurate knowledge of the relations between the snapping points and the geometrical dimensions is very important in order to achieve the best integration of the complete bistable system.

Because of the quite large error in  $d_{top}$ , special attention was paid during the design phase. The analysis of the evolution of the maximum stresses shows however a strong agreement between what was theorised and the result of the FEA, as shown in Fig. 3.18. The calculation of internal stresses in the beam during buckling is important for design purposes to determine the design limits in the elastic domain. In a context where the manufacturing process generates high behavioural non-linearity, the accurate determination of the relationship between beam dimensions and stress state can reduce/delay the failure of one of the pre-shaped beams.

The energy analysis confirms the existence of the two stable states of the bistable mechanism, with different energy levels due to the preformed manufacturing. Once again, a concordance between the analytical model used and the finite element simulation is found. The evolution of the strain energy obtained by simulation demonstrates the existence of 3 local minima justifying the existence of the 3 stable states of the tristable mechanism.

### 3.5. Convergence of analytical and numerical models to obtain a set of parameters, and experimental validation

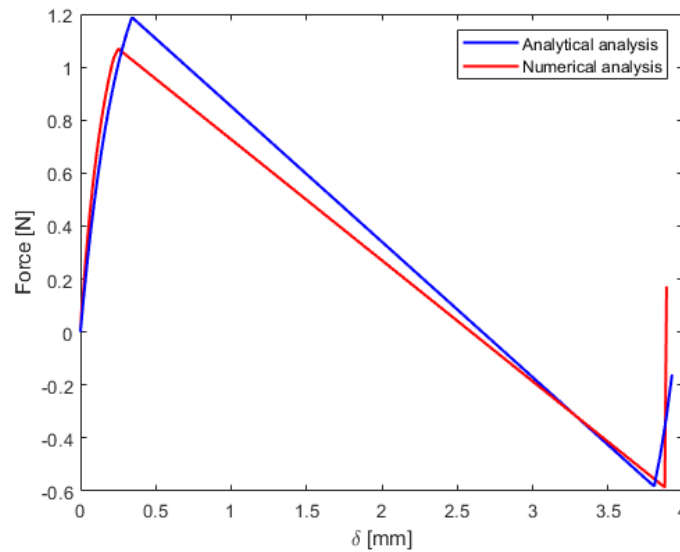


Figure 3.17 – Force-displacement curves comparison between analytic modelling and finite element analysis

#### 3.5.2 Experimental validations

##### Design and manufacture of a tristable module

The convergence obtained between the analytical and numerical models has made it possible to define a program that allows the definition of a set of parameters for the design and manufacture of a module, depending on the desired material and size.

The module is shown in Fig. 3.20. It consists of three mechanical components identified by numbers and three mechanisms identified by colours and letters. The module is manufactured in three three mechanical components, as shown in the exploded view, to enable the quality of manufacture to be assessed and their performance to be evaluated before assembly. As show in Fig. 3.20, note that A belongs to both pieces 1 and 2.

- The tristable mechanism (A) allows the module configurations to be changed or maintained.
- The flexible positioning mechanism (B) is capable of converting each stable state of A into an angle  $\alpha$  in the plane.
- The flexible coupling element (C) is used to ensure the maintenance of the boundary conditions for the proper functioning of A and B.

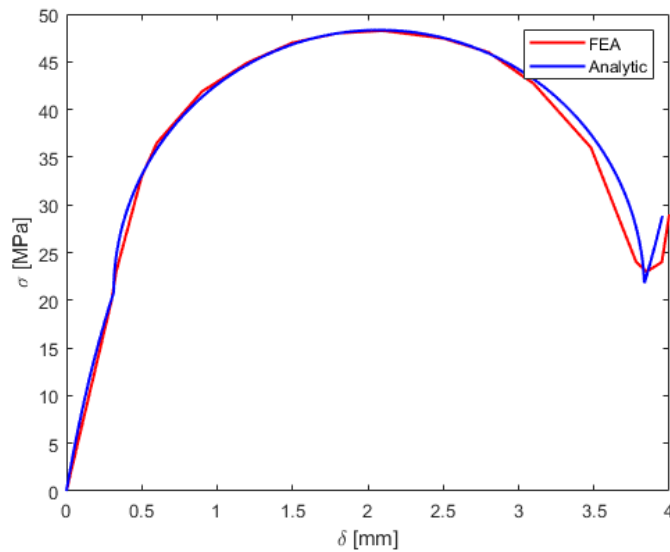


Figure 3.18 – Comparison between the maximal stress evolution during deflection between the analytic model and the FEA results

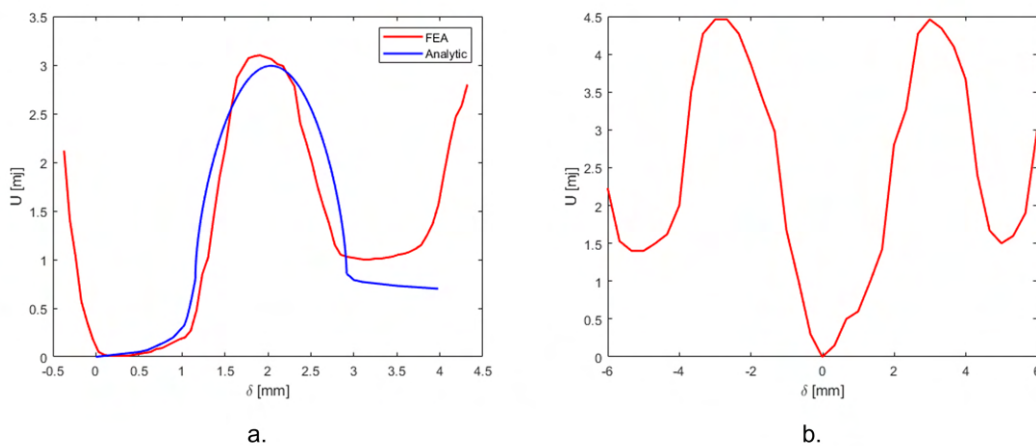


Figure 3.19 – Curves of the evolution of the deformation energy during the displacement. (a.) comparison of the analytical and numerical results of the energy study for the bistable mechanism, and (b.) result of the numerical analysis in the case of the tristable mechanism.

### 3.5.3 Tristable mechanism characterisation

In order to characterize the tristable mechanism, the following setup was used. It is composed of a force sensor (FK50, Sauter) able to measure a force up to 50 N with an accuracy of 0.02 N, and a laser-based displacement sensor (LK-H152, Keyence) capable of measuring a displacement in a range of 80 mm with a resolution of 0.25  $\mu\text{m}$ .

### 3.5. Convergence of analytical and numerical models to obtain a set of parameters, and experimental validation

---

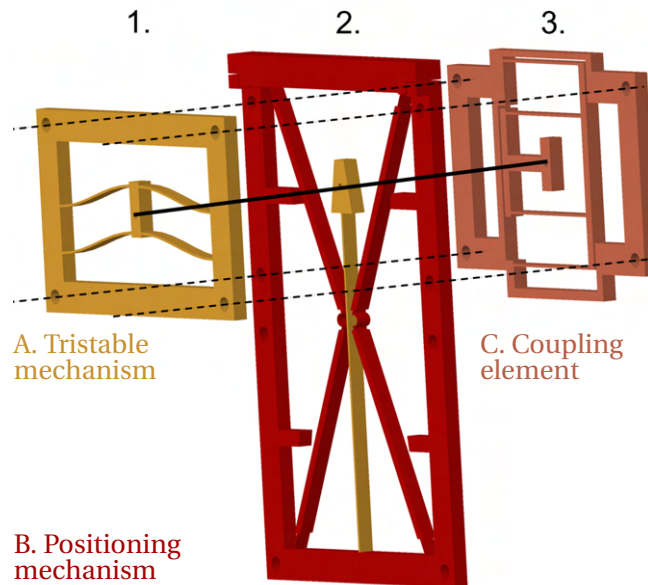


Figure 3.20 – Tristable module CAD model: Exploded view of the three mechanical components. The numbers indicate the pieces and the colours and the letters indicate the mechanisms. Actuators are shown schematically for ease of understanding (Left). 3D printed tristable module assembled (Right).

The force is applied on the shuttle of the bistable mechanism by moving the linear stage on which the force sensor is mounted and the induced displacement is measured using the displacement sensor. In order to determine the negative forces, the bistable mechanism has been reversed.

This setup is illustrated in Fig. 3.21. The results from this experiment are presented in Fig. 3.22 and are compared with the results from the analytical model and finite element analysis performed in Creo Simulate. The measured experimental results are in good accordance with what was estimated analytically and especially numerically.

The force was also applied on the vertical beam until the buckling. The average value measured was 0.28N allowing to validate the correspondence with the previously calculated critical force Eq. 3.16 which is consistent with the expected values. The minimum displacement linked to buckling was also estimated at 1.3 mm, in order to size the actuators.

#### 3.5.4 Experimental validation of a macroscopic module

A first set of large mechanisms was produced in PLA using an Ultimaker S3 printer. This first phase established the proof of concept and validity of the design. Experimental validation was carried out using the assembly illustrated below. Actuation of the mechanism was achieved using a shape memory alloy.

## Chapter 3. Design of the elementary multistable module

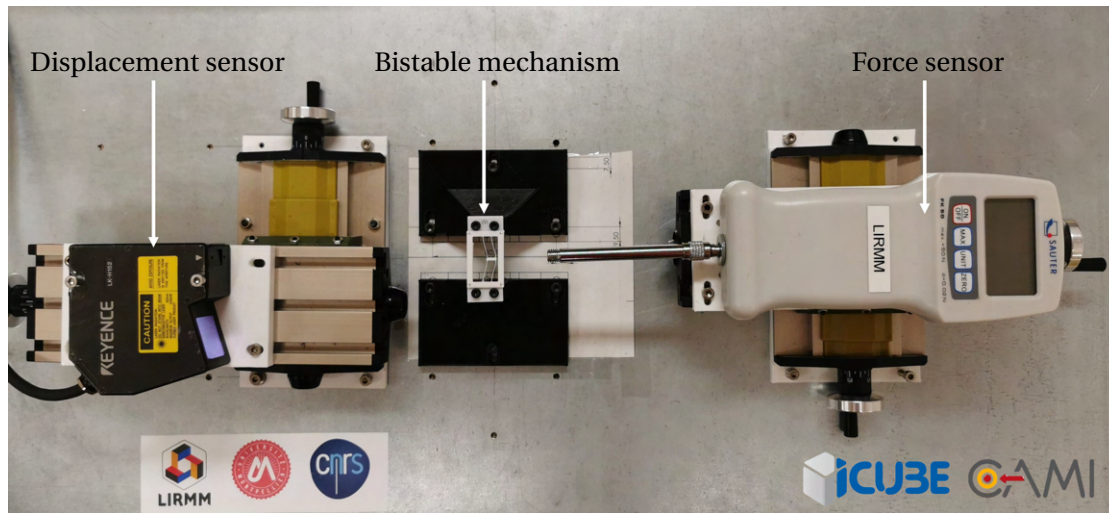


Figure 3.21 – Experimental setup to characterise the mechanism. The frame containing the tested mechanism measures  $32 \times 21$  mm.

The operation of the mechanism against a load was carried out using the setup shown in Fig. 3.23. This validation was carried out using a macroscopic mechanism attached horizontally to aluminium profiles. A load corresponding to  $n$  times the weight of the module was applied to this mechanism. In the case of this demonstrating prototype, which was carried out during preliminary work, the load was 5 times the weight of the module. The actuation was performed using shape memory alloy wires placed in opposition as presented in the previous section. A command (PWM) was sent to trigger the actuators. The choice of actuator was made by selecting the pin to be sent from the arduino.

The result of the actuation is shown in Fig. 3.24, where we can see the module in two stable and deformed states. The third stable state is the initial state shown in Fig. 5.8.

These mechanisms allowed us to raise two points already observed in previous works, namely a variation of the material behaviour in time and a problem of hyperstatism and fatigue within the bistable mechanisms. In parallel with our research into miniaturisation and the design of our robot, presented in the following chapter, a study was carried out to reduce these phenomena. The result of this work is detailed in the first part of Chapter 4.

### 3.5.5 Conclusion

In this chapter, the models used to successively dimension the different components of the module were detailed. These different models were then integrated into a Matlab algorithm allowing the generation of a module according to the desired dimensions or performances depending on a certain number of known parameters, such as the material parameters or the resolution of the used 3D printer.

The actuator sizing approach is then introduced and experimentally validated on the tristable

### 3.5. Convergence of analytical and numerical models to obtain a set of parameters, and experimental validation

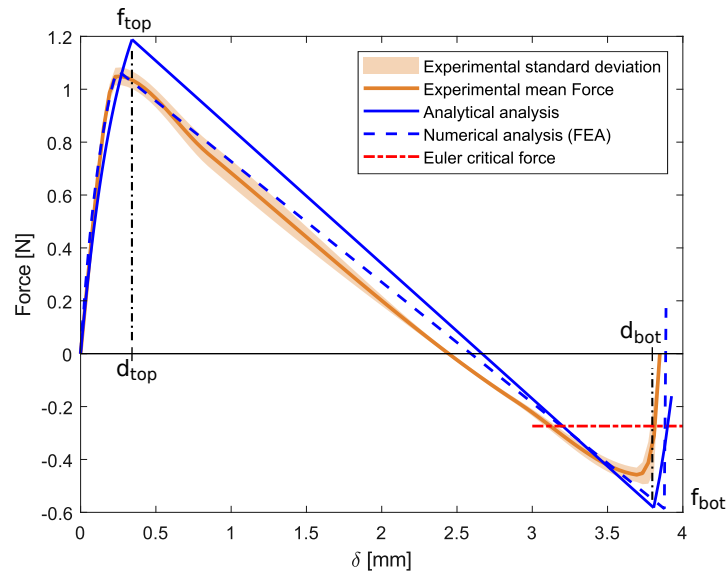


Figure 3.22 – Force-Displacement curves of the bistable mechanism: analytical model presented in continuous line, Finite Element Analysis (FEA) in dashed line and experimental results conducted on 10 mechanisms in orange.

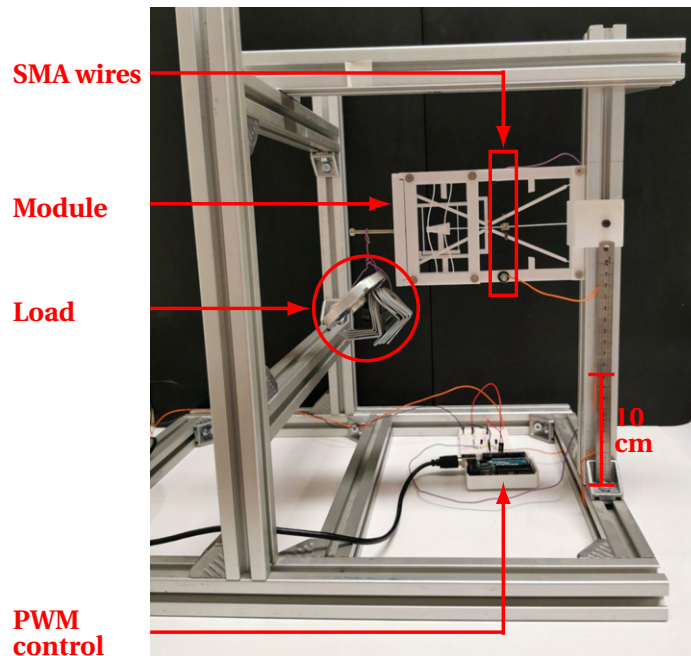


Figure 3.23 – Experimental setup used to validate the operation of the module A with a load. In this case the load is 5 times the weight of the module (63g).

### Chapter 3. Design of the elementary multistable module

---

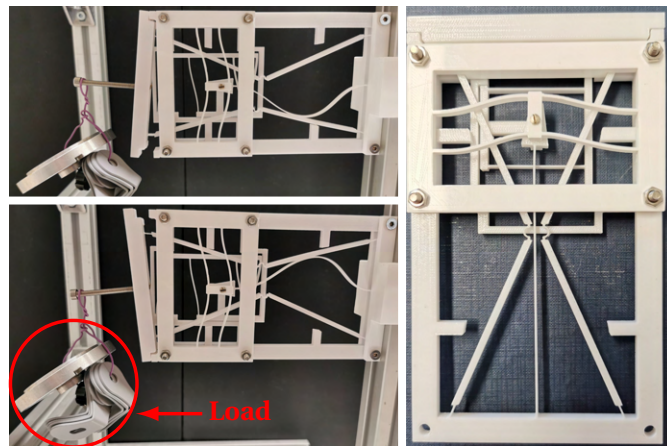


Figure 3.24 – Planar tristable mechanism: as fabricated on the right and, in the two other stable equilibrium positions on the left. The experimental setup is detailed in Fig. 5.8.

mechanism.

The possibility of using rotationally multistable mechanisms is not discussed in this chapter. The decision not to use them is based on two arguments [106]. The first relates to the stroke-to-space ratio. The second relates to their low resistance to loading [129].

Finally, experiments on an experimental module were performed. These preliminary results paved the way for the fabrication of the mesoscopic scale modules and which will constitute the robotic structure presented in the next chapter.

## 4 Distributed actuation snake-like robot

Chapter 3 was devoted to the design of a three stable state elementary module. The steps for the mechanical dimensioning of the different components of the module were given, as well as the choice and dimensioning of the actuators. The actuation and operation of the module under load were then tested. This allows the design of the robot by combining modules to be discussed and validated in this chapter.

Kinematic modelling aspects will then be addressed. In the case of the endoscopy application, the robot will be inserted into the body and controlled in open loop by the practitioner. All module stable states are then known. The position of the robot's end-effector is then derived from the direct kinematic model. By setting this direct model, the working space of the robot is also defined.

During an intervention, and despite a preoperative planning phase, it may be necessary to modify the robot configuration intra-operatively. This step results in the surgeon's wish to position the end-effector at a new set of desired coordinates. To determine the configurations that allow the robot to reach these new coordinates, the inverse kinematics model is used. The literature includes studies on open-loop controllable binary manipulators that provide performance in a hyper-redundant 2-D space. However, due to a high number of degrees-of-freedom, complex inverse kinematic models had to be developed [35, 125, 163]. Considering the constraints of the application and the particularity of our architecture, a geometrical resolution inspired by existing works has been chosen [152].

In the last part of this chapter, aspects of path planning will be discussed. So far, in the various models, the robot has been considered as embedded at its base and moving in an unconstrained space. The "advance" of the robot will then be taken into account. The robot incorporates a translational motion allowing it to be inserted. Finally, the environment in which the robot will be inserted is considered and the working space will be restricted to the patient's anatomy.

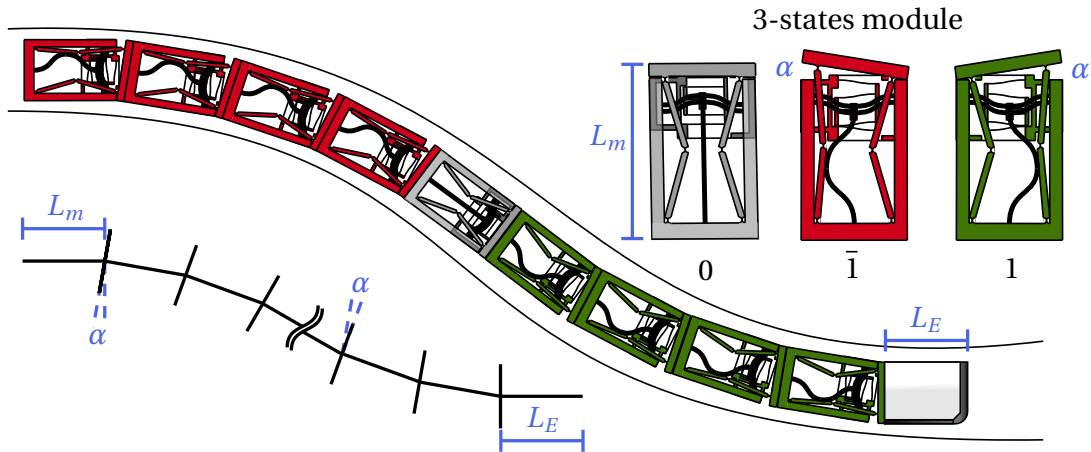


Figure 4.1 – Representation of a tristable double-beam based mechanism illustrated in its three stable equilibrium positions and their integration into the module based snake-like robot. The fabricated configuration corresponds to the first stable state.

## 4.1 Direct kinematic model and working space of the robot

The kinematic analysis of a robot consists of analysing the relationships between the joint angles  $\theta_i$  and the position and orientation of the end-effector. In the case of a planar robot, the position in  $x$  and  $y$  and the orientation are written as a vector  $[\delta_{Ex}, \delta_{Ey}, \beta_E]^T$ . If the known variables are the joint angles and the objective is to define the position of the end effector, the model used is called Direct Kinematic Model. If the aim is to calculate the joint angles from a known position of the end effector, the model used is called Inverse Kinematic Model.

In Chapter 2, the anatomical constraints of the digestive tract were established. The digestive tract can be considered as a small diameter bent tube in which the deployment is a planar problem. The chosen architecture consists of a serial assembly of elementary modules, as shown in Fig. 4.1. These elementary modules and their actuation having been validated previously.

In this section the direct kinematic model and the working space in the particular case of a proximal embedding will be derived.

### 4.1.1 Direct kinematic model

In order to obtain the direct kinematic model of the robot, it is necessary to start from the model of the elementary module defined in Section 3.2.3. The flexible structure takes the displacement of the tristable mechanism and converts it into signed angle  $\alpha$ .

An adaptation of Fig. 2.2 (Chapter 2) is shown in Fig. 4.1 taking into account the actual design of the modules and illustrating the achievement of  $\alpha$ . In the same figure, the kinematic model of the robot has also been represented using a bar chart.

## 4.1. Direct kinematic model and working space of the robot

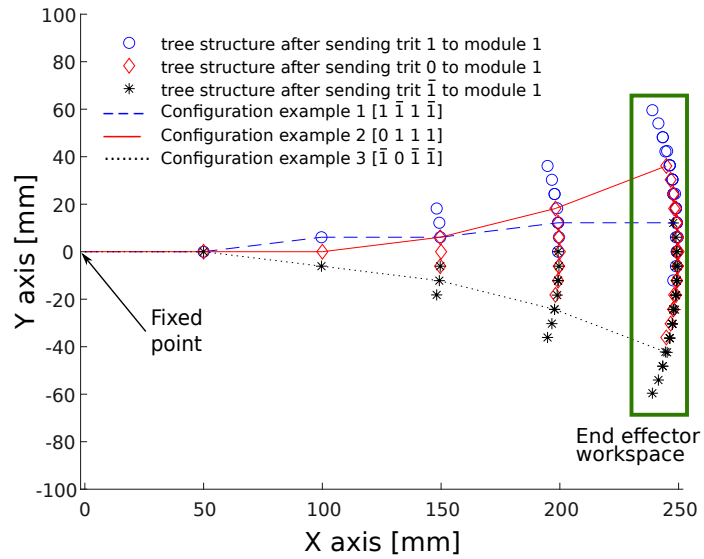


Figure 4.2 – End-effector workspace generated for a 4-module architecture with fixed proximal end and some configuration examples.

The pose of the end-effector can be expressed as a function of the state of every tristable module:

$$\begin{bmatrix} \delta_{Ex} \\ \delta_{Ey} \\ \beta_E \end{bmatrix} = \begin{bmatrix} L_m + \sum_{i=1}^n L_m \cos\left(\sum_{j=1}^i \alpha_j\right) + L_E \cos\left(\sum_{j=1}^{i+1} \alpha_j\right) \\ \sum_{i=1}^n L_m \sin\left(\sum_{j=1}^i \alpha_j\right) + L_E \sin\left(\sum_{j=1}^{i+1} \alpha_j\right) \\ \text{atan2}(\delta_{Ey}, \delta_{Ex}) \end{bmatrix} \quad (4.1)$$

where  $i$  correspond to the module number and  $i + 1$  correspond to the end effector.  $L_m$  is the length of the module and  $L_E$  is the length of the end-effector.  $\alpha_j$  can only take  $-\alpha$ ,  $0$  and  $\alpha$  as values.

### 4.1.2 Robot workspace

The robot workspace can be derived from the Fig. 4.1 for a given number of modules. Indeed, by using these equations in a loop to iterate through all possible combinations of angles, all positions that the end-effector can take can be easily calculated.

The case of a robot composed of 4 modules is illustrated in Fig. 4.2. The computed workspace is Cartesian and thus consists of 81 positions. This discrete workspace is partially redundant. Three of the possible robot configurations are represented by bars in this figure.

It is important to note that the workspace presented in Fig. 4.2 is established for a specified number of modules and for a fixed base. By adding a mobile base, performing a translation, the whole workspace can be translated by a chosen length  $L$ . If this translational guidance

is continuous then the workspace is no longer discrete. In order to maintain this characteristic, the translation must also be discrete. The use of discrete translation will be used in Section 4.3.2.

### 4.1.3 Addressing robot configurations

In order to address the points in the workspace, it is necessary to establish a notation convention for the module states as shown in figure 4.2. In order to simplify the notations, each state is described as a *Trit*. The trit is a bit equivalent belonging to the ternary numerical system, i.e. expressed in a base 3. More specifically, a balanced ternary signed-digit representation is used. This digit set is  $\mathcal{D} = (\bar{1}, 0, 1)$ .

Noting 0 as the neutral stable state of the tristable module (as fabricated), 1 as the second stable state (deformed up as shown in Fig. 4.2), and  $\bar{1}$  as the third stable state (deformed down as shown in Fig. 4.2).

The ternary word consists of the states of all the bistable modules of the robot (here 4 modules) and all these positions can be addressed using a 4-trit ternary word consisting of the state of each tristable module.

The configuration corresponding to the ternary word [0000], indicates that all modules are in neutral position and is at the central end of the workspace. Three examples of configurations are identified by their respective ternary words in Fig. 4.2.

The size of the workspace can be increased with the number of modules. As mentioned earlier, the number of discrete final positions follows a  $3^n$  law, e.g. by doubling the number of tristable modules, the number of reachable points becomes 6561 (addressable on a 8-trit ternary word).

## 4.2 Prototype assembly and experimental validation

Based on the module design in Chapter 3, a prototype consisting of 4 modules was produced as a proof of concept, visible in Fig. 4.3. The different modules were assembled with cyanoacrylate glue and SMA wires have been attached to the electrical wire by means of a crimped electrical connector.

The operating principle of the robot is shown in Fig. 4.4. The circuit diagram to control the SMA wires is on the right side of this figure. This reminds that all SMA wires are connected to a power supply wire. This wire runs through the centre of the structure. The actuation of an SMA wire is done through the transistor by grounding the corresponding wire on the sides of the structure, the dashed lines in Fig. 4.4. On the left side of this figure, the heating of an SMA wire is illustrated, causing its shortening and the module configuration to change.

As shown in Fig. 4.3, a component of mass  $M$ , equivalent to the weight of 4 additional modules was added to the prototype. The purpose of this prototype was to validate the operating principle, and the extra load was used to demonstrate the ability to carry more modules.

## 4.2. Prototype assembly and experimental validation

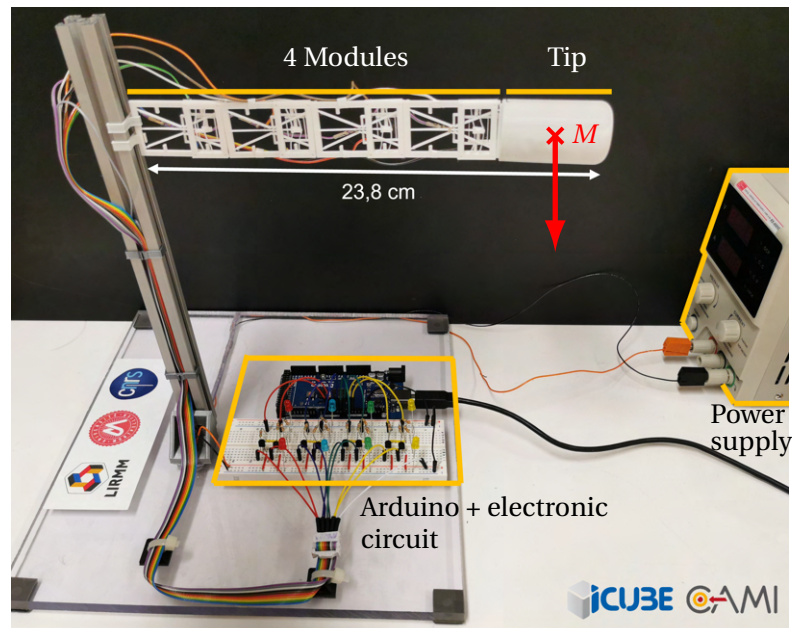


Figure 4.3 – Prototype with 4 modules in reference position without power supply.

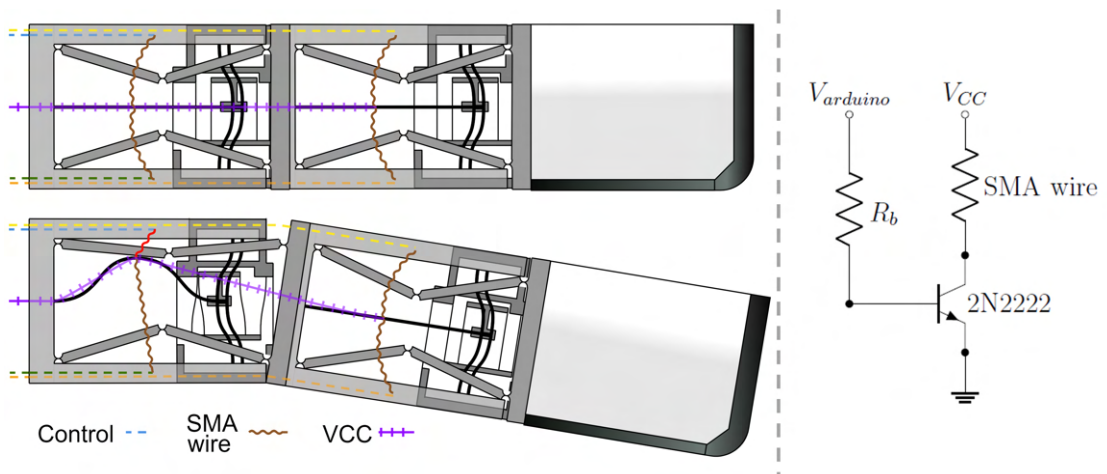


Figure 4.4 – Schematic representing routing and operating principle.

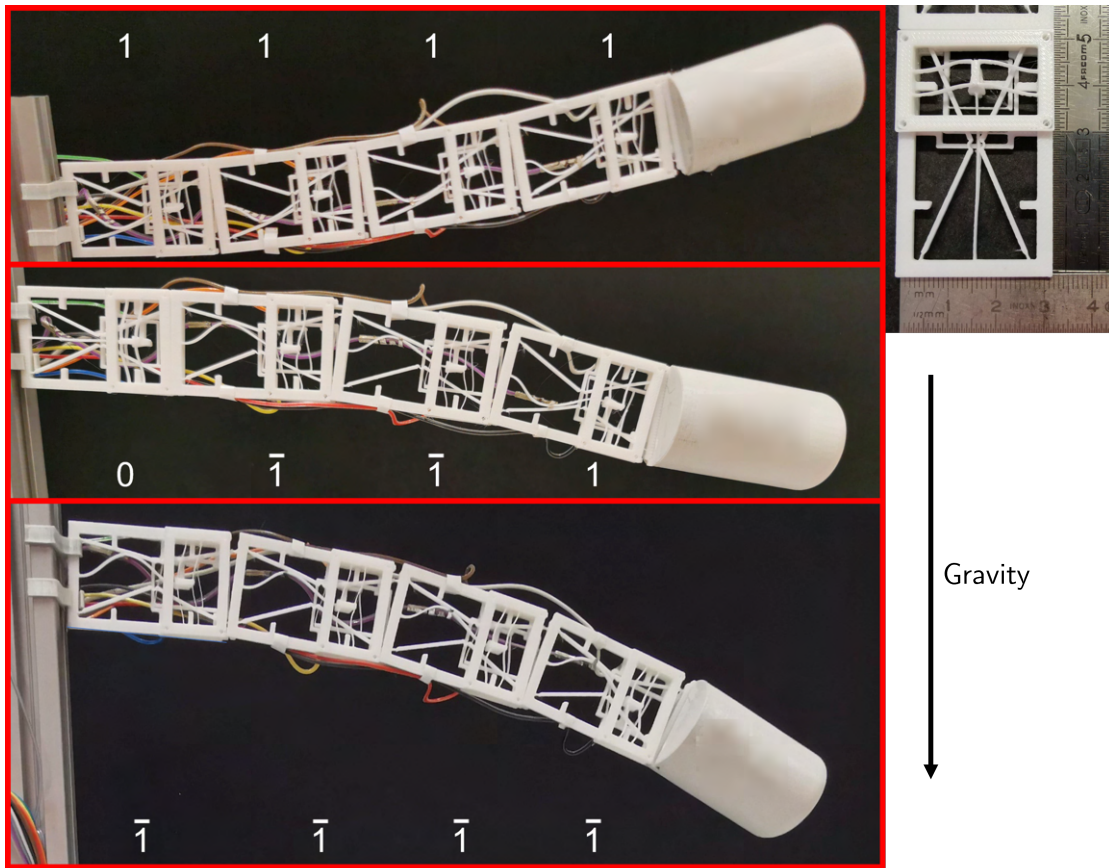


Figure 4.5 – Photos of three configurations taken by the robot with the associated ternary words.

#### 4.2.1 Experimental validation

Each module being independent, the robot takes a shape defined by a given 4-trit ternary word. Three of these sequences are shown on Fig. 4.5.

In order to validate the operation of the robot, a measurement of the position of the tip was carried out for each configuration and was compared to the estimated workspace calculated in Matlab as mentioned previously.

For each module, before assembly, a measurement of the output angles was made and an average angle of  $7.1^\circ$  was observed. Afterwards, the measurements were carried out and the results are presented in Fig. 4.6.

Three major remarks emerged from this first phase of experimentation.

The first observation is that the error between the measured position and the estimated position is smaller when the robot is controlled against gravity. A phenomenon already observed in the literature with other structures [41]. This result suggests that the torques exerted may result in a greater displacement than was anticipated in the design. It can also be

## 4.2. Prototype assembly and experimental validation

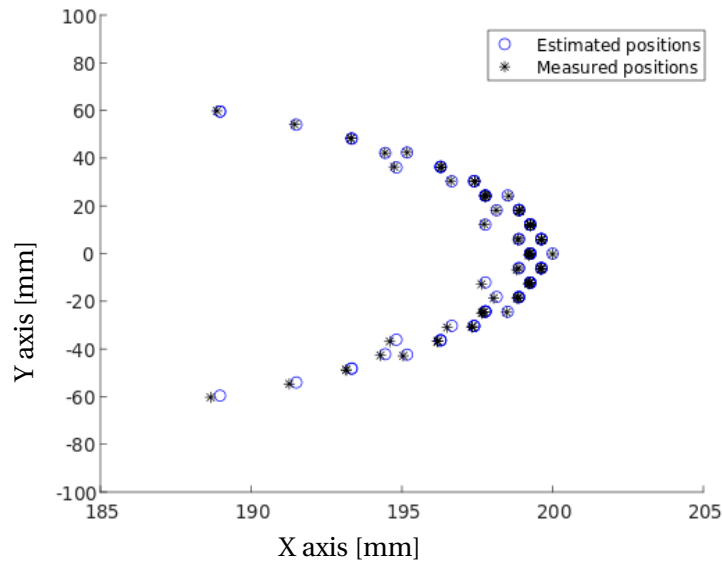


Figure 4.6 – Representation of the robot’s workspace envelope, with the estimated positions in blue ring and the measured positions in black star. A zoom is made along the X-axis with respect to Fig. 4.1 for the sake of readability.

explained by the nature of the material used and the fact that there is still an assembly phase. The assembly phase can bring its own set of inaccuracies influencing the performance of the prototype.

The second remark concerns the redundancy of the workspace. For  $n$  modules, the robot has  $3^n$  output positions, many of which are redundant and useful for path planning. As describe earlier, each addition of a module significantly increases the number of discrete positions in the workspace. The 4-modules robot has 81 positions, but with the addition of 4 modules, the workspace will reach 6561 reachable positions. During the measurements, due to some mechanical backlash of the modules, some configurations that should have given the same output position may have ended up with different values. A repeatability study will be carried out in future work in order to exploit them to enrich the robot’s workspace.

The workspace shown corresponds to that derived in Section 4.1.2 for a robot whose base is embedded and moves in an unconstrained space. However, the robot will be fixed to a linear actuator to realise an insertion as shown in Fig. 4.7. Since the actuations will be performed during a translation, this workspace will have an offset equivalent to the amplitude of the translation.

The third point concerns the vibration of the structure during the actuations. This phenomenon is more important for an actuation performed near the base than at the distal end of the robot and is due to the change of state of the mechanism within the structure. This can be controlled by heating the opposite wire in advance to use it as a damper. In the case of endoscopy, the architecture can be laid over soft tissue to dampen vibrations during actuation.

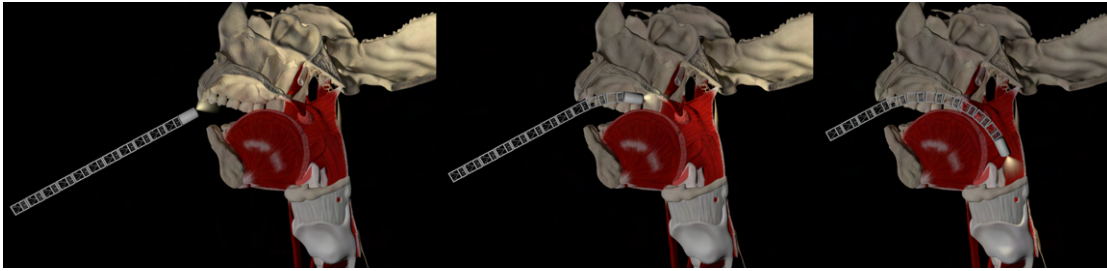


Figure 4.7 – Realistic rendering of the insertion of the robot into the body at three given moments. The modules used in this illustration have smaller dimensions than those of the prototype. In this case, the dimensions are those of the miniaturised modules presented in the outlook.

### 4.3 Inverse kinematic model and Path planning

Where traditional binary manipulator use complex algorithms based on the hyper-redundancy of their workspace and use the density of the workspace [37, 54, 125], a geometric approach was used to solve the inverse kinematic model [152]. This approach, although having limitations if the number of modules increases significantly, allows the inverse model to be solved in a relatively simple and efficient way.

#### 4.3.1 Geometrical Method for Computing the Inverse Kinematics

##### Search for the closest position to a desired position

The first step in solving the inverse kinematic model is to find the closest position(s) that can be reached. This step reduces the computation time to the determination of only those configurations that can reach the defined positions.

For this purpose, it is assumed that the number of modules is known. Given the application and the availability of preoperative images to define the length of the robot, this assumption is considered acceptable.

Based on the given number of modules, the workspace is derived in the same way as previously. A search is then made within the workspace for the positions closest to a desired position. For this purpose, a tolerance is set according to the user's needs in order to reduce or increase the number of acceptable positions of the end-effector.

Then find the position in the workspace that is closest to a desired position, the following approach was used:

1. Set the desired position and the tolerance for the difference between the desired and actual positions.
2. Set the initial values of the angles.

### 4.3. Inverse kinematic model and Path planning

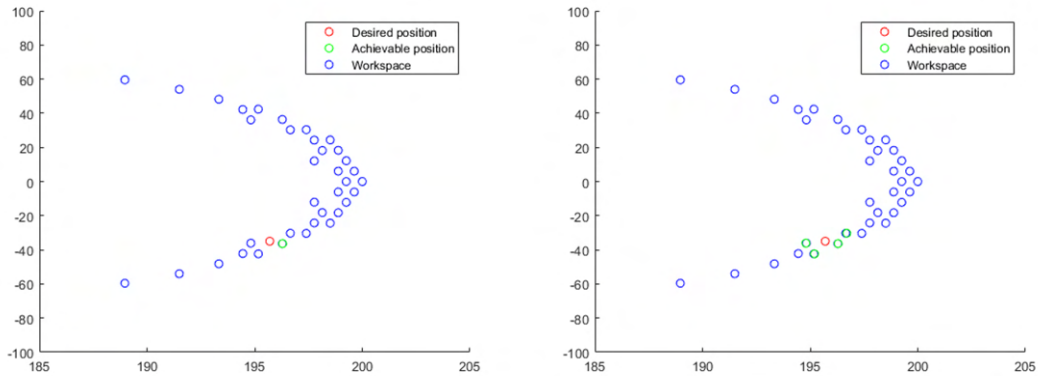


Figure 4.8 – Illustration of the search for the closest positions to a desired position for a 4-module robot. The desired position is in red and the closest positions that the robot can reach are in green. The tolerance has been increased in the case of the figure on the right. The position along the X and Y axes is given in mm.

3. Calculate the initial position of the end-effector.
4. Calculate the difference between the desired and actual positions.
5. Loop until the difference is within the tolerance:
  - (a) Set the step size for adjusting the angles.
  - (b) Set the initial value of the cost function.
  - (c) Loop through all possible values of the angles:
    - i. Calculate the position of the end-effector.
    - ii. Calculate the difference between the desired and actual positions.
    - iii. Calculate the cost function using the difference and the step size.
    - iv. If the cost function is less than the minimum cost, update the minimum cost and the corresponding angles.
  - (d) Update the angles with the angles corresponding to the minimum cost.
  - (e) Calculate the position of the end-effector with the updated angles.
  - (f) Calculate the difference between the desired and actual positions.
6. Return the position(s) of the end-effector.

An example is shown in Fig. 4.8. In the cases presented on the left of the figure, the set of tolerances is such that only one position of the prototype workspace with 4 modules is acceptable.

The necessary assumption for the existence of a solution is that for  $P_{M_1}$  the first module position, the distance between the position of the module base and the desired position  $P_d$

must be equal or less than the sum of the lengths of the remaining modules.

$$d(P_{M_1}, P_d) \leq L_E + \sum L_m \quad (4.2)$$

**Geometric resolution of the inverse kinematic model**

The working space defined above does not take into account translation. The latter will therefore not be taken into account at first for the resolution of the inverse kinematic model.

Knowing the coordinates of a close achievable position  $P_a$  and the position of module 1  $P_{M_1}$ , it is then possible to use the geometrical approach described [152].

The principle is based on finding the position of the median module of the structure, and then finding the position of the median modules of each sub-assembly formed. This step is repeated in order to calculate the positions of each intermediate module. In the case of an 8-module robot, as shown in Fig. 4.9, it is first determined the position of  $P_{M_4}$ , then  $P_{M_2}$  and  $P_{M_6}$ , and so on.

The median module is positioned along the height of the isosceles triangle thus described. Since modules can only take on 3 states, there is a finite number of values that  $h$  can take to position the module.

By varying the coordinates of  $P_{M_4}$ , the angle of the base changes and the subset of four modules change their configurations, as illustrated in Fig. 4.9. The angle of the base  $\phi$  is calculated according to the postulate of an isosceles triangle with  $d$  and  $c$  the respective lengths of the base and a side such that

$$\phi = \cos^{-1} \left( \frac{d}{2c} \right) \quad (4.3)$$

We then obtain by triangulation the coordinates of the intermediate point

$$P_{M_i} = P_{M_1} + \left( c \begin{bmatrix} \cos \phi \\ \sin \phi \end{bmatrix} \right) \quad (4.4)$$

$$\theta_i = \text{atan2}(P_{M_i} \otimes P'_{M_i}, P_{M_i} \odot P'_{M_i}) \quad (4.5)$$

The algorithm used is written is given in Alg. 1 and the result obtained for different desired positions is illustrated in Fig. 4.10.

The solution method described so far does not take into account any constraints on the acceptable workspace. Among the configurations found, a number of them may be impossible to obtain in the context of our application. In addition, the translational guidance of the structure has not yet been taken into account. These two elements will be taken into account in the next section where the path planning will be discussed.

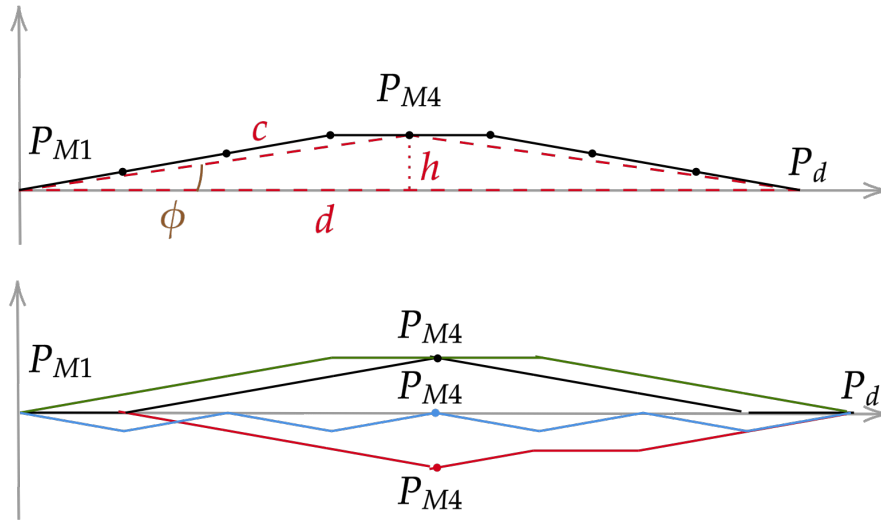


Figure 4.9 – Inverse kinematics model parameters identification: (top) locating the mid-point for the inverse kinematic computation and (bottom) alternative poses of a 8-modules robot for different values of the base angle  $\phi$ .

---

**Algorithm 1** Inverse Kinematics
 

---

```

1: procedure INVERSEKINEMATICS(base, end_effector, link_length, num_joint, workspace)
2:   distance  $\leftarrow$  norm(end_effector - base)
3:   if distance > 2 * link_length then
4:     throw ValueError("The end-effector cannot be reached with the given link lengths.")
5:   end if
6:   Initialize
7:    $P_{Mi} = \text{end\_effector}$ 
8:   for  $i \leftarrow 1$  to num_joints do
9:      $d \leftarrow$  norm( $P_{Mi}$  - base)
10:    Minimize  $h$ 
11:     $c \leftarrow \sqrt{h^2 + b/2^2}$ 
12:     $\phi \leftarrow \arccos(d/(2 * c))$ 
13:     $P_{Mi} \leftarrow \text{base} + [c * \cos(\phi), c * \sin(\phi)]$ 
14:  end for
15:  for  $i \leftarrow 1$  to num_joints do
16:     $P_{kMi} \leftarrow \min(P_{Mi}, \text{workspace})$ 
17:    angles.append( $P_{Mi} * P_{kMi}, P_{Mi}@P_{kMi}$ )
18:  end for
19:  return angles
20: end procedure
    
```

---

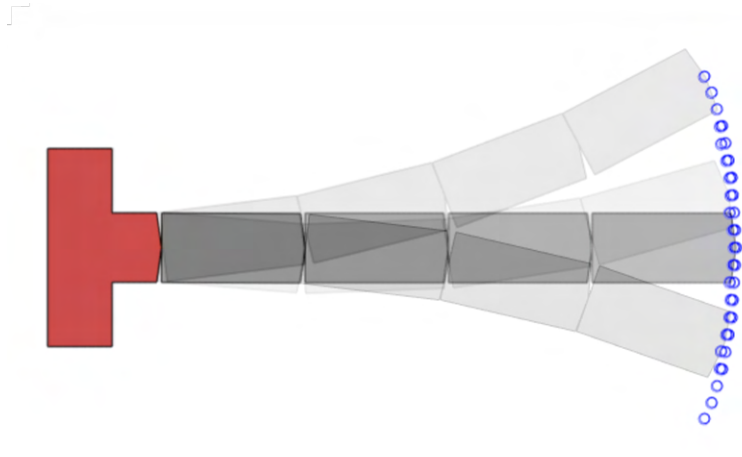


Figure 4.10 – End-effector workspace generated for a 4-module architecture with fixed proximal end and some configuration examples.

### 4.3.2 Path planning

Trajectory planning is the process of generating a smooth, collision-free path for a robot to follow in order to reach a desired goal. There are several approaches to trajectory planning, and the choice of approach depends on the specific requirements of the task at hand.

In the case of endoscopy, the robot will pass through the mouth to reach the stomach. It will therefore first have to pass the curvature of the throat before being deployed in a narrow environment where its acceptable working space will be significantly restricted.

The most simple approach to path planning is based on the direct kinematic model. This approach is based on the total or partial withdrawal of the robot in order to re-insert it in order to reach the new desired position. As for the first insertion, the position of the end device is recalculated per interval based on the knowledge of the actuation sequence. It is then verified that the user is approaching the desired position.

One advantage of this approach is that it is relatively simple and easy to implement. However, it faces the problem of managing friction with the environment in the case of multiple reinsertions.

To address this issue, an alternative approach is to use the inverse kinematic model, which calculates the joint angles required to achieve a desired end-effector position and orientation. This approach is more complex, but it allows to know all the robot's configurations before having to insert it. This approach would for example have a potential application in the context of preoperative path planning if one wished to deploy the robot in a semi-automatic way to a desired position.

---

### 4.3. Inverse kinematic model and Path planning

By entering a larger tolerance and increasing the number of degrees of freedom, more configurations can and will be found. Although this result can first be interpreted as an operational advantage related to the hyper-redundancy of the workspace, this approach does not lead to a clear optimal solution. It is necessary to weight each of these solutions

#### **Dynamic programming and Hidden Markov Model to find an optimal configuration**

In the field of robotics, dynamic programming and Markov Decision Process (MDP) are often used to solve problems involving decision-making and control [23, 222].

Dynamic programming is a method for solving optimization problems by breaking them down into smaller subproblems and storing the solutions to these subproblems in a table or array [10]. This allows us to avoid recalculating the solution of the same subproblem multiple times, which can be very efficient in cases where the subproblems overlap or have a recursive structure.

Dynamic programming can be used to solve a wide range of optimization problems in robotics, such as path planning. For example, a robot might use dynamic programming to find the optimal path through a maze, taking into account various constraints such as the robot's physical capabilities and the presence of obstacles in the environment[222]. In fact, the method of dynamic programming was originally developed by R. Bellman in the 1950s to solve MDPs [10].

MDPs are a useful tool for modeling decision-making problems in which an agent takes actions in a sequence of states and transitions to a new state based on certain probabilities. MDPs are often used to model robotic systems that operate in uncertain or changing environments, where the agent must make decisions based on incomplete or noisy information [23].

Among MDP, the Hidden Markov Model (HMM) is a type of statistical model that can be used to represent systems that exhibit temporal dependencies and where some of the underlying state variables are hidden or unobserved [16].

One possible use of an HMM in this context would be the estimation of the most likely sequence of module states that the robot take over time, given some observed data such as the robot's end-effector positions or the joint angles at certain time steps [107, 128].

To use an HMM for this purpose, the hidden state variables that represent the joint positions of the robot at each time step must be define, as well as the observed variables that represent the data that are available for estimating the joint positions. Then the probabilities that govern the transitions between the hidden states and the observations need to be specified, and use algorithms such as the Viterbi algorithm to estimate the most likely sequence of hidden states [138].

### Dynamic programming and Hidden Markov Model to find an optimal configuration

The Viterbi algorithm is a dynamic programming algorithm that can be used to find the most likely sequence of hidden states given a sequence of observations, by constructing a trellis diagram and using dynamic programming to find the path through the trellis that has the highest probability.

It is a classic example of dynamic programming, as it involves breaking down a larger optimization problem into smaller subproblems and storing the solutions to these subproblems in a table.

To estimate the sequence of module states that the designed robot took to move from a given configuration to an estimated position, the hidden state variables that represent the module angle at each time step have to be defined, as well as the observed variables that represent the data that are available for estimating the module positions. The probabilities governing transitions between hidden states and observations must be defined and specified.

One way to write the algorithm using an HMM to achieve the above mentioned objectives lies in the clear definition of the parameters:

- **The hidden state variables:** These correspond to the states of the robot modules at each time step. It is a matter of defining a hidden state variable for each state of the module, and specifying the possible values that each variable can take according to the constraints described in Chapter III (translation for insertion or retraction, this translation is also defined as discrete in steps of length  $L_m$  and the fact that the modules angle can only take 3 values).
- **The observed variables:** These correspond to the data available for estimating the positions of the robot modules. Among the variables observed for each time step, it can be the transmitted actuation sequence.
- **The transition probabilities:** These are the transition probabilities between the different hidden states over time. These probabilities are defined according to the actuation constraints described in Chapter III (for example, the actuators cannot be actuated for a certain time after an actuation in order to simulate cooling, this time is fixed at 10 seconds, and the cost of an actuation is higher the further the joint is from the end-effector). It also includes a penalty for the number of actuations to encourage the robot to use as few actuations as possible.

The algorithm is derived as follows and the result is illustrated in Fig. 4.11

In Fig. 4.11, the states taken by the robot are represented as a function of time. More concretely, this deployment is characterised by an advance of the structure to reach a desired position as shown in Fig. 4.12.



## Chapter 4. Distributed actuation snake-like robot

---

### Algorithm 2 Viterbi Algorithm for path planning

---

```
1: function VITERBI(observations, states, start_prob, trans_prob, emit_prob)
2:   viterbi_table  $\leftarrow$  [start_prob[i] * emit_prob[i][observations[0]]  $\forall i \in$  states]
3:   path_table  $\leftarrow$  [[i]  $\forall i \in$  states]
4:   for t  $\leftarrow$  1 to len(observations) do
5:     new_viterbi_table  $\leftarrow$  []
6:     new_path_table  $\leftarrow$  []
7:     for i  $\in$  states do
8:       max_prob, max_state  $\leftarrow$  max([(viterbi_table[j] * trans_prob[j][i] *
9:         emit_prob[i][observations[t]], j)  $\forall j \in$  states])
10:      new_viterbi_table.append(max_prob)
11:      new_path_table.append(path_table[max_state] + [i])
12:    end for
13:    viterbi_table  $\leftarrow$  new_viterbi_table
14:    path_table  $\leftarrow$  new_path_table
15:  end for
16:  max_prob, max_path  $\leftarrow$  max([(viterbi_table[i], path_table[i])  $\forall i \in$  states])
17:  return (max_prob, max_path)
18: end function
```

---

### Consideration of anatomical constraints

Once translation has been added to our structure, the last step is to add motion constraints so that the robot can be deployed without colliding with the tissue, this is called constraint-based motion planning.

This step was performed with python using the trimesh and OpenRAVEpy libraries. The first step consists in importing the 3D ".stl" file of the concerned organs in order to extract a 2D profile according to a given plane. The plane is defined in the form of a normal vector and a point belonging to it.

The algorithm presented below allows to recover a trimesh object containing the contour lines of the 2D profile.

### Algorithm 3 Extract 2D Profile from 3D STL

---

```
1: procedure EXTRACTPROFILE(STLFile, Plane, Point)
2:   mesh  $\leftarrow$  trimesh.load_mesh(STLFile)
3:   profile  $\leftarrow$  mesh.section(normal = Plane, plane_origin = Point)
4:   return profile
5: end procedure
```

---

To define the space between the two curves obtained previously as the workspace of the robot OpenRAVEpy was used. Once the curves are imported, they are defined as an "Environment" and the robot model is then added. Using the "SetAffineTranslationLimits" method, the limits of the robot's motion can then be contained in the space between the two curves.

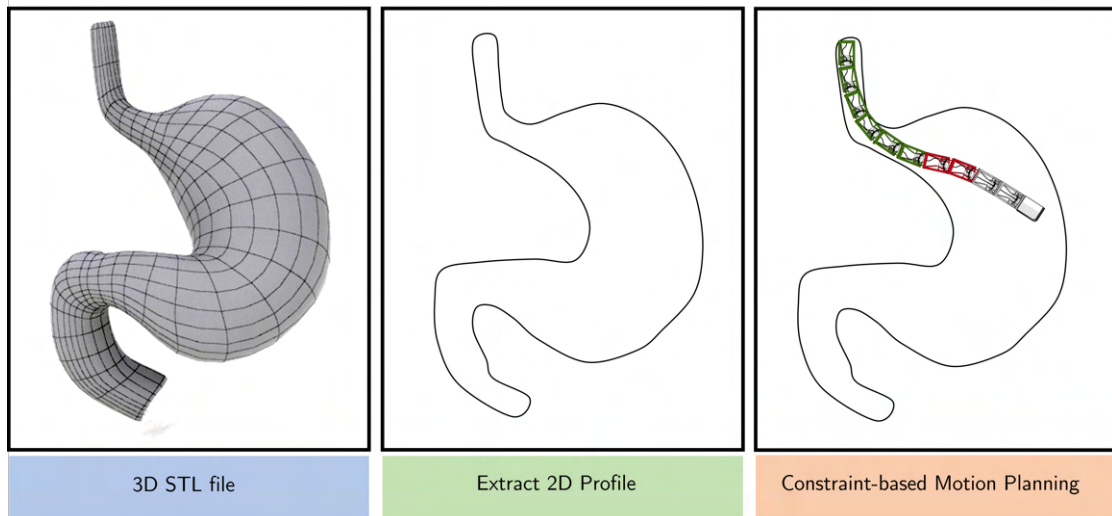


Figure 4.13 – Illustration of the steps involved in anatomically constrained modelling.

Finally, the path planning can then be carried out using the Viterbi algorithm defined earlier as described in Alg. 4 and illustrated in Fig. 4.13, taking into account the constraints of the workspace.

---

#### Algorithm 4 Constraint-based Motion Planning

---

- 1: **procedure** MOTIONPLAN
  - 2:   Create an OpenRAVE environment
  - 3:   Load the robot model into the environment
  - 4:   Define constraints on the robot's joints and environment
  - 5:   Define a start and goal configuration
  - 6:   Initialize the Viterbi algorithm with the robot and constraints
  - 7:   Plan a path from the start to the goal configuration
  - 8: **end procedure**
- 

## 4.4 Conclusion

In this chapter the direct and inverse kinematic models of the robot were successively detailed. Although initially relatively simple, the modelling has become progressively more complex due to the integration of translation and thermal actuation. With the exception of the direct model, the other algorithms could only be tested in simulation.



## 5 Enhancement of the mechanisms and contribution of 3D printing of composites

In the previous chapters, the validity of the proposed approach for the design of an endoscope based on a tristable module was demonstrated. However, during the prototyping and validation phases, two issues were highlighted, namely early failure of the bistable modules despite the sizing and the SMA wire assembly phase.

A study was therefore carried out during this thesis in order to address these two issues. The choice to focus on these challenges is justified by a potential application beyond the scope of this work. Indeed, it has been shown that bistable mechanisms have multiple application fields [232, 225, 11], which makes increasing their lifetime a relevant challenge. With regard to the problem of actuator assembly, the contribution comes from the approach used to address it. In this case, the research was done in such a way as to print the actuators to avoid their assembly.

Firstly, the question of the life span of the bistable mechanism, i.e. the number of cycles of a mechanism, will be addressed. As a reminder, failures were highlighted during the experimental phases. The research approach chosen and detailed in this section to solve this problem was to reduce the internal constraints by decreasing the degree of hyperstatism.

In the context of the work carried out in this thesis, the fatigue of the mechanisms is crucial. Indeed, for the robot, it was assumed that the control could be carried out in open loop due to the mechanical robustness of the architecture. However, this alteration in the behaviour of the mechanism leads to a reduction in the controllability of the modules.

Secondly, the issue of replacement of the actuators will be addressed. The SMAs performed perfectly well in terms of operation, but their assembly in the module remains tedious, especially because of their small size and the fact that they cannot be soldered. Technological advances in additive manufacturing have made it possible to exploit composite materials, such as carbon-doped filaments, synthesised for specific function with tailored properties. The integration of carbon fibres, with good electrical and thermal conductivity, within an insulating polylactic acid (PLA) matrix produces a conductive functional material. These properties make it possible to manufacture modules with electrothermal actuators directly

included, and even use them in more complex monolithic structures.

This chapter will therefore be divided into two sections. The first section deals with the mechanical optimisation of a compliant bistable mechanism with pre-shaped beam, by designing an improved version and incorporating it into the module of the robot. In the second section, the design of a printable thermal actuator and its incorporation into a complex structure is addressed. Finally, its incorporation into the module will also be discussed.

### 5.1 Enhanced bistable mechanism for improved lifetime and manufacturability by hyperstatism analysis

The bistability is conditioned during the design by the fulfilment of geometric conditions to guarantee its existence [165, 100]. One of these conditions is the Degree-Of-Hyperstatism (DOH), which causes stress and fatigue phenomena within the structure.

In the literature, the fatigue problems present in flexible mechanisms due to localised repetitive stresses in the elastic slender part has been studied in depth for a long time [91]. Various researches have thus considered the improvement of fatigue life and the evaluation of reliability [108]. Despite bistable mechanisms are also subjected to fatigue and hyperstatism, their analyses were initially neglected and the in-depth study of the failure mechanism is still recent. This study deals notably with the reliability and lifetime of bistable mechanisms by means of estimators such as the product-limit [215], i.e. the Kaplan-Meier estimator. However, although the symptom is studied, e.g. the stiffness degradation or the cumulative damage induced by actuation, the cause is not really considered. Moreover, the axes of research exploited since then has focused on solving part of the problem, i.e., increasing reliability by using topological optimisation to generate better flexible joints. The mechanism as a whole has been little studied [168]. In spite of the results of some experimental studies showing the existence of uncertainties in the structural behaviour due to the stochastic variation of material and geometric properties [137].

One of the most common methods used to address the problem of hyperstatism is the addition of a thicker intermediate section, i.e. crab-like bistable mechanism [205]. This approach allows to improve the stability, increase the triggering forces and overcomes certain approximations made during the modelling. However, this leads to stress concentrations at the thinning points. Although this only postpones the problem, it may be sufficient for some applications, but when the notion of fatigue and the number of cycles comes into play, the problem reappears. The challenge is to find the right compromise between structural modifications that minimise stresses while maintaining the same kinematic behaviour.

The Degree-Of-Freedom (DOF) of a flexible mechanism is usually defined in the design phase. The mechanism should have low stiffness along the desired DOF and high stiffness in all other directions. In the literature many approaches are described to achieve this design goal. Besides building block approaches or structural optimisation approaches, the rigid

## 5.1. Enhanced bistable mechanism for improved lifetime and manufacturability by hyperstatism analysis

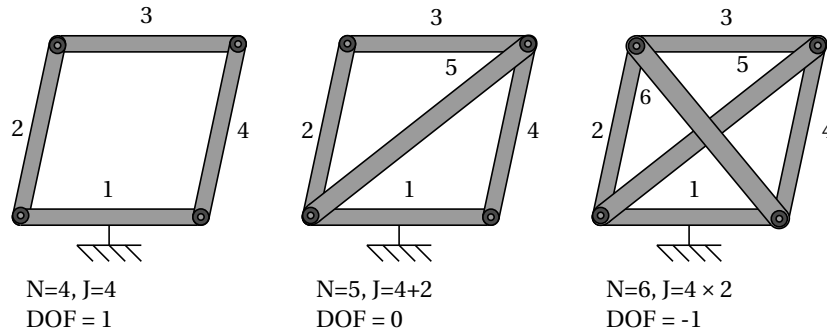


Figure 5.1 – DOF calculated for the planar mechanism according to the Kutzbach-Grübler criterion.

body replacement approach is the most widely used [93]. Because of the large number of rigid body mechanisms, pseudo-rigid body modelling and the already available optimisation tools make it an interesting approach. However, in this case the compliant structure already exists and the objective is here to efficiently replace it with an alternative structure in order to improve its performances. The use of a kinematic-based design approach, the method of Freedom And Constraint Topologies (FACT) [88], allows the constraints of the structure to be modelled through the screw theory. With this approach, it is then possible to reduce the number of redundant constraint screws and to propose an enhanced structure while fulfilling compactness requirements. When modelling flexible mechanisms using screw theory, small deflection of the flexible segments is generally assumed. However, and although some research has shown that it can be applied to the case of large deformation mechanisms [220], the perspective for using this approach will be slightly different. Indeed, the FACT method will be used from a design point of view with regard to the static state of the mechanism. The number of constraints will be reduced as much as possible without modifying the degree of freedom that will be used subsequently.

### 5.1.1 Degrees-of-freedom and constraint of a mechanism

A rigid body free of all constraints in space has 6 DOFs: 3 degrees of rotation and 3 degrees of translation. Each link that reduces this number of DOFs is called a Degree-Of-Constraint (DOC).

The number of DOFs of a traditional rigid body mechanism can be easily determined as the difference between: the sum of rigid body DOFs and the joint constraints, as shown in Fig. 5.1, by means of the Kutzbach-Grübler's formula:

$$\text{DOF} = m(N - 1 - J) + \sum_{i=1}^J f_i \quad (5.1)$$

Where  $N$  is the number of bodies, including the base,  $J$  is the number of joints,  $f_i$  the number

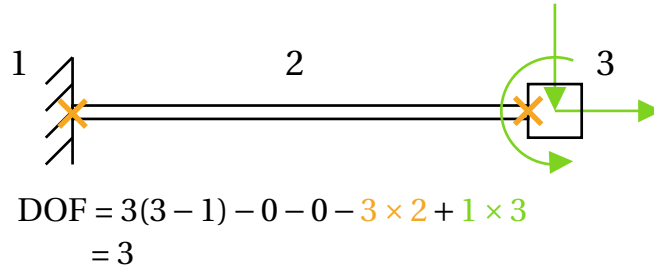


Figure 5.2 – Application of the generalised formula [147, 6] for the determination of the degrees of freedom of a flexible beam in the plane.

of kinematic joints that permit  $i$  relative motions between connected bodies and  $m$  is the number of possible DOFs, i.e. 6 if it is a spatial mechanism and 3 if it is planar mechanism. However, for compliant mechanisms, the identification of DOFs and DOCs, is more challenging due to a lack of clear boundaries between rigid and flexible parts. The uncertainty is related to the distribution and non-linearity of the deformation of the flexure elements, as well as to the existence of non-independent constraints. This phenomenon corresponds to the existence of redundant constraints within the mechanism, i.e. several constraints block the same DOF, namely the DOHs.

In the case of the pseudo-rigid body model, the DOFs of a compliant mechanism can be identified in the same way as for a traditional mechanism. This model is particularly effective for planar compliant mechanisms without redundant constraints or over-constrained mechanisms [94]. According to [147, 6], for a mechanism with known actuating forces, as shown in Fig. 5.2, the number of DOFs is determined by the following equation:

$$\text{DOF} = m(N - 1) - \sum_{j=1}^{m-1} (m - j)f_j - \sum_{j=1}^{m-1} (m - j)c_j - m \cdot n_{fix} + \sum_{j=1}^m j \cdot s_c \quad (5.2)$$

where  $c_j$  is the number of compliant joints which permit  $j$  relative motions,  $n_{fix}$  is the number of fixed connections,  $s_c$  is number of segment with segment compliance.  $N$  and  $m$  correspond respectively to the number of bodies and the number of possible DOFs, in agreement with what was defined for Eq. (5.1).

The limitation of this method is related to the characterisation of the DOFs calculated previously. Although they are defined as DOFs by the equation, their identification within the mechanism is done by means of a quantification of the displacements obtained at the mechanism output following the application of a loading. Whenever one of the displacements is larger than all the other ones along the same axis, it can be identified as a DOF. However, this equation does not indicate whether the DOF is a pure translation or rotation, or a coupled motion.

## 5.1. Enhanced bistable mechanism for improved lifetime and manufacturability by hyperstatism analysis

---

Another approach is to use screw theory [197] that also allows the analysis of DOFs and/or DOCs of compliant mechanisms. This method is based on two screw entities, namely the wrench, which represents the forces and moments acting on a rigid body, and the twist, which represents a helical motion that includes rotational and translational displacements. A DOF then corresponds to a displacement possibility and conversely a DOC to a force or moment transmission. All the mathematical expressions will be represented by means of the FACT method [89, 90].

### 5.1.2 Screw algebra

It is well known that motions and constraints can be represented by screws: twists and wrenches respectively, that are elements of the Lie algebra of the Lie group SE(3). In an XYZ frame, the wrench,  $\mathcal{W}$ , representing loading and the twist,  $\mathcal{T}$ , representing motion are expressed as follows:

$$\mathcal{W} = \begin{Bmatrix} f_x \\ f_y \\ f_z \\ m_x \\ m_y \\ m_z \end{Bmatrix} = \begin{bmatrix} F \\ M \end{bmatrix}, \quad \mathcal{T} = \begin{Bmatrix} \omega_x \\ \omega_y \\ \omega_z \\ v_x \\ v_y \\ v_z \end{Bmatrix} = \begin{bmatrix} \Omega \\ V \end{bmatrix} \quad (5.3)$$

where for the wrench  $F \in \mathbb{R}^3$  and  $M \in \mathbb{R}^3$ , two three-dimensional vectors which represent force and moment acting on the rigid body. Similarly,  $\Omega$  and  $V$  are two three-dimensional vectors which represent rotational and translational motions. The sum of all the degrees of freedom of a rigid body forms its motion space. It is therefore represented mathematically by a matrix,  $\Pi_{\mathcal{T}}$ , composed by  $m$  independent twists.

$$\Pi_{\mathcal{T}} = \begin{bmatrix} \mathcal{T}_1 \\ \mathcal{T}_2 \\ \vdots \\ \mathcal{T}_n \end{bmatrix} = \begin{bmatrix} \Omega_1 & V_1 \\ \Omega_2 & V_2 \\ \vdots & \vdots \\ \Omega_n & V_n \end{bmatrix} \quad (5.4)$$

The set of twists  $\mathcal{T}_n$  covering the motion space constitute the matrix  $\Pi_{\mathcal{T}}$  whose  $m$  indicates the dimension. In a similar way, the set of constraints preventing movements forms what is called the constraint space, which is mathematically modelled by the matrix  $\Pi_{\mathcal{W}}$  composed by  $n$  independent wrenches

$$\Pi_{\mathcal{W}} = \begin{bmatrix} \mathcal{W}_1 \\ \mathcal{W}_2 \\ \vdots \\ \mathcal{W}_m \end{bmatrix} = \begin{bmatrix} F_1 & M_1 \\ F_2 & M_2 \\ \vdots & \vdots \\ F_m & M_m \end{bmatrix} \quad (5.5)$$

Again, the set of elementary wrenches  $\mathcal{W}_i$  covers the constraint space and composes the matrix

**Chapter 5. Enhancement of the mechanisms and contribution of 3D printing of composites**

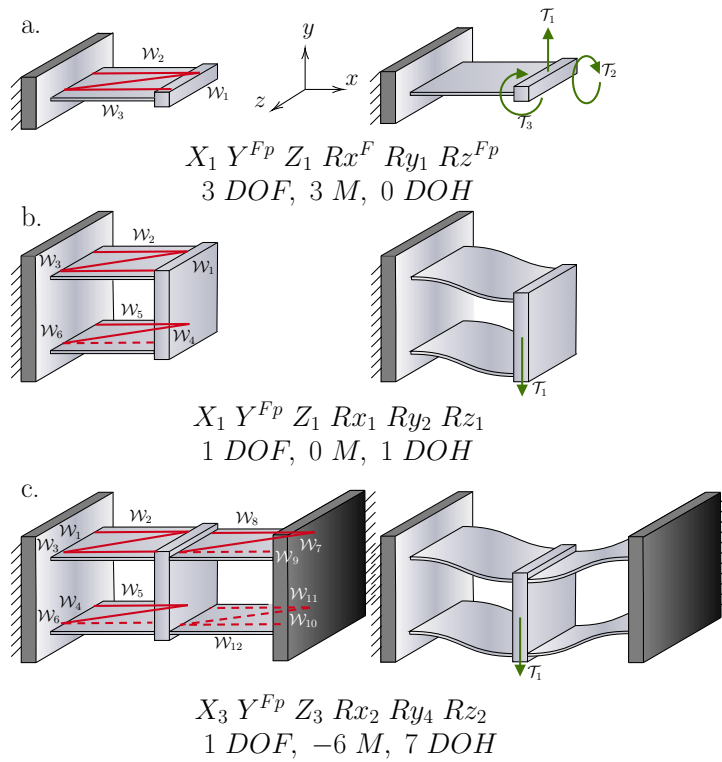


Figure 5.3 – Constraint and freedom space of compliant mechanisms : (a) a 3-DOF leaf spring, (b) a 1-DOF parallel spring stage, and (c) a 1-DOF double parallel spring stage use as basis for bistable mechanisms. The illustrations show the mechanism before axial loading, but this does not affect the analysis of the bistable.

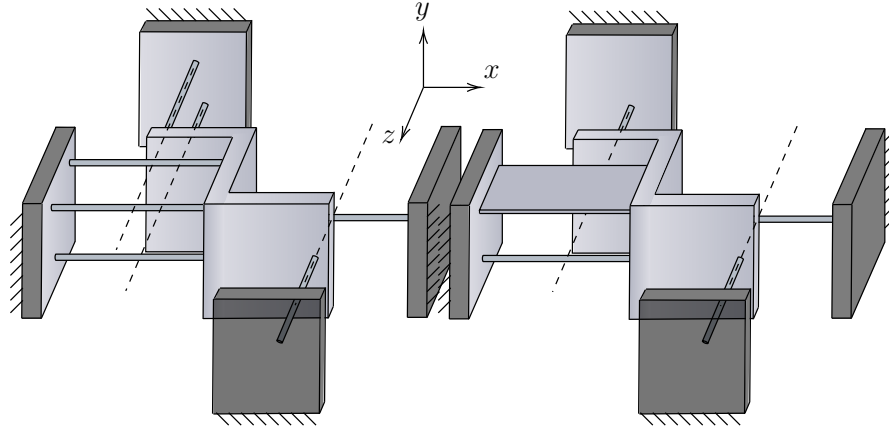
$\Pi_{\mathcal{W}}$  of rank  $n$ .

An interesting point to take into account is that if the matrix  $\Pi_{\mathcal{W}}$  does not fully fill the rank, then a number of wrenches are redundant and their removal does not affect mobility.

Using the FACT method, it is then possible to give these mathematical entities a geometric representation. Thus a one-dimensional space can be represented as a line. Two distinct lines forming a surface can represent a two-dimensional space, etc. [89, 90]. The geometric representation of a constraint can be compared to a rod of infinite axial stiffness linking the body to an embedding point.

An example is shown in Fig. 5.3 through the embedding of a rigid body by means of a beam whose  $t \ll w$ . This beam prevents all translations but allows all rotations in the XY plane. It prevents rotation about the X axis and allows translation, accompanied by a parasitic motion, along the Y axis. In screw theory, this type of beam is modelled using three ideal constraints represented by three independent wrenches in the XY plane. These constraints are modelled in Fig. 5.3 by two parallel wrenches,  $\mathcal{W}_1$  and  $\mathcal{W}_2$ , to the X axis intersecting the Z axis at two

## 5.1. Enhanced bistable mechanism for improved lifetime and manufacturability by hyperstatism analysis



$$\begin{array}{c} X_2 \ Y^{Fp} \ Z_1 \ R_{x_1} \ R_{y_2} \ R_{z_1} \\ 1 \ DOF, \ -1 \ M, \ 2 \ DOH \end{array}$$

Figure 5.4 – A rod-based version (a) of the mechanism and a hybrid rod-blade version (b) justifying the realisation of a design with minimal constraints.

points, and a wrench parallel  $\mathcal{W}_3$  to the X axis. Each constraint is represented by a red line and the possible mobilities by green arrows.

By representing the spaces of constraints and motions necessary for the proper functioning of the mechanism, which can be modelled, as follows in Eq. 5.6, with 5 independent wrenches, it is easy to understand the large number of redundancies present in the third mechanism shown in Fig. 5.3c., composed of 12 wrenches.

$$\Pi_{\mathcal{F}} = [\mathcal{F}_1] = \begin{bmatrix} 1 \\ 0 \\ 0 \\ 0 \\ 0 \\ 0 \\ 0 \end{bmatrix}, \quad \Pi_{\mathcal{W}} = \begin{bmatrix} \mathcal{W}_1 \\ \mathcal{W}_2 \\ \mathcal{W}_3 \\ \mathcal{W}_4 \\ \mathcal{W}_5 \end{bmatrix}^T = \begin{bmatrix} 0 & 0 & 0 & 0 & 0 \\ 1 & 1 & 0 & 0 & 1 \\ 0 & 0 & 1 & 1 & 0 \\ 0 & 0 & 0 & 0 & 1 \\ 0 & 0 & 0 & 1 & 0 \\ 0 & 1 & 0 & 0 & 0 \end{bmatrix} \quad (5.6)$$

### 5.1.3 Theoretical optimal version of the double preshaped beam bistable mechanism

The mechanisms described in Fig. 5.3 have shown the existence of a number of redundant constraints inducing hyperstatism. It also reveals the impossibility of obtaining an isostatic mechanism due to the requirement of a persistent DOH along the  $\vec{x}$  axis. The description

## Chapter 5. Enhancement of the mechanisms and contribution of 3D printing of composites

---

of the DOF in Fig. 5.3 was done according to the convention used by Henein [81], namely a capital letter describing the type of motion ( $X, R_x$ ), a subscript indicating the DOC ( $\dots_n$ ) and a superscript indicating the DOF ( $\dots^F$ ). When the DOC is strictly greater than 1, then the DOH is equal to  $n - 1$ . A DOF may be accompanied by a subscript  $p$ , e.g.  $X^{F_p}$  indicating the existence of a parasitic motion.

Using the method described above, it is possible to redesign the mechanism according to our needs, i.e. a single translational mobility along the  $\vec{x}$  axis. This corresponds to a twist  $\mathcal{T} = \begin{bmatrix} 0 & 0 & 0 & 1 & 0 & 0 \end{bmatrix}^T$ , which translates in the constraint space by wrenches where  $f_x = 0$  and thus all the ideal constraints of the constraint space are modelled by  $\mathcal{W} = \begin{bmatrix} 0 & f_y & f_z & M_x & M_y & M_z \end{bmatrix}^T$ .

In order to obtain a mechanism with a minimal number of constraints, it is necessary to have a minimum of 5 independent and 1 redundant constraints in the constraint space. The screw theory and FACT method allows to propose three mechanisms based mainly on rods reducing the constraint degrees to a strict minimum, respectively represented in Fig. 5.4 and Fig. 5.6. To ensure a bistable behaviour, this mechanism cannot be isostatic, and has at least one degree of hyperstatism due to the need to axially constrain both sides of the shuttle.

The shape of the central shuttle, in Fig. 5.4, is due to the need to position the rods oriented along  $\vec{z}$  so that their lines of action, dotted in Fig. 5.4, are facing the centre of rotation of the rod oriented along  $\vec{x}$ . Failure to comply with this rule leads to a variation in stiffness and an increase in parasitic motion. Although if 3D printing is considered, a manufacturing problem can be anticipated by replacing round section rods with square section rods ( $w_r = t_r$ ) [77].

It is necessary to evaluate the potential of such a design partially replacing beams ( $\dots^b$ ) by rods ( $\dots^r$ ) by performing a differential analysis of the stiffnesses  $K_{cis}$  and admissible strokes  $\lambda_{cis}$ :

$$K_{cis}^b = \frac{12EI_b}{l^3} \quad K_{cis}^r = \frac{12EI_r}{l^3} \quad (5.7)$$

$$= \frac{Ewt^3}{l^3} \quad = \frac{3Ed^4}{16l^3} \quad (5.8)$$

where  $E$  is the Young's modulus and  $I$  is the second moment of area. The geometric parameters characterising the beam are its thickness  $t$ , width  $w$  and length  $l$ , and the rod is characterised by its diameter  $d$ . The values of these parameters are given in Tab. 5.21

It is therefore necessary to express  $d$  as a function of  $w$  and  $t$ , in order to find an equivalent

## 5.1. Enhanced bistable mechanism for improved lifetime and manufacturability by hyperstatism analysis

Table 5.1 – Design parameters in mm

Parameters		$E$ [MPa]	$h$	$w$	$l$	$t$	$T$
Test 1	classic	1820	3.6	5	147	1	
	enhanced	1820	3.6	5	147		1.25
Test 2	classic	1944	1	1.26	23	0.2	
	enhanced	1944	1	1.25	23		0.25

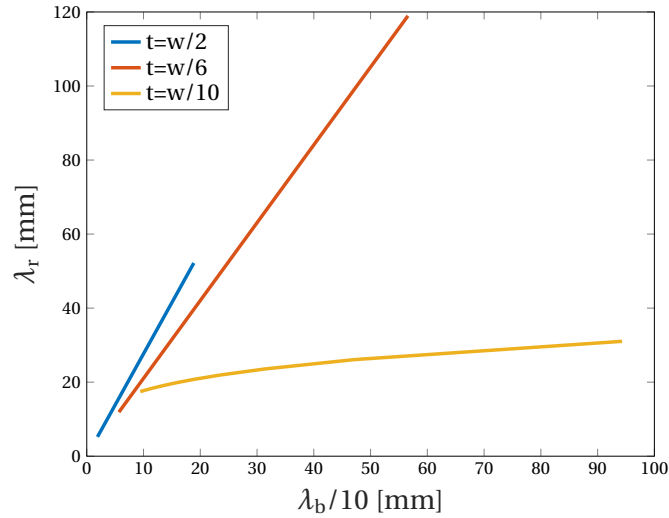


Figure 5.5 – Comparison of the permissible stroke between a beam and a rod, obtained after successively calculating the diameter  $d$  for different  $t - w$  ratios

stiffness

$$K_{cis}^b \iff K_{cis}^r \quad (5.9)$$

$$d = 4 \sqrt[4]{\frac{wt^3}{3}}$$

with  $t$  being always much smaller than  $w$ , and  $d$  the diameter.

Using the value of  $d$  obtained in the previous equation, we can then calculate the allowable stroke as a function of the admissible stress,  $\sigma_{adm}$ :

$$\lambda_{cis}^b = \frac{\sigma_{adm} l^2}{3Et}, \quad \lambda_{cis}^r = \frac{\sigma_{adm} l^2}{3Ed} \quad (5.10)$$

The graph in Fig. 5.5 illustrates the impossibility of satisfying both the stiffness and the allowable stroke criteria.

Furthermore, the proposed theoretical versions require a larger footprint than the conventional mechanism, despite the different approach and attempts at a hybrid version based on both beams and rods, as shown in Fig. 5.4.

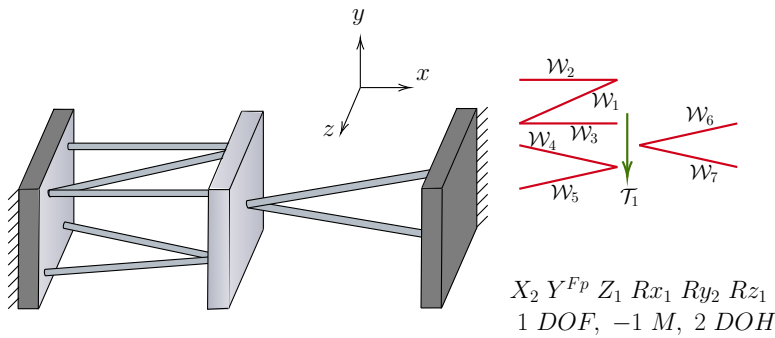


Figure 5.6 – Representation of a theoretical bistable mechanism, before axial loading and buckling of the rods, justifying minimal constraints based on the FACT method.

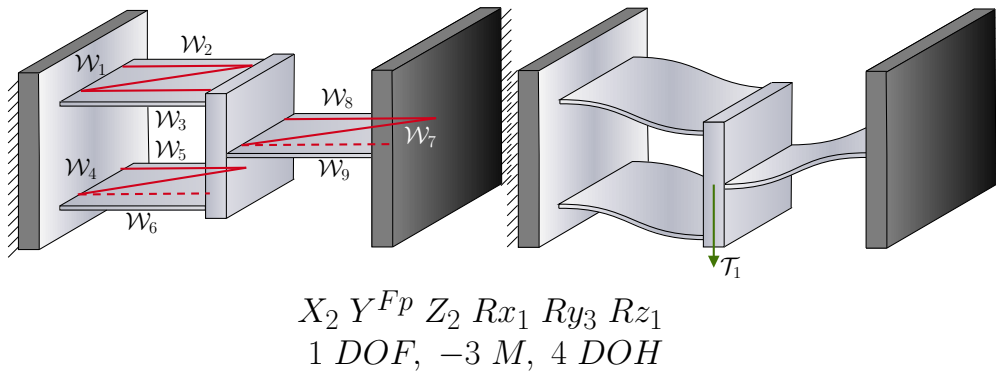


Figure 5.7 – Constraint and freedom space of enhance bistable mechanism

This result favours the conservation of the use of beams only and justifies the design proposed in Fig. 5.7 and whose characterisation will be made in the following section. With this design, which will be referred to as the "enhanced" bistable mechanism in the rest of this study, the DOH have been reduced to an acceptable compromise.

**5.1.4 Mechanism characterisation**

**Classical bistable mechanism**

In this study, a bistable mechanism consisting of a pairs of pre-shaped beams connected to each other at mid-length will be referred to as a *classic* mechanism. It is the one that was used for the design of the modules.

All the design steps described in Chapter 3 will not be repeated, but the system of equations governing the operation of the mechanism will be recalled. These equations are the ones allowing the calculation of the beam shape  $\eta(x)$ , the bistability criterion  $Q$ , and the position  $\delta$

## 5.1. Enhanced bistable mechanism for improved lifetime and manufacturability by hyperstatism analysis

---

and maximum values of the snapping forces  $f$  required to leave the stable configurations.

$$\begin{cases} \eta(x) = \frac{h}{2} \left[ 1 - \cos\left(2\pi\frac{x}{l}\right) \right] \\ Q = h/t, \quad Q > 2.31 \\ \delta_{top}, \delta_{bot} = h \left( \frac{28}{27} \pm \frac{2\pi}{3} \sqrt{\frac{1}{6} + \frac{16}{81\pi^2} - \frac{1}{Q^2}} \right) \\ f_{top}, f_{bot} = \frac{Ewt^3h}{l^3} \frac{32\pi^2}{9} \left( \frac{4}{9} \mp \pi \sqrt{\frac{1}{6} + \frac{16}{81\pi^2} - \frac{1}{Q^2}} \right) \end{cases} \quad (5.11)$$

### Enhanced bistable mechanism

The removal of one of the beams to decrease the DOH requires to adapt the analytical model. Thus, the approach considers the bistable mechanism as a parallel spring stage under the load of an opposite spring to determine an equivalent stiffness, as was done previously for stiffness reduction [118]. According to [171], the tangential stiffness for the single beam and for the two-beams parallel spring stage,  $K_1$  and  $K_2$  respectively, can be very well approximated by

$$K_1 = \frac{12EI}{l^3} - \frac{3F_x}{5l} \quad \text{and} \quad K_2 = \frac{24EI}{l^3} - \frac{6F_x}{5l}, \quad (5.12)$$

where  $F_x$  is the compression load. The conservation of the kinematics of the shuttle between the one- and two-beam parts is linked to the dimensional conservation of the beam lengths and to the initial configuration of the preformed beams. Moreover, in order to preserve the bistability, the ratio  $Q$  must be maintained for all beams. Since the shuttle rotation is still blocked with 3 blades, mode 2 is always constrained and the limit  $Q$  for the double-beam mechanism given in Eq. 3.10 is still the reference for the bistability existence. It is then possible to derive the relationship between the thickness of the single beam  $T$  as a function of the thickness of one of the beams of the parallel spring stage  $t$  as follows:

$$T^3 = 2t^3, \quad T > t > t_{min} \quad (5.13)$$

with  $t_{min}$  corresponding to the manufacturing limits of the machine. This result can also be found by analysing the stiffness and compliance matrices, as illustrated in the Appendix A.

Given the constraints imposed and the entanglement of the parameters, there is no other solution. By removing the footprint preservation constraint, other solutions could be found. Assuming that there would be an asymmetrical configuration, with different profiles  $\eta$  for the single and double beams, which would preserve the rectilinear movement of the shuttle, it would be more voluminous and more dimensionally demanding. This result comes from the fact that if the same amplitude of displacement  $\delta$  wishes to be kept, it is necessary to keep the beam geometrical parameters of one of the two sides. Therefore, if the shape  $\eta$  is changed, it will result in an increase in length  $l$  and thus an increase in volume according to Eq. 5.11. Furthermore, a change in length results in the need to increase  $t$  in order to maintain the

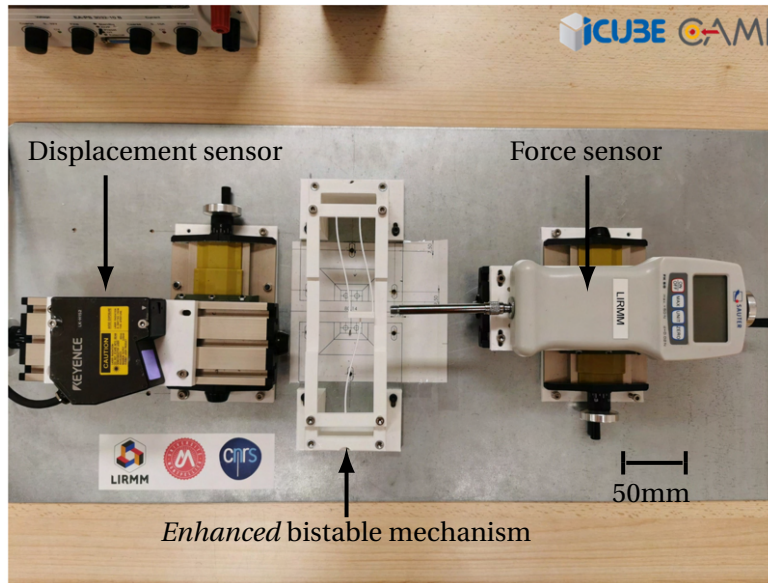


Figure 5.8 – Set-up used for the experimental characterisation of bistable mechanisms.

equivalent stiffness. However, the modification of  $t$  has an impact on the bistability criterion  $Q$ , as presented in Eq. 5.11, and requires to increase the values of the apex  $h$ . Finally modifying  $h$  induces an asymmetry of the displacement amplitude  $\delta$ . Finding a good equilibrium in this set of parameters in order to obtain a result equivalent to that obtained with Eq. 5.13 remains therefore much more demanding.

### 5.1.5 Experimental set-up and protocol validation

In order to characterise the bistable mechanisms, the set-up described in Fig. 5.8 was used. It consists of the same force sensor and laser-based displacement sensor as described in Section 3.5.2.

The fabrication was carried out using two FDM 3D printers, i.e. an Ultimaker S3 and a Fortus 450 (Stratasys). The values of the parameters used for the mechanisms are given in Table 5.21 in Subsection 5.1.4.

The mechanisms were manufactured within a closed frame which was then fixed to the support by means of screws, to prevent any risk of modification of the boundary conditions during the experiment.

The force was applied on the shuttle of the bistable mechanism and measured with mean of the force sensor. The induced displacement was measured using the displacement sensor. Once the measurements have been performed until the bistable mechanism is triggered, it is necessary to reverse it to measure the negative forces.

## 5.1. Enhanced bistable mechanism for improved lifetime and manufacturability by hyperstatism analysis

---

The *classic* and *enhanced* mechanisms were tested successively. Two tests were carried out with a pool of 10 mechanisms of each type.

The evolution of the behaviour of the mechanisms over time was evaluated in the first test. For each mechanism, 10 cycles were performed immediately after being manufactured, at  $t_0$ , a second round of 10 cycles was performed after 7 days and a third round of 10 cycles was performed after 30 days.

In the case of printing miniaturised mechanisms as described in previous work [12], with  $t = t_{min}$  the manufacturing limit leads to amplify the problem of hyperstatism. The second test, which aimed to assess the cycling actuation limit of the miniaturised mechanisms was therefore evaluated under these conditions. All 20 mechanisms were triggered until failure in order to compare the life span of a *classical* mechanism with that of an *enhanced* mechanism.

Another phase of testing was conducted to determine the effects of loss of symmetry due to the removal of one of the four beams. To obtain this information, a measurement of the parasitic motion of the shuttle during its travel between the two stable states has been carried out. The laser sensor was no longer positioned in front of the shuttle motion but orthogonally. These measurements were carried out on 6 mechanisms, 3 *classical* and 3 *enhanced*, with 6 back and forth actuation cycles per mechanism.

### 5.1.6 Experimental results

All force-displacement curves were averaged and plotted in Fig. 5.9 with the standard deviation for comparison between models. The analytical model was solved in Matlab R2019B and the finite element analysis (FEA) was performed with the native solver of Creo Simulate. The experimental results show good agreement with the models and particularly with FEA.

#### Inflection points and fatigue

The fatigue state of the beams of the mechanism is visualised at the inflection points and the evolution of the buckling modes observed between these points. The first deflection mode,  $M_1$ , of a beam corresponds to the non-linear areas of Fig. 5.9 :

$$M_1 \in [0, d_{top}] \cup [d_{bot}, d_{final}] \quad (5.14)$$

This means that all the high buckling modes are located in the linear zone of the force-displacement characteristic curve. It is observed that for the fabricated mechanisms, the deformation pattern tends to remain similar at first and then vary with time in Test 1 and with cycling in Test 2, as presented in Fig. 5.10.

It is also observed that over time the initial configuration of the classic mechanism tends to change. This result is presented in Fig. 5.11. As this phenomenon can be linked to a

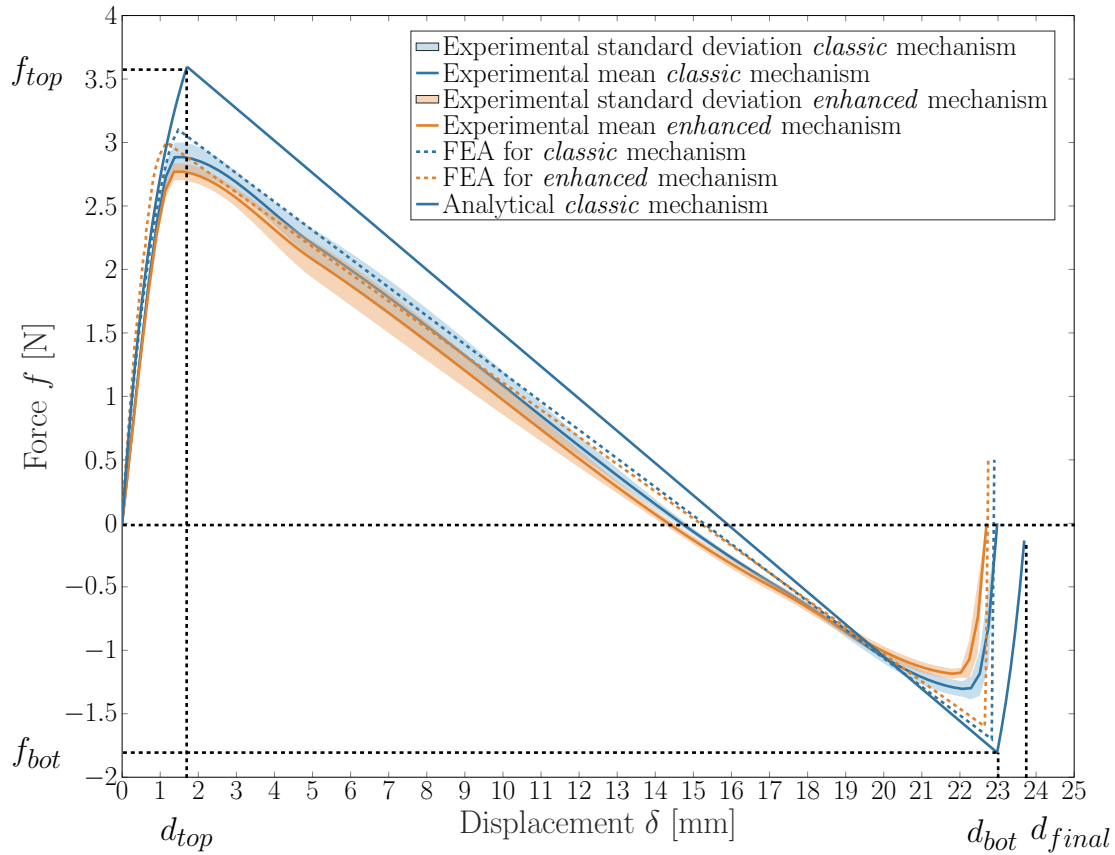


Figure 5.9 – Comparative graph of analytical, numerical and experimental results of the evolution of the snapping force in function of displacement for the *classic* and *enhanced* mechanism.

combination of fatigue, hyperstatism and stress relaxation within the material [87], it is one of the reasons for the addition of Test 2, which allows to reveal the impact of fatigue on the mechanism.

The phenomenon of relaxation within a 3D printed structure has already been observed with respect to the lengthening of the beams [11]. However, contrary to [11], here the frame of the mechanism is closed and an increase of  $h$  is observed. It should be noted that although with the analytical model an increase in  $h$  induces an increase in the triggering force, which is not the case here. This result can be explained, by referring to the characterisation results obtained with an Euler-Bernoulli beam, demonstrating a more important variation of the Young's modulus than  $h$ .

**Mechanism lifetime comparison**

The study of the distribution of triggering forces over time, i.e. Test 1, was carried out following a classification by type, *classic* and *enhanced*. The data obtained experimentally are

## 5.1. Enhanced bistable mechanism for improved lifetime and manufacturability by hyperstatism analysis

---



Figure 5.10 – Illustrations of half-mechanisms showing the beams of *classic* bistable mechanisms in various buckling mode.



Figure 5.11 – Illustration of the alteration of the initial shape of the beams due to the relaxation of the material three weeks after printing for one of the mechanism used.



Figure 5.12 – Photograph of an *enhanced* mechanism made with 3D printing in its two stable configurations: a. Fabricated and b. Deformed

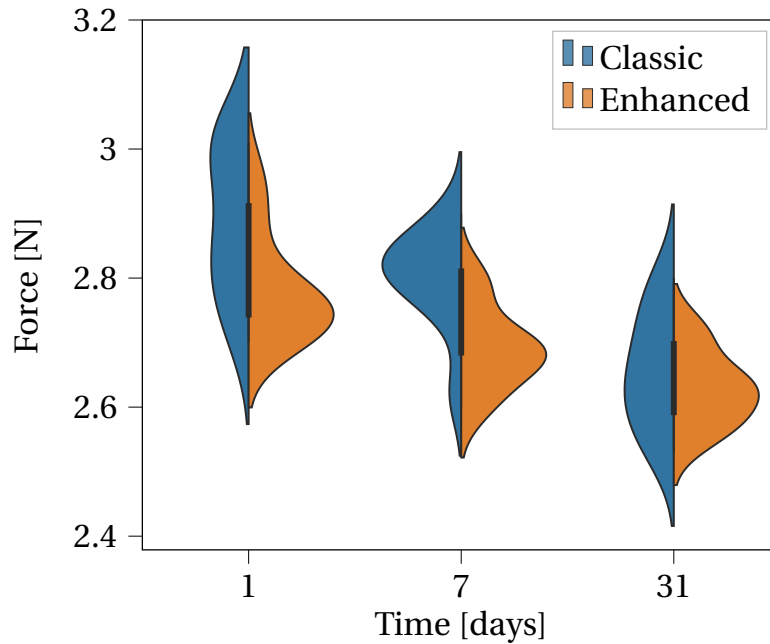


Figure 5.13 – Experimental triggering force  $f_{top}$  distribution for each of the mechanisms studied over time.

represented using violin diagrams, Fig. 5.13 for the comparison of  $f_{top}$  and Fig. 5.14 for  $f_{bot}$ , allowing to switch from one stable state to the other as shown in Fig. 5.12. This type of representation was preferred to box plots, because of the multimodal nature of the results, as they also allow the probability density of the data to be shown at different values and smoothed by a kernel density estimator.

Firstly, it is noted that a greater dispersion of triggering forces is obtained for the *classic* mechanism. This phenomenon persists over time for the  $f_{bot}$  forces. Conversely, large variations in the density are observed for  $f_{top}$ , which shows that the triggering forces of certain *classic* mechanisms have significantly decreased over the time. Secondly, it appears that the *enhanced* mechanism shows lower dispersion, better lifespan and better repeatability.

The results obtained in the second test are shown in Fig. 5.15. The major point highlighted in this figure is the average increase of 8% in the number of possible triggers with the *enhanced* mechanism.

### Parasitic error quantification

During the state change, the stiffness of the beams is highly non-linear and the shuttle does not perform a perfect translational motion. The quantification of this phenomenon for both variants of the mechanism is presented in Fig. 5.16. It can be seen that the amplitude of this

### 5.1. Enhanced bistable mechanism for improved lifetime and manufacturability by hyperstatism analysis

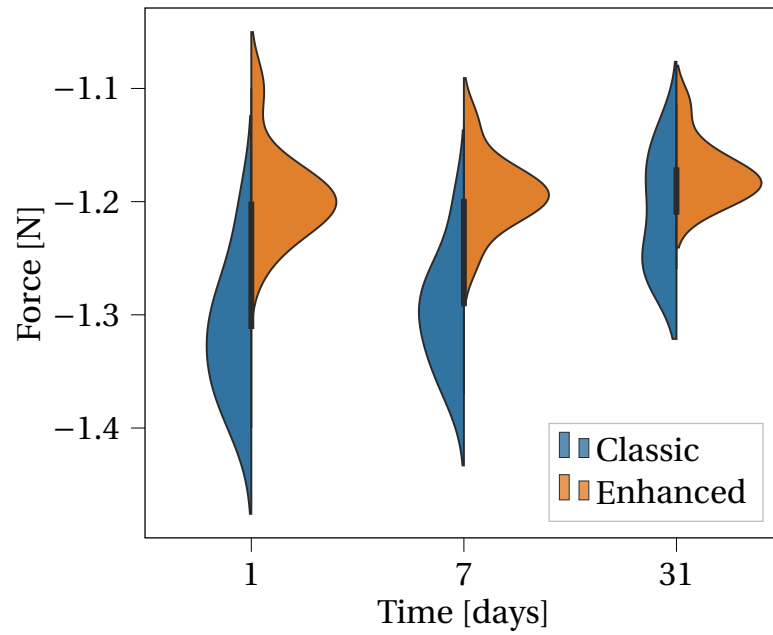


Figure 5.14 – Experimental triggering force  $f_{bot}$  distribution for each of the mechanisms studied over time.

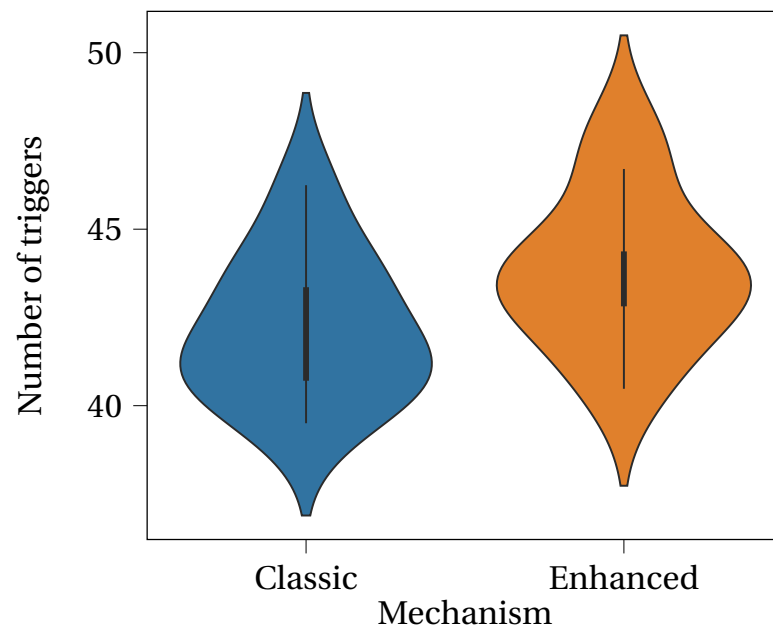


Figure 5.15 – Comparison of the experimentally measured maximum number of actuations before breaking for each of the two variations (10 of each).

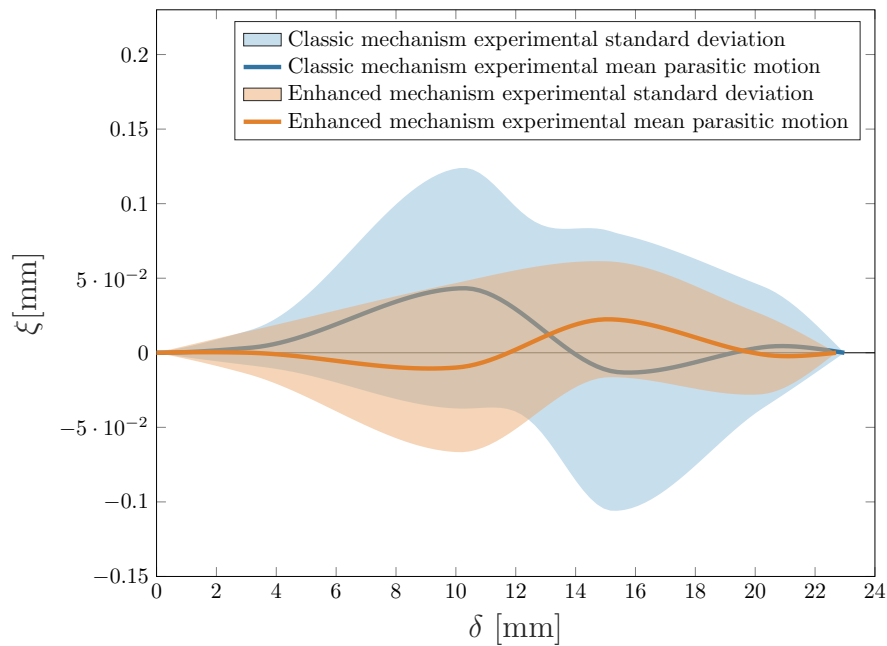


Figure 5.16 – Evolution of the parasitic displacement of the shuttle  $\xi$  during the state change.

parasitic motion is smaller for the *enhanced* version than for the *classic* version.

As for the force measurements, the dispersion difference between the mechanisms is particularly noticeable. This result tends to demonstrate that despite the fact that the analysis of hyperstatism was made with respect to a static state, its reduction tends to decrease and homogenise the internal stresses exerted during the dynamic state change phenomenon.

### **Benefit on manufacturing using the enhanced mechanism**

Finally a study was also conducted to compare the impact of removing a beam on the manufacturing of the new mechanism using the 3D printer with filament deposit. This impact is quantified in a temporal and quantitative way, i.e. to compare the evolution of the manufacturing time as well as the quantity of material used during the printing. For the enhanced mechanisms a decrease in printing time of 20% and a 16% lower material requirement is observed.

The difference in the amount of consumed material can be easily explained by the fact that  $T < 2t_1$ . The consequences can be seen in the analysis of the geometrical commands interpreted by the printer, and more particularly in the commands instructing the extrusion of the material as well as the extrusion speed, as explained in Fig. 5.17. The decrease of the amount of material correspond mainly to 3 printing sequences, corresponding to the printing of the outer wall, the skin and the travel time whose decreases are 21%, 17% and 33%. This result must be weighted

## 5.1. Enhanced bistable mechanism for improved lifetime and manufacturability by hyperstatism analysis

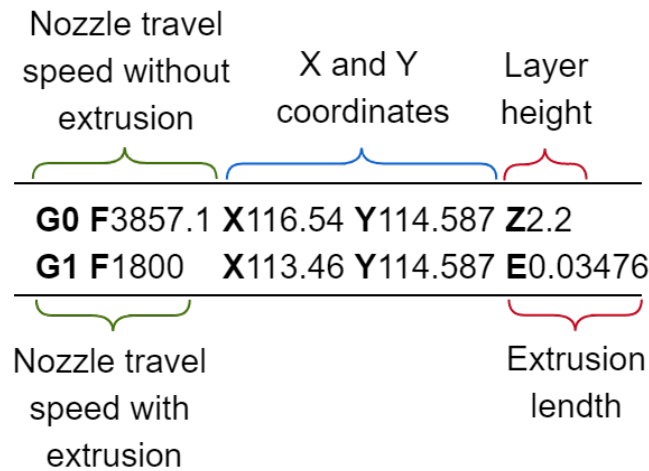


Figure 5.17 – Extraction of information from the G-code commands of a 3D printer.

by specifying that the reduction of the time of printing, related to the extrusion of material, is done mainly at the time of the printing of the external wall. This section being composed at 98% of G1 command coding for a linear displacement accompanied by a material extrusion. It is also to be noted that the arguments coding for the height of the deposited layer, Z, and for the speed of displacement, F, have been constrained in the same way for both types of mechanism, as well as the number of slices. The elimination of three factors responsible for premature fatigue in functional 3D printed mechanical parts described in the literature was also considered [186]. The factors considered are the orientation of the raster angle, the presence of a central neutral fibre in the beams and the optimisation of the parameters according to the material characteristics.

The proposed enhanced mechanism thus reveals to have not only behavioural interest, as detailed in the previous sequence, but also in terms of time and material costs, at least in the context of 3D printing.

### 5.1.7 Integration of the new bistable mechanism within the module

After modelling and experimental validation of the three-beam bistable mechanism, it was printed on a reduced scale for implementation in the module. Fig. 5.18 shows the operation of the module containing the improved version of the bistable mechanism. The two cases where the mechanism has to maintain the deformed configuration are illustrated.

This first conclusive result makes it possible to consider using this module for the design of new versions of the robot. However, a new study of the durability of this new version of the module needs to be carried out.

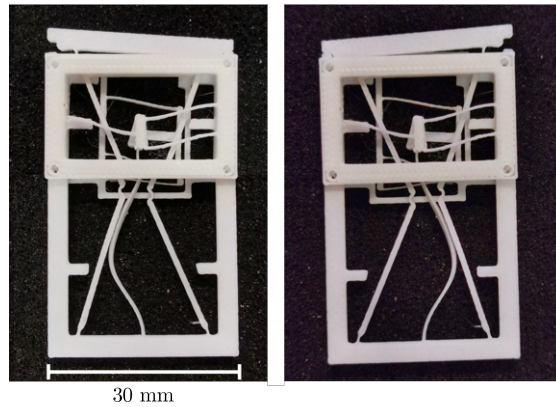


Figure 5.18 – Illustration of the operation of the module including the 3-beam bistable mechanism.

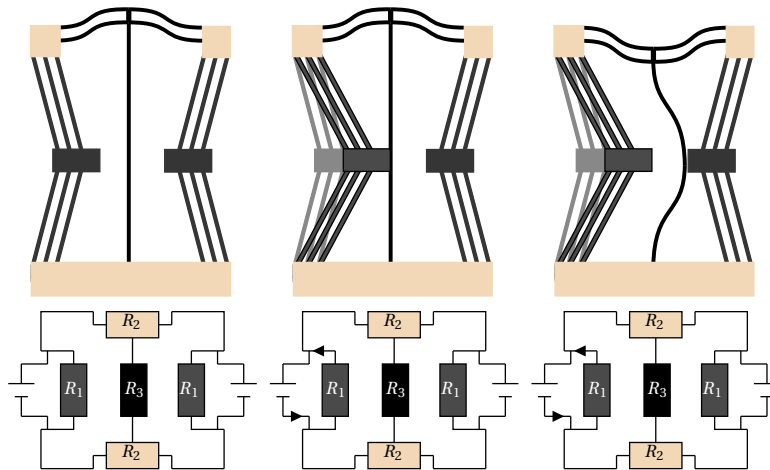


Figure 5.19 – Electrical representation based on a resistor set equivalent to the monolithic positioning system.

## 5.2 Fully 3D printed module with integrated actuation system

The miniaturisation of traditional devices such as electric motors, pneumatic and hydraulic actuators comes at the cost of a significant decrease in performance [159]. Thus, in Chapter 2, the main families of actuators that can replace traditional actuation technologies were introduced. These include thermomechanical actuators [162], some of which can be regarded as flexible mechanisms. U-shaped [101], V-shaped and Z-shaped actuators [227] are the three main thermomechanical flexible actuators able to produce planar displacements. In addition to being scalable, these actuators can be included in the design phase within the structure and can be integrated monolithically with the other mechanical components.

Technological development related to the additive manufacturing method and the research for new types of materials have led to more freedom in design. Composite materials, such as

## 5.2. Fully 3D printed module with integrated actuation system

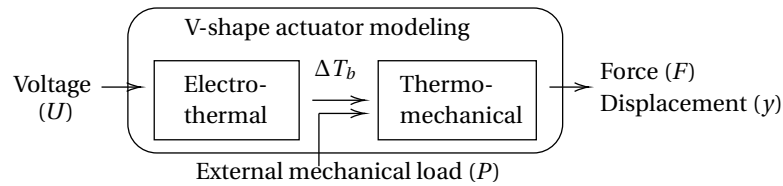


Figure 5.20 – Schematic representation of the analytical modelling of the actuator

carbon-doped PLA, obtained by infusing carbon fibres into a polymer matrix, have resulted in a functional material with improved mechanical behaviour and new physical properties [113]. Carbon fibres are particularly known in engineering for their good mechanical characteristics due to their crystalline structure. They also have good conductive properties due to the  $sp^2$  hybridisation of the carbon atoms. The initially insulating polymer becomes, for a minimal inclusion of carbon fibres, a conductive composite material. The characterisation of such materials and their electrothermal properties is a hot topic of research [113]. The design of actuators based on doped material, e.g. carbon doped resin, using Joule effect and thermal expansion have already been investigated [207].

In order to replace the assembly phase linked to the incorporation of shape memory alloy, a new design was then proposed incorporating V-shape actuators in order to actuated the module. The proposed design idea is represented in Fig. 5.19. In this illustration, the conceptual design is introduced and the electrical counterpart is designed to isolate the two actuators.

One major limitation is the manufacturing process. This material is demanding for the printer feeder as it is very abrasive. The use of this material is therefore incompatible with the printer used for the down-scaled module, i.e. the Stratasys Fortus 450, and, to the author's knowledge, there is no commercial carbon/metal doped resin available to use stereolithography as an alternative.

Thus, in order to prove the interest of this approach, it was chosen to design a positioning platform based on the same actuator but in macroscopic size printable with an Ultimaker S3.

### 5.2.1 Design and modelling of the electrothermal actuator

In order to build a 2D positioning system, V-shaped actuators will be used. Z-shaped actuators showed lower performance in terms of output force and motion [227], and since rectilinear motion is expected, U-shaped actuators are excluded. The V-shaped actuator consists of two beams, inclined at an angle of  $\alpha$ , fixed to a central shuttle on one end and an anchor on the other.

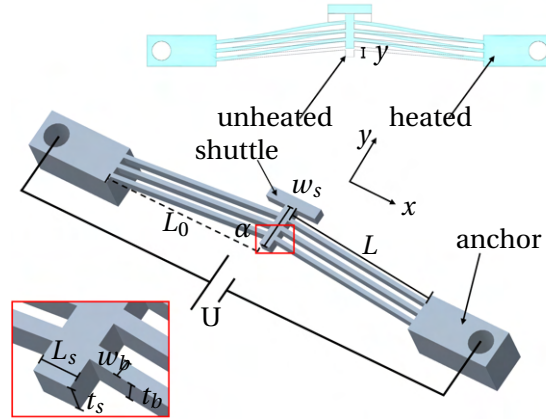


Figure 5.21 – CAD model illustration of the V-shaped electrothermal actuator and parameter identification.

### V-shape actuator analytical model

The design and functioning of this actuator are based on the use of carbon fibres within the PLA. When a voltage is applied to the actuator, the natural electrical resistance induces Joule heating. The temperature generated leads to thermal expansion, symmetrically varying the length of the beams and thus causing the displacement of the central shuttle  $y$ . Consequently, the analytical modelling of this type of actuator is done in two steps, a first step to model the electrothermal effect and a second step to model the thermomechanical effect, as shown in Fig. 5.20.

### Electrothermal Model

When a voltage is applied, the heat generated by the Joule effect is dissipated simultaneously by radiation and convection until a steady state thermal equilibrium is reached. Both of this thermal mechanisms can be neglected at first with small scale actuator. According to [228], the average temperature increase along the beams  $\Delta T_b$  is defined as function of the input voltage  $U$ , geometrical parameters of the beam  $\Pi$  and the material properties  $Q$  as follows:

$$\Delta T_b = \frac{1}{L} \int_0^L (T_s - T_0) = Q\Pi U^2 \quad (5.15)$$

with,

$$Q = \frac{1}{k_a \rho}, \quad \Pi = \frac{(1 - e^{L\Gamma})^2}{Le^{L\Gamma}\Gamma} \varphi + \left( \frac{1 - e^{L\Gamma}}{Le^{L\Gamma}\Gamma} + 1 \right) \chi \quad (5.16)$$

where  $\Gamma = \sqrt{k_a/(kt_b)}$ ,  $L$  is the beam length,  $k_a$  is the thermal conductivity of the air,  $k$  is the thermal conductivity of beam,  $\rho$  is the electric resistivity. The calculation details of  $\varphi$  and  $\chi$ , which are depending on the geometrical parameters, shown in Fig. 5.21, are presented in [228].

## 5.2. Fully 3D printed module with integrated actuation system

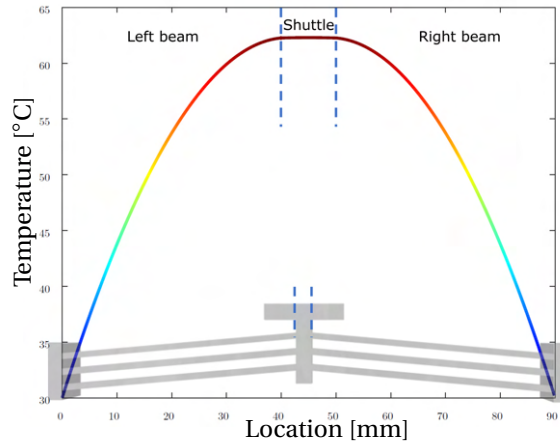


Figure 5.22 – Temperature distribution within the actuator based on the analytical model.

In Fig. 5.22, the temperature distributions along the actuator, analytically calculated, is given for  $U = 50V$ . The shuttle has the highest temperature due to its greater resistivity. The temperature of 60 degrees is the limit for PLA before glass transition. Exceeding this glass transition temperature in real case will result in a change in the behaviour of the material, which will tend to a plastic deformation.

### Thermomechanical Model

According to [228], considering the symmetry of the actuator and the shuttle as infinitely rigid and not subject to thermal expansion, then the shuttle displacement is obtained from the following Castigliano theorem:

$$y = \Delta L_T \sin \alpha - \int_0^L \frac{N}{EA_b} \frac{\partial N}{\partial P} dx - \int_0^L \frac{M}{EA_b} \frac{\partial M}{\partial P} dx \quad (5.17)$$

where  $\Delta L_T$  is the axial elongation of the beam linked to thermal expansion,  $\alpha$  is the inclination angle of the beam and  $A_b$  the beam cross section area.  $M$  and  $N$  are the bending moment and the axial force on the beam.  $E$  is the Young's modulus of the beam material. This equation can be simplified by substituting boundary conditions, such as

$$y = \left( \alpha L \Phi \sin \alpha \quad -L \frac{\Phi}{EA_b} \right) \begin{pmatrix} \Delta T_b \\ P \end{pmatrix}, \quad (5.18)$$

where  $\alpha$  is the coefficient of thermal expansion and  $\Phi = L_0^2 / (h_0^2 \cos^4 \theta + L_0^2 \sin^2 \theta)$ .  $L_0$  is the distance between the two anchor points of the beam. The elements of the left-hand side of Eq. (5.18) thus represent the flexibility of the actuator in response to the temperature and in response to an external load  $P$ . The load  $P$  will be the spring force of the actuator mounted in opposition in the case of the positioning system, as shown in Fig. 5.31.

**Combined actuator models**

By combining the two models, Eq. (5.18) can be rewritten as follows :

$$y = \left( \alpha L_0 \Gamma \sin \theta Q T \quad - \frac{L_0 \Gamma}{EA_b \cos \theta} \right) \begin{pmatrix} U^2 \\ P \end{pmatrix} \quad (5.19)$$

$$= (\kappa_1 - \kappa_2) \begin{pmatrix} U^2 \\ P \end{pmatrix} \quad (5.20)$$

By modelling the force related to an input voltage as a spring pushing the shuttle, the equation for the force  $F$  produced by the actuator can be obtained as follows [228]:

$$F = \xi U^2 - P \quad \text{with} \quad \xi = \frac{\kappa_1}{\kappa_2} \quad (5.21)$$

**5.2.2 Design and analysis of a proof of concept: the XYZ $\theta$  positioning system**

The positioning system is based on an arrangement of several components that allow different motions in the workspace as shown in Fig. 5.23. Fig. 5.24 shows a top view of the platform with the identification of the three major components dimensioned here, namely the system allowing linear displacement along the X and Y axes, in a dashed line, the system allowing the rotation around the Z-axis, outlined in a solid line, and the linear displacement along Z in profile view and framed by a dotted line. The rotational guiding component is present twice in a symmetrical manner in order to be able to carry out clockwise and counter-clockwise rotations. These components will be successively characterised in this section.

**Compliant mechanism for X and Y linear motions**

**Operational principle**

The first component of the platform studied is the compliant mechanism allowing a two-axis linear movement, as illustrated in Fig. 5.25. This mechanism consists of a central shuttle and four actuators in opposition two by two. Each actuator is connected to the platform by means of a beam and a flexible joint, i.e. circular hinges. The choice of a circular hinges rather than the more kinematically efficient crossbar pivot joint is related to the 3D printing manufacturing process. A circular hinge is easier to print because of its flat geometry and are less cumbersome. These passive links allow the platform to move in the workspace in response to the actuators, as shown in Fig. 5.26. When a force  $F$  is produced by one or two actuators, the platform changes its position according to single or dual axis components,  $O' = (\delta_x, \delta_y)^T$ .

## 5.2. Fully 3D printed module with integrated actuation system

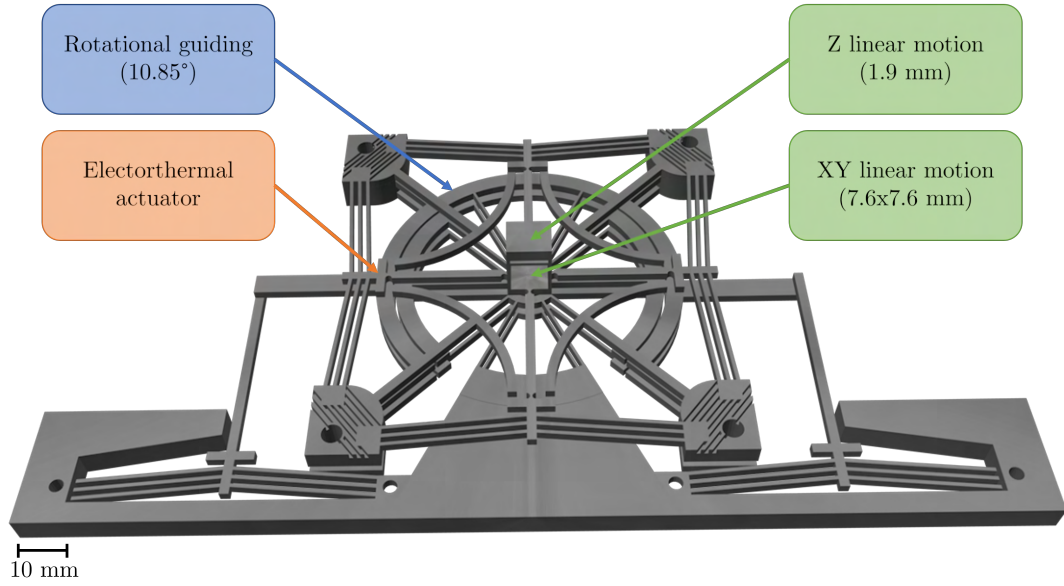


Figure 5.23 – Structure of the 3D-printed monolithic  $XYZ\theta$  positioning system.

### Actuation against opposite actuators

The actuators are in opposition two by two. When one is actuated, the other is loaded and deformed. It is therefore necessary to calculate the force-displacement relationship of the actuator at rest when it is loaded. This quantity allows to know the minimum force  $F$  that the active actuator must provide to deform the one at rest depending on the geometrical parameters of the actuator, i.e.  $\alpha$  the angle of inclination of the beams and  $L$  the length of the beams. The force-displacement characteristic curve of this pre-shaped mechanism has two domains. A linear domain in which the evolution of the force  $f$ , is calculated as follows [100]:

$$f = 8\pi^2 \frac{EI \sin \alpha}{(L)^2} \left( \frac{4}{3} - \frac{y}{L \sin \alpha} \right) \quad (5.22)$$

And a non-linear domain where the relationship between the force  $f$ , the normalized axial force  $N$  and the deformation generated by the active actuator  $y$  is calculated according to [100], as follows:

$$f = \frac{EI \sin \alpha}{8(L)^2} \left( \frac{N^3}{\frac{N}{4} - \tan \frac{N}{4}} \right) \left( \frac{N^2}{N^2 - 4\pi^2} - \frac{y}{L \sin \alpha} \right) \quad (5.23)$$

$$\frac{3}{16N^4} \left( 1 + \frac{\tan^2(N/4)}{3} - \frac{\tan(N/4)}{(N/4)} \right) f^2 - \frac{4\pi^2}{(N^2 - 4\pi^2)^2} f + \frac{N^2}{12(L \sin \alpha / w_b)^2} - \frac{N^2 \pi^2 (N^2 - 8\pi^2)}{4(N^2 - 4\pi^2)^2} = 0 \quad (5.24)$$

where  $I$  is the quadratic moment of the beam and  $N = \sqrt{\mu(2L)^2/(EI)}$  with  $\mu$  the axial force. The solution is given by a numerical method.

## Chapter 5. Enhancement of the mechanisms and contribution of 3D printing of composites

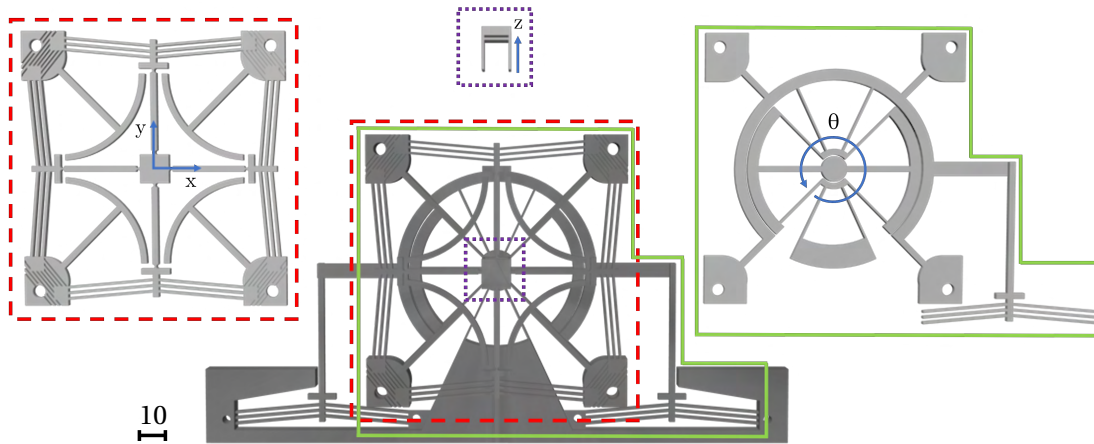


Figure 5.24 – Structure of the 3D-printed monolithic  $XYZ\theta$  positioning system (unit: mm). The movements allowed per component are indicated by the arrows.

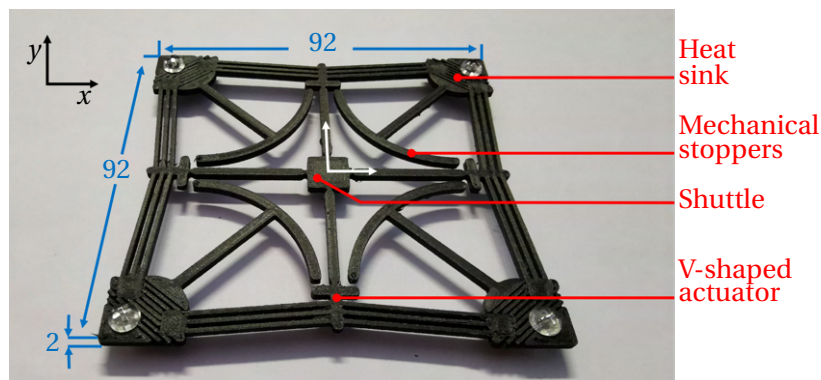


Figure 5.25 – 3D-printed monolithic compliant mechanism for XY linear guiding (unit: mm).

### Compliant mechanism for rotational guiding

The achievement of a pure and large rotational motion with flexible mechanisms is less trivial. Among the solutions presented in the literature, the flexible butterfly pivot was chosen. This choice was made due to the amplitude of movement allowed by this type of joint, the optimisation of which can lead to angles close to  $\theta = \pi/2$ , and the small parasitic shift of the centre of rotation.

This joint was described by Henein et al. [81] as a series connection of four RCC (Remote Center of Compliance) pivots with two beams, shown in Fig. 5.27. The four pivots have the particularity of having the same centre of rotation. The performance described above is due to this high degree of symmetry.

### Angular stiffness and admissible angular stroke

The calculation of the angular stiffness of an RCC connection is defined by the ratio between

## 5.2. Fully 3D printed module with integrated actuation system

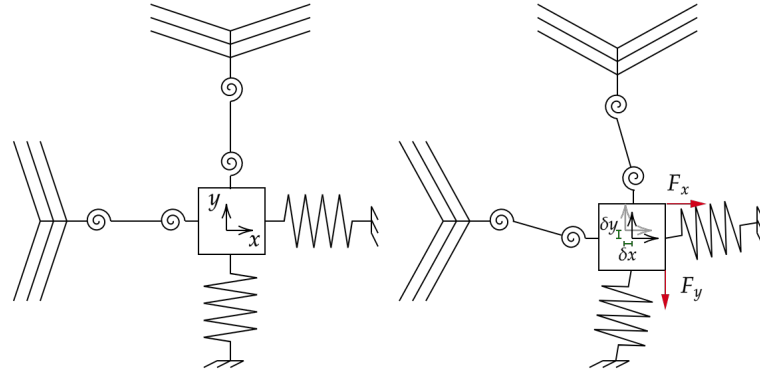


Figure 5.26 – Operational principle of the linear compliant mechanism for two axes translational motions.

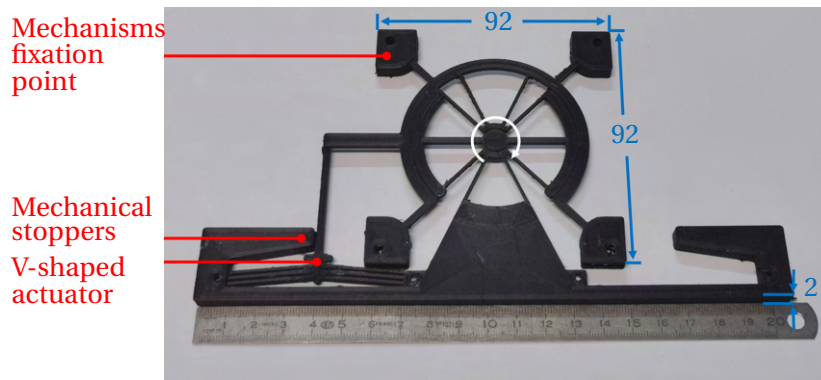


Figure 5.27 – 3D-printed monolithic compliant mechanism for  $\theta$  rotational guiding (unit: mm).

the moment applied to the joint  $M$  and the resulting angular motion  $\theta$ . According to [82], this stiffness can be calculated according to the following equation:

$$K_{\theta} = \frac{M}{\theta} = \frac{8EI}{l} \left( 1 + \frac{3p}{l} + \frac{3p^2}{l^2} \right) \quad (5.25)$$

With  $p$  and  $l$  the geometrical distance parameters shown in Fig. 5.28. The applied moment generates mechanical stresses in the beams with a maximum value at the central anchoring point. The maximum admissible angle stroke can be derived according to the admissible stress  $\sigma_{adm}$  [82]:

$$\theta_{adm} = \frac{\sigma_{adm} l^2}{Ew(2l + 3p)} \quad (5.26)$$

with  $w$  the thickness of the beam. A version with a reinforced structure against out of plane motion, inspired by previous work [195], should be considered if there is a need to increase

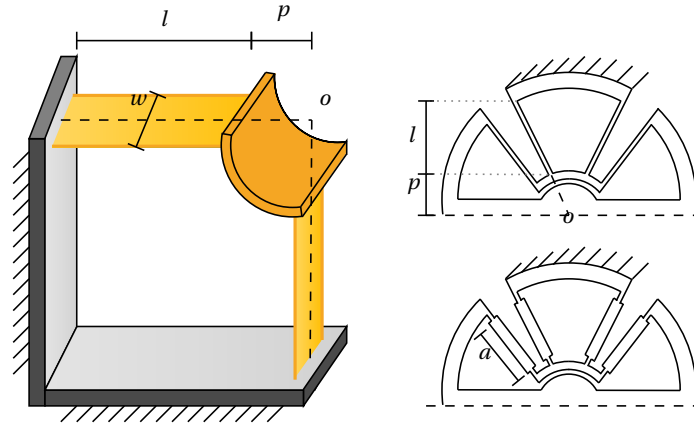


Figure 5.28 – Schematic of a two-blade RCC pivot and its integration into a half-pin (symmetrical on both sides of the axis)

transverse stiffness. The stiffness  $K_{\theta|R}$  and the angular deflection  $\theta_{adm|R}$  are then written:

$$K_{\theta|R} = EI \frac{a^2 + al + 4(l^2 + 3lw + 3w^2)}{(l-a)(a^2 + al + l^2)} \quad (5.27)$$

$$\theta_{adm|R} = \frac{4\sigma_{adm}}{Ew} \frac{(l-a)(a^2 + al + l^2)}{a^2 + al + 2l(2l + 3w)} \quad (5.28)$$

with  $a$  the length of the reinforcing element, as shown in Fig. 5.28.

### Actuation of the Butterfly joint

When sizing the actuator, two elements must be taken into account. The force to be produced and the displacement. In order to limit the size of the structure, the constraint was set to use an actuator identical to those used for the linear guide. This constraint allows a dimensioning with equivalent stiffness. In other words, the sizing is done in such a way that the stiffness of the butterfly link is equal to that of a V-shaped actuator at rest [86], which means that the equations are solved according to whether the joint is reinforced or not:

$$K_{\theta} = K_{\theta|R} = K_a = \frac{2nE(12I \cos^2 \theta + A_b L^2 \sin^2 \theta)}{L^3} \quad (5.29)$$

Assuming that the arc  $\lambda$  produced by the force  $F$  can be approximated by a linear motion because of the small angles,  $\lambda = \Delta x$ , it is then possible to express the achievable  $\theta_{\max}$  as

$$\theta_{\max} = \text{atan} \left( \frac{\lambda}{l+p+d} \right) \simeq \frac{\lambda}{l+p+d} \quad (5.30)$$

where  $d$  is the distance between  $l$  and the anchor on the actuator as shown in Fig. 5.29. In order to allow control of the rotation in both directions, the choice was made to stack two

## 5.2. Fully 3D printed module with integrated actuation system

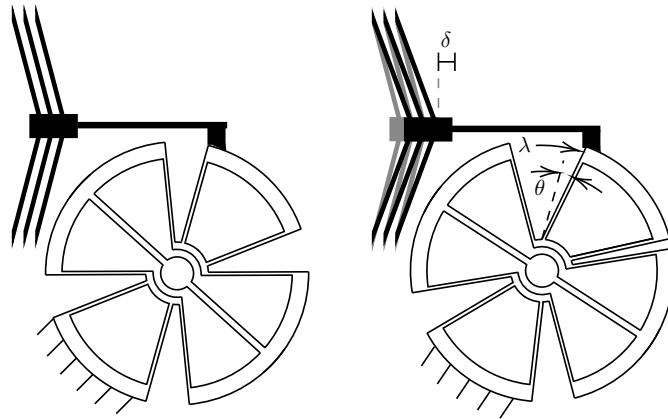


Figure 5.29 – Schematic of a two-blade RCC pivot and its integration into a half-pin (symmetrical on both sides of the axis)

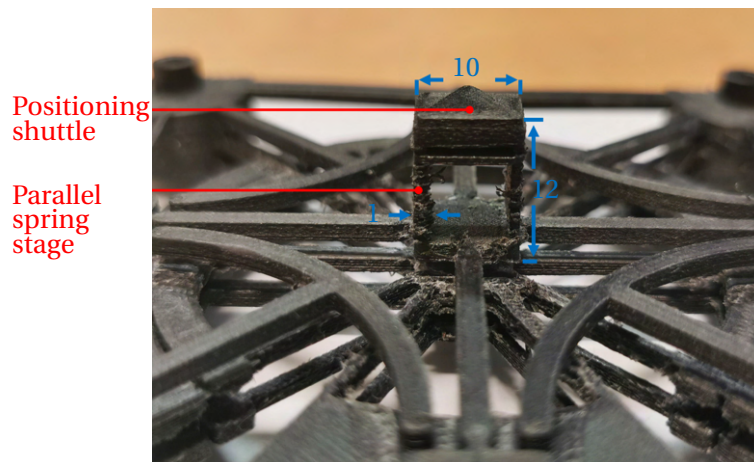


Figure 5.30 – 3D-printed monolithic Z linear guiding (unit: mm).

butterfly joints on top of each other, with an offset by an angle  $\beta = \pi/2$ . Each of these joints was operated by an independent actuator.

### Implementation of a motion along Z

The addition of the Z-translation was achieved by adding a variant of a thin parallel spring stage, as shown in Fig. 5.30. This mechanism was designed to rely solely on the principle of thermal expansion due to the passage of an electric current. On the same principle as the thermal actuator used, following the application of a current, thermal expansion due to the Joule effect will allow the central shuttle to move along the Z-axis.

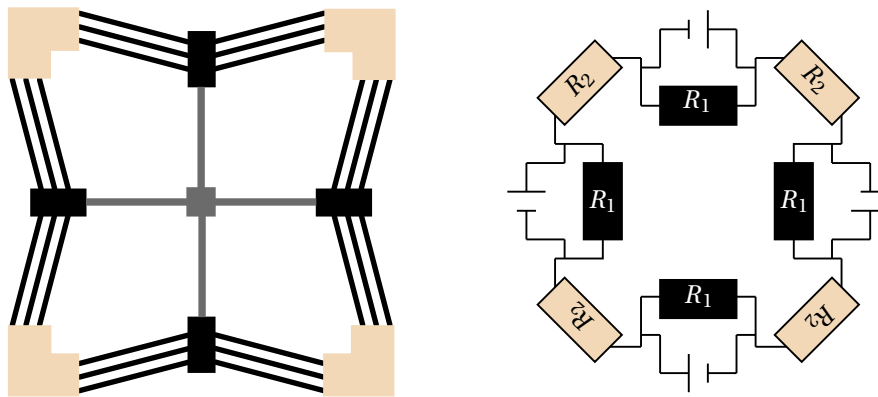


Figure 5.31 – Electrical representation based on a resistor set equivalent to the monolithic positioning system.

### 5.2.3 Voltage distribution in the monolithic in the XY compliant mechanism

In order to produce the 2D positioning system, the insulation of the part between the different actuators must be done. The first approach is only relevant for certain category of 3D printers, able to extrude different materials during the same printing process. This option offers the opportunity to print the entire platform as a single rigid piece by connecting the actuators, printed in carbon PLA, with an electrically insulating polymer, as shown in Fig. 5.32a.

The main contribution is done for single extruder printers, in order to make it compatible with the largest number of printers, the phenomena of electrical and thermal conduction in the design have to be considered, as shown in Fig. 5.32d. The first step is to model the mechanism as a series of resistors. A perfect electrical insulator has infinite resistance, which can be expressed in the design, according to Fig. 5.31, as  $R_2 \gg R_1$ . In order to increase the resistance  $R$ , the length  $l$  and resistivity  $\rho$  have to be maximised and the cross-section  $s$  has to be minimised, according to the following equation:

$$R = \rho \frac{l}{s} \quad (5.31)$$

Although the material has become conductive due to the carbon, it must be considered that it retains a high electrical resistivity. Then, the conductive properties of the printed material are dependent of the orientation of the neutral fibres, which is defined by the direction of movement of the nozzle. According to [49], a 100% infill pattern with lines was then chosen to maximise the electrical resistivity.

During the design process, the application of a simple pattern allowed the cross-section to be reduced by exploiting the smallest printing parameters allowed by the printer. The pattern to reduce the cross-sectional area was also chosen to exploit the laminar flow cooling properties of the heat sinks and thus avoid heat conduction to the adjacent actuators.

## 5.2. Fully 3D printed module with integrated actuation system

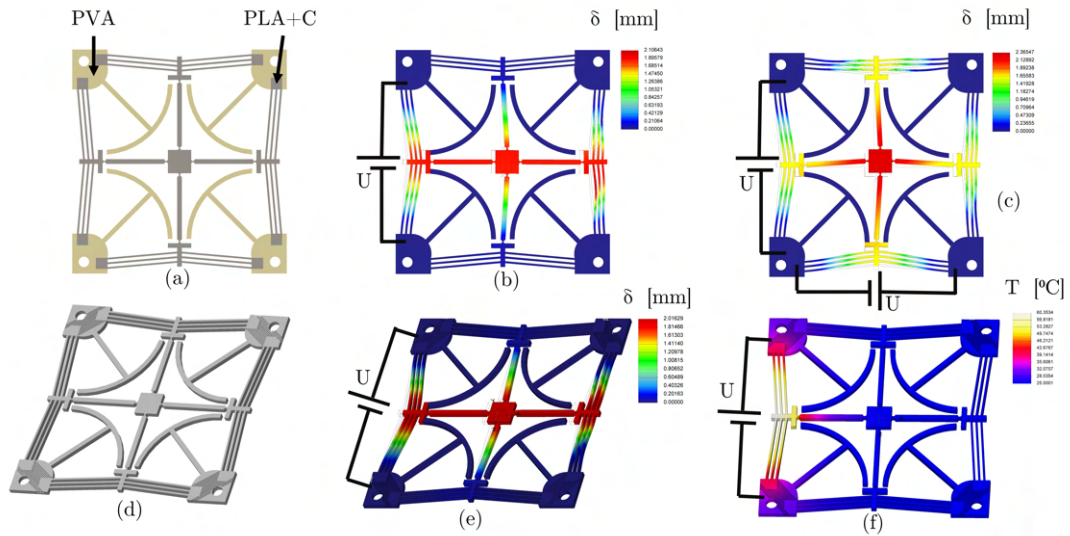


Figure 5.32 – Finite element simulation result for a 2D positioning system. (5.32a) represents the CAD of the positioning system manufactured in bi-material. (5.32b) and (5.32c) illustrate the simulation results obtained by FEA following the actuation of the left actuator and the left and bottom actuators. (5.32d) represents the CAD of the monolithic positioning system. (5.32e) and (5.32f) illustrate the thermomechanical and electrothermal FEA results of the same simulation, following the actuation of the left actuator with the monolithic positioning system. The sub-figures (5.32d)(5.32e)(5.32f) are illustrated in perspective in order to visualise the pattern used to increase the resistance of the sections between actuators.

Hence, from the previously calculated maximum force of the actuator  $F_{max}$ , it is possible to define the maximum deformation and thus the maximum displacement of the positioning system platform. Knowing  $F_{max}$  and  $y_{max}$  of the actuator calculated in the electro-thermo-mechanical model, it is then possible to define the expected motion of the manipulator.

### 5.2.4 Finite element analysis and experimental characterisation

#### Multiphysics Finite Element Analysis

The multiphysics numerical simulation was performed with the ANSYS solver implemented in Creo Parametric 6.0. The analyses were conducted by coupling the electrical, thermal and mechanical fields. The geometrical parameters used for the XY compliant mechanism are shown in Tab. 5.2. The properties of the material used in the simulations are derived from an experimental characterisation phase, i.e. the Young Modulus  $E'$  and the resistance  $R'$ , as explained in Subsection 5.2.4.

The model is set to couple the multiphysics phenomena, while assuming constant materials properties. In other words, the electric current flowing through the actuator will heat the

## Chapter 5. Enhancement of the mechanisms and contribution of 3D printing of composites

Table 5.2 – Design parameters

Material parameters						
E [MPa]	E' [MPa]	R [Ohm]	R' [Ohm]	$\rho$ [Ohm.m]	d [Kg.m <sup>-3</sup> ]	k [Wm <sup>-1</sup> K <sup>-1</sup> ]
3300	3140	800-1200	900	0.06	1150	0.366
Geometric parameters						
L [mm]	$\alpha$	L <sub>0</sub> [mm]	t <sub>s</sub> = t <sub>b</sub> [mm]	w <sub>s</sub> [mm]	w <sub>b</sub> [mm]	L <sub>s</sub> [mm]
30	5	29.89	2	8	0.8	2

material, but the increase in temperature and deformation of the material will not affect the current. Non-linearities will be integrated in future optimisation study.

For the thermoelectric simulation a voltage was applied to the conductive material and thus simulate heat generation by Joule effect. The faces of the actuator are set to a convective heat boundary condition, simulating the air temperature around with the heat flux option.

The simulation results for the positioning system are shown in Fig. 5.32. Simulations have been carried out for a dual-material positioning system and for a single-material positioning system. Simulation results with one or two actuators operating simultaneously are presented Fig. 5.32b and Fig. 5.32c. The feasibility of the single-material mechanism is shown in Fig. 5.32e and Fig. 5.32f corresponding to the same simulation, illustrating mechanical and thermal analysis respectively.

The stroke of the mechanism is almost the same as for the mechanism with insulating material, which proves that the design does not affect the performance. The electro-thermal simulation shows that the temperature in the actuator, through which the current flows, does increase. It also shows that the temperature in the other actuators is not affected by the heating. The actuators can therefore be controlled independently.

The butterfly joint simulations validated the stiffness design model as the actuator achieves the same order of magnitude of displacement as previously with the linear guide for the same temperature, as shown in Fig. 5.33. This performance is slightly lower for the monolithic mechanism, as shown in Fig. 5.34. The result for a coupled actuation at a temperature of 40°C is a displacement of 2.03mm in X, 1.97mm in Y, 1.2mm in Z and a rotation of 3.8°. For a maximum temperature of 58°C, the maximum rotation is 5.85° for one butterfly joint and thus 11.7° for two. This movement can be coupled with displacements of 4.1mm along X and Y and 2mm along Z. According to these results, the platform moves in a simulated space of 105.6mm<sup>3</sup>.

### Experimental characterisation of the material

The material used for these experiments is Original Carbon Fiber PLA (Proto Pasta). It was printed with an Ultimaker S3 at an extrusion temperature of 240°C degrees, at a speed of 30mm/s on a bed heated to 60°C.

## 5.2. Fully 3D printed module with integrated actuation system

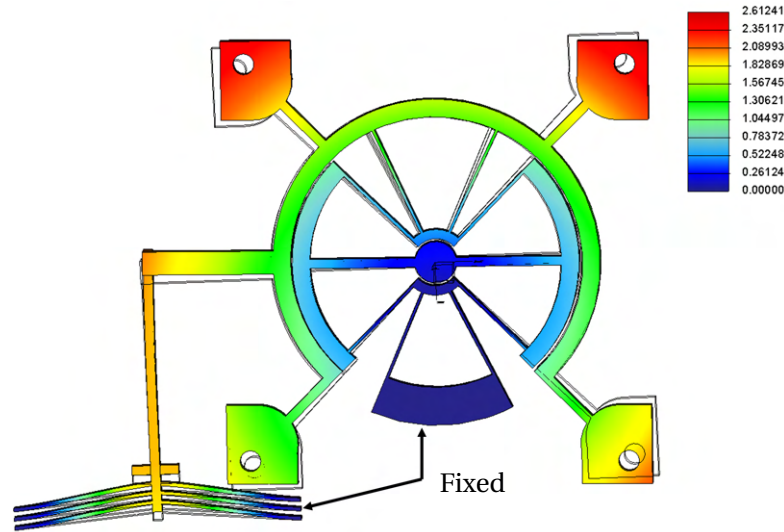


Figure 5.33 – Finite element simulation result of the rotational guiding system (displacement in mm).

Resistance  $R'$  was measured with an ohmmeter. The sample to be measured was placed between the probes of the ohmmeter. The resistivity  $\rho$  was then calculated according to Eq. (5.31). Electrical heating performance of the sample was determined based on surface temperature with various applied voltages while using a DC power supply. The range of applied voltage was from 20V to 50V with 5V intervals. As the contact could not be made by soldering, it was made by means of a screw-nut embedding. A K-type thermocouple was used to measure the surface temperature after applying different voltages.

The mechanical characterisation of the material was carried out with the FK50 force sensor (Sauter) and the LK-H152 laser-based displacement sensor (Keyence), as detailed in [11]. A beam was printed with carbon-PLA and the Young's modulus  $E'$  was characterised using Euler Bernoulli's relationship between applied force  $F$  and measured displacement  $\delta$ :

$$E' = \frac{FL^3}{3\delta I} \quad (5.32)$$

where  $I$  the quadratic moment of the cross section and  $L$  the length of the beam. The characterized Young's modulus is 3140MPa, which is consistent with some earlier characterisation of the material [55].

### Experimental characterisation of the V-shaped electrothermal actuator

The behaviour of the actuator was characterised experimentally by means of the experimental set-up shown in Fig. 5.35. The shuttle displacement was measured for different voltage values ranging from 10 to 50V in 5V steps and with a return to room temperature in between. The experimental results are presented in Fig. 5.36. The experimentally measured values are in good accordance with the results of previous models.

**Chapter 5. Enhancement of the mechanisms and contribution of 3D printing of composites**

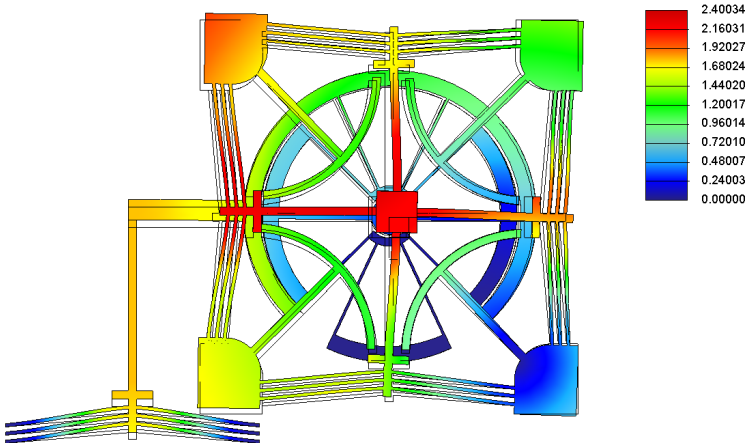


Figure 5.34 – Finite element simulation result of the monolithic XYZθ system (displacement in mm).

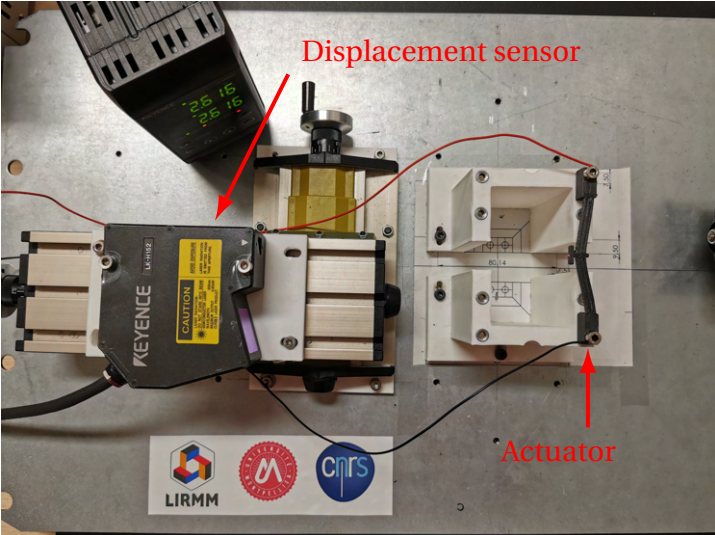


Figure 5.35 – Experimental set-up for the characterisation of the electro-thermal actuator

At 55V, the temperature of the measured actuator was 64°C, i.e. beyond the glass transition phase indicated by the manufacturer. It is noted that after reaching this temperature, the actuator does not recover its initial configuration. The displacement sensor indicates a position of 0.13mm despite the mechanism returning to room temperature.

**Experimental characterisation of the positioning system**

The performance of the positioning system has been analysed using the same equipment as before, as shown in Fig 5.37. After applying a voltage to one of the actuators, the displacement of the central shuttle was measured using the displacement sensor. By driving an actuator with a conservative voltage of 50V, an average motion range of 3.34mm is achieved, as shown in Fig. 5.38. This also corresponds to a total motion range of 6.68 mm along each axis. For a

## 5.2. Fully 3D printed module with integrated actuation system

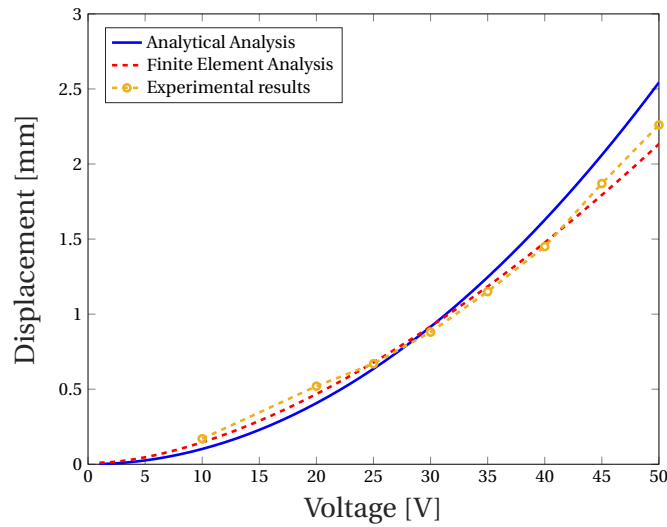


Figure 5.36 – Displacement obtained for the electrothermal actuator as a function of the input voltage.

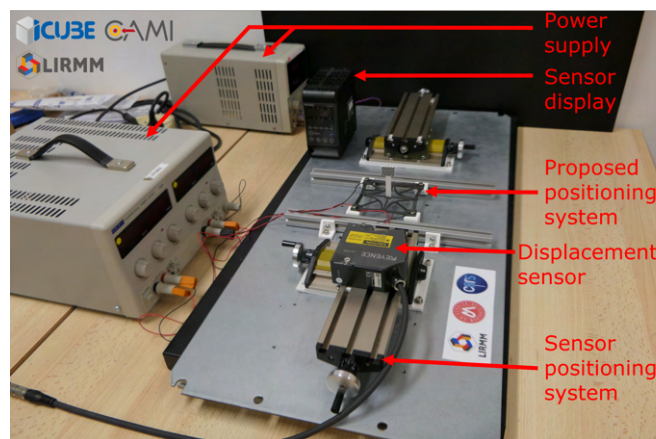


Figure 5.37 – Experimental setup of the XY positioning system.

given desired position, the manipulator was operated 21 times with a open loop voltage of 40V. The average displacement measured was 2.17mm and the standard deviation was 0.19mm. An error of 17% is found between the actuator estimated and measured values. However, an error of only 4% is found between the measured and estimated force-displacement relationship with respect to the opposite actuator. In line with the fact that these are preliminary results obtained with an open-loop control and with a 3D printed composite material, thus particularly non-linear, the error obtained shows that the order of magnitude of the model estimates is satisfying. As presented in Tab. 5.3 and in Tab. 5.4, given the millimetre range of motion achieved, the objective of designing a compact and low-cost positioning system is successfully achieved. The presence of nonlinear effect requires the implementation of control strategy in order to achieve a precision positioning. The precepts are introduced in the following section.

**Chapter 5. Enhancement of the mechanisms and contribution of 3D printing of composites**

---

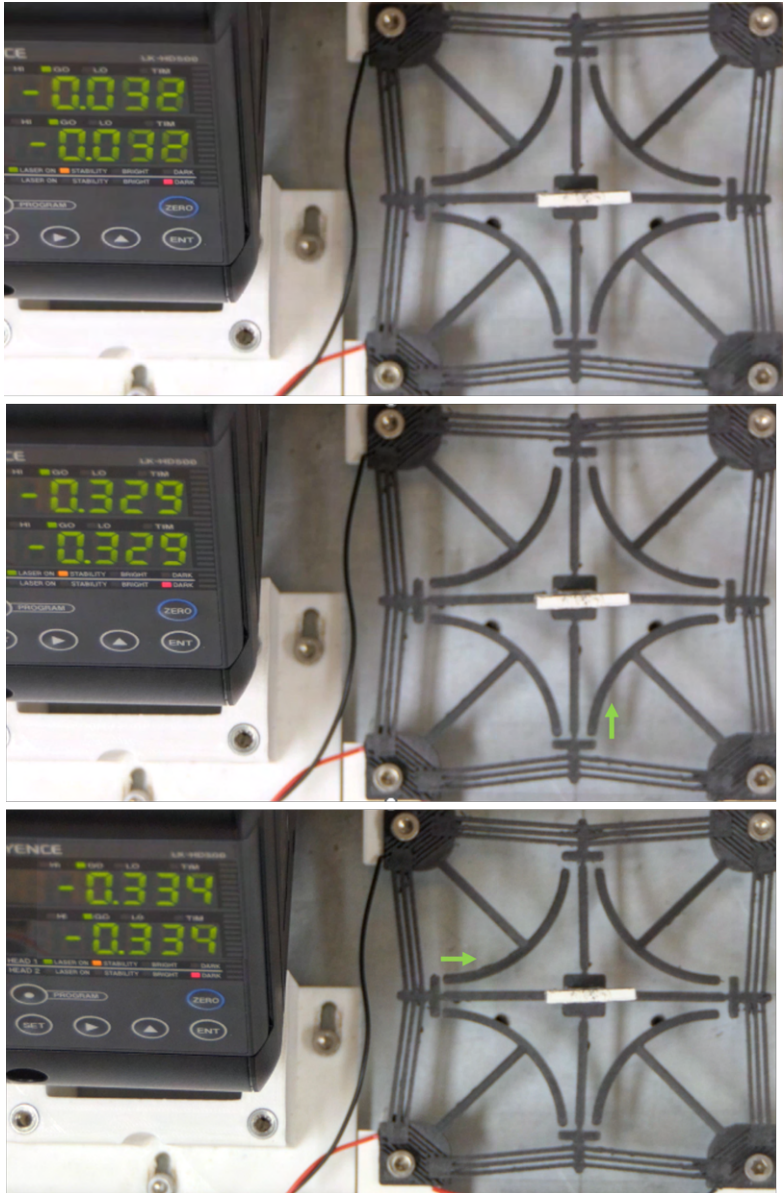


Figure 5.38 – Experimental characterisation of the XY positioning system. The numbers on the dials of the Keyence sensor show the displacement in centimetres. The top image (a.) represents the initial state and the middle (b.) and bottom (c.) images show the amount of displacement in the direction of the arrows in response to an actuation.

Carbon composite is still a fairly demanding material and requires a number of fine tunings of the printer to achieve a structure as complex as the one presented in Fig. 5.39. Despite this, the individual performance of the actuators within the platform allows linear displacements of up to 3.8 mm and a Z-displacement of 1.9 mm, i.e. a real handling space of 86mm, in agreement with the simulation results. However, these performances tend to decrease during coupling due to some plane contacts or surface alignment. These preliminary results are

## 5.2. Fully 3D printed module with integrated actuation system

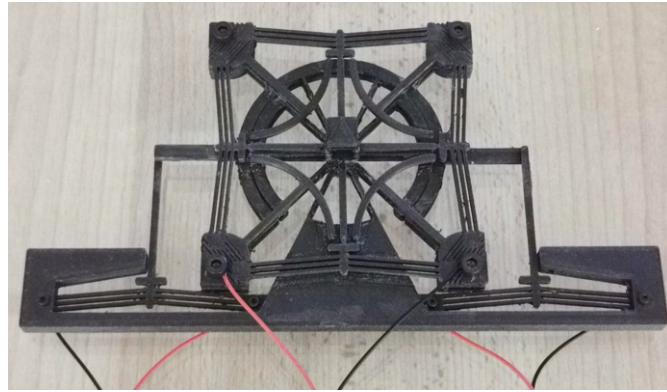


Figure 5.39 – 3D printed monolithic XYZθ positioning system

Table 5.3 – Performance comparisons between the proposed XY positioning system and previous reported parallel stages (\*FEA results).

Ref	Actuator	Dimension [mm]	Motion range
[64]	piezoelectric	50×50×10	14,32×14,32 [μm]
[217]	electromagnetic	120×120×25	11,75×11,6 [mm]
[230]	<i>theoretic*</i>	300×300×27	5×5 [mm]
[76]	<i>theoretic*</i>	200×200×10	4×4 [mm]
Proposed	electrothermic	92×92×2	3,7×3,7 [mm]

encouraging, but further researches are needed before the control system proposed below can be considered at this time.

### 5.2.5 Control strategy of the actuator

The temperature rise takes much longer than the temperature-position conversion time, which induces a large dead-time  $\tau$ , as shown in Fig. 5.40. The process is modelled by  $\frac{ke^{-\tau s}}{1+Ts}$ , identified from an open loop step response shown in Fig. 5.40. The Broïda method was chosen as the identification method because it is adapted to a stable system with a delay. It consists in observing the response and assimilating it to the response of a first order system (of time constant T), with a delay  $\tau$ . The 28% and 40% ordinate points (giving respectively the times  $t_1$  and  $t_2$ ) allow to calculate T and  $\tau$  by the formulas [18]:

$$\tau = 2,8t_1 - 1,8t_2 \quad (5.33)$$

$$T = 5,5(t_2 - t_1) \quad (5.34)$$

$$k = \frac{\Delta D}{\Delta V} \quad (5.35)$$

## Chapter 5. Enhancement of the mechanisms and contribution of 3D printing of composites

Table 5.4 – Performance comparisons between the proposed XYZ $\theta$  positioning system and previous reported parallel stages (\*estimated).

Ref	Actuator	Dimension [mm]	Motion range [mm]
[79]	piezoelectric	105×105×105	1.5×1.5×1.5 [XYZ]
[194]		200×200×1	0.369×0.369, 1.28° [XY $\theta$ ]
[131]	linear actuator	250×250×(?)*	2.5×2.5, 10° [XY $\theta$ ]
Proposed	electrothermic	206x109x21	3,8×3,8×2, 10.85° [XYZ $\theta$ ]

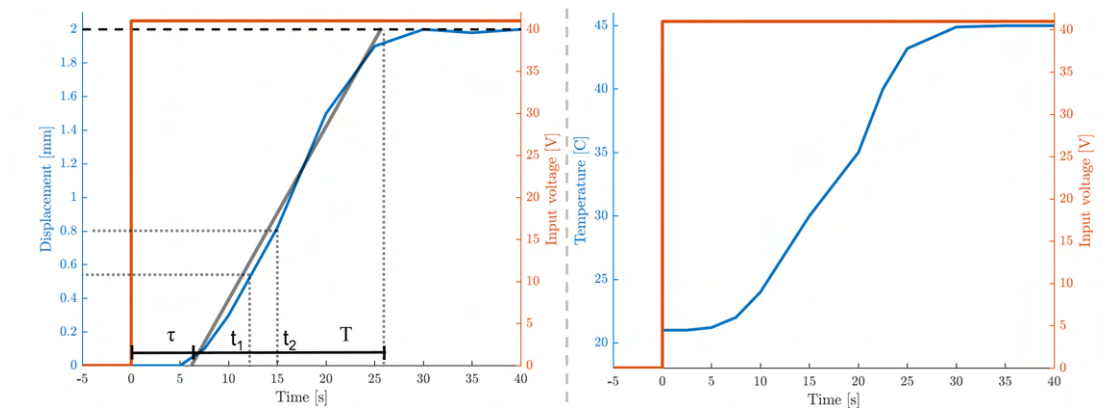


Figure 5.40 – On the left, the step response of the system representing the displacement of the actuator as a function of time following power-up. On the right, the intermediate response of the system where the temperature evolution after power up is represented. The delay is present during the temperature rise of the system.

where  $k$  is the static gain of the system equal to the ratio between the output displacement and the input voltage.

The delay has already been observed in previous research using carbon-doped polymers [231]. By considering the time delay of some composites, it can be supposed that it is related to the quantity and quality of the carbon doping [7]. According to this hypothesis, which should be verified, a high carbon saturation could reduce or even cancel the delay as the behaviour of the composite would tend to approach that of a conducting material.

The use of a PID would be limited since the time delay would enter the loop and considerably decrease the performance of the control. A Smith predictor is a predictive controller designed to control systems with a significant feedback delay and here proposed with a PI controller. The PI controller is therefore set for a process without delay and then a final controller for the process with delay is calculated from the previous one, as shown in Fig. 5.41. After prior identification of the process,  $k' = k$ ,  $\tau' = \tau$  and  $T' = T$  are set to have a process modelled as a

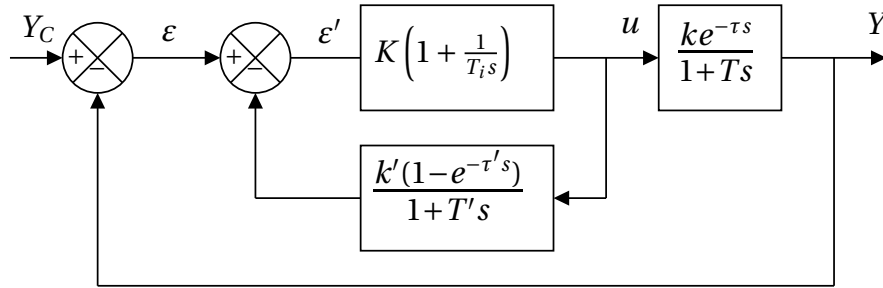


Figure 5.41 – Structure of Smith predictor based on PI control strategy.

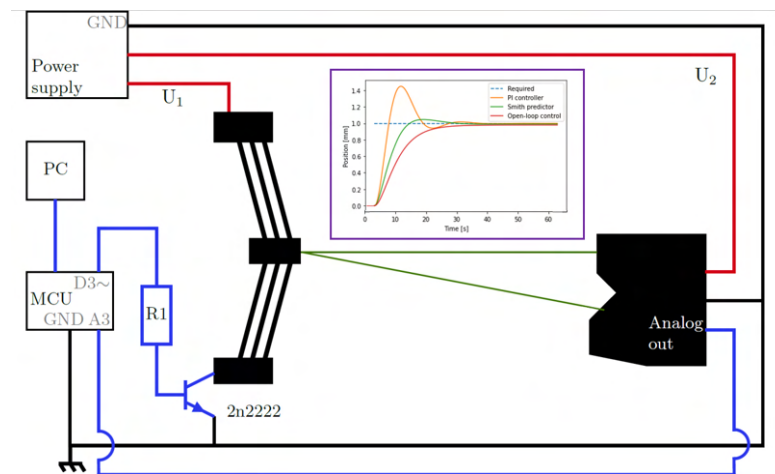


Figure 5.42 – Schematic of the experimental set-up used to validate the actuator control strategy and step response in open-loop, with the PI controller and with the Smith Predictor.

first order system. According to [18], the PI controller was tuned such as  $T_i = T$  and  $K = 0,7 \frac{T}{\tau k}$ . The step response of the system is shown in Fig. 5.40. The validation of this control strategy was done using the set-up illustrated in Fig. 5.42. In view of the preliminary experimental results, this control strategy seems encouraging.

### 5.3 Conclusions

After demonstrating for the classic double preshaped beam the existence of a large number of constraint redundancies using the FACT method, the modelling of a theoretical bistable mechanism with a minimum of constraints was presented and then adapted to meet the constraints of compactness and manufacturability.

The results show the interest of using this *enhanced* mechanism rather than the *classic* version. Indeed, the *enhanced* mechanism has shown improved reliability and repeatability in terms of actuation forces after manufacturing and improved lifetime. This result shows that reducing hyperstaticism allows a better tolerance to fatigue and relaxation phenomena of the material.

## **Chapter 5. Enhancement of the mechanisms and contribution of 3D printing of composites**

---

Therefore the *enhanced* mechanism shows a significant improvement over the *classic* one.

In a second step, the use of doped polymer to design integrated actuators was demonstrated. Here, it was shown that a proof of concept was available to investigate a method of fabricating the model with its actuator assembly. To the best of the author's knowledge and according to the latest reviews of the literature on electroactive polymers [4, 46, 207, 187, 179], this is the first 3D printable electro-thermo-active structure with built-in actuator.

# Conclusion

The work carried out in this thesis is motivated by the design of new robotic architectures to assist the surgeon due to the increasing complexity of MIS procedures. The target application is the subject to strong constraints inherent to the procedures exploiting natural orifices as access. The robot must be extremely compact and able to follow complex trajectories. The approach taken to address these issues has been to move away from traditional design methods and focus on designing an elegant robotic architecture based entirely on compliant mechanisms. In this thesis, the design, modelling, fabrication, and control of a digital snake robot are presented. This robot is based on a tristable module that allows the generation of a discrete and redundant workspace and its control without the use of sensors.

After presenting the background and approaches developed to enable minimally invasive surgical procedures, the interest of hyper-redundant robots and digital robots is introduced. These robots are based on an arrangement of binary actuators to reach precise positions in a discrete working space using simple open-loop control.

The main objective of this research is to propose a new design of snake-like robots allowing deployment in confined spaces, simplified control, and minimal space requirements. The choice of a serial architecture responds to anatomical constraints and multistable mechanisms are an alternative to traditional mechanisms due to downscaling constraints. The design, fabrication, kinematic modelling, and control of this robot represent the core of our contributions.

Our contributions to the design part include the development of a tristable module from a combination of compliant mechanisms by exploiting their stability to maintain a certain configuration. The chosen approach has allowed us to propose a monolithic elementary module that generates 3 stable configurations. The specificity of being able to be manufactured in a monolithic way allows to avoid tedious assembly phases and to avoid precision defects linked to the mechanical play. A study for dimensioning the previous compliant mechanisms was then carried out by finite element simulation in order to validate the dimensions and the choices made. It has also been correlated with an experimental validation.

This module has made it possible to propose a new snake-type robot architecture. Its construction and analysis have highlighted the interest of the design work carried out at the module level.

In addition, we proposed an enhanced design of the bistable mechanism allowing ton in-

## Conclusion

---

crease its lifetime and mechanical performance. This solution was tested and validated in 3D printing, where it demonstrated the possibility of obtaining a better longevity and manufacturability of the mechanisms.

Thanks to 3D printing of composite materials, we also have demonstrated the feasibility of manufacturing monolithic architectures integrating both mechanisms and actuators. This approach has allowed us to propose a particularly compact XYZ $\Theta$  positioning system that can be directly used after being printed. This approach also allowed us to validate a hypothesis of replacement of the actuators within the mother structure of this thesis and to remove from the assembly phase its most constraining step.

The kinematic modelling of the direct and inverse robot allowed us to calculate and define the reachable positions of our robot. A geometric method is used to derive the inverse kinematic model. This approach reduced the usual difficulty encountered due to hyper-redundancy. The first open-loop control tests have been carried out with the proposed robotic architecture and give a glimpse of the capabilities of this robot.

A preliminary control strategy was also investigated to control the thermal actuators of the positioning platform and showed promising results.

From an application point of view, this work provides several interesting results. The use of a system that is fully and easily controllable by the surgeon facilitates its acceptance and also reduces the learning time. In addition, its ability to maintain a configuration could relieve the surgeon of the task of performing the operation. It could be much less traumatic for the tissues of the oesophagus. The memorization of the previous configurations by the modules makes it possible to consider the automation of the removal without having to exert a traction.

Finally, this work sets the path of designing multistable snake like robots for surgical robotics with a proof of concept giving promising results. Different aspects of this work need to be pursued, but in the end, all aspects of robotics will have been addressed to provide an elegant and functional solution.

## 6 Perspectives

At the end of these three years of research, many aspects remain to be explored based on this work. In this chapter, three of the major aspects for which work has already been initiated will be detailed. The choice has been made to present them in the order of research progress. In the first section, miniaturisation by additive manufacturing will be discussed. In the next section, the distribution of the control system within each module and the means of inter-module communication will be addressed. In a final section, the prospects of extension to a second bending plane and the development of a functional head module will be considered.

### 6.1 Explore areas for improvement in 3D printing

The manufacture of the 4-module prototype and experimental characterisation validate the theoretical considerations and the viability of this approach. Although this prototype has allowed the first tests to be carried out, it is still too large to be used even for tests on phantoms<sup>1</sup> by surgeons. The challenge is therefore to build a miniaturised and monolithic version of the module.

#### 6.1.1 Stereolithography (SLA): a miniaturisation approach

During the successive manufacturing phases, it was apparent that additive manufacturing by fused deposition would not allow the fabrication of a module small enough to be used in the medical context. The resolution of the machine is no longer sufficient to allow further miniaturisation. Other manufacturing processes provide better resolution or use materials whose behaviour is more reproducible, e.g. the stereolithographic printing. This approach allows for much greater precision because it depends on the size of a pixel.

However one of the encountered issues was the lack of prior characterisation of the resins used. In addition, SLA printing is based on the use of photomasks, unlike G-code for FDM. A

---

<sup>1</sup>Test phantoms are devices that can be used to test and evaluate the performance of a device, such as the proposed robot, while simulating human anatomy.

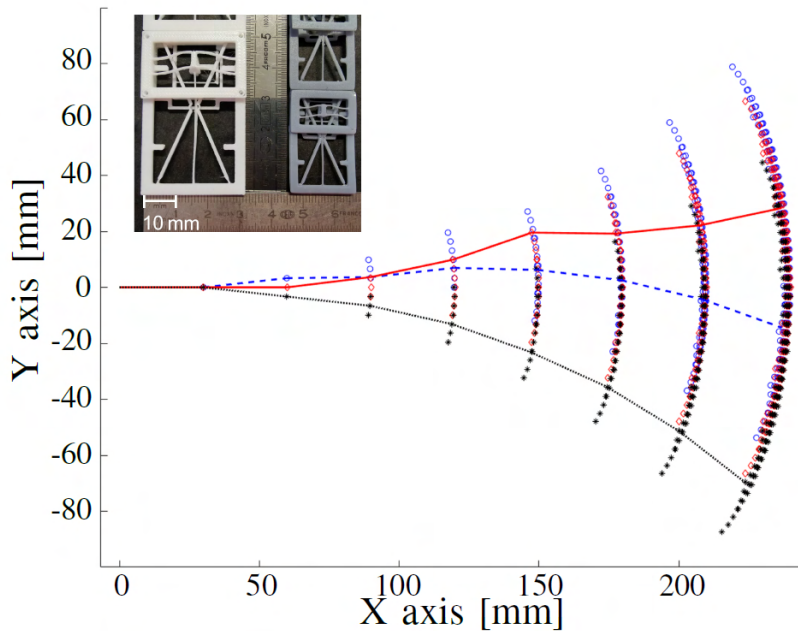


Figure 6.1 – Photograph of miniaturised modules obtained by stereolithography (in grey) and representation of the achievable workspace, and some configurations (solid, dashed and dotted lines), with a prototype of equivalent length but composed of the miniaturised module.

trial-and-error test phase and refinement of the printing parameters was therefore carried out, following which scaled-down versions of the mechanism were printed.

The SLA printed modules are 33% smaller than the original prototype modules, as shown in Fig. 6.1. They are then characterised in the same way as the prototype mechanisms, and the maximum angle obtained is  $\pm 6.3^\circ$ . For a prototype of the same length as the one studied in this work, but composed of miniaturised modules, the working space becomes much larger, as shown in Fig. 6.1. In terms of size and performance, this result allows the proposed architecture to become clinically acceptable, as shown in Fig. 6.2. With this manufacturing approach, it is possible to consider reducing the size of the module by a further 10%, which would make it viable for the vast majority of anatomical curvatures.

## 6.2 Implementation of communication protocols for robot control

One of the limitations of the first version of the prototype is the number of electrical wires. In the first version, all actuators had a common ground and an individual power wire. This meant that each additional module was accompanied by two additional cables. In addition, the presence of all these wires added weight and could limit certain module triggers, altering the desired configuration of the robot.

The first solution considered, before incorporating the actuators, is to use electronic circuit in

## 6.2. Implementation of communication protocols for robot control

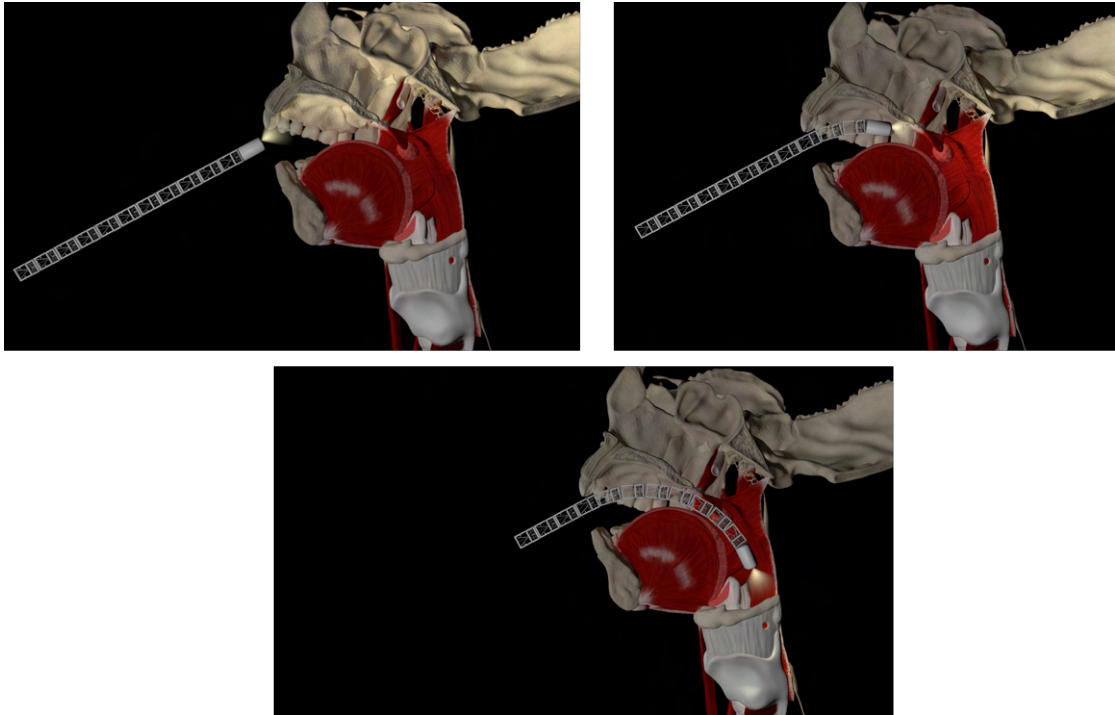


Figure 6.2 – Scale illustration with realistic rendering for the mechanism printed in SLA.

each module. The modular approach is extended to control and to reduce the number and length of wires running through the architecture. Each electronic board contains the components needed to operate the actuators and a microprocessor to manage the communication protocol.

### 6.2.1 Communication protocol and evaluation

In a test version, the module is equipped with an Arduino mini Pro. This minimalist version of the widely marketed board allowed the manufacturing process to be dispensed with, as it directly embedded the outputs for sending the PWM (pulse width modulation) control to activate the SMA wires. In addition, it allows the use of the I<sup>2</sup>C (Inter-Integrated Circuit) communication protocol.

The robot is based on a modular architecture, where each module must be able to communicate with the others. Two protocols were initially chosen, SPI and I<sup>2</sup>C, but for dimensional constraints the I<sup>2</sup>C protocol is chosen. The I<sup>2</sup>C protocol requires only four wires for the entire structure, regardless of the number of modules. This system uses two communication cables, SDA and SCL, the first corresponding to the data line and the second to the clock and synchronisation line. The other two cables are for power and ground.

This protocol also makes it possible to connect several masters and slaves to the communication bus, and to promote a slave to master status and vice versa. This protocol is not the

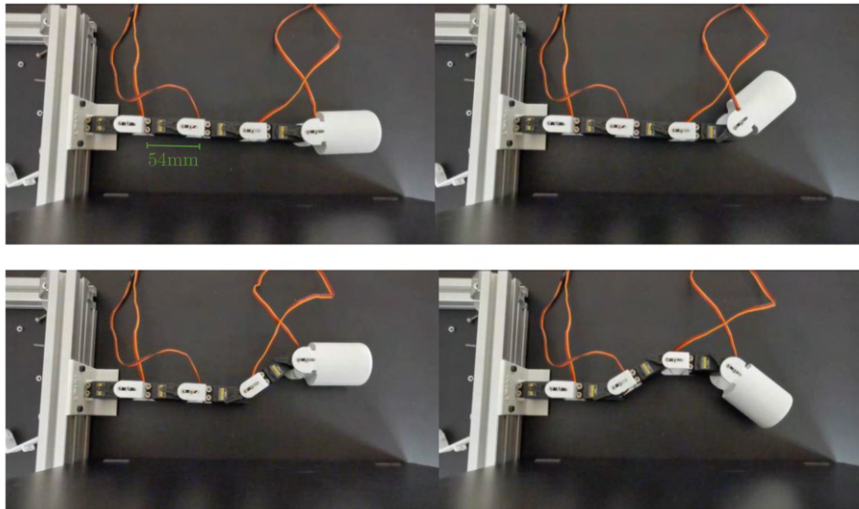


Figure 6.3 – Illustration of the movement performed by the robot following the sending of information from a master board to slave boards controlling the motors.

fastest, but it is more than sufficient for the frequency of operation of our robot.

Two approaches were explored to make the modules communicate with each other. The first approach is serial communication. This choice is based on the desire to implement a Follow-The-Leader architecture. To do this, information is sent to the remote module, i.e. the one that is furthest from the base. With each new information sent, the information of the  $n$  module changes, and its previous information is transmitted to the  $n - 1$  module, and so on. The advantage of this communication is that, when the robot has to be retracted, all configurations are stored in all modules.

A more advanced version was also implemented to centralise the information in order to keep a global view of the robot configuration. This version was tested on a motorised robot, as shown in the Fig. 6.3, due to the inaccessibility of components during/after the Covid-19 crisis.

### 6.2.2 Implementation of PCBs

In order to reduce the assembly phase to a minimum, a part was added to the mechanism to hold and stabilise the PCB. The constraint of having the actuators on the back of the PCB means that screws or other penetrating elements cannot be used. Furthermore, in order to remain consistent with the rest of the module, a compression spring system is designed to constrain the board as shown in Fig. 6.4.

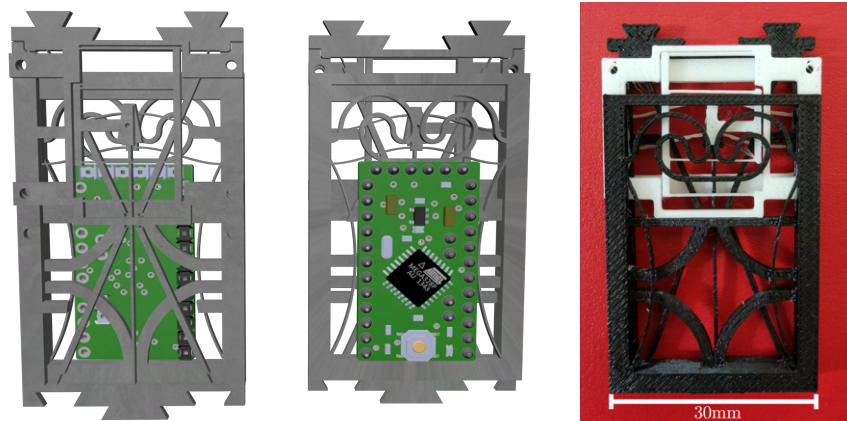


Figure 6.4 – Realistic rendering of the holding system of the electronic board inside the module and the 3D printed version.

## 6.3 Considerations for improving the robot architecture

### 6.3.1 Extension to a second bending plane

Among the axes of perspective, it is possible to consider the design of an architecture allowing two planes of bending and thus generate a discrete workspace in 3 dimensions. One possible approach can be directly inspired by the one developed in this work as shown in Fig. 6.5. The modelling is then similar to the one already carried out since it consists in alternating one module out of two by a  $\pi/2$  rotation about the robot axis. Under these conditions, the extension can be considered now.

The other option studied lies in the dimensioning of a second module responsible for the rotation. It would then be necessary to dimension a multistable mechanism like the one designed in this study, but this time allowing to obtain a rotation. This approach is probably less cumbersome than the previous one, but poses a problem in terms of the achievable angle. Obtaining an angle of at least  $\pi/2$  from the multistable mechanism is not trivial.

Now that the proof of concept has been completed, another possibility would be to reconsider some elements of the prototype and redesign them to incorporate the second bending plane through a pentastable mechanism.

### 6.3.2 The last but not least module

Behind the principle of this modular architecture, there is still one module that has not yet been explored in concrete terms, namely the endoscope head module. In a longer term vision, it is quite possible to consider the design of a fully equipped head module that would be attached to this architecture.

Since there is a power supply and a control protocol, one could assume that the head could

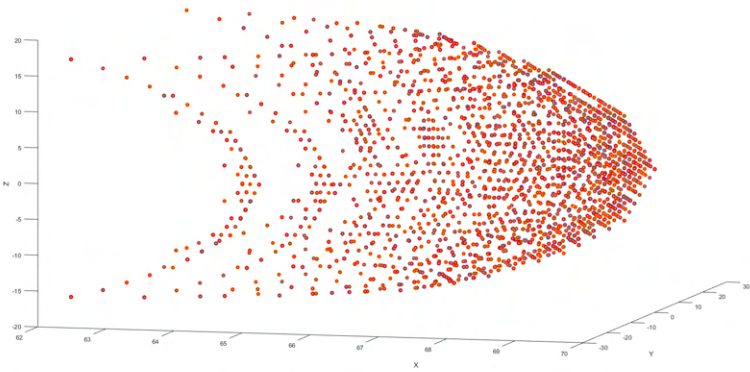


Figure 6.5 – Simulated workspace of the ternary robot with 8 modules alternating successively by an angle of  $\pi/2$ . The positions in the X, Y and Z axes are given in millimetres.

simply be attached at the beginning of the procedure, and could be specific to that procedure.

## 7 List of publications

### **International peer-reviewed journal:**

B. Calmé, L. Rubbert and Y. Haddab, "Towards a Discrete Snake-Like Robot Based on SMA-Actuated Tristable Modules for Follow the Leader Control Strategy," in IEEE Robotics and Automation Letters, vol. 8, no. 1, pp. 384-391, Jan. 2023, doi: 10.1109/LRA.2022.3224659.

### **International peer-reviewed conferences and publication of proceedings:**

B. Calmé, L. Rubbert and Y. Haddab, "Towards a Discrete Snake-Like Robot Based on SMA-Actuated Tristable Modules for Follow the Leader Control Strategy," - IEEE International Conference on Robotics and Automation, 2023 [Accepted]

B. Calmé, L. Rubbert and Y. Haddab, "Towards a compact and low-cost mesoscopic XY positioning system using 3D printing of conductive polymers," 2022 International Conference on Manipulation, Automation and Robotics at Small Scales (MARSS), Toronto, ON, Canada, 2022, pp. 1-6, doi: 10.1109/MARSS55884.2022.9870471.



# A Stiffness and compliance matrix analysis

In the previous section, the analysis was done by considering the mechanism as an assembly of two sub-entities, which consisted of two parallel spring stage. Knowing that according to the theory of elasticity, the twist and the wrench are related in terms of deformation and loading by the following relations.

$$\mathcal{F} = [C]\mathcal{W}, \quad \mathcal{W} = [K]\mathcal{F}, \quad \text{with} \quad [C] = [K]^{-1} \quad (\text{A.1})$$

The goal here is to confirm the previously calculated value through a mobility matrix analysis and to compare the stiffnesses and compliances between the two studied mechanisms. It is possible to obtain the compliance matrix of a beam directly from the Timoshenko beam theory, in the XYZ coordinate system used in the pictures, as follows:

$$C_i = \begin{bmatrix} 0 & 0 & 0 & l/GJ & 0 & 0 \\ 0 & 0 & -l^2/2EI_y & 0 & l/EI_y & 0 \\ 0 & l^2/2EI_z & 0 & 0 & 0 & l/EI_z \\ l/EA & 0 & 0 & 0 & 0 & 0 \\ 0 & l^3/3EI_z & 0 & 0 & 0 & l^2/2EI_z \\ 0 & 0 & l^3/3EI_y & 0 & -l^2/2EI_y & 0 \end{bmatrix} \quad (\text{A.2})$$

This compliance matrix is derived at the free end of the blade for practical purposes. In

## Appendix A. Stiffness and compliance matrix analysis

accordance with Eq. A.1 it is possible to obtain the stiffness matrix from Eq. A.2 as follows:

$$K_i = \frac{EI_z}{l} \begin{bmatrix} 0 & 0 & 0 & 12/t_i^2 & 0 & 0 \\ 0 & 0 & -6/l & 0 & 12/l^2 & 0 \\ 0 & 6/l\psi & 0 & 0 & 0 & 12/l^2\psi \\ \Lambda & 0 & 0 & 0 & 0 & 0 \\ 0 & 4/\psi & 0 & 0 & 0 & 6/l\psi \\ 0 & 0 & 4 & 0 & -6/l & 0 \end{bmatrix} \quad (\text{A.3})$$

with  $\Lambda = (JG)/(I_z E) \approx 4/(2(1-\nu))$  and where  $\nu$  is the Poisson's ratio and  $\psi = t^2/w^2$ . This matrix corresponds to the one found by [198] and echoes the one used by [78], with the difference that  $\mathcal{W}$  is defined here according to the 3 force vectors then by the three moment vectors.

Two tests were carried out during the experimentation phase to compare the performance of the *enhanced* mechanism, shown in Fig 5.7, with the classic one. The nature of these tests will be detailed in Section 5.1.5, but one set of parameter values needs to be used to validate the analytical approach. As described in Table 5.21, the mechanisms used in these tests had different design and manufacturing parameters. Arbitrarily the parameter values from Test 1 will be used for the demonstration, knowing that the same results can be obtained with the parameter values from Test 2.

$$C_t = \begin{bmatrix} 0 & 0 & 0 & 0.551 & 0 & 0 \\ 0 & 0 & -0.143 & 0 & 0.003 & 0 \\ 0 & 3.562 & 0 & 0 & 0 & 0.097 \\ 0.008 & 0 & 0 & 0 & 0 & 0 \\ 0 & \mathbf{174.534} & 0 & 0 & 0 & 3.5612 \\ 0 & 0 & 6.981 & 0 & -0.143 & 0 \end{bmatrix} \quad (\text{A.4})$$

$$C_T = \begin{bmatrix} 0 & 0 & 0 & 0.276 & 0 & 0 \\ 0 & 0 & -0.113 & 0 & 0.003 & 0 \\ 0 & 0.139 & 0 & 0 & 0 & 0.049 \\ 0.006 & 0 & 0 & 0 & 0 & 0 \\ 0 & \mathbf{87.267} & 0 & 0 & 0 & 1.781 \\ 0 & 0 & 5.54 & 0 & -0.113 & 0 \end{bmatrix} \quad (\text{A.5})$$

$$K_t = 1 \times 10^3 \begin{bmatrix} 0 & 0 & 0 & 0.12 & 0 & 0 \\ 0 & 0 & 0 & 0 & 0 & 0 \\ 0 & 0.021 & 0 & 0 & 0 & 0 \\ 0.015 & 0 & 0 & 0 & 0 & 0 \\ 0 & 1.03 & 0 & 0 & 0 & 0.02 \\ 0 & 0 & 0.04 & 0 & 0 & 0 \end{bmatrix} \quad (\text{A.6})$$

$$K_T = 1 \times 10^3 \begin{bmatrix} 0 & 0 & 0 & 0.16 & 0 & 0 \\ 0 & 0 & 0 & 0 & 0 & 0 \\ 0 & 0.03 & 0 & 0 & 0 & 0 \\ 0.03 & 0 & 0 & 0 & 0 & 0 \\ 0 & 1.3 & 0 & 0 & 0 & 0.03 \\ 0 & 0 & 0.08 & 0 & 0 & 0 \end{bmatrix} \quad (\text{A.7})$$

The next step is to generalise and focus on the compliance of the whole mechanisms. The transformation matrices used for this are dependent on the space between the beams  $\lambda$  as well as the side of the mechanism along the y-axis of symmetry ( $\Gamma_{left}$   $\Gamma_{right}$ ), and represented as follows:

$$\Gamma_{left} = \begin{bmatrix} 1 & 0 & 0 & 0 & 0 & -\lambda/2 \\ 0 & 1 & 0 & 0 & 0 & 0 \\ 0 & 0 & 1 & \lambda/2 & 0 & 0 \\ 0 & 0 & 0 & 1 & 0 & 0 \\ 0 & 0 & 0 & 0 & 1 & 0 \\ 0 & 0 & 0 & 0 & 0 & 1 \end{bmatrix} \quad \Gamma_{right} = \begin{bmatrix} 1 & 0 & 0 & 0 & 0 & \lambda/2 \\ 0 & 1 & 0 & 0 & 0 & 0 \\ 0 & 0 & 1 & -\lambda/2 & 0 & 0 \\ 0 & 0 & 0 & 1 & 0 & 0 \\ 0 & 0 & 0 & 0 & 1 & 0 \\ 0 & 0 & 0 & 0 & 0 & 1 \end{bmatrix} \quad (\text{A.8})$$

The compliance matrix is then obtained using Eqs. (5.12) and (A.8)

$$C_M = \left[ \sum_{j=1}^j \Gamma_j^T K_j \Gamma_j \right]^{-1} \quad (\text{A.9})$$

and which, after substitution by values used previously gives

$$C_{classic} = 1 \times 10^4 \begin{bmatrix} 0 & 0 & 0 & 0 & 0 & 0 \\ 0 & 0 & 0 & 0 & 0 & 0 \\ 0 & 0.09 & 0 & 0 & 0 & 0 \\ 0 & 0 & 0 & 0 & 0 & 0 \\ 0 & 4.4 & 0 & 0 & 0.09 & 0 \\ 0 & 0 & 0.21 & 0 & 0 & 0 \end{bmatrix} \quad (\text{A.10})$$

## Appendix A. Stiffness and compliance matrix analysis

---

$$C_{enhanced} = 1 \times 10^4 \begin{bmatrix} 0 & 0 & 0 & 0 & 0 & 0 \\ 0 & 0 & 0 & 0 & 0 & 0 \\ 0 & 0.09 & 0 & 0 & 0 & 0 \\ 0 & 0 & 0 & 0 & 0 & 0 \\ 0 & 4.4 & 0 & 0 & 0.09 & 0 \\ 0 & 0 & 0.17 & 0 & 0 & 0 \end{bmatrix} \quad (\text{A.11})$$

As highlighted in Eqs. (A.10), for the classic mechanism, and (A.11), for the *enhanced* mechanism, the translation along the  $\vec{y}$  axis is predominant and then the only degree of freedom retained by the mechanism. It can be seen that the *enhanced* mechanism has almost the same compliance than its four-beam counterpart.

## Bibliography

- [1] D. J. Abbott, C. Becke, R. I. Rothstein, and W. J. Peine, "Design of an endoluminal NOTES robotic system," in *2007 IEEE/RSJ International Conference on Intelligent Robots and Systems*, Oct. 2007, pp. 410–416.
- [2] H. Abdul-Muhsin and V. Patel, "History of Robotic Surgery," in *Robotics in General Surgery*, K. C. Kim, Ed. New York, NY: Springer, 2014, pp. 3–8.
- [3] M. A. Ahmad, M. Ourak, C. Gruijthuijsen, J. Legrand, T. Vercauteren, J. Deprest, S. Ourselin, and E. Vander Poorten, "Design and Shared Control of a Flexible Endoscope with Autonomous Distal Tip Alignment," in *2019 19th International Conference on Advanced Robotics (ICAR)*, Dec. 2019, pp. 647–653.
- [4] K. Alblalaid, J. Overton, S. Lawes, and P. Kinnell, "A 3D-printed polymer micro-gripper with self-defined electrical tracks and thermal actuator," *Journal of Micromechanics and Microengineering*, vol. 27, no. 4, Apr. 2017.
- [5] E. Amanov, T.-D. Nguyen, and J. Burgner-Kahrs, "Tendon-driven continuum robots with extensible sections—A model-based evaluation of path-following motions," *The International Journal of Robotics Research*, vol. 40, no. 1, pp. 7–23, Jan. 2021.
- [6] G. K. Ananthasuresh and L. L. Howell, "Case Studies and a Note on the Degrees-of-Freedom in Compliant Mechanisms." Irvine, USA: American Society of Mechanical Engineers Digital Collection, 1996.
- [7] Z. P. Bažant, "Delayed thermal dilatations of cement paste and concrete due to mass transport," *Nuclear Engineering and Design*, vol. 14, no. 2, pp. 308–318, Dec. 1970.
- [8] D. Baek, J.-H. Seo, J. Kim, and D.-S. Kwon, "Hysteresis Compensator with Learning-based Pose Estimation for a Flexible Endoscopic Surgery Robot," in *2019 IEEE/RSJ International Conference on Intelligent Robots and Systems (IROS)*, Nov. 2019.
- [9] A. Bajo and N. Simaan, "Hybrid motion/force control of multi-backbone continuum robots," *The International Journal of Robotics Research*, vol. 35, no. 4, pp. 422–434, Apr. 2016.
- [10] R. Bellman, *Dynamic programming*. Princeton, NJ: Princeton Univ. Pr, 1984.

## Bibliography

---

- [11] M. Ben Salem, G. Aiche, Y. Haddab, L. Rubbert, and P. Renaud, "Additive Manufacturing of a Bistable Mechanism Using Fused Deposition Modeling: Experimental and Theoretical Characterization." Anaheim, California, USA: American Society of Mechanical Engineers, Aug. 2019.
- [12] M. Ben Salem, H. Hussein, G. Aiche, Y. Haddab, P. Lutz, L. Rubbert, and P. Renaud, "Characterization of bistable mechanisms for microrobotics and mesorobotics: Comparison between microfabrication and additive manufacturing," *Journal of Micro-Bio Robotics*, vol. 15, no. 1, pp. 65–77, Jun. 2019.
- [13] P. Berthet-Rayne, S. M. H. Sadati, G. Petrou, N. Patel, S. Giannarou, D. R. Leff, and C. Bergeles, "MAMMOBOT: A Miniature Steerable Soft Growing Robot for Early Breast Cancer Detection," *IEEE Robotics and Automation Letters*, vol. 6, no. 3, pp. 5056–5063, Jul. 2021, conference Name: IEEE Robotics and Automation Letters.
- [14] T. M. Bieze, F. Largilliere, A. Kruszewski, Z. Zhang, R. Merzouki, and C. Duriez, "Finite element method-based kinematics and closed-loop control of soft, continuum manipulators," *Soft Robotics*, vol. 5, no. 3, p. 348, 2018.
- [15] R. A. Bilodeau and R. K. Kramer, "Self-Healing and Damage Resilience for Soft Robotics: A Review," *Frontiers in Robotics and AI*, vol. 4, 2017.
- [16] J. Boudnaya, A. Haytoui, O. Eddayer, and A. Mkhida, "Prediction of Robot Localization States Using Hidden Markov Models," Jan. 2021, pp. 253–262.
- [17] I. Bouhadda, A. Mohand-Ousaid, G. Bourbon, P. L. Moal, P. Lutz, H. Hussein, and Y. Haddab, "Repeatability and Reproducibility Analysis of a Multistable Module Devoted to Digital Microrobotics," in *2018 IEEE/RSJ International Conference on Intelligent Robots and Systems (IROS)*, Oct. 2018, pp. 4889–4894.
- [18] J.-F. Bourgeois, "Automatisme et régulation des équipements thermiques," *Thermique pour l'industrie*, Jul. 1998.
- [19] M. N. Boushaki, C. Liu, and P. Poignet, "Task-space position control of concentric-tube robot with inaccurate kinematics using approximate Jacobian," in *2014 IEEE International Conference on Robotics and Automation (ICRA)*, May 2014, iSSN: 1050-4729.
- [20] F. Boyer, V. Lebastard, F. Candelier, and F. Renda, "Dynamics of continuum and soft robots: a strain parametrization based approach," *IEEE Transactions on Robotics*, Nov. 2020.
- [21] A. Bruyas, F. Geiskopf, L. Meylheuc, and P. Renaud, "Combining Multi-Material Rapid Prototyping and Pseudo-Rigid Body Modeling for a new compliant mechanism," in *2014 IEEE International Conference on Robotics and Automation (ICRA)*, May 2014, pp. 3390–3396.

- [22] J. Burgner-Kahrs, D. C. Rucker, and H. Choset, "Continuum Robots for Medical Applications: A Survey," *IEEE Transactions on Robotics*, pp. 1261–1280, Dec. 2015, conference Name: IEEE Transactions on Robotics.
- [23] J. Bурlet, O. Aycard, and T. Fraichard, "Robust motion planning using Markov decision processes and quadtree decomposition," in *IEEE International Conference on Robotics and Automation, 2004. Proceedings. ICRA '04. 2004.* New Orleans, LA, USA: IEEE, 2004.
- [24] B. Camescasse, "Actionnements statique et dynamique d'un mécanisme bistable : aspects modélisation, conception et expérimental," These de doctorat, Paris 6, Jan. 2013.
- [25] F. Campisano, F. Gramuglia, I. R. Dawson, C. T. Lyne, M. L. Izmaylov, S. Misra, E. De Momi, D. R. Morgan, K. L. Obstein, and P. Valdastri, "Gastric Cancer Screening in Low-Income Countries: System Design, Fabrication, and Analysis for an Ultralow-Cost Endoscopy Procedure," *IEEE Robotics & Automation Magazine*, vol. 24, no. 2, pp. 73–81, Jun. 2017, conference Name: IEEE Robotics & Automation Magazine.
- [26] N. Cauche, M. Hiernaux, A. Chau, V. Huberty, M. Ibrahim, A. Delchambre, and J. M. Deviere, "Endomina : the Endoluminal Universal Robotized Triangulation System: Description and Preliminary Results in Isolated Pig Stomach," *Gastrointestinal Endoscopy*, vol. 77, no. 5, 2013.
- [27] P. Cazottes, "Actionnement des systèmes bistables : modélisation et études expérimentales," These de doctorat, Paris 6, Jan. 2009.
- [28] V. Chalvet, Y. Haddab, and P. Lutz, "A Microfabricated Planar Digital Microrobot for Precise Positioning Based on Bistable Modules," *IEEE Transactions on Robotics*, pp. 641–649, Jun. 2013.
- [29] M. Chandler, "Tracheal intubation and sore throat: a mechanical explanation," *Anaesthesia*, vol. 57, no. 2, pp. 155–161, 2002.
- [30] G. Chen, Q. T. Aten, S. Zirbel, B. D. Jensen, and L. L. Howell, "A Tristable Mechanism Configuration Employing Orthogonal Compliant Mechanisms," *Journal of Mechanisms and Robotics*, Feb. 2010.
- [31] G. Chen, B. Xiong, and X. Huang, "Finding the optimal characteristic parameters for 3R pseudo-rigid-body model using an improved particle swarm optimizer," *Precision Engineering*, vol. 35, no. 3, pp. 505–511, Jul. 2011.
- [32] Q. Chen, Y. Haddab, and P. Lutz, "Microfabricated bistable module for digital micro-robotics," *Journal of Micro-Nano Mechatronics*, vol. 6, no. 1, pp. 1–12, Feb. 2011.
- [33] Y. Chen, J. Liang, and I. W. Hunter, "Modular continuum robotic endoscope design and path planning," in *2014 IEEE International Conference on Robotics and Automation (ICRA)*, May 2014.

## Bibliography

---

- [34] M. T. Chikhaoui, J. Granna, J. Starke, and J. Burgner-Kahrs, "Toward Motion Coordination Control and Design Optimization for Dual-Arm Concentric Tube Continuum Robots," *IEEE Robotics and Automation Letters*, vol. 3, no. 3, pp. 1793–1800, Jul. 2018, conference Name: IEEE Robotics and Automation Letters.
- [35] G. S. Chirikjian, "Theory and Applications of Hyper-Redundant Robotic Manipulators," phd, California Institute of Technology, 1992.
- [36] G. Chirikjian, "A binary paradigm for robotic manipulators," in *Proceedings of the 1994 IEEE International Conference on Robotics and Automation*, May 1994, pp. 3063–3069.
- [37] G. Chirikjian and D. Lees, "Inverse kinematics of binary manipulators with applications to service robotics," in *Proceedings 1995 IEEE/RSJ International Conference on Intelligent Robots and Systems. Human Robot Interaction and Cooperative Robots*, Aug. 1995, pp. 65–71.
- [38] M. Cianchetti, T. Ranzani, G. Gerboni, I. De Falco, C. Laschi, and A. Menciassi, "STIFF-FLOP surgical manipulator: Mechanical design and experimental characterization of the single module," in *2013 IEEE/RSJ International Conference on Intelligent Robots and Systems*, Nov. 2013, pp. 3576–3581.
- [39] F. Connolly, P. Polygerinos, C. J. Walsh, and K. Bertoldi, "Mechanical Programming of Soft Actuators by Varying Fiber Angle," *Soft Robotics*, vol. 2, no. 1, pp. 26–32, Mar. 2015.
- [40] T. da Veiga, J. H. Chandler, P. Lloyd, G. Pittiglio, N. J. Wilkinson, A. K. Hoshier, R. A. Harris, and P. Valdastrì, "Challenges of continuum robots in clinical context: a review," *Progress in Biomedical Engineering*, 2020.
- [41] A. Damani, "An Empirical Model of Piezoelectric Stick-Slip Actuation Of The KLEINDIEK MM3A Micromanipulator," Ph.D. dissertation, University of Utah, Utah, 2013.
- [42] A. De Donno, L. Zorn, P. Zanne, F. Nageotte, and M. de Mathelin, "Introducing STRAS: A new flexible robotic system for minimally invasive surgery," in *2013 IEEE International Conference on Robotics and Automation*, May 2013.
- [43] G. Decroly, P. Lambert, and A. Delchambre, "A Soft Pneumatic Two-Degree-of-Freedom Actuator for Endoscopy," *Frontiers in Robotics and AI*, vol. 8, 2021.
- [44] A. Degani, H. Choset, A. Wolf, and M. Zenati, "Highly articulated robotic probe for minimally invasive surgery," in *Proceedings 2006 IEEE International Conference on Robotics and Automation, 2006. ICRA 2006.*, May 2006, pp. 4167–4172.
- [45] A. Diaz Lantada, "Systematic Development Strategy for Smart Devices Based on Shape-Memory Polymers," *Polymers*, p. 496, Oct. 2017.
- [46] A. Dijkshoorn, P. Werkman, M. Welleweerd, G. Wolterink, B. Eijking, J. Delamare, R. Sanders, and G. J. M. Krijnen, "Embedded sensing: integrating sensors in 3-D printed structures," *Journal of Sensors and Sensor Systems*, vol. 7, no. 1, pp. 169–181, Mar. 2018.

- 
- [47] B. K. Dinh, L. Cappello, M. Xiloyannis, and L. Masia, "Position control using adaptive backlash compensation for bowden cable transmission in soft wearable exoskeleton," in *2016 IEEE/RSJ International Conference on Intelligent Robots and Systems (IROS)*, Oct. 2016, pp. 5670–5676.
- [48] A. Diodato, M. Brancadoro, G. De Rossi, H. Abidi, D. Dall'Alba, R. Muradore, G. Ciuti, P. Fiorini, A. Menciassi, and M. Cianchetti, "Soft Robotic Manipulator for Improving Dexterity in Minimally Invasive Surgery," *Surgical Innovation*, vol. 25, no. 1, pp. 69–76, Feb. 2018.
- [49] A. Dorigato, V. Moretti, S. Dul, S. H. Unterberger, and A. Pegoretti, "Electrically conductive nanocomposites for fused deposition modelling," *Synthetic Metals*, vol. 226, pp. 7–14, Apr. 2017.
- [50] M. Doumit, A. Fahim, and M. Munro, "Analytical Modeling and Experimental Validation of the Braided Pneumatic Muscle," *IEEE Transactions on Robotics*, vol. 25, no. 6, pp. 1282–1291, Dec. 2009.
- [51] R. Dreyfus, Q. Boehler, and B. J. Nelson, "A Simulation Framework for Magnetic Continuum Robots," *IEEE Robotics and Automation Letters*, vol. 7, no. 3, Jun. 2022.
- [52] P. E. Dupont, J. Lock, B. Itkowitz, and E. Butler, "Design and Control of Concentric-Tube Robots," *IEEE Transactions on Robotics*, vol. 26, no. 2, pp. 209–225, Apr. 2010.
- [53] P. E. Dupont, B. J. Nelson, M. Goldfarb, B. Hannaford, A. Menciassi, M. K. O'Malley, N. Simaan, P. Valdastri, and G.-Z. Yang, "A decade retrospective of medical robotics research from 2010 to 2020," *Science Robotics*, vol. 6, no. 60, Nov. 2021.
- [54] I. Ebert-Uphoff and G. Chirikjian, "Inverse kinematics of discretely actuated hyper-redundant manipulators using workspace densities," in *Proceedings of IEEE International Conference on Robotics and Automation*, vol. 1, Apr. 1996, pp. 139–145.
- [55] A. El Magri, K. El Mabrouk, S. Vaudreuil, and M. Touhami, "Mechanical properties of CF-reinforced PLA parts manufactured by fused deposition modeling," *Journal of Thermoplastic Composite Materials*, vol. 32, May 2019.
- [56] G. Fagogenis, C. Bergeles, and P. E. Dupont, "Adaptive nonparametric kinematic modeling of concentric tube robots," in *2016 IEEE/RSJ International Conference on Intelligent Robots and Systems (IROS)*, Oct. 2016, pp. 4324–4329.
- [57] I. D. Falco, M. Cianchetti, and A. Menciassi, "A soft multi-module manipulator with variable stiffness for minimally invasive surgery," *Bioinspiration & Biomimetics*, vol. 12, no. 5, Sep. 2017.
- [58] V. Falkenhahn, A. Hildebrandt, R. Neumann, and O. Sawodny, "Dynamic Control of the Bionic Handling Assistant," *IEEE/ASME Transactions on Mechatronics*, vol. 22, no. 1, pp. 6–17, Feb. 2017.

## Bibliography

---

- [59] V. Falkenhahn, T. Mahl, A. Hildebrandt, R. Neumann, and O. Sawodny, "Dynamic Modeling of Bellows-Actuated Continuum Robots Using the Euler–Lagrange Formalism," *IEEE Transactions on Robotics*, vol. 31, no. 6, pp. 1483–1496, Dec. 2015.
- [60] J. Faulkner and S. Dirven, "A generalised, modular, approach for the forward kinematics of continuum soft robots with sections of constant curvature," in *2017 24th International Conference on Mechatronics and Machine Vision in Practice (M2VIP)*, Nov. 2017, pp. 1–6.
- [61] Femtoprint, "DeviceMed Septembre/Octobre 2022," *DeviceMed*, no. 5, pp. 48–49, Sep. 2022.
- [62] D. Friedrich, V. Modes, T. Hoffmann, J. Greve, P. Schuler, and J. Burgner-Kahrs, "Teleoperated tubular continuum robots for transoral surgery – feasibility in a porcine larynx model," *The International Journal of Medical Robotics and Computer Assisted Surgery*, vol. 14, no. 5, 2018.
- [63] J. B. Gafford, S. Webster, N. Dillon, E. Blum, R. Hendrick, F. Maldonado, E. A. Gillaspie, O. B. Rickman, S. D. Herrell, and R. J. Webster, "A Concentric Tube Robot System for Rigid Bronchoscopy: A Feasibility Study on Central Airway Obstruction Removal," *Annals of Biomedical Engineering*, vol. 48, no. 1, pp. 181–191, Jan. 2020.
- [64] X. Gao, Y. Liu, S. Zhang, J. Deng, and J. Liu, "Development of a Novel Flexure-Based XY Platform Using Single Bending Hybrid Piezoelectric Actuator," *IEEE/ASME Transactions on Mechatronics*, pp. 1–11, 2022.
- [65] L. Garcia, G. Kerns, K. O'Reilley, O. Okesanjo, J. Lozano, J. Narendran, C. Broeking, X. Ma, H. Thompson, P. Njapa Njeuha, D. Sikligar, R. Brockstein, and H. M. Golecki, "The Role of Soft Robotic Micromachines in the Future of Medical Devices and Personalized Medicine," *Micromachines*, vol. 13, no. 1, p. 28, Jan. 2022.
- [66] E. Gautreau, A. Thomas, J. Sandoval, M. A. Laribi, and S. Zeghloul, "Design of an 8-DoF Redundant Robotic Platform for Medical Applications," in *Mechanism Design for Robotics*, S. Zeghloul, M. A. Laribi, and M. Arsicault, Eds., 2021.
- [67] D. C. Gazis, R. Herman, and R. W. Rothery, "Nonlinear Follow-the-Leader Models of Traffic Flow," *Operations Research*, vol. 9, no. 4, pp. 545–567, Aug. 1961.
- [68] M. W. Gifari, H. Naghibi, S. Stramigioli, and M. Abayazid, "A review on recent advances in soft surgical robots for endoscopic applications," *The international journal of medical robotics + computer assisted surgery: MRCAS*, vol. 15, no. 5, Oct. 2019.
- [69] C. Girerd and T. K. Morimoto, "Design and Control of a Hand-Held Concentric Tube Robot for Minimally Invasive Surgery," *IEEE Transactions on Robotics*, vol. 37, no. 4, pp. 1022–1038, Aug. 2021.
- [70] C. Girerd, K. Rabenorosa, and P. Renaud, "Combining Tube Design and Simple Kinematic Strategy for Follow-the-Leader Deployment of Concentric Tube Robots," *Advances in Robot Kinematics*, p. 9, 2016.

- 
- [71] R. E. Goldman, A. Bajo, and N. Simaan, "Compliant Motion Control for Multisegment Continuum Robots With Actuation Force Sensing," *IEEE Transactions on Robotics*, vol. 30, no. 4, pp. 890–902, Aug. 2014.
- [72] T. Gomm, L. L. Howell, and R. H. Selfridge, "In-plane linear displacement bistable microrelay," *Journal of Micromechanics and Microengineering*, vol. 12, no. 3, p. 257, 2002.
- [73] Y. Haddab, G. Aiche, H. Hussein, M. B. Salem, P. Lutz, L. Rubbert, and P. Renaud, "Mechanical Bistable Structures for Microrobotics and Mesorobotics from Microfabrication to Additive Manufacturing." IEEE, Jul. 2018, p. 1.
- [74] Y. Haddab, V. Chalvet, Q. Chen, and P. Lutz, "Digital Microrobotics Using MEMS Technology," in *Advanced Mechatronics and MEMS Devices*, ser. Microsystems, D. Zhang, Ed. New York, NY: Springer, 2013, pp. 99–116.
- [75] M. Hafez, M. Lichter, and S. Dubowsky, "Optimized binary modular reconfigurable robotic devices," *IEEE/ASME Transactions on Mechatronics*, vol. 8, no. 1, pp. 18–25, Mar. 2003.
- [76] G. Hao, "A 2-Legged XY Parallel Flexure Motion Stage with Minimised Parasitic Rotation," *ARCHIVE Proceedings of the Institution of Mechanical Engineers Part C Journal of Mechanical Engineering Science 1989-1996 (vols 203-210)*, Dec. 2014.
- [77] —, *Cross-section Considerations for Wire-beam Based Translational Compliant Parallel Manipulators*, Jan. 2014.
- [78] G. Hao and X. Kong, "A normalization-based approach to the mobility analysis of spatial compliant multi-beam modules," *Mechanism and Machine Theory*, vol. 59, pp. 1–19, Jan. 2013.
- [79] G. Hao and H. Li, "Design of 3-legged XYZ compliant parallel manipulators with minimised parasitic rotations," *Robotica*, vol. 33, no. 4, pp. 787–806, May 2015.
- [80] G. Hao and J. Mullins, "On the comprehensive static characteristic analysis of a translational bistable mechanism," *Proceedings of the Institution of Mechanical Engineers, Part C: Journal of Mechanical Engineering Science*, vol. 230, no. 20, pp. 3803–3817, Dec. 2016.
- [81] S. Henein, "Flexures: simply subtle," *Diamond Light Source Proceedings*, 2011.
- [82] —, "Conception des structures articulées à guidages flexibles de haute précision," Ph.D. dissertation, EPFL, 2000.
- [83] P. W. J. Henselmans, "Mechanical Snakes: Path-Following Instruments for Minimally Invasive Surgery," 2020.

## Bibliography

---

- [84] P. Henselmans, S. Gottenbos, G. Smit, and P. Breedveld, “The Memo Slide : An explorative study into a novel mechanical follow-the-leader mechanism,” *Proceedings of the Institution of Mechanical Engineers, Part H: Journal of Engineering in Medicine*, vol. 231, Nov. 2017.
- [85] S. Hirose and A. Morishima, “Design and Control of a Mobile Robot with an Articulated Body,” *The International Journal of Robotics Research*, vol. 9, no. 2, pp. 99–114, Apr. 1990.
- [86] K. T. Hoang, D. T. Nguyen, and P. H. Pham, “Impact of design parameters on working stability of the electrothermal V-shaped actuator,” *Microsystem Technologies*, 2019.
- [87] G. L. Holst, G. H. Teichert, and B. D. Jensen, “Modeling and Experiments of Buckling Modes and Deflection of Fixed-Guided Beams in Compliant Mechanisms,” *Journal of Mechanical Design*, vol. 133, no. 5, 2011.
- [88] J. B. Hopkins, “Design of parallel flexure systems via Freedom and Constraint Topologies (FACT),” Thesis, Massachusetts Institute of Technology, 2007.
- [89] J. B. Hopkins and M. L. Culpepper, “Synthesis of multi-degree of freedom, parallel flexure system concepts via Freedom and Constraint Topology (FACT) – Part I: Principles,” *Precision Engineering*, vol. 34, no. 2, pp. 259–270, Apr. 2010.
- [90] ———, “Synthesis of multi-degree of freedom, parallel flexure system concepts via freedom and constraint topology (FACT). Part II: Practice,” *Precision Engineering*, vol. 34, no. 2, pp. 271–278, Apr. 2010.
- [91] L. L. Howell, S. S. Rao, and A. Midha, “Reliability-Based Optimal Design of a Bistable Compliant Mechanism,” *Journal of Mechanical Design*, vol. 116, no. 4, pp. 1115–1121, Dec. 1994.
- [92] L. L. Howell, “Compliant Mechanisms,” in *Encyclopedia of Nanotechnology*, B. Bhushan, Ed. Springer, Dordrecht, 2016, pp. 604–611.
- [93] L. L. Howell, S. P. Magleby, and B. M. Olsen, Eds., *Handbook of compliant mechanisms*. United Kingdom: John Wiley & Sons, Inc, 2013.
- [94] L. L. Howell and A. Midha, “Determination of the Degrees of Freedom of Compliant Mechanisms Using the Pseudo-Rigid-Body Model Concept,” vol. 2, Milano, Italy, 1995, pp. 1537–1541.
- [95] S. Huang, D. Meng, X. Wang, B. Liang, and W. Lu, “A 3D Static Modeling Method and Experimental Verification of Continuum Robots Based on Pseudo-Rigid Body Theory,” in *2019 IEEE/RSJ International Conference on Intelligent Robots and Systems (IROS)*, Nov. 2019, pp. 4672–4677.
- [96] P. Hughes, W. Sincarsin, and K. Carroll, “Trussarm—A Variable-Geometry-Truss Manipulator,” *Journal of Intelligent Material Systems and Structures*, vol. 2, no. 2, pp. 148–160, Apr. 1991.

- 
- [97] H. Hussein, "Contribution to digital microrobotics: modeling, design and fabrication of curved beams, U-shaped actuators and multistable microrobots," Ph.D. dissertation, Université de Franche Comté, Besancon, Sep. 2015.
- [98] H. Hussein, V. Chalvet, P. Le Moal, G. Bourbon, Y. Haddab, and P. Lutz, "Design optimization of bistable modules electrothermally actuated for digital microrobotics," in *2014 IEEE/ASME International Conference on Advanced Intelligent Mechatronics*, Jul. 2014, pp. 1273–1278.
- [99] H. Hussein, P. Le Moal, R. Younes, G. Bourbon, Y. Haddab, and P. Lutz, "On the design of a preshaped curved beam bistable mechanism," *Mechanism and Machine Theory*, vol. 131, pp. 204–217, Jan. 2019.
- [100] H. Hussein, P. Moal, G. Bourbon, Y. Haddab, and P. Lutz, "Modeling and Stress Analysis of a Pre-Shaped Curved Beam : Influence of High Modes of Buckling," *International Journal of Applied Mechanics*, vol. 7, no. 4, p. 20 p, 2015.
- [101] H. Hussein, A. Tahhan, P. L. Moal, G. Bourbon, Y. Haddab, and P. Lutz, "Dynamic electro-thermo-mechanical modelling of a U-shaped electro-thermal actuator," *Journal of Micromechanics and Microengineering*, vol. 26, no. 2, Jan. 2016.
- [102] H. Hussein and M. I. Younis, "Analytical Study of the Snap-Through and Bistability of Beams With Arbitrarily Initial Shape," *Journal of Mechanisms and Robotics*, vol. 12, no. 4, Feb. 2020.
- [103] K. Ikuta, H. Ichikawa, K. Suzuki, and D. Yajima, "Multi-degree of freedom hydraulic pressure driven safety active catheter," in *Proceedings 2006 IEEE International Conference on Robotics and Automation, 2006. ICRA 2006.*, May 2006, pp. 4161–4166.
- [104] H. C. Jacobaeus, "Über Laparo- Und Thorakoskopie," in *Beiträge zur Klinik der Tuberkulose und spezifischen Tuberkulose-Forschung*, 1912, vol. 25, pp. 185–354.
- [105] B. D. Jensen, M. B. Parkinson, K. Kurabayashi, L. L. Howell, and M. S. Baker, "Design Optimization of a Fully-Compliant Bistable Micro-Mechanism," in *Micro-Electro-Mechanical Systems (MEMS)*. New York, New York, USA: American Society of Mechanical Engineers, Nov. 2001, pp. 357–363.
- [106] H. Y. Jeong, S.-C. An, I. C. Seo, E. Lee, S. Ha, N. Kim, and Y. C. Jun, "3D printing of twisting and rotational bistable structures with tuning elements," *Scientific Reports*, vol. 9, no. 1, p. 324, Jan. 2019.
- [107] Y. Jia and S. Ma, "A Coach-Based Bayesian Reinforcement Learning Method for Snake Robot Control," *IEEE Robotics and Automation Letters*, vol. 6, no. 2, pp. 2319–2326, Apr. 2021.
- [108] H.-S. Jung and S. Cho, "Reliability-based topology optimization of geometrically nonlinear structures with loading and material uncertainties," *Finite Elements in Analysis and Design*, vol. 41, no. 3, pp. 311–331, 2004.

## Bibliography

---

- [109] A. N. Kalloo, V. K. Singh, S. B. Jagannath, H. Niiyama, S. L. Hill, C. A. Vaughn, C. A. Magee, and S. V. Kantsevoy, "Flexible transgastric peritoneoscopy: a novel approach to diagnostic and therapeutic interventions in the peritoneal cavity," *Gastrointestinal Endoscopy*, vol. 60, no. 1, pp. 114–117, Jul. 2004.
- [110] S. Kamrava, D. Mousanezhad, H. Ebrahimi, R. Ghosh, and A. Vaziri, "Origami-based cellular metamaterial with auxetic, bistable, and self-locking properties," *Scientific Reports*, vol. 7, no. 1, Apr. 2017.
- [111] W. Khalil and E. Dombre, Eds., *Modeling, Identification and Control of Robots*. Oxford: Butterworth-Heinemann, Jan. 2002.
- [112] C. Kim, S. C. Ryu, and P. E. Dupont, "Real-time adaptive kinematic model estimation of concentric tube robots," in *2015 IEEE/RSJ International Conference on Intelligent Robots and Systems (IROS)*, Sep. 2015.
- [113] H. Kim and S. Lee, "Characterization of Electrical Heating of Graphene/PLA Honeycomb Structure Composite Manufactured by CFDM 3D Printer," *Fashion and Textiles*, vol. 7, p. 8, Mar. 2020.
- [114] Y.-J. Kim, S. Cheng, S. Kim, and K. Iagnemma, "A Stiffness-Adjustable Hyperredundant Manipulator Using a Variable Neutral-Line Mechanism for Minimally Invasive Surgery," *IEEE Transactions on Robotics*, vol. 30, no. 2, pp. 382–395, Apr. 2014.
- [115] M. Koehler, A. M. Okamura, and C. Duriez, "Stiffness Control of Deformable Robots Using Finite Element Modeling," *IEEE Robotics and Automation Letters*, vol. 4, no. 2, p. 469, 2019.
- [116] D. R. Kohli and J. Baillie, "3 - How Endoscopes Work," in *Clinical Gastrointestinal Endoscopy (Third Edition)*, V. Chandrasekhara, B. J. Elmunzer, M. A. Khashab, and V. R. Muthusamy, Eds. Philadelphia: Elsevier, Jan. 2019, pp. 24–31.e2.
- [117] P. Krielen, M. W. J. Stommel, P. Pargmae, N. D. Bouvy, E. A. Bakkum, H. Ellis, M. C. Parker, E. A. Griffiths, H. van Goor, and R. P. G. ten Broek, "Adhesion-related readmissions after open and laparoscopic surgery: a retrospective cohort study (SCAR update)," *The Lancet*, vol. 395, no. 10217, pp. 33–41, Jan. 2020.
- [118] P. R. Kuppens, J. L. Herder, and N. Tolou, "Permanent Stiffness Reduction by Thermal Oxidation of Silicon," *Journal of Microelectromechanical Systems*, vol. 28, no. 5, pp. 900–909, Oct. 2019.
- [119] Y. Kwoh, J. Hou, E. Jonckheere, and S. Hayati, "A robot with improved absolute positioning accuracy for CT guided stereotactic brain surgery," *IEEE Transactions on Biomedical Engineering*, vol. 35, no. 2, pp. 153–160, Feb. 1988.
- [120] K.-W. Kwok, K. Hung Tsoi, V. Vitiello, J. Clark, G. C. T. Chow, W. Luk, and G.-Z. Yang, "Dimensionality Reduction in Controlling Articulated Snake Robot for Endoscopy Under

- Dynamic Active Constraints,” *IEEE Transactions on Robotics*, vol. 29, no. 1, pp. 15–31, Feb. 2013.
- [121] P. Lambert, J. Szewczyk, and P. Renaud, “Actionneurs non conventionnels pour la robotique,” *Robotique*, May 2016.
- [122] D. Lees and G. Chirikjian, “A combinatorial approach to trajectory planning for binary manipulators,” in *Proceedings of IEEE International Conference on Robotics and Automation*, vol. 3, Apr. 1996, pp. 2749–2754.
- [123] —, “An efficient method for computing the forward kinematics of binary manipulators,” in *Proceedings of IEEE International Conference on Robotics and Automation*, vol. 2, Apr. 1996, pp. 1012–1017 vol.2.
- [124] M. Li, R. Kang, D. T. Branson, and J. S. Dai, “Model-Free Control for Continuum Robots Based on an Adaptive Kalman Filter,” *IEEE/ASME Transactions on Mechatronics*, vol. 23, no. 1, pp. 286–297, Feb. 2018.
- [125] M. Lichter, V. Sujan, and S. Dubowsky, *Computational Issues in the Planning and Kinematics of Binary Robots.*, Jan. 2002.
- [126] J.-T. Lin, C. Girerd, J. Yan, J. T. Hwang, and T. K. Morimoto, “A Generalized Framework for Concentric Tube Robot Design Using Gradient-Based Optimization,” *IEEE Transactions on Robotics*, pp. 1–18, 2022.
- [127] G. S. Litynski, “Laparoscopy - The Early Attempts: Spotlighting Georg Kelling and Hans Christian Jacobaeus,” *JSLs : Journal of the Society of Laparoendoscopic Surgeons*, vol. 1, no. 1, pp. 83–85, 1997.
- [128] L. Liu, X. Guo, and Y. Fang, “A Reinforcement Learning-Based Strategy of Path Following for Snake Robots with an Onboard Camera,” *Sensors*, vol. 22, no. 24, p. 9867, Jan. 2022.
- [129] Y. Liu, L. Binhong, T. Yin, X. Yuhai, H. Zhou, and S. Qu, “Bistable rotating mechanism based On dielectric elastomer actuator,” *Smart Materials and Structures*, Oct. 2019.
- [130] A. Loeve, P. Breedveld, and J. Dankelman, “Scopes Too Flexible...and Too Stiff,” *Pulse, IEEE*, vol. 1, pp. 26–41, Jan. 2011.
- [131] G. Z. Lum, M. T. Pham, T. J. Teo, G. Yang, S. H. Yeo, and M. Sitti, “An  $\theta$  flexure mechanism with optimal stiffness properties,” in *2017 IEEE International Conference on Advanced Intelligent Mechatronics (AIM)*, Jul. 2017, pp. 1103–1110.
- [132] A. M. Lyapunov, “The general problem of the stability of motion,” *International Journal of Control*, vol. 55, no. 3, pp. 531–534, Mar. 1992.
- [133] T. Mahl, A. Hildebrandt, and O. Sawodny, “A Variable Curvature Continuum Kinematics for Kinematic Control of the Bionic Handling Assistant,” *IEEE Transactions on Robotics*, vol. 30, no. 4, pp. 935–949, Aug. 2014.

## Bibliography

---

- [134] L. Manfredi, E. Capoccia, G. Ciuti, and A. Cuschieri, "A Soft Pneumatic Inchworm Double balloon (SPID) for colonoscopy," *Scientific Reports*, vol. 9, no. 1, Jul. 2019.
- [135] A. D. Marchese, R. K. Katzschmann, and D. Rus, "A Recipe for Soft Fluidic Elastomer Robots," *Soft Robotics*, vol. 2, no. 1, pp. 7–25, Mar. 2015.
- [136] A. D. Marchese and D. Rus, "Design, kinematics, and control of a soft spatial fluidic elastomer manipulator," *The International Journal of Robotics Research*, vol. 35, no. 7, pp. 840–869, Jun. 2016.
- [137] K. Maute and D. M. Frangopol, "Reliability-based design of MEMS mechanisms by topology optimization," *Computers & Structures*, vol. 81, no. 8, pp. 813–824, May 2003.
- [138] P. Mazurek, "Viterbi Algorithm for Noise Line Following Robots," in *Image Processing & Communications Challenges 6*, R. S. Choraś, Ed. Cham: Springer International Publishing, 2015, pp. 111–118.
- [139] Z. Mitros, M. Khadem, C. Seneci, S. Ourselin, L. Da Cruz, and C. Bergeles, "Towards Modelling Multi-Arm Robots: Eccentric Arrangement of Concentric Tubes," in *2018 7th IEEE International Conference on Biomedical Robotics and Biomechatronics (Biorob)*, Aug. 2018, pp. 43–48.
- [140] Z. Mitros, S. Sadati, S. Nousias, L. Da Cruz, and C. Bergeles, "Design and Quasistatic Modelling of Hybrid Continuum Multi-Arm Robots," in *2022 International Conference on Robotics and Automation (ICRA)*, May 2022, pp. 9607–9613.
- [141] K. Miura, H. Furuya, and K. Suzuki, "Variable geometry truss and its application to deployable truss and space crane arm," *Acta Astronautica*, vol. 12, no. 7, pp. 599–607, Jul. 1985.
- [142] M. Miyasaka, M. Haghhighipanah, Y. Li, and B. Hannaford, "Hysteresis model of longitudinally loaded cable for cable driven robots and identification of the parameters," in *2016 IEEE International Conference on Robotics and Automation (ICRA)*, May 2016, pp. 4051–4057.
- [143] A. S. Y. Mohamed, "Smart Materials Innovative Technologies in architecture; Towards Innovative design paradigm," *Energy Procedia*, vol. 115, pp. 139–154, Jun. 2017.
- [144] O. C. Mora, P. Zanne, L. Zorn, F. Nageotte, N. Zulina, S. Gravelyn, P. Montgomery, M. de Mathelin, B. Dallemagne, and M. J. Gora, "Steerable OCT catheter for real-time assistance during teleoperated endoscopic treatment of colorectal cancer," *Biomedical Optics Express*, vol. 11, no. 3, pp. 1231–1243, Mar. 2020.
- [145] B. Mosadegh, P. Polygerinos, C. Keplinger, S. Wennstedt, R. F. Shepherd, U. Gupta, J. Shim, K. Bertoldi, C. J. Walsh, and G. M. Whitesides, "Pneumatic Networks for Soft Robotics that Actuate Rapidly," *Advanced Functional Materials*, vol. 24, no. 15, pp. 2163–2170, 2014.

- [146] A. Munshi, "Do not use robotic surgery in oncology patients when conventional surgical approaches are equally effective," *The Lancet Oncology*, vol. 20, no. 5, May 2019.
- [147] M. D. Murphy, A. Midha, and L. L. Howell, "On the Mobility of Compliant Mechanisms." Minneapolis, USA: ASME, 1994, pp. 475–479.
- [148] F. Nageotte, L. Zorn, P. Zanne, and M. De Mathelin, "STRAS: A Modular and Flexible Telemanipulated Robotic Device for Intraluminal Surgery," in *Handbook of Robotic and Image-Guided Surgery*, M. H. Abedin-Nasab, Ed., Jan. 2020, pp. 123–146.
- [149] M. Neumann and J. Burgner-Kahrs, "Considerations for follow-the-leader motion of extensible tendon-driven continuum robots," in *2016 IEEE International Conference on Robotics and Automation (ICRA)*, May 2016, pp. 917–923.
- [150] T.-D. Nguyen and J. Burgner-Kahrs, "A tendon-driven continuum robot with extensible sections," in *2015 IEEE/RSJ International Conference on Intelligent Robots and Systems (IROS)*, Sep. 2015, pp. 2130–2135.
- [151] Y. S. Oh and S. Kota, "Synthesis of Multistable Equilibrium Compliant Mechanisms Using Combinations of Bistable Mechanisms," *Journal of Mechanical Design*, vol. 131, no. 021002, Jan. 2009.
- [152] O. Omisore, S. Han, L. Ren, N. Zhang, and L. Wang, *A geometric solution for inverse kinematics of redundant teleoperated surgical snake robots*, Mar. 2017, pages: 714.
- [153] A. L. Orekhov, C. Abah, and N. Simaan, "Snake-Like Robots for Minimally Invasive, Single Port, and Intraluminal Surgeries," in *Encyclopedia of Medical Robotics*, Oct. 2018, pp. 203–243.
- [154] K. Ozsoy, A. Ercetin, and Z. A. Cevik, "Comparison of Mechanical Properties of PLA and ABS Based Structures Produced by Fused Deposition Modelling Additive Manufacturing," no. 27, pp. 802–809, Nov. 2021.
- [155] A. Pagoli, F. Chapelle, J.-A. Corrales-Ramon, Y. Mezouar, and Y. Lapusta, "Review of soft fluidic actuators: classification and materials modeling analysis," *Smart Materials and Structures*, vol. 31, no. 1, p. 013001, Dec. 2021.
- [156] N. Patel, C. Seneci, G.-Z. Yang, A. Darzi, and J. Teare, "Flexible platforms for natural orifice transluminal and endoluminal surgery," *Endoscopy International Open*, vol. 2, pp. 117–123, Jun. 2014.
- [157] B. Payne, "'Kindergarten Theory' The Elementary School Teacher and Course of Study," pp. 295–297, 1901.
- [158] S. J. Phee, S. C. Low, Z. L. Sun, K. Y. Ho, W. M. Huang, and Z. M. Thant, "Robotic system for no-scar gastrointestinal surgery," *The International Journal of Medical Robotics and Computer Assisted Surgery*, vol. 4, no. 1, pp. 15–22, 2008.

## Bibliography

---

- [159] T. Poignonec, P. Zanne, B. Rosa, and F. Nageotte, “Towards In Situ Backlash Estimation of Continuum Robots Using an Endoscopic Camera,” *IEEE Robotics and Automation Letters*, vol. 5, no. 3, pp. 4788–4795, Jul. 2020.
- [160] D. A. Porter and T. A. Berfield, “A bi-stable buckled energy harvesting device actuated via torque arms,” *Smart Materials and Structures*, vol. 23, no. 7, p. 075003, May 2014.
- [161] R. A. Porto, F. Nageotte, P. Zanne, and M. d. Mathelin, “Position control of medical cable-driven flexible instruments by combining machine learning and kinematic analysis,” in *2019 International Conference on Robotics and Automation (ICRA)*, May 2019.
- [162] A. Potekhina and C. Wang, “Review of Electrothermal Actuators and Applications,” p. 28, 2019.
- [163] J. Qian, X. Sun, and J. Xu, “A data-driven reconstruction method for dynamic systems with multistable property,” *Nonlinear Dynamics*, vol. 111, Nov. 2022.
- [164] J. Qiu, J. Lang, and A. Slocum, “A centrally-clamped parallel-beam bistable MEMS mechanism,” in *Technical Digest. MEMS 2001. 14th IEEE International Conference on Micro Electro Mechanical Systems (Cat. No.01CH37090)*, Jan. 2001, pp. 353–356.
- [165] ———, “A curved-beam bistable mechanism,” *Journal of Microelectromechanical Systems*, vol. 13, no. 2, pp. 137–146, Apr. 2004.
- [166] T. Ranzani, G. Gerboni, M. Cianchetti, and A. Menciassi, “A bioinspired soft manipulator for minimally invasive surgery,” *Bioinspiration & Biomimetics*, vol. 10, no. 3, p. 035008, May 2015.
- [167] P. Rao, Q. Peyron, S. Lilge, and J. Burgner-Kahrs, “How to Model Tendon-Driven Continuum Robots and Benchmark Modelling Performance,” *Frontiers in Robotics and AI*, Feb. 2021.
- [168] J. Reinisch, E. Wehrle, and J. Achleitner, “Multiresolution Topology Optimization of Large-Deformation Path-Generation Compliant Mechanisms with Stress Constraints,” *Applied Sciences*, vol. 11, no. 6, p. 2479, 2021.
- [169] R. J. Roesthuis and S. Misra, “Steering of Multisegment Continuum Manipulators Using Rigid-Link Modeling and FBG-Based Shape Sensing,” *IEEE Transactions on Robotics*, vol. 32, no. 2, pp. 372–382, Apr. 2016.
- [170] S. Rost, M. Uhlemann, K.-H. Modler, Y. Sklyarenko, F. Schreiber, and W. Schumacher, *On the joint design and hydraulic actuation of octahedron VGT robot manipulators*, Aug. 2011.
- [171] L. Rubbert, R. Bitterli, N. Ferrier, S. Fifanski, I. Vardi, and S. Henein, “Isotropic springs based on parallel flexure stages,” *Precision Engineering*, pp. 132–145, Jan. 2016.

- 
- [172] L. Rubbert, "Conception de mécanismes compliants pour la robotique chirurgicale," These de doctorat, Strasbourg, Dec. 2012.
- [173] D. C. Rucker, B. A. Jones, and R. J. Webster III, "A Geometrically Exact Model for Externally Loaded Concentric-Tube Continuum Robots," *IEEE Transactions on Robotics*, vol. 26, no. 5, pp. 769–780, Oct. 2010.
- [174] D. C. Rucker and R. J. Webster III, "Statics and Dynamics of Continuum Robots With General Tendon Routing and External Loading," *IEEE Transactions on Robotics*, vol. 27, no. 6, pp. 1033–1044, Dec. 2011.
- [175] J. G. Ruitter, G. M. Bonnema, M. C. van der Voort, and I. A. M. J. Broeders, "Robotic control of a traditional flexible endoscope for therapy," *Journal of Robotic Surgery*, vol. 7, no. 3, pp. 227–234, Sep. 2013.
- [176] M. Runciman, A. Darzi, and G. P. Mylonas, "Soft Robotics in Minimally Invasive Surgery," *Soft Robotics*, vol. 6, no. 4, pp. 423–443, Aug. 2019.
- [177] D. Rus and M. T. Tolley, "Design, fabrication and control of soft robots," *Nature*, vol. 521, no. 7553, pp. 467–475, May 2015.
- [178] Z. Ruzhen, Y. Yao, and Y. Luo, "Development of a Variable Stiffness Over Tube Based on Low-Melting-Point-Alloy for Endoscopic Surgery," *Journal of Medical Devices*, vol. 10, Feb. 2016.
- [179] K. R. Ryan, M. P. Down, N. J. Hurst, E. M. Keefe, and C. E. Banks, "Additive manufacturing (3D printing) of electrically conductive polymers and polymer nanocomposites and their applications," *eScience*, vol. 2, no. 4, pp. 365–381, Jul. 2022.
- [180] J. Ryu, H. Y. Ahn, H. Y. Kim, and J. H. Ahn, "Analysis and simulation of large deflection of a multi-segmented catheter tube under wire tension," *Journal of Mechanical Science and Technology*, vol. 33, no. 3, pp. 1305–1310, Mar. 2019.
- [181] M. Saif, "On a tunable bistable MEMS-theory and experiment," *Journal of Microelectromechanical Systems*, vol. 9, no. 2, pp. 157–170, Jun. 2000.
- [182] V. D. Sars, S. Haliyo, and J. Szewczyk, "A practical approach to the design and control of active endoscopes," *Mechatronics*, no. 2, pp. 251–264, Mar. 2010.
- [183] J. Seetohul and M. Shafiee, "Snake Robots for Surgical Applications: A Review," *Robotics*, vol. 11, no. 3, p. 57, Jun. 2022.
- [184] C. Seneci, J. Shang, and G.-Z. Yang, "Design of a Bi-Manual End-Effector for an Endoscopic Surgical Robot," in *Surgical Endoscopy*, vol. 26, Apr. 2012, pp. 1010–1020.
- [185] J. Shang, D. Noonan, C. Payne, J. Clark, M. Sodergren, A. Darzi, and G.-Z. Yang, "An articulated universal joint based flexible access robot for minimally invasive surgery," in *2011 IEEE International Conference on Robotics and Automation*, May 2011.

## Bibliography

---

- [186] V. Shanmugam, O. Das, K. Babu, U. Marimuthu, A. Veerasimman, D. J. Johnson, R. E. Neisiany, M. S. Hedenqvist, S. Ramakrishna, and F. Berto, "Fatigue behaviour of FDM-3D printed polymers, polymeric composites and architected cellular materials," *International Journal of Fatigue*, vol. 143, 2021.
- [187] S. Shin and H. So, "Time-dependent motion of 3D-printed soft thermal actuators for switch application in electric circuits," *Additive Manufacturing*, vol. 39, p. 101893, Mar. 2021.
- [188] J. Shintake, H. Sonar, E. Piskarev, J. Paik, and D. Floreano, "Soft pneumatic gelatin actuator for edible robotics," in *2017 IEEE/RSJ International Conference on Intelligent Robots and Systems (IROS)*, Sep. 2017, pp. 6221–6226.
- [189] B. Siciliano, L. Sciavicco, L. Villani, and G. Oriolo, *Robotics modelling, planning and control*, ser. Advanced Textbooks in Control and Signal Processing, M. J. Grimble and M. A. Johnson, Eds. London: Springer London, 2009.
- [190] N. Simaan, K. Xu, A. Kapoor, W. Wei, P. Kazanzides, P. Flint, and R. Taylor, "Design and Integration of a Telerobotic System for Minimally Invasive Surgery of the Throat," *The International journal of robotics research*, vol. 28, no. 9, pp. 1134–1153, Sep. 2009.
- [191] N. Simaan, R. M. Yasin, and L. Wang, "Medical Technologies and Challenges of Robot-Assisted Minimally Invasive Intervention and Diagnostics," *Annual Review of Control, Robotics, and Autonomous Systems*, vol. 1, no. 1, pp. 465–490, May 2018.
- [192] M. A. Skylar-Scott, J. Mueller, C. W. Visser, and J. A. Lewis, "Voxelated soft matter via multimaterial multinozzle 3D printing," *Nature*, vol. 575, no. 7782, pp. 330–335, Nov. 2019.
- [193] M. Sobczyk and T. Wallmersperger, "Modeling and simulation of the electro-chemical behavior of chemically stimulated polyelectrolyte hydrogel layer composites," *Journal of Intelligent Material Systems and Structures*, vol. 27, no. 13, pp. 1725–1737, Aug. 2016.
- [194] B. SP and R. Bharanidaran, "Design and testing of a compliant mechanism-based XY stage for micro/nanopositioning," *Australian Journal of Mechanical Engineering*, vol. 20, no. 4, pp. 1185–1194, Aug. 2022.
- [195] M. Stranczl, E. Sarajlic, M. Gijs, and C. Yamahata, "High-Angular-Range Electrostatic Rotary Stepper Micromotors Fabricated With SOI Technology," *IEEE/ASME Journal of Microelectromechanical Systems*, vol. 21, pp. 605–620, Jun. 2012.
- [196] H.-J. Su, "A Pseudorigid-Body 3R Model for Determining Large Deflection of Cantilever Beams Subject to Tip Loads," *Journal of Mechanisms and Robotics*, vol. 1, no. 2, Jan. 2009.
- [197] H.-J. Su, D. Dorozhkin, and J. Vance, "A Screw Theory Approach for the Conceptual Design of Flexible Joints for Compliant Mechanisms," *ASME Journal of mechanisms and robotics*, vol. 1, pp. 041 009–1, Nov. 2009.

- 
- [198] H.-J. Su, H. Shi, and J. Yu, "A Symbolic Formulation for Analytical Compliance Analysis and Synthesis of Flexure Mechanisms," *Journal of Mechanical Design*, vol. 134, no. 5, 2012.
- [199] V. A. Sujan and S. Dubowsky, "Design of a Lightweight Hyper-Redundant Deployable Binary Manipulator," *Journal of Mechanical Design*, vol. 126, no. 1, pp. 29–39, Mar. 2004.
- [200] S. Tappe, M. Dörbaum, J. Kotlarski, B. Ponick, and T. Ortmaier, "Kinematics and dynamics identification of a hyper-redundant, electromagnetically actuated manipulator," in *2016 IEEE International Conference on Advanced Intelligent Mechatronics (AIM)*, Jul. 2016, pp. 601–607.
- [201] R. H. Taylor, A. Menciassi, G. Fichtinger, P. Fiorini, and P. Dario, "Medical Robotics and Computer-Integrated Surgery," in *Springer Handbook of Robotics*, ser. Springer Handbooks, B. Siciliano and O. Khatib, Eds., 2016.
- [202] T. G. Thuruthel, E. Falotico, M. Manti, A. Pratesi, M. Cianchetti, and C. Laschi, "Learning Closed Loop Kinematic Controllers for Continuum Manipulators in Unstructured Environments," *Soft Robotics*, Sep. 2017.
- [203] S. Timoshenko, *History of Strength of Materials: With a Brief Account of the History of Theory of Elasticity and Theory of Structures*. Courier Corporation, Jan. 1983.
- [204] S. P. Timoshenko and J. M. Gere, *Theory of Elastic Stability*. New York: McGraw-Hill, 1961.
- [205] N. D. K. Tran and D.-A. Wang, "Design of a crab-like bistable mechanism for nearly equal switching forces in forward and backward directions," *Mechanism and Machine Theory*, vol. 115, pp. 114–129, 2017.
- [206] J. Troccaz, G. Dagnino, and G.-Z. Yang, "Frontiers of Medical Robotics: From Concept to Systems to Clinical Translation," *Annual Review of Biomedical Engineering*, vol. 21, no. 1, pp. 193–218, Jun. 2019.
- [207] O. Ulkir, "Design and fabrication of an electrothermal MEMS micro-actuator with 3D printing technology," *Materials Research Express*, vol. 7, no. 7, Jul. 2020.
- [208] M. Vangbo, "An analytical analysis of a compressed bistable buckled beam," *Sensors and Actuators A: Physical*, vol. 69, no. 3, pp. 212–216, Sep. 1998.
- [209] E. Vazquez, C. Randall, and J. Pinto Duarte, "Shape-changing architectural skins: a review on materials, design and fabrication strategies and performance analysis | Journal of Facade Design and Engineering," 2019.
- [210] V. Vitiello, S.-L. Lee, T. P. Cundy, and G.-Z. Yang, "Emerging Robotic Platforms for Minimally Invasive Surgery," *IEEE Reviews in Biomedical Engineering*, vol. 6, pp. 111–126, 2013.

## Bibliography

---

- [211] S. Wakimoto, J. Misumi, and K. Suzumori, "New concept and fundamental experiments of a smart pneumatic artificial muscle with a conductive fiber," *Sensors and Actuators A: Physical*, vol. 250, pp. 48–54, Oct. 2016.
- [212] Z. Wang, Z. Sun, and S. J. Phee, "Haptic feedback and control of a flexible surgical endoscopic robot," *Computer Methods and Programs in Biomedicine*, vol. 112, no. 2, pp. 260–271, Nov. 2013.
- [213] R. J. Webster and B. A. Jones, "Design and Kinematic Modeling of Constant Curvature Continuum Robots: A Review," *The International Journal of Robotics Research*, vol. 29, no. 13, pp. 1661–1683, Nov. 2010.
- [214] R. J. Webster, A. M. Okamura, and N. J. Cowan, "Toward Active Cannulas: Miniature Snake-Like Surgical Robots," in *2006 IEEE/RSJ International Conference on Intelligent Robots and Systems*, Oct. 2006, pp. 2857–2863.
- [215] J. Wu, S. Yan, J. Li, and Y. Gu, "Mechanism reliability of bistable compliant mechanisms considering degradation and uncertainties: Modeling and evaluation method," *Applied Mathematical Modelling*, vol. 40, no. 23-24, 2016.
- [216] K. Xu and N. Simaan, "Intrinsic Wrench Estimation and Its Performance Index for Multisegment Continuum Robots," *IEEE Transactions on Robotics*, vol. 26, no. 3, pp. 555–561, Jun. 2010.
- [217] Q. Xu, "Design and Development of a Compact Flexure-Based XY Precision Positioning System With Centimeter Range," *IEEE Transactions on Industrial Electronics*, vol. 61, no. 2, pp. 893–903, Feb. 2014.
- [218] W. Xu, J. Chen, H. Y. Lau, and H. Ren, "Data-driven methods towards learning the highly nonlinear inverse kinematics of tendon-driven surgical manipulators," *The International Journal of Medical Robotics and Computer Assisted Surgery*, vol. 13, no. 3, p. e1774, 2017.
- [219] H. D. Yang, B. T. Greczek, and A. T. Asbeck, "Modeling and Analysis of a High-Displacement Pneumatic Artificial Muscle With Integrated Sensing," *Frontiers in Robotics and AI*, vol. 5, 2019.
- [220] Z. Yang, R. Lee, and J. B. Hopkins, "Hexblade positioner: A fast large-range six-axis motion stage," *Precision Engineering*, vol. 76, pp. 199–207, Jul. 2022.
- [221] O. D. Yirmibesoglu, J. Morrow, S. Walker, W. Gosrich, R. Cañizares, H. Kim, U. Daalkhaijav, C. Fleming, C. Branyan, and Y. Menguc, "Direct 3D printing of silicone elastomer soft robots and their performance comparison with molded counterparts," in *2018 IEEE International Conference on Soft Robotics (RoboSoft)*, Apr. 2018, pp. 295–302.
- [222] Q. Yongqiang, Y. Hailan, R. Dan, K. Yi, L. Dongchen, L. Chunyang, and L. Xiaoting, "Path-Integral-Based Reinforcement Learning Algorithm for Goal-Directed Locomotion of Snake-Shaped Robot," *Discrete Dynamics in Nature and Society*, vol. 2021, Feb. 2021.

- 
- [223] H. Yuan and Z. Li, “Workspace analysis of cable-driven continuum manipulators based on static model,” *Robotics and Computer-Integrated Manufacturing*, vol. 49, pp. 240–252, Feb. 2018.
- [224] M. Zanaty, “Programmable Multistable Mechanisms: Synthesis and Modeling,” Ph.D. dissertation, EPFL, 2018.
- [225] M. Zanaty, T. Fussinger, A. Rogg, A. Lovera, D. Lambellet, I. Vardi, T. J. Wolfensberger, C. Baur, and S. Henein, “Programmable Multistable Mechanisms for Safe Surgical Puncturing,” *Journal of Medical Devices*, vol. 13, no. 2, Jun. 2019.
- [226] M. Zanaty, H. Schneegans, I. Vardi, and S. Henein, “Reconfigurable Logic Gates Based on Programmable Multistable Mechanisms,” *Journal of Mechanisms and Robotics*, vol. 12, no. 2, Feb. 2020.
- [227] Z. Zhang, Y. Yu, X. Liu, and X. Zhang, “Dynamic modelling and analysis of V- and Z-shaped electrothermal microactuators,” *Microsystem Technologies*, vol. 23, no. 8, pp. 3775–3789, Aug. 2017.
- [228] Z. Zhang, W. Zhang, Q. Wu, Y. Yu, X. Liu, and X. Zhang, “Closed-form modelling and design analysis of V- and Z-shaped electrothermal microactuators,” *J. Micromech. Microeng.*, p. 13, 2017.
- [229] Y. Zhong, R. Du, L. Wu, and H. Yu, “A Novel Articulated Soft Robot Capable of Variable Stiffness through Bistable Structure,” in *2020 IEEE International Conference on Robotics and Automation (ICRA)*, May 2020.
- [230] J. Zhu, G. Hao, S. Li, S. Yu, and X. Kong, *A Mirror-Symmetrical XY Compliant Parallel Manipulator With Improved Performances Without Increasing the Footprint*, Aug. 2021.
- [231] Y. Zhuang, W. Song, G. Ning, X. Sun, Z. Sun, G. Xu, B. Zhang, Y. Chen, and S. Tao, “3D-printing of materials with anisotropic heat distribution using conductive polylactic acid composites,” *Materials & Design*, vol. 126, pp. 135–140, Jul. 2017.
- [232] S. A. Zirbel, K. A. Tolman, B. P. Trease, and L. L. Howell, “Bistable Mechanisms for Space Applications,” *PLOS ONE*, vol. 11, no. 12, Dec. 2016.

## **Bibliography**

---